İSTANBUL TEKNİK ÜNİVERSİTESİ ★ FEN BİLİMLERİ ENSTİTÜSÜ

SİLİNDİRLER ETRAFINDA AYRILMIŞ AKIŞLARIN SİMULASYONU

Yüksek Lisans Tezi

Ali Ruhşen ÇETE, Müh.

Ana Bilim Dalı : UÇAK MÜHENDİSLİĞİ

Programı : UÇAK MÜHENDİSLİĞİ

ŞUBAT 1995

ISTANBUL TECHNICAL UNIVERSITY ★ INSTITUTE OF SCIENCE AND TECHNOLOGY

SIMULATION OF SEPARATED FLOW AROUND CYLINDERS

M.Sc. THESIS

Ali Ruhşen ÇETE, B.Sc.

Date of Submission : JANUARY 13, 1995

Date of Approval : FEBRUARY 03, 1995

Superviser : Prof.Dr. M. Fevzi ÜNAL

Member : Assoc.Prof.Dr. Veysel ATLI

Member : Asst.Prof.Dr. Savaş AYDÖRE

FEBRUARY 1995

ACKNOWLEDGEMENTS

I would like to thank my supervisor Prof. M. Fevzi ÜNAL for his valuable support, encouragement and guidance during this study. Then I would like to thank Assoc.Prof. Rüstem ASLAN for his encouragement, impetus and friendship.

I would like to thank my dear friends and colleagues Cuma YARIM, Aydın MISIRLIOĞLU, Murat VURAL and Alpay YILMAZ for their friendships and help.

Of course I am thankful to my parent for everything they have done for me. I know that to thank is not enough so I would like to dedicate this thesis and my future studies to my lovely wife Hülya who is the most beautiful thing in my life and always by me for everything.

CONTENTS

SUMMARY

In this study, separated flows around various cylinders have been investigated, these are an aerofoil and the circular cylinder with and without splitter plate. In general, the vortex formation mechanisms of separated flows and fluctuating forces created by them have been studied and the methods for the control of these mechanisms have been tried. It was firstly worked on the flow around plane circular cylinder in order to test the method and to take into account a basic case of the separated flow. As a result of this investigation the success of the method was provide and near and far wake vortex structure were held in addition.

The next step is to investigate the oscillatory flow around a circular cylinder which is a passive control of wake. The results of different oscillation frequency were obtained and compared. The conclusion can be drawn here as follows, the near wake region is more sensitive to the effect of oscillation than the far wake region is, where Von Karman vortex street is always observed. The next study is to control of the wake by means of attaching splitter plate in different lengths to the circular cylinder. The result is obtained and compared for different plate lengths. The longer splitter plate results in the narrower wake and reduction of the forces on the body.

The last study is to investigate the separated flow around airfoil for low Reynolds number (Re = 1000) for different angles of the attack the flow around airfoil was solved for the incidence among 0° and 24° and the results were analyzed with respect to incidence variation. As the incidence increases the character of flow around slender body turns into the flow around the bluff body.

In this study, two different numerical method have been used, the first one is Lagrangian Discrete Vortex Method which was for the circular cylinder with and without splitter plate. In the second one is Viscous Discrete Vortex Method, which was used for the calculations of the flow around airfoil.

ÖZET

IZ AKIŞLARI VE İZİN KONTROLÜ

Küt cisimler etrafındaki akış ve bu akışın oluşturduğu iz bölgesi birçok mühendislik dalının ilgi alanına girmektedir. Yüksek binaların rüzgar etkisi altındaki tasarımı veya ısı değiştiricilerinin tasarımı bu konunun inşaat mühendisliğinden makina mühendisliğine kadar uzanan geniş bir uygulama alanını göstermektedir. Uçak mühendisliğinde de aerodinamiğin bir kolu küt cisimler etrafındaki akışla ve bu akışın izi ile ilgilidir. Akıma uygun profil tipindeki yapılar yanında bir küt cisim olarak dairesel silindirin akışkanlar mekaniğinde özel bir yeri vardır. Çünkü dairesel silindir, geometrisi sebebiyle geniş bir fiziksel uygulama sahasına haizdir. Isı değiştirici tüp demetleri, denizaltı yapılarının bağlantı elemanları veya köprü ayaklarının suyun içinde kalan bölümleri etrafındaki akışlar bunun en çok bilinen örnekleridir. İlmi çalışmalarda da, bu özelliğinden dolayı, üzerinde en çok çalışma yapılan küt cisim olmuştur. 100 yılı aşkın bir zamandır yapılan deneylerle, ve tabii ki analitik çalısmalarla, hemen hemen tüm akış karakterlerinin belirlendiği dairesel silindir, geliştirilen her yeni yöntemin de ilk uygulandığı ve denendiği geometri olmuştur. Bu NACA0012 içinde böyledir ve çoğu çalışmada bu profil yöntemin sınanması için kullanılır.

Tasarım ve geliştirme açısından küt cisimlerin izinin kontrolü de geniş bir uygulama alanına sahiptir. Aktif ve pasif olarak ikiye ayrılabilecek olan kontrol, pasif olarak;

- Akım alanına dışardan akışkan üflenmesi
- Akım alanından akışkan emilmesi
- Cismin ısıtılması veya soğutulması
- Akım alanına farklı bir akışkan enjekte edilmesi
- Akım alanına ses dalgalarının gönderilmesi vs...
- Akım alanına ikinici bir cismin yerleştirilmesi
- Cismin şeklinin değiştirilmesi cismin ardına ayırıcı bir levha bağlanması vs...

başlıkları altında toplanabilir.

Bir dairesel silindir etrafındaki akış tanımlanmak istenirse ; Akışkan parçacığı ön durma noktasından itibaren 90°'ye kadar hızlanır. Buradan itibaren ise yavaşlamaya başlar. Viskozite etkisi olmayan bir durumda akım cisim cidarını takip ederek arka durma noktasına kadar gelir ve akım üstü bölgesinde izlediğinin tam simetriği bir yol izleyerek akım altına ilerler. Bu duruma bakıldığında silindir etrafındaki akış tam simetriktir. Fakat gerçekte mükemmel akışkan akışından farklı olarak, viskozite etkisi cisim üzerinde çok ince bir tabakada (sınır tabaka) yoğunlaşmıştır. Bu tabaka içindeki sürtünme kuvvetleri akışkan parçacığını yavaşlatır. Bu kuvvetler sebebiyle akışkan parçacığı ön durma noktasından 90°'ye gelene kadar kinetik enerjisinin büyük bir kısmını kaybeder. Kalan kinetik enerji ise, akışkan parçacığını cismin cidarında tutmaya yetecek kadar yüksek değildir. Böylece dış basınç akışkanı ters yönde haraket etmeye zorlar ve akışkan cidardan ayrılır. Bu hadiseye, dairesel silindir için sınır tabaka ayrılması denir. Alt ve üst yarıdan ayrılan sınır tabakalar, kararsızlıkları sebebiyle gelişip vorteks (girdap) denilen yapıları oluştururlar. Bu yapıların alt ve üstten periyodik olarak ayrılması ve akım alanında ilerlemesi ile küt cisim için iz yapısı oluşur. Bu yapıya Von Karman Caddesi adı verilir. Periyodik olarak ayrılan vorteksler cisim üzerinde çalkantılı taşıma ve sürükleme kuvvetlerinin doğmasına yol açarlar. İz kontrolünün de amacı bu yapıya etki ederek akım karakterlerinin iyileştirilmesini sağlamaktır. Yani sürükleme ve taşıma kuvvetlerini hem azaltmak hem de çalkantılarını düşürmek, vorteks oluşum frekansını kontrol altına almaktır.

Bu çalışmada ikiside ayrık vorteks yöntemi grubu içinde yer alan 'Lagrange'sal-Euler'sel' hibrid, viskoz ayrık vorteks yöntemi ve 'Lagrange' sal ayrık vorteks yöntemleri kullanılmıştır. Özellikle küt cisim aerodinamiği konusunda, önemli sayıda araştırmacı, 'Lagrange' sal ayrık vorteks yönteminin, iligilenilen cismin etrafında bir ağ yapısı oluşturulmasını gerektiren 'Euler' yaklaşımına göre sağladığı kolaylıktan yararlanmakta ve örneğin, deneysel olarak gözlenen iz akışı global yapısını başarıyla hesaplayabilmektedir. Ayrık vorteks yönteminde temel kabul, içinde sürekli bir çevri dağılımı bulunan sonlu kalınlıktaki ayrılmış sınır tabakanın bir dizi noktasal vorteksle temsil edilebileceğidir. Böylece, tabakanın zaman içindeki gelişimi, noktasal vortekslerin birbirlerine indüklediği hızların potansiyel teori yardımıyla bulunması ve her hesaplama adımı sonundaki yeni konumlarına ilerletilmesi ile belirlenebilmektedir. Rosenhead, birbirlerine ters yönde ve eşit hızlara sahip iki üniform akımı ayıran yüzeyi bu şekilde modellemiş ve potansiyel vorteks dizisinin, sinüzoidal bir başlangıç bozuntusuna, kıvrılarak vorteks kümesi oluşturma şeklinde cevap verdiğini göstermiştir. Ancak daha sonra, Birkhoff ve Fisher' in daha hassas olarak tekrarladığı hesaplama, noktasal vortekslerin kümeleşerek büyük ölçek vorteksler oluşturmakla beraber, hareketlerinin düzensiz olduğunu ve kümeleşme sırasında yörüngelerinin birbirlerini kestiğini göstermiştir. Bu davranışın önlenmesi, her hesap adımı sonunda noktasal vorteks konumlarının, sirkülasyon dağılımı ve sirkülasyon birinci momentini korumak üzere düzenlenmesini gerektirmektedir. Abernathy ve Kronauer, Rosenhead (Sarpkaya, 1989' da atıfta bulunulmuştur) tarafından önerilen yöntemi bir adım ileriye götürerek, küt cisim iz akışı oluşumunu, birbirlerine paralel, sonsuz uzunluktaki iki noktasal vorteks dizisinin etkileşimi şeklinde modellemiştir. Model, deneysel çalışmalarda gözlenen, iz akışının akımaltı doğrultuda genişlemesi gibi bazı özelliklerle uyum içinde sonuçlar üretmektedir. Ancak, vorteks dizisi sistemi, deneysel çalışmalarda rastlananın aksine, belirli bir frekansta değil, çalışmada denenen tüm frekanslarda vorteks caddesi benzeri bir yapının oluşumuna yol açmaktadır. Clements (1973), daha gerçekci bir modelleme ile, sonsuz genişlikteki bir bölge içindeki sonsuz uzunluktaki vorteks dizileri yerine, küt cismi temsil etmek üzere, katı bir cidarla sınırlı bir bölge içine, akım ayrılma noktalarından belirli zaman aralıklarıyla bırakılan noktasal vorteksler halini göz önüne almıştır. Bu durumda da, noktasal vortekslerin anlık dağılımı, vortekslerin birbirlerine indüklediği hızlar uyarınca bulunmaktadır. Ancak, katı cidarı temsil etmek için, cisim içinde bulunduğu düşünülen imaj vorteksler, cisim civarındaki hız alanını önemli ölçüde değiştirmektedir. Daha da önemlisi, artık noktasal vorteks dizileri, başlangıç bozuntusundan bağımsız olarak, belirli bir frekansta vorteks kümesi oluşumuna izin vermektedir. Bu uygulamada belirlenen, boyutsuz vorteks oluşum frekansı *(St)* deneysel çalışmalarda belirlenenle büyük bir uyum içindedir. Clements (1973) tarafından yapılan bu çalışma, aynı yöntemin kullanıldığı ve birden çok cismin etkileşimli iz akışı gibi daha karmaşık problemlerin ele alındığı çok sayıdaki araştırmaya esin kaynağı olmuştur.

Ancak, iz akışının kararlılık analizi açısından sahip olduğu öneme karşın, ortalama hız dağılımının, ayrık vorteks yöntemiyle ne derece doğru hesaplanabildiği konusuna ilişkin bir çalışma literatürde bulunmamaktadır. Burada sunulan çalışmada, iz bölgesi ortalama hız alanı belirlenmekte ve ayrıca çalkantı hızlarının akıma dik doğrultudaki davranışına da değinilmektedir. Ayrıca, içinde yer aldığı serbest akıma, bu akım boyunca sinüzoidal salınımlar verilmesinin dairesel bir silindirin iz yapısı ve yüklenmesine etkisi Lagrange'sal ayrık vorteks yöntemi ile araştırılmaktadır. Salınımsız haldeki doğal vorteks oluşum frekansının tam katlarındaki salınımlar göz önüne alınmaktadır. Salınım etkisi ile ortaya çıkan küçük ölçek vortekslerin etkileşimleri sonucu, büyük ölçek vorteks oluşum frekansının salınımsız hale göre önemli bir farklılık göstermediği ve global iz akışının bütün salınım frekansları için üniversal bir yapıya (klasik Von Karman vorteks caddesine) kavuştuğu gösterilmektedir.

Literatürde ayırıcı levha dairesel silindir etkileşimi üzerinde çok fazla sayıda çalışma bulunmamaktadır. Deneysel olarak iki çalışma yapılmıştır. Ilki 1954 de Roshko, ikincisi 1973 de Apelt, West ve Sczewczyk tarafından yapılan bu deneylerde ayırıcı levhanın sürükleme kuvvetini azalttığı ve Strouhal sayısını düşürdüğü görülmüştür. Kawai tarafından yapılan 1990 da yapılan sayısal çalışmalarda ise bunlara ek olarak taşıma kuvvetinin çalkantısının da düştüğü gözlemlenmiştir. Ancak çalkantıdaki bu düşüş ayırıcı levhayı ayrı bir cisim olarak ele alıp, silindire monte edilmemiş gibi kabul edilmesi sebebiyledir. Aslında ayırıcı levha sebebiyle cisim üzerindeki taşıma kuvvetinde artış olacaktır. Bu, Bearman tarafında Imperial College'de yapılan, yayınlanmamış , deneylerde de görülmüştür.

Çalışmada elde dilen sonuçların, bu konu üzerinde yapılan deneylerle karşılaştırıldığında, deney sonuçları ile iyi bir uyum içinde olduğu görülmüştür. Ize yerleştirilen ayırıcı levhanın sürükleme kuvvetini düşürdüğü ve vorteks oluşum frekansını azalttığı, sürükleme ve taşıma kuvvet katsayıları C_D ve C_L'nin zamana bağlı değişimlerinden görülebilir. Ayrıca yine deneylerde görüldüğü gibi taşıma kuvveti çalkantısının da artan ayırıcı levha boyuyla arttığı bulunmuştur.

Çalışmanın son kısmında, 'Lagrange'sal-Euler'sel' hibrid, viskoz ayrık vorteks yöntemi yardımıyla, NACA0012 etrafında düşük Reynolds sayısındaki akış incelenmiştir. Profil etrafında düşük Reynolds sayılarındaki akış konusunda literatürde yeteri sayıda çalışmaya rastlanmammaktadır. Burada, profil etrafında girdap ve sonuç olarak kuvvet çalkantıları oluşum mekanizması detaylı olarak incelenmiş, ve düşük Reynolds sayılı profil etrafındaki akışların yüksek Reynolds sayılı akışlardan farkları vurgulanmıştır. Ayrıca hücüm açısının değişimide gözönüne alınarak 0°'den 24°'ye kadar 15 değişik hücüm açısında çözümler elde edilerek, genel olarak narin cisimden küt cisime geçiş incelenmiş ve yukarda bahsedilen yüksek Reynolds sayılı, düşük Reynolds sayılı akış karşılaştırması hücüm açısı değişimi büyüklüğüne göre yapılmıştır.

Düşük Reynolds sayılarında, stall yüksek Reynolds sayılı akıştan oldukça geç oluşmaktadır (22°). Hücum açısının 8° değerinden itibaren gözlenmeye başlanan hücum kenarı ayrılması kendini, kuvetlerin çalkantısını artırmada göstermektedir ve 22° civarında çalkantının miktarı ortalama kuvvetin %20'ne kadar yükselmektedir.

Profil etrafındaki akışı çözdüğümüz yöntem ilk yöntemin aksine viskoziteyi göz önüne almaktadır. Yöntem iki boyutlu Navier–Stokes denklemlerinden elde edilen Girdaplılıgın Taşınımı Denklemini'ni (GTD) (Vorticity Transport Equation) çözer. İki boyutta Navier-Stokes denklemleri;

$$\frac{\partial u}{\partial t} + u\frac{\partial u}{\partial x} + v\frac{\partial u}{\partial y} = -\frac{1}{\rho}\frac{\partial p}{\partial x} + \nu\left[\frac{\partial^2 u}{\partial x^2} + \frac{\partial^2 u}{\partial y^2}\right]$$

$$\frac{\partial v}{\partial t} + u\frac{\partial v}{\partial x} + v\frac{\partial v}{\partial y} = -\frac{1}{\rho}\frac{\partial p}{\partial y} + \nu\left[\frac{\partial^2 v}{\partial x^2} + \frac{\partial^2 v}{\partial y^2}\right] \qquad (1)$$

şeklindedir. Bu denklemlerin çapraz türevleri alınır ve basınç terimi yok edilirse GTD elde edilir:

$$\frac{\partial \omega}{\partial t} + (\vec{U}\,\nabla)\,\omega = \nu\,\nabla^2\,\omega \qquad (2)$$

Bu denklem Difüzyon (3) ve Taşınım (4) olarak iki parçaya ayrılabilir.

$$\frac{\partial\omega}{\partial t} = \frac{1}{Re} \nabla^2 \omega \tag{3}$$

$$\frac{\partial\omega}{\partial t} = -(\vec{U} \nabla) \omega \tag{4}$$

Bu parçaların ayrı ayrı çözümlerinin toplamı ise tüm denklemin bir çözümüdür. Bu, non--lineer yapıdaki taşınım terimini esas denklemden ayırarak çözüm kolaylığı sağlar. Ayrıca yöntemin, difüzyon ve taşınım için değişik çözüm teknikleri ve değişik yaklaşımlar kullanılmasına da izin vermesi bir diğer avantajıdır. Bu çalışmada tercih edilen, difüzyonun Euler'sel, taşınımın ise Lagrange'sal yaklaşımla çözümü yönteme melez bir yapı kazandırır.

Bu denklemler iteratif veya doğrudan metodlarla çözülebilir. Bu çalışmada eliptik yapıdaki Poisson denkleminin çözümü için ÇFD (Fast Fourier Transform) kullanılmıştır. Her bir ağ noktasındaki akım fonksiyonu değerleri elde edildikten sonra difüzyon denkelemi için sınır şartı koyulur. Bu şart duvarda, yani cisim cidarında, kaymama şartıdır (9). Bu şart altında ağ üzerinde difüzyon uygulanıp tekrar Poisson denklemi çözülür ve yeni akım fonksiyonu değerleri bulunur.

Taşınım için yapılan modelleme 1950'lerin başında ortaya atılan ve zamanla gelişip çok popüler olan Hücre içinde Girdap (Vortex--in--Cell) tekniğidir. Bu teknikte her bir vorteks içinde bulunduğu hücrenin köşeleriyle etkileşim halindedir. Poisson denkleminin ve difüzyonun çözümünde kullanılan ag noktasındaki çevri degerleri vortekslerin hücre içindeki konumuna göre alan interpolasyonuyla köşelere dağıtılır. Daha sonra akım fonksiyonu degerlerinden ağ noktası hızları bulunur. Bu hızlardan tekrar geriye interpolasyonla vorteksler üzerine indüklenen hızlara geçilir ve taşınım sağlanır.

Bu teknikle, Biot--Savart indüksiyon metodunda olduğu gibi her bir vorteks üzerindeki hız diğer vortekslerin etkisiyle hesaplanmaz. Bu yüzden merkezi işlem zamanı bir hayli kısalmaktadır. Biot--Sawart indüksiyon ile gereken ortalama işlem sayısı N^2 (N Vorteks sayısı) iken, bu yöntemde M $\log_2$ M (M ağ nokta sayısı) dir.

Özetle, bu çalışmada iki-boyutlu dairesel yapıların iz akışı ve iz kontrolü incelenmiştir. Önce sabit dairesel silindir etrafında akış incelenmiş ve bu referans alınarak kullanılan yöntem geliştirilmiş sonra bir basamak ilerleyerek bir iz kontrol yöntemi olan çalkantılı akış içindeki dairesel silindir etrafındaki akış incelenmiş ve dairesel silindir etrafındaki akışlara daha kapsamlı olan ayırıcı levhalı dairesel silindir etrafındaki akışlarda incelenerek nokta konulmuştur. Son olarak bir pasif iz kontrol yöntemi olan ayırıcı levha ekli dairesel silindir incelenmiştir. Bundan sonra çok yaygın olarak bilinen NACA 0012 profili etrafındaki akışa hücüm açısı etkisi incelenmiştir.

CHAPTER 1

MECHANISM OF VORTEX FORMATION FROM BLUFF BODIES

1.1.Boundary Layer Separation

The behaviour of a boundary layer in a positive pressure gradient, i.e. pressure increasing with increasing in distance downstream, may be considered with reference to Fig.[1.1], which shows a length of surface which has a gradual but steady convex curvature, such as the surface of an aerofoil beyond the point of maximum thickness. In such a flow region, because of the retardation of the mainstream flow, the static pressure in the mainstream will rise (Bernoulli's equation). The variation in static pressure along a normal to the surface through the boundary layer thickness is essentially zero, so that the pressure at any point in the mainstream, adjacent to the edge of the boundary layer, is transmitted unaltered through the layer to the surface. In the light of this, consider the small element of fluid (Fig.[1.1]), marked ABCD. On face AC, the pressure is p, while on face BD the pressure has increased to $p+(\partial p/\partial x)\delta x$. Thus the net pressure force on the element is tending to retard its velocity. This retarding force is in addition to the viscous shears which act along AB and CD and it will continuously slow the element down as it progresses downstream.

This slowing down effect will be more pronounced near the surface where the elements are remote from the accelerating effect, via shearing actions, of the mainstream, so that successive profile shapes in the streamwise direction will change as shown in Fig.[1.1].

Ultimately, at a point S on the surface, the profile slope $(\partial u/\partial y)_w$ becomes zero. Apart from the change in shape of the profile it thickens rapidly under these conditions, in order to satisfy continuity within the layer. Downstream of point S, the flow adjacent to the surface may well be in an upstream direction, so that a circulatory movement, in a plane normal to the surface, may take place near the surface. A line (shown dotted in Fig.[1.1]) may be drawn from the point S such that the mass flow above this line corresponds to the mass flow ahead of point S. The line represents the continuation of the lower surface of the upstream boundary layer, so that, in effect, the original boundary layer separates from the surface at point S. This is termed the separation point.

Reference to the velocity profiles for laminar and turbulent layers (Fig.[1.1] and Fig.[1.2]) makes it clear that, due to a greater extent of lower energy fluid near the surface

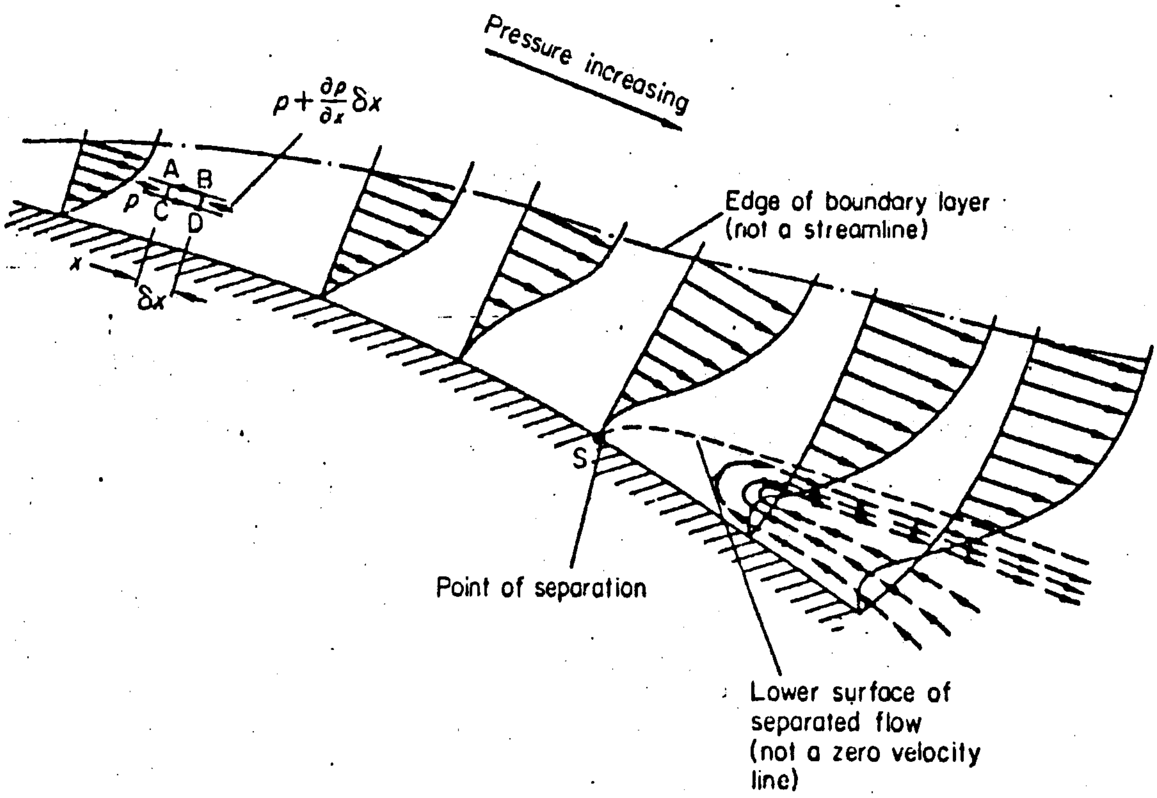

Figure 1.1 Mechanism of Separation (Houghton & Carpenter, 1993).

under, the effect of a positive pressure gradient a turbulent layer sticks to the surface better than a laminar one.

The result of separation on the rear half of an aerofoil is to increase the thickness of the wake flow, with a consequent reduction in the pressure rise near the trailing edge. In other words, the forward acting pressure force components on the rear part of the aerofoil can not offset the rearward acting pressures near the front stagnation point, and the pressure drag of the aerofoil increases. In face, of boundary layers, there would be a stagnation point at the trailing edge and the boundary layer pressure drag, as well as the surface friction drag, would be zero. If the aerofoil incidence is sufficiently large, the separation may take place close to the minimum pressure (maximum suction) point, and thus a large wake may develop. This will cause such a redistribution of the flow over the aerofoil that the large low pressure field at the upper surface leading is seriously reduced, with an accompanying reduction in the lift force. This condition is referred to as the stall. A negative pressure gradient will obviously have the reverse effect, since the streamwise pressure forces will cause energy to be added to the slower moving fluid near the surface, decreasing any tendency for the layer adjacent to the surface to come to rest.

1.1.2 Separation Bubbles

On many aerofoils, with relatively large upper surface curvatures, high local curvature over the forward part of the chord may initiate a laminar separation when the aerofoil is at quite a moderate angle of incidence (Fig.[1.2]).

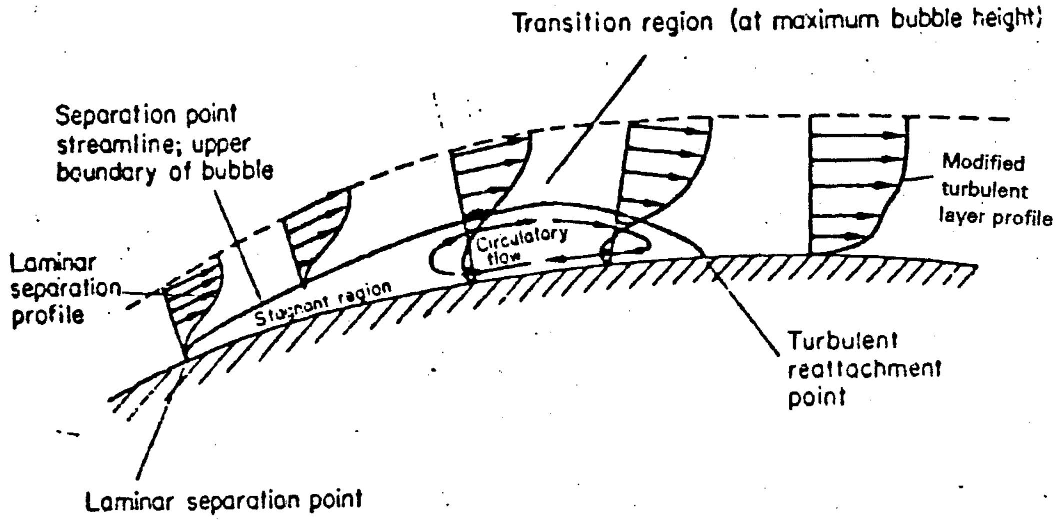

Figure 1.2 Mechanism of separation bubbles (Houghton & Carpenter, 1993).

Small disturbances grow much more readily at low Reynolds numbers in separated, as compared to attached, boundary layer. Consequently the separated laminar layer may well undergo transition to turbulence with a rapid thickening. This rapid thickening may be sufficient for the lower edge of the rear turbulent, shear layer to come back into contact with the surface and re-attach as a turbulent boundary layer on the surface. In this way a bubble of fluid is trapped under the separated shear layer between the separation and re-attachment points. Within the bubble, whose boundary is usually taken to be the streamline which leaves the surface at the separation point, two regimes exist. In the upstream region a pocket of stagnant fluid at constant pressure extends back some way and behind this a circulatory motion develops as shown in Fig.[1.2], the static pressure in this latter region increases rapidly towards the re-attachment point.

1.2. Flow Past Cylinders and Spheres

Some of the properties of boundary layers discussed above help in the explanation of the behaviour, under certain conditions, of a cylinder or sphere immersed in a uniform free stream. If the attention is restricted to the flow over bodies of reasonably streamline form, behind which a relatively thin wake is formed. The drag forces are largely due to surface friction, i.e. to shear stresses at the base of the boundary layer. On the other hand when dealing with non-streamlined or bluff bodies, it is found that, because of the adverse effect of a positive pressure gradient on the boundary layer, the layer usually separates somewhere near points at the maximum cross-section, and leads to a broad wake. As a result, the surface friction drag is relatively small, and the major part of the total drag now consists of pressure drag due to the large area separated with a reduced pressure at rear of the body. Experimental observation of the flow past a sphere or cylinder indicate that the drag of the body is markedly influenced by the cross-sectional area of the wake, a broad wake being accompanied by a relatively high drag and vice versa.

The variation with respect to Reynolds number of the flow pattern around a bluff body may be considered with reference to the flow past a circular cylinder. For the most part the flow past a sphere also behaves in a similar way. At very low Reynolds number ($Re = U_\infty D/\nu$, where U_∞ is the free stream velocity, ν is the kinematic viscosity coefficient in the free stream and D is the cylinder diameter.) , i.e. less than unity, the flow behaves as if it were purely viscous with negligible inertia. Such flow is known as creeping or Stokes flow. For such flows there are no boundary layers and the effects of viscosity are felt in the whole flow domain. The streamlines are completely symmetrical fore and aft, as depicted in Fig.[1.3.(a)]. In appearance the streamline pattern is superficially similar to that for potential flow. For creeping flow, however, the influence of the cylinder on the stream lines extend to much greater distances than for potential flow. Skin-friction drag is the only force generated by the fluid flow on the cylinder. Consequently the body with the lowest drag for a fixed volume is the sphere. Perhaps it is for this reason that microscopic swimmers such as protozoa, bacteria and spermatozoa tend to be near-spherical. In the range $1 < Re < 5$ the streamline pattern remains fairly similar to that of Fig [1.3.(a)], except that as Re is increased within this range a more and more pronounced asymmetry develops between the fore and aft directions. Nevertheless the flow remains attached.

When Re exceeds a value of about 5, a much more profound change in the flow pattern occurs. The flow separates from the cylinder surface to form a closed wake of recirculating flow see Fig.[1.3.(b)]. The wake grows progressively in length as *Re* is increased from 5 up to 41. The flow pattern is symmetrical about the horizontal axis and is steady, i.e. it does not change with time. At these comparatively low Reynolds numbers, the effects of viscosity still extend a considerable distance from the surface, so it is not valid to use the concept of the boundary layer, nevertheless the explanation for flow separation occurring is substantially the same.

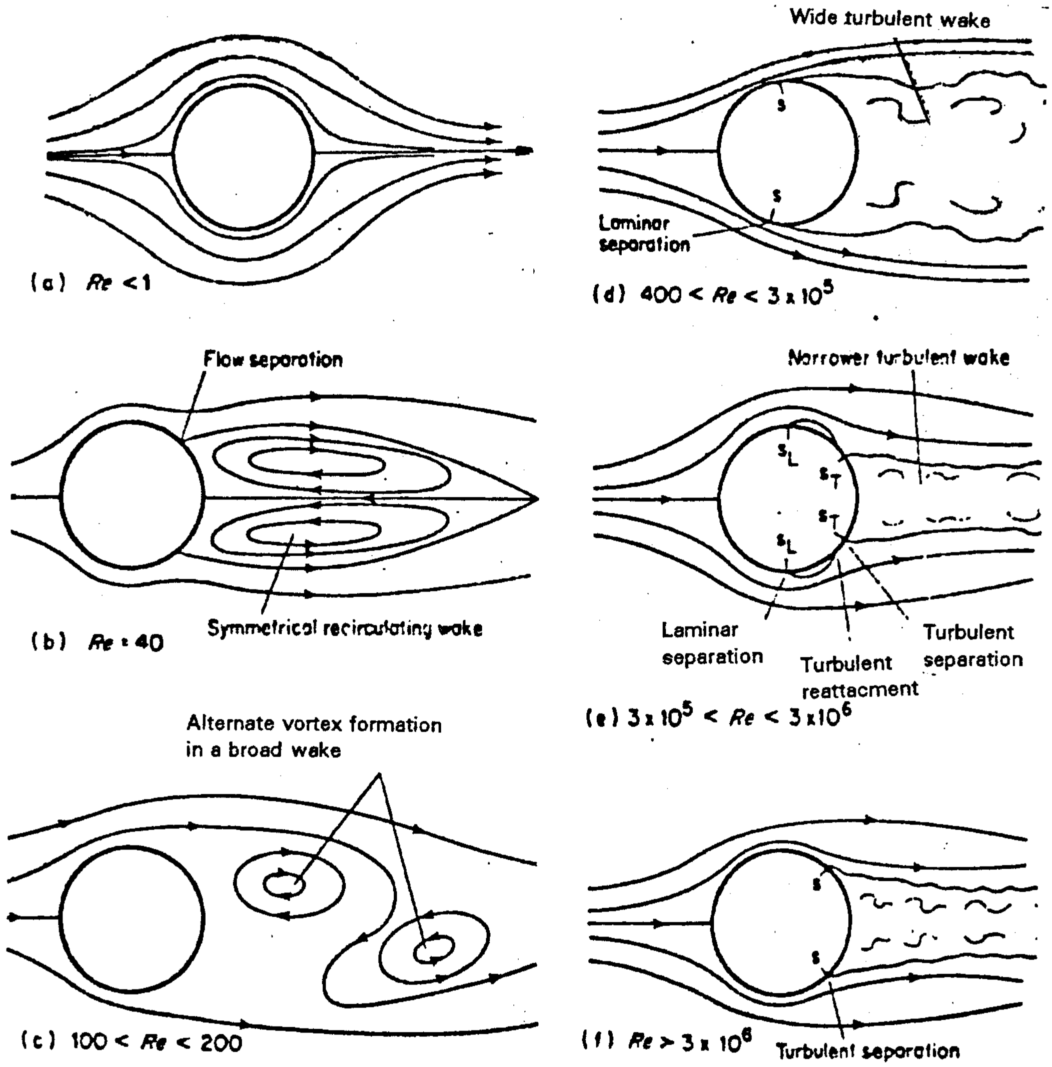

Figure 1.3 Regimes of fluid flow across generalized bluff bodies (Houghton&Carpenter, 1993). Note that the Reynolds number limits quoted are only approximate.

When *Re* exceeds a value of about 41 another profound change occurs; steady flow becomes impossible. In some respects what happens is similar to the early stages of laminar-turbulent transition (Houghton & Carpenter, 1993), in that the steady recirculating wake flow, seen in Fig.[1.3.(b)], becomes unstable to small disturbances. In this case, though, the small disturbances develop as vortices rather than waves. Also in this case, the small disturbances do not develop into turbulent flow, but rather a steady laminar wake develops into an unsteady, but stable, laminar wake. The vortices are generated periodically on alternate sides of the horizontal axis through the wake and the centre of the cylinder. In this way a row of vortices are formed similar to that shown in Fig.[1.3.(c)], except that the vortices are formed further downstream in the wake. The vortex row persists for a considerable distance downstream. This phenomenon was first explained theoretically by von Karman in the first decade of the twentieth century.

For Reynolds numbers between just above 40 and about 100 the vortex street develops from amplified disturbances in the wake. However, as the Reynolds number rises an identifiable thin boundary layer begins to form on the cylinder surface and the disturbance develops increasingly closer to the cylinder. Finally, above about $Re = 100$ eddies are shed alternately from the laminar separation points on either side of the cylinder. Thus, a vortex will be generated in the region behind the separation point on one side, while a corresponding vortex on the other side will break away from the cylinder and move downstream in the wake. When the attached vortex reaches a particular strength, it will in turn break away and a new vortex will begin to develop again on the second side and so on.

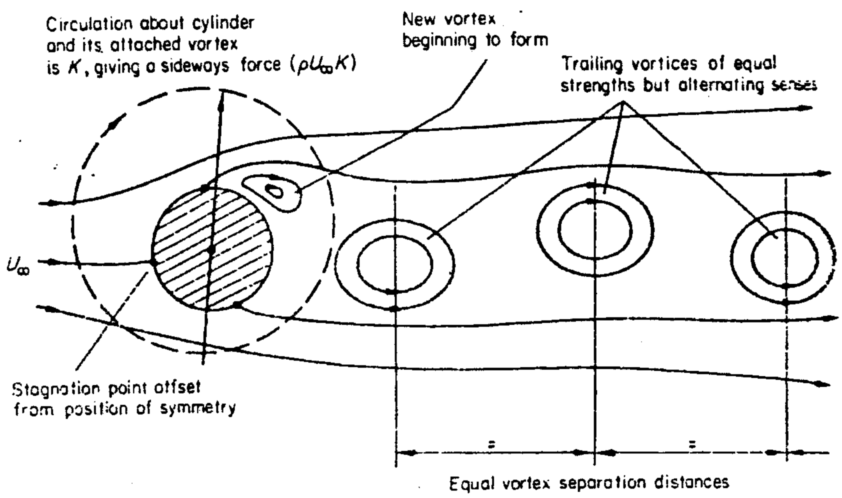

Figure 1.4 Formation of vortex and wake (Houghton&Carpenter, 1993). Flow patterns and sideways force reverses when vortex detaches and a new vortex begins to form on the opposite side.

The wake thus consists of a procession of equal strength vortices, equally spaced but alternating in sign. This type of wake, which can occur behind all long cylinders of bluff cross-section, including flat plates normal to the flow direction, is termed a von Karman vortex street or trail (see Fig.[1.4)]. In a uniform stream flowing past a cylinder the vortices move downstream at a speed somewhat less than the free stream velocity, the reduction in speed being inversely proportional to the streamwise distance separating alternate vortices.

It will be appreciated that, during the formation of any single vortex while it is bound to the cylinder, an increasing circulation will exist about the cylinder, with the consequent generation of a transverse (lift) force. With the development of each successive vortex, this force will change sign, giving rise to an alternating transverse force on the cylinder at the same frequency as the vortex shedding frequency. The oscillating pressure field and net force on a cylinder are shown in Fig.[1.5] for a portion of the shedding cycle.

A unique relationship is found to exist between the Reynolds number and a dimensionless parameter involving the shedding frequency. This parameter, known as the Strouhal number, is defined by the expression $S=nD/U_{\infty}$, where n is the frequency of vortex shedding, Fig.[1.6] shows the typical variation of S with Re in the vortex street range.

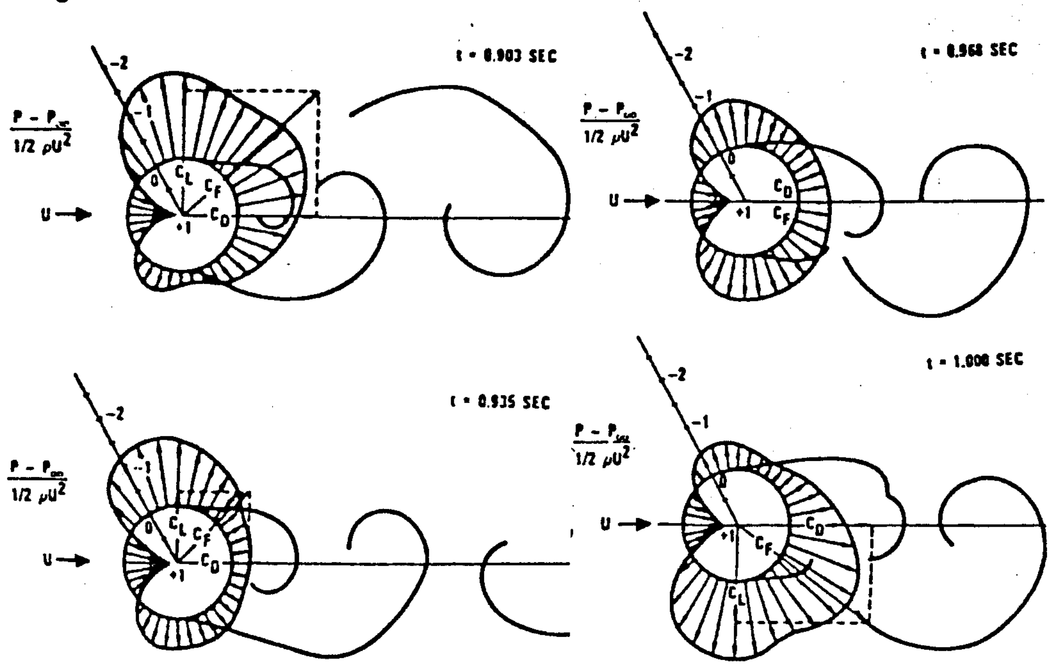

Figure 1.5 A sequence of simultaneous surface pressure fields and wake forms at Re=112000 for approximately one of one cycle of vortex shedding. (Blevins, 1974).

Despite the many other changes (or transitions), described below, which occur in the flow pattern as Re increases still further, markedly periodic vortex shedding remains to be a characteristic flow around the circular cylinder and other bluff bodies up to the highest Reynolds numbers. If the frequency of vortex shedding happens to coincide with the natural frequency of oscillation of the cylinder, however it may be supported, then appreciable vibration may be caused. This phenomenon is responsible, for example, for the singing of telegraph wires in the wind (Aeolian tones), and can have important consequences in engineering applications. A dramatic example was the failure of the Tacoma Narrows Bridge (in Washington State, USA) in 1940. In this case the natural frequency of the bridge deck was close to its shedding frequency in a brisk wind, thereby leading to resonance and disastrous consequences.

For two ranges of Reynolds number, namely $200<Re<400$ and $3x10^5<Re<3x10^6$, the regularity of vortex shedding is greatly diminished. In the former range very considerable scatter occurs in values of Strouhal number, while for the latter range all periodicity disappears except very close to the cylinder. The values of Reynolds number marking the ends of these two ranges are associated with pronounced changes in the flow pattern. At $Re=400$ and $3x10^6$ the transitions in flow pattern are such as to restore periodicity.

Below $Re=200$ the vortex street persists to great distances downstream. Above this Reynolds number, transition to turbulent flow occurs in the wake thereby destroying the periodic vortex wake far downstream. At this Reynolds number the vortex street also becomes unstable to three-dimensional disturbances leading to greater irregularity.

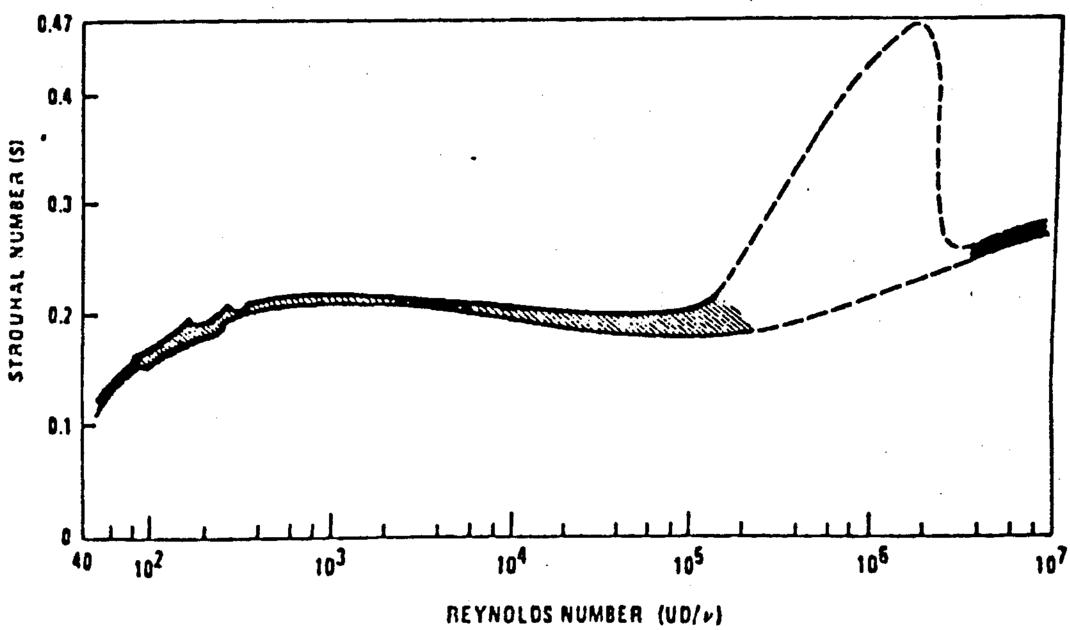

Figure 1.6 The Strouhal-Reynolds number relationship for a circular cylinder (Blevins, 1974).

At $Re=400$ a further change occurs. Transition to turbulence now occurs close to the separation points on the cylinder. Rather curiously, perhaps, this has a stabilizing effect on the shedding frequency even though the vortices themselves develop considerable irregular fluctuations. This pattern with laminar boundary-layer separation and a turbulent vortex wake persists until $Re=3x10^5$, and is illustrated in Fig.[1.3.(d)]. Note that with laminar separation the flow separates at points on the front half of the cylinder, thereby forming a large wake and producing a high level of form drag. In this case the contribution of skin-friction drag is all but negligible.

When the Reynolds number reaches a value in the vicinity of $3x10^5$ the laminar boundary layer undergoes transition to turbulence almost immediately after separation. The increased mixing re-energizes the separated flow causing it to reattach as a turbulent boundary layer, thereby forming a separation bubble (as described in Section 1.1.2) - see Fig.[1.3.(c)].

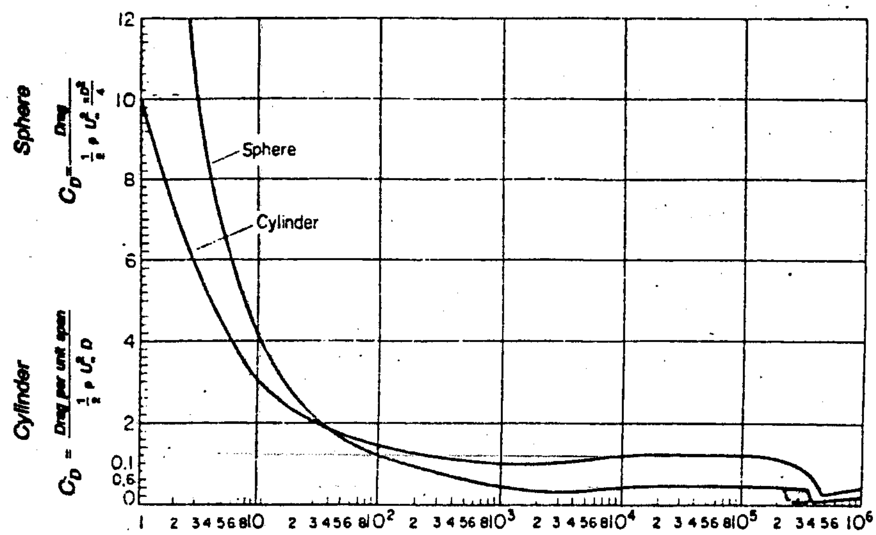

Figure 1.7 Approximate values of C_D with ***Re*** for spheres and circular cylinders (Goldstein, et.al. ,1965).

At this critical stage the second and final point of separation, which now takes place in a turbulent layer, moves suddenly downstream, because of the better sticking property of the turbulent layer, and the wake width is very appreciably decreased. This stage is therefore accompanied by a sudden decrease in the total drag of the cylinder. For this reason the value of ***Re*** at which this transition in flow pattern occurs is often called the Critical Reynolds number. The wake vorticity remains random with no calculable frequency. With further increase in Reynolds number the wake width will gradually increase to begin with, as the turbulent separation points slowly move upstream round the rear surface. The total drag continues to increase steadily in this stage, due to both pressure and surface friction drag increases, although the drag coefficient, defined by; tends to become constant, at about 0.6, for values of $Re > 1.3x10^6$. The final change in the flow pattern occurs at $Re = 3x10^6$ when the separation bubble disappears, see

$$C_D = \frac{drag\ per\ unit\ span}{1/2\ \rho_\infty U_\infty^2 D} \qquad (1.1)$$

Fig.[1.3.(f]). This transition has a stabilizing effect on the shedding frequency which becomes discernable again. C_D changes little for $Re > 3x10^3$.

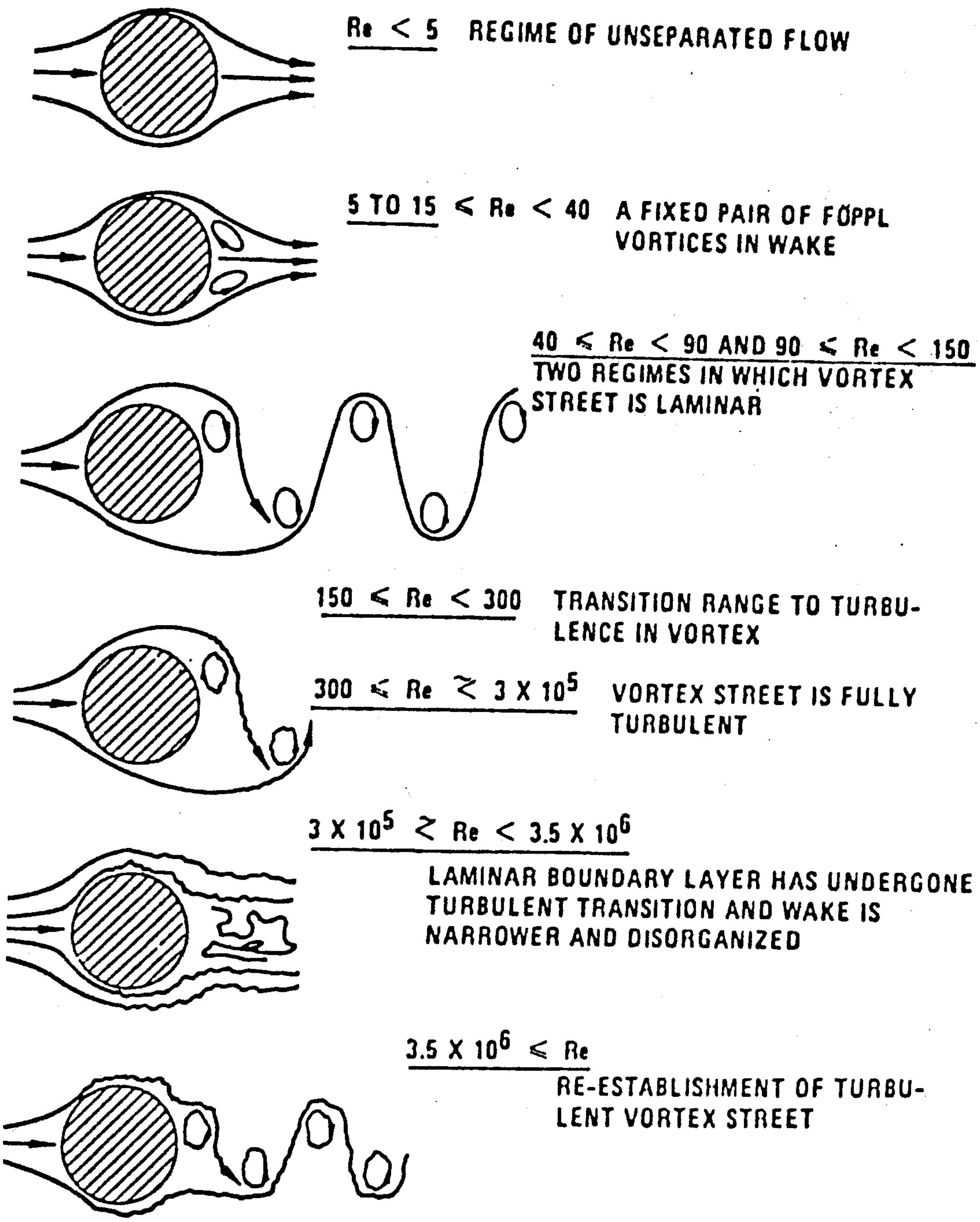

Figure 1.8 Regimes of fluid flow across circular cylinders (Blevins, 1974).

The actual value of the Reynolds number at the critical stage when the dramatic drag decrease occurs depends, for a smooth cylinder, on the small-scale turbulence level existing in the oncoming free stream. Increased turbulence, or, alternatively, increased surface roughness, will provoke turbulent reattachment, with its accompanying drag decrease, at a lower Reynolds number. The behaviour of a smooth sphere under similarly varying conditions exhibits the same characteristics as the cylinder, although the Reynolds numbers corresponding to the changes of flow regime are somewhat different. One marked difference in behaviour is that the eddying vortex street, typical of bluff cylinders, does not develop in so regular a fashion behind a sphere. Graphs showing the variations of drag coefficient with Reynolds number for circular cylinders and sphere are given in Fig.[1.7]. A graph which summarize regimes of fluid around cylinder with respect to Reynolds number is given at Fig.[1.8]

1.3. Some Significant Features of Laminar Wakes

The terminology "street" refers to the multitude of vortices in a regular alternating arrangement (Chang, 1970). The fluid dynamic theory of inviscid and viscous flows indicates that vortex streets can be produced experimentally in air, and the rate of periodic shedding is an important phenomenon of wake flow.

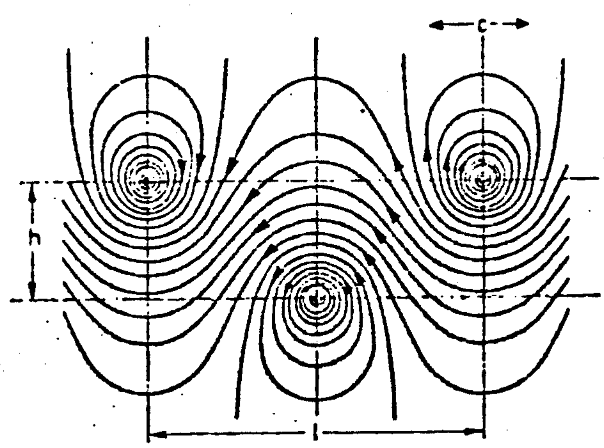

Figure 1.9 Karman vortex street (diagrammatic). Stream lines drawn in a system of coordinates moving with the vortex street.

Karman (as referred to in Chang, 1970) found that for two-dimensional infinitesimal displacements, a staggered arrangement of vortices is stable if

$$\sinh\left(\frac{\pi h}{l}\right) = 1 \quad and \quad h/l = 0.281, \tag{1.2}$$

where l is the horizontal spacing of the vortices and h is the vertical spacing Fig.[1.9].

This special case involving only the so-called Karman coefficient $h/l = 0.281$ is possible for vanishing viscosity and vanishing time, as proved by Domm (as referred to in Chang, 1970) through his analysis. Domm proved, furthermore, that a single row street is unstable. In general, flow can be stable for all ratios of *h/l*, if the mean values of *h* and *l* are used. The instability present is associated only with the periodicity (Chang, 1970).

The other formula which has been given independently for stability is

$$\sin\left(\frac{\pi c}{l}\right) = \sinh\left(\frac{\pi h}{l}\right) \qquad (1.3)$$

where *c/l* is the dislocation ratio. The symbol *c* refers to an arbitrary length, $0 \leq c \leq l$. For a value of *c*, there is a corresponding value of *h/l* for the stable vortex behaviour.

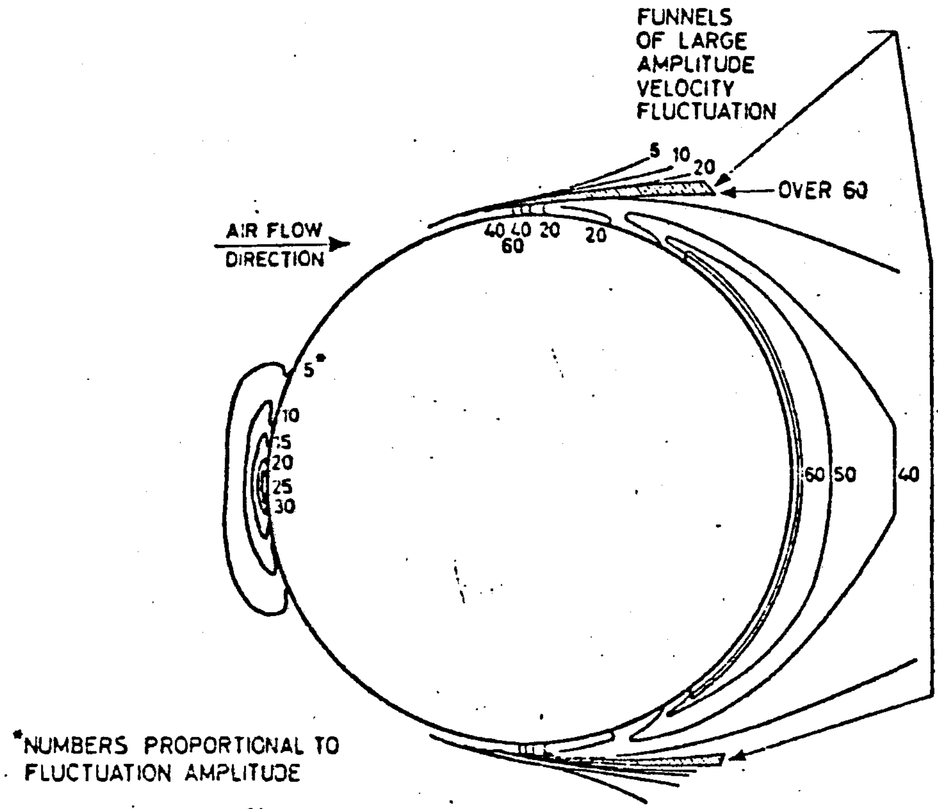

Figure 1.10 Velocity fluctuations in the vicinity of cylinder surface [4].

The flow velocity fluctuations measured close to the forward stagnation point were surprisingly large (Chang, 1970). This disturbance seems to damp out and disappear into the boundary layer as it moves towards the wake, but the large velocity fluctuations in the vicinity of the forward stagnation point may become an important precursor of the wake generation. Particularly, the "funnel of vorticity" in the vicinity of the separation point seems to be the starting point of large vortices in the wake. In the funnel of vorticity, the amplitude of fluctuation is large. These fluctuations are fed by the agglomeration of smaller vibrations occurring in the separating boundary layer.

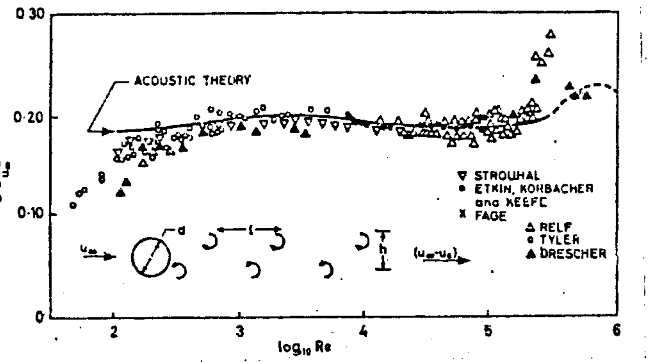

Figure 1.11 A comparison of experimental Strouhal numbers with Shaw's acoustic theory (Chang, 1970).

The acoustic energy effect in the wake is a new subject involving turbulence (Chang, 1970). The velocity fluctuations in a turbulent wake and the fluctuating stresses at the body surface act as acoustic sources, generating sound the intensity of which varies exponentially with relative fluid velocity. For circular cylinder flow there are three centres of disturbances: two strong areas are at the separation points, and a weak one at the stagnation point. Acoustic pressure pulse sources are limited to these three centres. The pulses travel in the cylinder boundary layer and through the ambient flow at sonic velocities (Fig.[1.10]). Shaw (as referred to in Chang, 1970) found that the frequency is about $3a/2\pi d$, where a is the speed of sound and d is body diameter. The shed vortex oscillating at this frequency sends back pulses of the attached layer, and due to Doppler's effect, the frequency is then reduced in the ratio $1-(u_\infty-u_s)/a$, where u_s is velocity of the vortices relative to stream velocity. An interaction takes place between the acoustic vibrations of attached flow (which has the original frequency) and the shed vortex, which produces strong pulses with beat frequency $\frac{3a}{2\pi d}\left(\frac{u_\infty-u_s}{a}\right)$. These strong pulses cause the shedding of the vortex. The shedding frequency of the vortex pair is then $(1/2)(2/3)x(1/\pi d)(u_\infty-u_s)$, and the Strouhal Number may be written by

$$St = \frac{3}{4\pi}\left(1 - \frac{u_s}{u_\infty}\right) \tag{1.4}$$

The distance between consecutive vortices is equal to $4\pi d/3$ and is invariant, which is confirmed by experiment. As shown in Fig.[1.11], a good agreement between theoretical Strouhal Number and experimental results is obtained.

A further study and comparison of Shaw's theory with experimental data may lead toward the much desired information on self-generated sound-energy effect on wake flow. The effect of sound-energy injection to the laminar flow was studied by Schade and Michalke (as referred to in Chang, 1970).

1.4. Bluffness of a Body

With the result of the free streamline theory of Roshko (1955), the idea of "Bluffness" has been put on a firm basis and correlated with experimental observations. The main features associated with blufness may be enumerated as follows.

(1) Of two bodies having the same frontal area, the bluffer one tends to diverge the flow more, to create a larger wake, and to experience a higher drag. The results of the free streamline theory are quite in accord with this definition.

(2) It is a matter of observation that bluffer cylinders have lower Strouhal Numbers. This explains why the bluffer cylinders, which have wider wakes, have lower shedding frequencies and correspondingly lower Strouhal Numbers.

(3) For different cylinders the base pressures are approximately equal, within about 10 percent, provided there is no interference in the wake. Whatever variations of base pressure do exist do not show any systematic variation with bluffness but appear, rather, to be related to Reynolds Number effects. Thus the variation between different cylinders is no more than what may be obtained for the same cylinder at different Reynolds Numbers. The remarks here apply to a range of Reynolds Numbers of about 500 to 10^5 for the circular cylinder and to even higher values for the other two. This is the range in which C_D is ordinarily described as being constant, but actually this also varies somewhat with Re, and, in fact, the variations are associated with those in C_{ps}. Likewise, the Strouhal Number may be described as constant only to the same degree, its variations also being associated with the variations in C_{ps}. Over this Reynolds Number range the values of C_D and St are within 10 percent of those given in Table [1.1] and, for our present purposes, may be assumed to be constant.

(4) The above remarks apply to cylinders with undisturbed wakes. If interference elements are placed in the wake, as described in the above experiments, then significant changes are produced in C_{ps}, and correspondingly in C_D and St . The important results is that, for a given cylinder, a decrease in drag is accompanied by a decrease in shedding

Table 1.1 Approximately C_D and St value at range of Re Numbers of about 500 to 10^5 for the circular cylinder and to even higher values for the other two (Roshko, 1955).

	C_D	St
Circular cylinder	1.0	0.21
90° wedge	1.3	0.18
Bluff plate	1.7	0.14

frequency. This is at odds with the behaviour indicated in Table [1.1] for different cylinders, but it will be seen to be entirely in agreement with the observation that shedding frequency decreases when wake width increases. This seems contrary to intuition, but it may be pointed out that the increase in wake width is accompanied by a decrease in wake velocities sufficient to give a net decrease in wake energy.

(5) The wake structure of different bluff bodies is similar. That is, the shape, or bluffness, of the body has no characteristic effect on the wake other than to determine its geometrical and velocity scales.

These several observations on the characteristics of bluffness may be incorporated into a simple dimensional analysis. Consider the two parallel vortex sheets, which are intended to be some bluff body. If these vortex layers roll up to form vortices, then the frequency with which this occurs should depend only on the characteristic velocity, U_s, and the dimension, d', associated with the configuration. It should not depend on the body that created it. In other words, there should be a Strouhal Number for the wake, defined as

$$St^* = \frac{n\, d'}{U_s} \tag{1.5}$$

which should be universal for the vortex shedding from different bluff bodies (Roshko, 1955). Of course it may be expected that there will be some variation with Reynolds Number, just as for the ordinary Strouhal Number. For the present, Roshko propose to take this into account only roughly, by defining a wake Reynolds Number (Roshko, 1955)

$$R_e^* = \frac{U_s\, d'}{\nu} \tag{1.6}$$

To take the Reynolds Number effects into account more precisely will complicate matters considerably. For instance, the shear layers set up by different bluff bodies will not be the same, even at the same Re^*, for they may have had different histories up to the point where they start to roll up. Thus they may be thicker or thinner, may have become turbulent earlier or later, etc., and these features will have an important influence on the vortex dynamics. They will therefore be extremely important for the vortex dynamics and the base pressure. However, Roshko's considerations are only kinematic, and, for that, the secondary Reynolds Number effects, the details of the free streamline shape, etc., may be less important.

To confirm that such a universal wake Strouhal Number exists, some measurements were made on the three different cylinders, with and without wake interference, as follows. The wake Strouhal Number is related to the ordinary Strouhal Number by

$$St^* = \frac{nd}{U_\infty} \frac{d'}{d} \frac{U_\infty}{U_s} = \frac{St}{k} \frac{d'}{d} \tag{1.7}$$

To determine St^*, two measurements are needed. St is determined in the usual way from a measurement of the shedding frequency. k is determined from a measurement of the base pressure (Roshko, 1955).

$$k = \sqrt{1 - C_{ps}} \tag{1.8}$$

This relation may be regarded as the essential one in the coupling between the potential flow and the wake, for it determines, for a given cylinder, the wake velocity and dimension in terms of the base pressure. The results, plotted in Fig.[1.12], show that there is indeed a universal relation, $St^* = St^*(Re^*)$. Possibly the scatter is too large to show any functional trend, as has been attempted with the solid line, and one should simply assume that St^* is constant at about the value 0.16.

1.5. Wake Controlling and Effects of Splitter Plate

There are several methods existing for the purpose of artificial controlling the behaviour of the boundary layer over any bluff bodies.

The aim of this control is to change the structure of boundary layer by effecting to

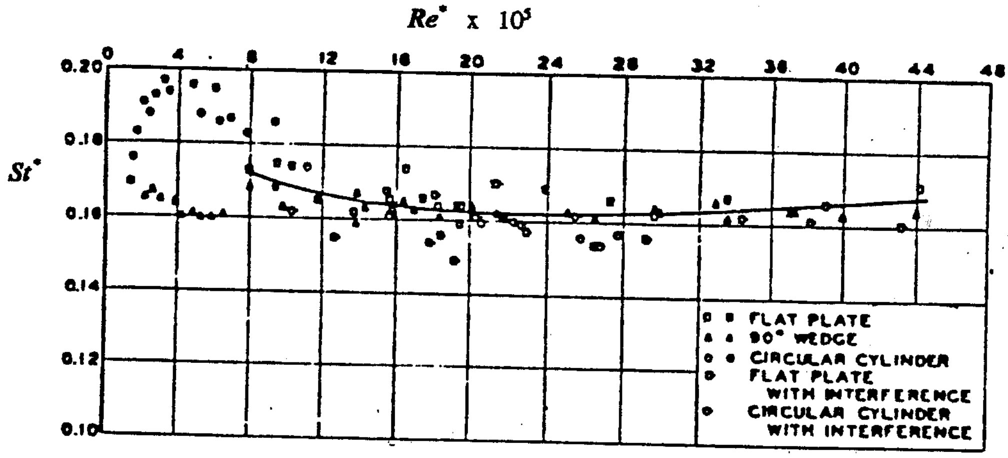

Figure 1.12 The wake Strouhal number S^* according to The wake Reynolds number R_e^*

whole flow field and as a result of this change to provide improvements in desired direction in the quantities of flow. Without controlling, how the boundary layer develops, vortex formation occurs and what the flow characteristics are, are given before. Many researches were investigated for the aim of reducing the amplitudes of fluctuating lift and drag forces and decreasing the drag force by controlling the instabilities in the periodically separating boundary layer. There are two strategies for this: Active and Passive control. Basically, the main methods in passive control can be put out as follows:

(i) Motion of solid wall
(ii) Acceleration of boundary layer (blowing, base bleed)
(iii) Injection of different gas
(iv) Cooling of the wall

The purpose of these mentioned methods is to increase the kinetic energy of boundary layer and to provide it to surmount the high pressure gradient forcing it to apart from the surface.

Blowing or introducing bleed in a convenient rate from the base of bluff bodies has a particular importance which has been subject of many studies. What is tried to do here is to displace the formation region of the vortex street away from the body. For increasing rate of bleed, the regular shedding of vortices ceases intermittently at first and then completely. Yılmaz (1990)] tried to simulate numerically the wake from a flat plate with blunt trailing edge with base bleed.

Passive control of wakes by means a secondary body interference has been investigated many authors. Yılmaz (1990) and Strykowsky & Sreenivosan (1990) placed a little control cylinder near the cylinder in various arrangements. Strykowsky &

Sreenivosan pointed out that the suppression of the vortex street corresponds to the global decay of modes that would be temporally amplified under normal circumstances. Yılmaz stated the changes of stagnation and separation points over a circular cylinder with a nearby circular cylinder with very small diameter. Controlling wake passively by means of a splitter plate placed in the wake of circular cylinder with different arrangements has been studied by many authors since the early experiment of Roshko (1955). He used different lengths of splitter plates, set them up in different distances of downstream of the wake. He found that the different arrangements between the splitter plate and the cylinder have different effects on the pressure and the wake. The most recent research of Ünal & Rockwell (1988) is similar to the work of Roshko, in that they placed a wake plate in downstream of the cylinder with various separation. Interaction of the wake of a circular cylinder with a downstream splitter plate has been also investigated by Smith & Karamcheti (1975). According to the above mentioned studies, the body wake is less sensitive than a streamlined body is, when a splitter plate is introduced downstream of the wake. The brief physics of this feature can be explained as follows: The wake impinging upon the splitter plate creates unsteady pressure fluctuations there; in turn, these pressure fluctuations induce an upstream influence at the sensitive region near separation points of the boundary layers. This phenomenon occurs between separation and impingement simultaneously i.e. they are not of consequence of each other. They form a close loop. The near wake of a bluff body has a high degree of self-control and therefore is insensitive such an upstream influence (Ünal & Rockwell, 1988 - Smith & Karamcheti, 1975).

According to Bearman (1965), splitter plate attached to the base of bluff body rather than being placed downstream has different effects. Such a wake controlling has been tried by many investigators e.g. Bearman (1965), Kawai (1990), Apelt et.al. (1973), Çete (1989), Çete & Ünal (1992), Mısırlýoğlu (1992).

In Bearman's study, the splitter plate attached to the blunt trailing edge increases the distance between the vortex formation region and the body that this formation occurs after the end of the splitter plate unless the length rate of plate is smaller than a definite amount. At higher amounts, no formation occurs. The most renowned experiment on the effects of a splitter plate attached to the end of circular cylinder was done by Apelt et.al. (1973). They found remarkable effects of splitter plate on the wake and features of them in the range $10^4 < R^e < 5x10^4$. In their experiments, the maximum length of splitter plate is equal to the cylinder diameter. Reductions in Strouhal number and drag coefficient, followed by increases with increasing splitter plate length were observed. Then definition of "Long" and "Short" splitter plates was given as a result of above observation.

When the length of the splitter plate is short, the amplitude is reduced and the frequency is altered, indicating that periodic wake is influenced by the early stage of wake rather than the downstream flow. If a splitter plate of sufficient length is used, the stagnation occurs on the solid surface, and lateral oscillation of the wake is prevented, although the cavity flow near to the splitter plate remains.

Although first numerical approaches to the effects of splitter plate have short history, similar characters with the experiments have been found (Kawai, 1990 - Çete & Ünal, 1992 - Mısırlıoglu, 1992)

CHAPTER 2

FLOW AROUND AN AEROFOILS

An aerofoil yields optimum aerodynamic characteristics of high lift and low drag if the flow is attached to the surface. However, if the aerofoil is under a sufficiently large angle of attack, then the flow on the upper surface separates as indicated in Fig.[2.1], and the stream pattern over the upper surface is far apart from the optimum design condition. Furthermore, a considerable size of separated region is created with the formation of vortices. This kind of separation on an aerofoil is called "stalling", expressing the unfavourable aspect of engineering application.

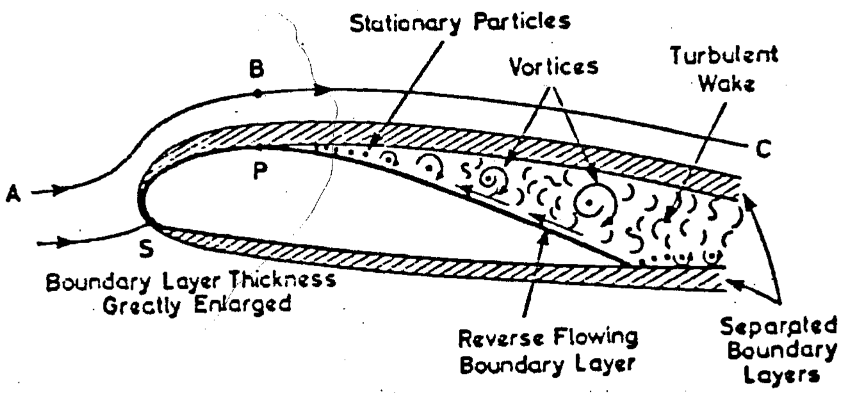

Figure 2.1 Viscous effects in flow around an aerofoil (positive angle of attack) (Chang, 1970).

The stalling is closely connected with closed separation bubbles, which are due to dynamical characteristics of flow setting up circulating motion on the aerofoil surface. Depending upon the length, the closed bubbles are short or long. The short bubble is enclosed between the points of separation and reattachment, and its length is the order of 1 percent of chord length, which does not significantly influence the pressure distribution. But if the short bubble of a laminar layer breaks down on the aerofoil, then leading edge stall occurs and causes sudden increase of drag and loss of lift.

With a long bubble whose length is about 2 or 3 percent of chord, pressure distribution slightly changes, but its breakdown does not lead to a complete separation of flow; instead, the separated flow passes over the body surface and reattaches further downstream.

2.1. The Velocity Distribution in the Boundary Layer at the Surface of an Aerofoil

The boundary layer of an aerofoil resembles that of a flat plate in that at a sufficiently high Reynolds number there is a region of laminar flow at the nose, then a transitional region in which the distribution of mean velocity changes more or less erratically with time, and finally a region of fully developed turbulent motion. A further resemblance is that turbulence in the general stream, and irregularities on the surface near the nose, cause an earlier transition to turbulent flow. But separation eventually occurs on the upper surface of an aerofoil, no matter what the shape may be when the angle of incidence is increased.

The relative extends of the laminar, transitional, and turbulent boundary layers, and the position of the separation (if any) depend on the shape and incidence of the aerofoil, on the Reynolds number, on surface roughness, and on the turbulence in the free stream.

In wind tunnels of ordinary type (compressed air and full-scale tunnels excluded) some difficulty may be experienced in obtaining details of the flow in the boundary layer of an aerofoil at large incidence, because when the chord is large compared with the width of the tunnel stream, the walls (for a closed jet) or free boundary (for an open jet) introduce a large interference with the flow. On the other hand, when the interference is lessened by making the chord relatively small, the boundary layer becomes too thin to permit reliable measurements. Further, flow phenomena in a wind tunnel have generally to be observed at a low Reynolds number; if in addition the flow in the tunnel is turbulent, the results may give misleading information on the behaviour of the same section in free flight at a higher Reynolds number-especially at the stall. For these reasons information on boundary layer flow has been sought not only on the model but also from flight experiments: in these experiments the flow is not two-dimensional, but results of great practical value are obtained.

It follows that the conditions of the experiment were such that the combined effects of an increase of Reynolds number and of a decrease of lift coefficient were measured. These two influences affect the position of the transition from laminar to turbulent flow in opposite ways: increase of Reynolds number moves the transition region towards the nose, whereas decrease of lift coefficient is associated with a decrease of the pressure gradient along the chord, which tends to make the transition occur later. Researcher (Goldstein, et.al., 1965) found the transition region on the upper surface at about 0.1c to 0.3c from the leading edge .This results is typical of thick sections. Transition occurs just beyond the position of minimum pressure. (For a thin section this position is just behind the leading edge, so transition may be appreciably closer to the leading edge on a thin section than on Stüper's thick section). Stüper's observations also indicated that on the under surface the transition occurred earlier than on the upper surface, but the position could not be determined with precision (Goldstein, et.al., 1965).

The velocity graphs obtained by Stüper (as referred to in Goldstein, et.al., 1965) in the second series of measurements (Reynolds number 3.62×10^6; lift coefficient 0.55) are reproduced in Fig.[2.2], where graphs of U/U_o against y are shown, U being the velocity in the boundary layer at a distance y from the surface and U_o the velocity of the wing relative to the undisturbed air.

If θ is the momentum thickness defined as $\int_0^\delta (1-U/U_1)(U/U_1)dy$, where δ is the thickness of the boundary layer and U_1 the velocity just outside the layer, then Stüper found that $U_1\theta/v$ lies between 250 and 650 at the transition to turbulence.

2.2. The Flow at the Stall. Forward and Rear Separation

On all aerofoils the first sign of an approaching stall is the formation of a thick region of low total head over the upper surface near the trailing edge (see the free-hand sketch in Fig.[2.3.(a)]), but without definite separation of the stream from the surface. The formation of this region is associated with a progressive fall in the rate of increase of C_L with incidence (before this region forms C_L increases linearly wit incidence), and with a slight rise in the rate of increase of drag; during or before this stage (which precedes the true stall) the air-stream may separate from the upper surface near the leading edge, and thin quickly rejoin the surface to form a kind of shallow "bubble" in which the flow is turbulent. This "bubble" of turbulence is probably due to a failure of the potential flow to force its way against a sharply rising pressure gradient, so that the stream-line which otherwise would coincide with the surface is separated from it for a short distance.

Some aerofoils show large discontinuities in the lift and drag curves at the stall: such discontinuities are due to a sudden and complete separation of the stream from the upper surface near the leading edge, the boundary of the stream passing well above the surface, with a region of permanent uniform low pressure occurring over practically the whole of it. There may be a small incidence range within which either the stalled state or the unstalled state of flow may occur and be maintained for a considerable time, with the corresponding parts of the lift curve (and of the drag curve) overlapping. The changes of flow may be sudden, and are then associated with large differences in the values of the lift and drag coefficients. When the differences are not large the boundary of the stream

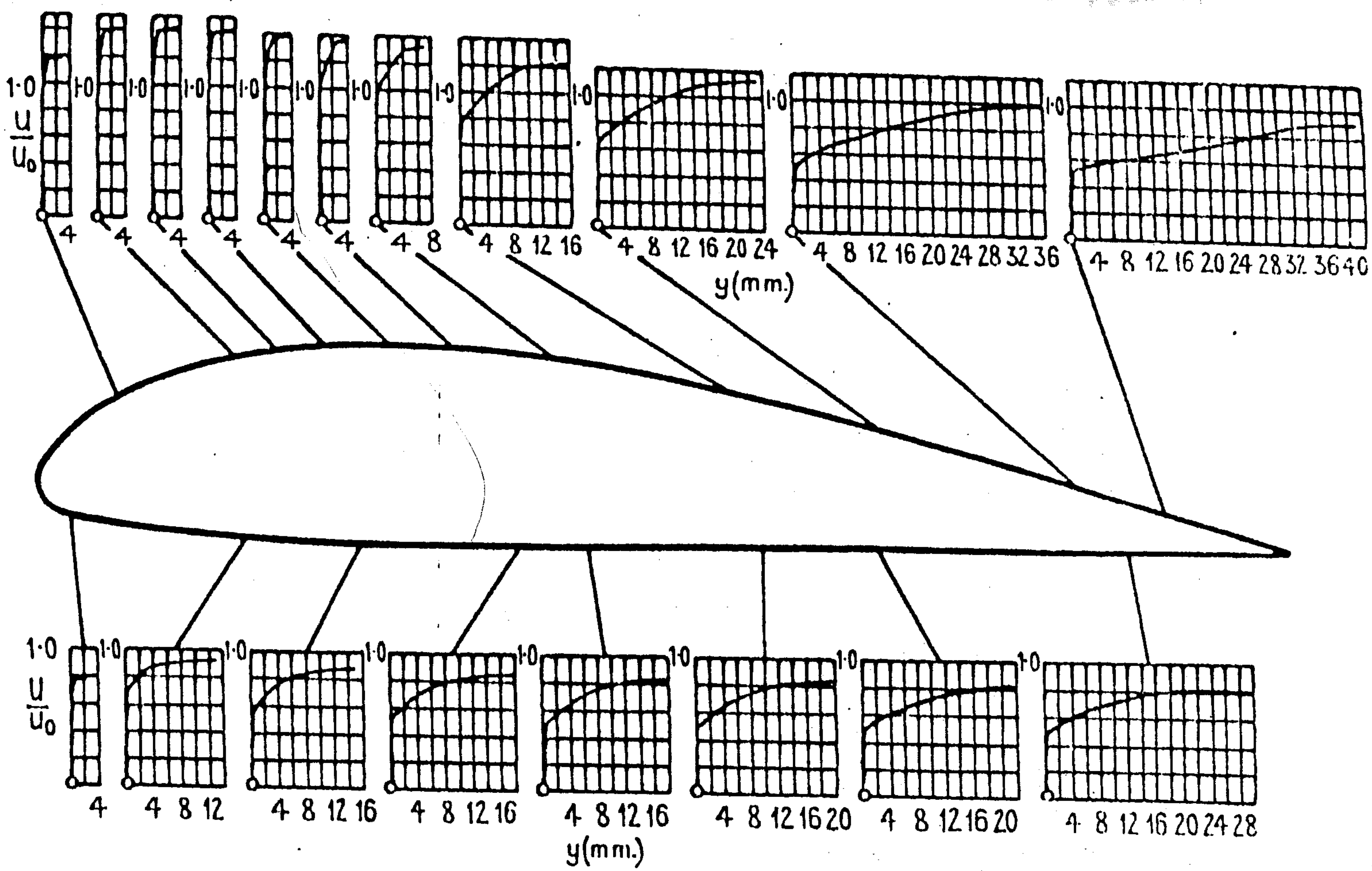

Figure 2.2 The velocity graphs obtain by Stüper (Re; 3.63×10^6, C_L; 0.55) are reproduced (Goldstein, et.al., 1965).

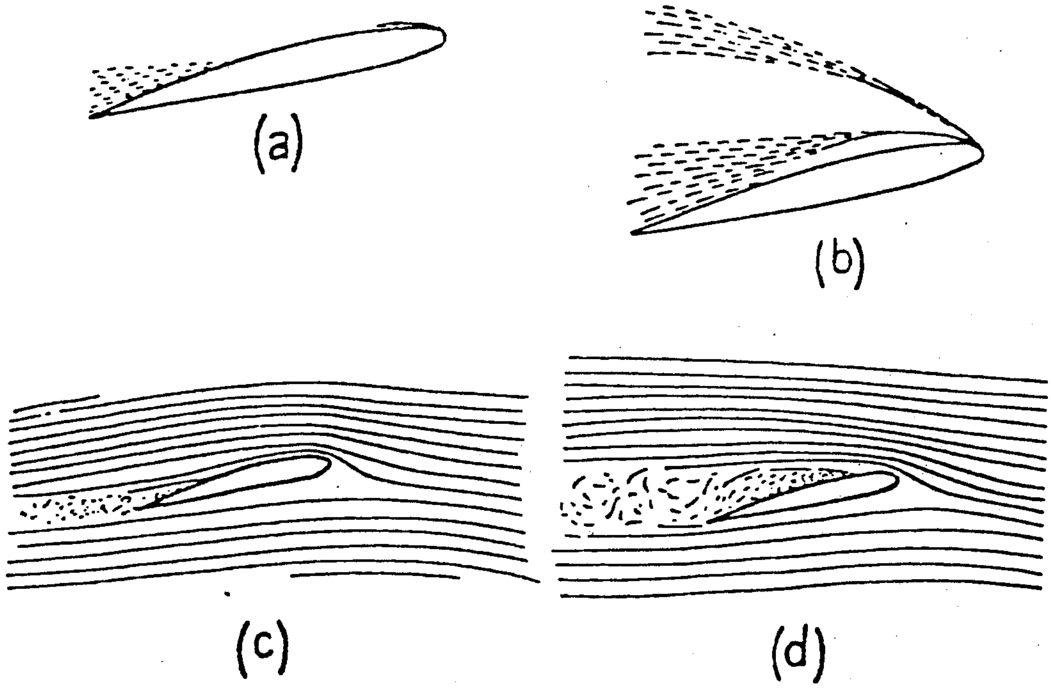

Figure 2.3 The samples of flow at the stall (Goldstein, et.al., 1965).

alternates between two fairly distinct forms, roughly outlined in Fig.[2.3.(b)]: one of these forms represents the completely stalled state, whereas in the other the separated layer, clearly defined at first, remains above the surface over about half the chord, and finally becomes diffused and hard to define. Alternation between these two forms of flow is responsible for the violent fluctuations often observed on a model aerofoil in a wind tunnel. Apart from the turbulence bubble which may form at low incidence on the upper surface behind the leading edge, the first signs of separation from the leading edge are either discontinuities in the lift and drag curves or the onset of violent fluctuations: these phenomena do not necessarily happen at the incidence of maximum lift.

With some aerofoils, particularly when they are thick and the maximum thickness is well back from the leading edge, the first definite separation occurs near the trailing edge, and a dead-air region appears of the form illustrated in Fig.[2.3.(c)]. With increasing incidence this dead-air region gradually extends until the form shown in Fig.[2.3.(d)] is obtained, and during this growth the lift gradually falls without any serious discontinuities or fluctuations. Eventually, even in these circumstances, the flow separates suddenly from the leading edge and characteristic fluctuations occur, but at an incidence well beyond that of maximum lift.

It appears that as the incidence of an aerofoil of moderate thickness increases there are two positions in the boundary layer where the conditions may give rise to separation from the surface; one of these is near the leading edge and the other near the trailing edge. If separation occurs first at the front, violent fluctuations mark the attainment of maximum lift, whereas if rear separation occurs first, violent fluctuations are postponed to incidence well above that of maximum lift.

2.4. The Hysteresis Loop in the Lift-incidence Curve for a Stalled Aerofoil.

A balance has been designed by W.S. Farren (as referred to in Goldstein, et.al., 1965) for the Aeronautics Laboratory, Cambridge to record automatically the aerodynamic force acting on an aerofoil whose lift is rapidly changing, and researches (Goldstein, et.al., 1965) with this balance have shown that, when an aerofoil is started suddenly at an incidence well above that at which the stall occurs in steady motion, the flow remains unstalled during the first few chords of travel. This phenomenon suggests that the lift of an aerofoil whose angle of incidence is rising rapidly, from a value below the normal stalling angle to one well above it, may appreciably exceed that measured at a fixed angle of incidence above the stall; and this was found to be the case.

This latter phenomenon, and those associated with fluctuations of flow at the stall, were investigated on aerofoils of various shapes and thicknesses, under conditions of two-dimensional flow. It was found that a large hysteresis effect exists above the stall, the shape of the force incidence curve depending both on the rate of change of incidence and on the sense of the change. The general nature of this phenomenon is illustrated in Fig.[2.4]. The lift curve for a very slow change of incidence is shown by a broken line, and that for the fluctuating region by a band. When the angle of incidence is changing 1° in the time the wind takes to travel 2.5 chords (the greatest rate of change which was investigated), the lift follows the full lines: no consistent difference is found in the lower part of the curve, but the whole of the stalled part of the curve lies above the mean curve for slow changes when the incidence is increasing, and below it when the incidence is decreasing. Near the fluctuating region there is, with increasing incidence, a notable "peak" of high lift over a small incidence range: the position of this peak depends on the shape of the aerofoil section. In Farren's experiments the recorded lift exceeded the mean lift at fixed angles by 15 to 20 percent.

Records of force fluctuations were taken by Farren at fixed angles of incidence near the stall: the fluctuations were nearly harmonic, the period for the slower oscillations being the time taken by the wind to travel a distance of about 13 chords; the fluctuations in lift were about ± 15 per cent of the mean value.

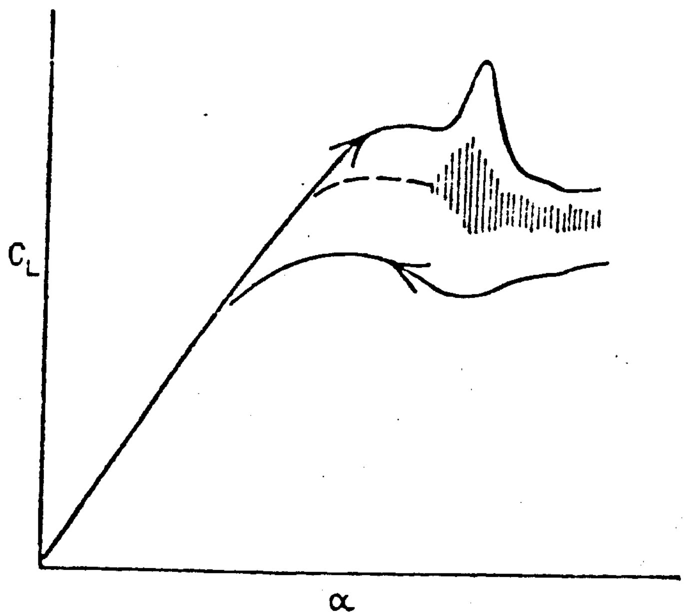

Figure 2.4 The lift-incidence curve for a stalled aerofoil.

2.5. Pressure Distribution on an Aerofoil

The pressure on the surface of an aerofoil in flight is not uniform. Fig.[2.5] shows some typical pressure distributions for a given section at various angles of incidence. It is convenient to deal with non-dimensional pressure differences with p_∞, the pressure far upstream, being used as the datums. Thus the coefficient of pressure is introduced below

$$C_p = \frac{(p - p_\infty)}{\frac{1}{2}\rho V^2} \tag{2.1}$$

Looking at the sketch for zero incidence ($\alpha = 0$) it is seen that there are small regions at the nose and tail where C_p is positive but that over most of the section C_p is negative. At the trailing edge the pressure coefficient comes close to +1 but does not actually reach this value. More will be said on this point later. The reduced pressure on the upper surface is tending to draw the section upwards while that on the lower surface has the opposite effect. With the pressure distribution as sketched, the effect on the upper surface is the larger, and there is a resultant upwards force on the section, which is the lift.

As incidence is increased from zero the following points are noted:

(i) The pressure reduction on the upper surface increases both in intensity and extent until, at large incidence, it actually encroaches on a small part of the front lower surface

(ii) The stagnation point moves progressively further back on the lower surface, and the increased pressure on the lower surface covers a greater proportion of the surface. The pressure reduction on the lower surface is simultaneously decreased in both intensity and extent.

The large negative values of C_p reached on the upper surface at large incidence, e.g. 15 degrees, are also noteworthy. In some cases values of -6 or -7 are found. This corresponds to local flow speeds of nearly three times the speed of the undisturbed stream.

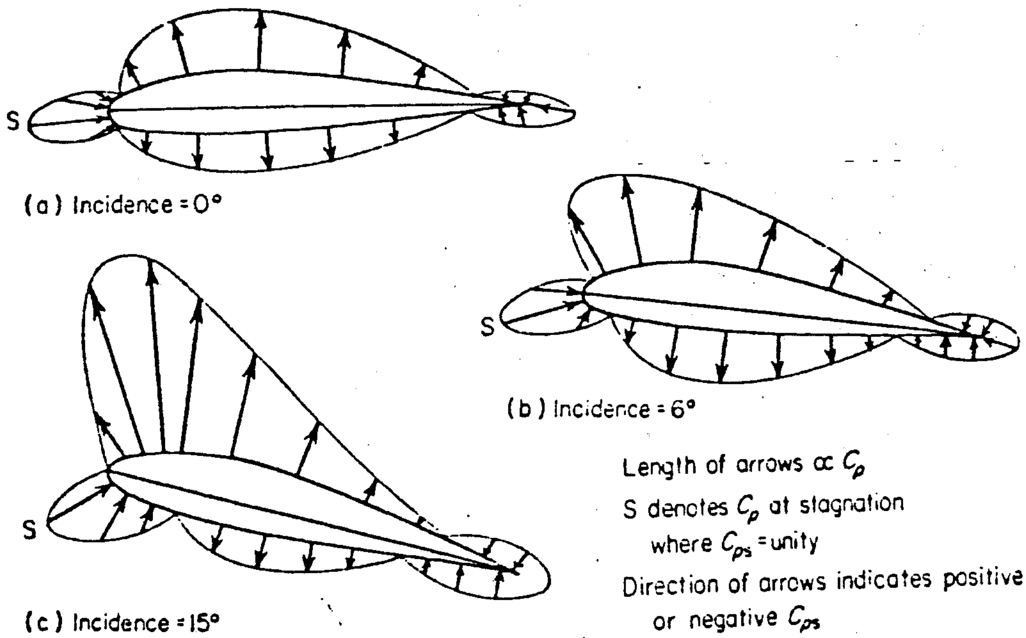

Figure 2.5 Typical pressure distribution on an aerofoil section (Houghton & Carpenter, 1993).

From the foregoing, the following conclusions may be drawn:

(i) at low incidence the lift arises from the difference between the pressure reductions on the upper and lower surfaces

(ii) at higher incidence the lift is partly due to pressure reduction on the upper surface and partly due to pressure increase on the lower surface.

At angles of incidence around 18° or 20° the pressure reduction on the upper surface suddenly collapses and such little lift as remains is due principally to the pressure increase on the lower surface. A picture drawn for one small negative incidence (for this aerofoil section, about -4°) would show equal suction effects on the upper and lower surfaces, and the section would give no lift. At more negative incidence the lift would be negative.

CHAPTER 3

AN OVERVIEW OF THE DISCRETE VORTEX METHODS

In 1858, Helmholtz (as referred to in Sarpkaya, 1989) was the first to show one of the most important contributions to fluid mechanics, showed that in an inviscid fluid vortex lines remain continually composed of the same fluid elements and flows with vorticity can be modelled with vortices of appropriate circulation and infinitely small cross section. This brings forth the discretization of the compact region of vorticity into an assembly of vortices embedded in an otherwise potential flow. Such a discretization of vorticity field with point vortices leads to the Lagrangian approach for calculating the evolution of the vorticity field: Point vortices are introduced into the flow field and traced numerically by applying the Biot-Savart law of induction.

Flows around bluff bodies may be supposed to consist of boundary layer, wake region and inviscid region. Boundary layer where develops from surface of body separates and this boundary layer forms vortex sheets. After this layer completes its developing in the near wake region, it involves to form vortices. The boundary layers which separated from top and bottom surface of body form consecutive vortices with a certain difference of phase. The review is organized around two major sections. Theoretical foundations and practical applications of vortex methods.

3.1 Theoretical Foundations

The vorticity transport equation for a fluid of uniform density (ρ) and viscosity (ν) subjected only to irrotational body forces, is derived from the momentum equation in the form

$$\frac{D\vec{\omega}}{Dt} = \frac{\partial\vec{\omega}}{\partial t} + \vec{U}\ \nabla\ \vec{\omega} = \vec{\omega}\nabla\vec{U} + \nu\nabla^2\vec{\omega} \tag{3.1}$$

in which use is made of the relations that the divergence of velocity and the vorticity are zero. The term ($\vec{U}\ \nabla\ \vec{\omega}$) represents the rate of change due to convection of fluid. The term ($\vec{\omega}\ \nabla\ \vec{U}$) represents the rate of deformation of the vortex lines and exists only in a three-dimensional flow. The last term represents the rate of change due to molecular diffusion of vorticity. Therefore, the motion of an incompressible fluid can be represented as the creation and subsequent evaluation of a self-interacting vorticity field can be assumed to be through an essentially inviscid mechanism. Consequently, the momentum equation becomes;

$$\frac{D\vec{\omega}}{Dt} = 0 \tag{3.2}$$

meaning that the vorticity is a kinematic property of a given fluid particle, and that the vortex lines remains composed of the same elements of fluid as the flow develops. Consequently calculating the evolution of the array of vortices leads to a Lagrangian description of the fluid flow. In certain flow cases vorticity is confined to thin layers rather than being distributed to whole flow field. Unsteady fully separated flows over two dimensional bluff bodies at sufficiently high Reynolds numbers is one of the examples to these flow cases. In simulation the evolution of the separated layers from a bluff body using the Discrete Vortex Method (DVM), a typical approach is to represent the layers by an array of discrete vortices introduced into the flow field at appropriate time intervals at some points near separation. The obvious advantage of the above-mentioned Lagrangian description is that, in order to calculate the evaluation of the self interacting vorticity field only the velocities at the locations of the discrete vortices need to be calculated.

The method of calculation of the velocity field due to the point vortices placed at locations ($\vec{r}'$) is to use the Biot-Savart law;

$$\vec{u}\,(\,\vec{r}, t\,) = -\frac{1}{4\pi}\iiint\frac{(\,\vec{r} - \vec{r}'\,)}{|\,\vec{r} - \vec{r}'\,|}\,dV(\,\vec{r}'\,) \tag{3.3}$$

For two dimensions this gives azimuthal and radial components of velocity field as;

$$u_\theta = \frac{\Gamma}{2\pi\,|\,r - r'\,|} \qquad , \qquad u_r = 0 \tag{3.4}$$

In order to calculate the evaluation of the vortex arrays velocity field due to each point vortex of circulation Γ is superimposed onto the velocity fields of the other point vortices and the irrotational potential flow (If the reader wants to inquire about detail of theoretical foundation of vortices methods, he refers Sarpkaya, 1989). Being grid free, this method eliminates the problem of numerically generated viscosity.

3.2 Practical Applications of Vortex Methods

There are difficulties associated with the Biot-Savart approach even for two-dimensional flow simulations with point vortices. First, the point vortices are singularities, and therefore, create large velocities in their neighbourhood. This causes instabilities and physically impossible sheet crossings along and near the edge of the sheet represented with an array of discrete vortices. The second difficulty is that the number of operations required for the velocity field calculation is proportional to N^2 where N is the number of vortices. Therefore the computation time for complex flow with high number of vortices becomes too long to be practice. To cope with these difficulties various smoothing techniques such as amalgamation and rediscretization of vortices and hybrid methods making the use of Eulerian-Lagrangian approaches are used. Some smoothing techniques will be treated at the next section, but for a detail, the reader may refer to a recent review by Sarpkaya (1989).

At the DVM, because circulations do not diffuse and have the same values all the time and infinitely small point vortices occurs singularity. Both force values are high and vortex distribution is chaotic. Most of the smoothing technique found on decreasing the circulation. On the contrary rediscretization method improve chaotic distribution of vortex locations by organizing the vortex locations at every time step.

3.2.1 Overview of The Applications of The Discrete Vortex Method

Discretization of the compact regions of vorticity into an assembly of vortices embedded in an otherwise potential flow began with the realization that in an inviscid fluid vortex lines remain continually composed of the same fluid elements and that flows with vorticity can be modelled with vortices of appropriate circulation and infinitely cross-section (Sarpkaya, 1989). Naturally, calculating the evolution of the assembly of the vortices leads to a Lagrangian description. However, as a response to the need for using large number of discrete vortices for adequate description of a vortical flow field, a mixed Lagrangian-Eulerian approach is the one that is being preferred in most of the recent studies. Here after, the Lagrangian description will be referred to as the Lagrangian Discrete Vortex Method (DVM) while referring to the mixed Eulerian-Lagrangian description as the Vortex In Cell (VIC) method.

3.2.1.1 Lagrangian Discrete Vortex Method

Similar to the early experimental investigations, in pioneering studies of bluff-body-wakes (Karman 1911 as referred to in Sarpkaya, 1989) using the Lagrangian DVM, far-wake region has received the primary attention. The primary task in these studies was to find out the conditions for which a stable pattern of vortex street may exist. In these studies, no reference has been made to the body responsible for the wake and the array of potential vortices are employed in representing the actual vortical structures encountered in the wake. Von Karman taking into consideration two parallel rows of vortices extending to infinity in both directions, found a value of the ratio of the lateral spacing between the rows to longitudinal spacing between two consecutive vortices in the same row, at which the idealized vortex street remained to be stable. Using a similar approach, in 1962, Abernathy & Kronauer (as referred to in Sarpkaya, 1989) studied the non-linear interaction of two infinitely-long vortex sheets, initially a fixed distance apart, in an inviscid and incompressible fluid. They demonstrated that, as a result of the interaction, the point vortices cluster into clouds configuration of whose simulates the vortex street forming behind bluff bodies. However, they did not consider the effect of the bluff body on the non-linear interaction of separated layers.

Recent studies take into account the presence bluff body and, by representing the separated boundary layers from the body by a row of potential vortices aim to concentrate into the vortex formation mechanism taking place in the near-wake region. Of course, in contrast to the Karman example, this time the potential vortices are not in an infinitely large flow field but limited with a solid boundary representing the body. Therefore, in an inviscid analysis, in order to satisfy the "no-flow normal to the boundary" condition image vortices in the body should be accounted for.

Need to use the method of images brings forth the difficulty that not all the geometries can easily be taken into consideration : Only the geometries which are suitable for transformation to planes in which the location of the images can be easily found. For example, Clements (1973), in a study of wake formation from a blunt-based flat plate uses a semi-infinite half plane for the transformation plane. For a circular cylinder on the other hand, no transformation plane is needed since the image vortices are simply introduced to the inverse points in the cylinder (Sarpkaya & Schoaff, 1979 - Ünal, et.al., 1992). In these studies, the discrete vortices are introduced from separation points in an otherwise potential flow with a constant time step and are tracked using a Lagrangian approach.

There are many problems associated with the application of the DVM in an inviscid analysis. One of them is the randomization of the potential vortices for large non-dimensional times. To avoid this, a method named as re-discretization is used (Sarpkaya & Schoaff, 1979). In this method at, each time step of integration, potential vortices are redistributed to their new locations on a line in such a way that the circulation and the first moment of circulation are conserved. Second problem encountered is that the potential vortices never decay. This results in high values in calculated drag and fluctuating lift forces. Although contradicting with the potential theory,these higher values are avoided using some kind of a decaying mechanism for vortices. Also in the same line of thought, vortices getting too close to each other are removed from the field or amalgamated into a single vortex. This also applies to vortices approaching very near to their images.i.e. they are removed too. Therefore unrealistic velocities induced by vortices are avoided. A second way to avoid this problem is to employ vortices having viscous cores. Therefore, these vortices will not induce unrealistic velocities. Also, they will decay in accordance with the exact solution and will make finding more realistic lift and drag values possible.

Another difficulty encountered, when taking the bluff body into analysis, is the fact that not all the geometries have fixed separation points, and therefore a proper criterion should be employed for predicting the points of separation. This problem can be overcome by taking a form of body for which the separation points are fixed geometrically. For instance, Clements (1973) studies the vortex formation from a blunt trailing -end for which the corners of the edge are the separation points. Nevertheless, for geometries having no sharp corners there are studies in which the separation points are assumed to be fixed. Of course, a more proper approach is one which takes into account the nature of the separation points and uses for instance an integral approach to predict the locations of the separation points. This was done by Sarpkaya & Schoaff (1979) and results that fit to actual physical situation are found.

Before closing, it should be added that, using the panel method. it is possible to overcome the above-mentioned constraint about the geometry of the body arising from the application of the method of images. A recent review paper by Sarpkaya (1989) can be resorted to for this and other computational methods with vortices.

An important outcome of these studies is that the Strouhal number of vortex shedding can be correctly predicted. However, in order to predict the drag and fluctuating lift forces correctly, some kind of circulation reduction technique needs to be employed. Of course at the expense of violating the 'preservation of circulation' principle. Nevertheless, from an engineering point of view, applications of the classical DVM can be regarded as successful in not only predicting the frequency of vortex shedding but also in disclosing certain details about loading of bluff bodies due to alternate shedding.

3.2.1.2 Vortex-in-Cell Method

Being grid-free, the Lagrangian DVM is an advantageous one when compared with a grid dependent method. However, in view of the number of operations needed to calculate the velocities at vortex positions for each time step, it becomes impractical and in certain applications stretches the capability of even the fastest computers of the day. In view of this, the Vortex-in-Cell method provides a great advantage, in that, instead of computational time increasing as $\boldsymbol{N^2}$, it is proportional to $\boldsymbol{M \log_2 M}$, where $\boldsymbol{N}$ and $\boldsymbol{M}$ are the number of vortices and the number of grid points.

Following its development at Los Alamos at the middle of 1950's, the Vortex-in-Cell method has provided basis for many studies. Since its application allows the physical processes of vorticity creation, diffusion and convection to be modelled in conceptually clear manner, the viscous Vortex-in-Cell method can make a major contribution to increased understanding of the underlying physics of the flow.

In the area of vortex formation from sharp edges and bluff bodies, most notable studies using the VIC method are those of Graham (1980), Cozens (1988), Graham & Cozens (1988) and Stansby & Dixon (1982). For a comprehensive information, reader is referred to the recent review article by Sarpkaya (1989).

In this study, two method for solving the flows is used. First method is DVM that uses conformal mapping for body representation and second method is a viscous DVM. This method uses the time splitting of the vorticity transport equation. While solving the convection part using the VIC method the diffusion of vorticity is solved directly on the mesh using finite difference technique. Detailed description of the solution procedures are in the following two chapter.

CHAPTER 4

THEORY AND TECHNIQUE OF LAGRANGIAN DISCRETE VORTEX METHOD AND AN APPLICATION TO FLOW AROUND CIRCULAR CYLINDERS WITH AND WITHOUT SPLITTER PLATE

4.1 Stationary Circular Cylinder

The vorticity transport equation for a fluid of uniform density (ρ) and viscosity (ν) subjected only to irrotational body forces is derived from the momentum equation in the form;

$$\frac{D\vec{\omega}}{Dt} = \frac{\partial\vec{\omega}}{\partial t} + \vec{U}\,\nabla\,\vec{\omega} = \vec{\omega}\nabla\vec{U} + \nu\nabla^2\vec{\omega} \tag{4.1}$$

At high Reynolds numbers, the evolution of the self-interacting vorticity field can be assumed to be through an essentially inviscid mechanism. Therefore, if flow is also two-dimensional, the momentum equation for the scalar vorticity w becomes,

For two dimensional flow of an inviscid fluid, the vorticity (ω) convection equation,

$$\frac{D\omega}{Dt}=0 \tag{4.2}$$

or its Lagrangian equivalent,

$$\frac{\partial\lambda_j(\omega)}{\partial t} = U_j(\omega) \tag{4.3}$$

allows for calculation of the position of each vortex after a small time interval δt; where λ_j is the complex co-ordinate of the position of a potential vortex having vorticity ω and a corresponding complex velocity U_j. The vorticity field is represented by a summation over all the vortices in the flow field,

$$\omega(\lambda,t) \doteq \sum_{j=1}^{N} \Gamma_j \delta \left(\lambda - \lambda_j(t) \right) \tag{4.4}$$

where $\lambda_j(t)$ is the instantaneous position of a point vortex having circulation Γ_j ,and δ is the Dirac distribution, and thus in order to determine evolution of the array of vortices representing the separated boundary layers, only the velocities at locations of potential vortices need to be calculated. The complex conjugate velocity induced at a location $z = x + iy$ is calculated from the below expression which is obtained by taking the derivative of the total complex potential due to the basic flow.

4.1.1 Potential Theory

For incompressible, irrotational and two-dimensional flow,

$$u = \frac{\partial \phi}{\partial x} = \frac{\partial \psi}{\partial y} \quad , \qquad v = \frac{\partial \phi}{\partial y} = -\frac{\partial \psi}{\partial x} \tag{4.5}$$

where u and v is the velocity components in x and y directions. ψ is stream function and ϕ is potential function, so;

$$\frac{\partial \phi}{\partial x} = \frac{\partial \psi}{\partial y} \quad , \qquad \frac{\partial \phi}{\partial y} = -\frac{\partial \psi}{\partial x} \tag{4.6}$$

can be order from Eq.(4.5), and these equation is known Cauchy-Riemann equations, so a complex potential can be occur by using ψ and ϕ function;

$$f = \phi + i\,\psi \tag{4.7}$$

derive this equation with respect to the z,

$$\frac{df}{dz} = \frac{\partial \phi}{\partial x} + i\,\frac{\partial \psi}{\partial x} \tag{4.8}$$

where df/dz is complex conjugate velocity.

$$\frac{df}{dz} = \frac{\overline{dz}}{dt} = u - i\,v \tag{4.9}$$

Therefore we need to a complex potential which represents flow around the circular cylinder. Circle theorem is written as;

$$f(z) = f_o(z) + \bar{f}_o(\frac{a^2}{z}) \tag{4.10}$$

where $f_o(z)$ is complex potential of mean flow. In this study, the mean flow is uniform flow (free stream) and $f(z)$ is complex potential of basic flow that is embedded circle to mean flow. An overbar indicates a complex conjugate. The mean flow is as a uniform flow;

$$f_o(z) = U_o\, z \tag{4.11}$$

where U_o is free stream velocity. We write again using Eq.(4.11),

$$f(z) = U_o\, z + \bar{U}_o \frac{a^2}{z} \tag{4.12}$$

where a is radius of circle. In the other hand, flow due to a vortex of circulation Γ placed z_o is given by the complex potential;

$$g(z) = -\frac{i\Gamma}{2\pi} \log(z - z_o) \tag{4.13}$$

We must add image vortex term to satisfy the zero normal velocity on the cylinder.

$$g'(z) = \frac{i\Gamma}{2\pi} \log(z - \frac{a^2}{z_o}) \tag{4.14}$$

where z_o is image vortex position and, $z_o' = a^2/z_o$; Therefore the complex potential of flow around circular cylinder with point cortices is; $w(z)$

$$w(z) = U_o\, z + \frac{\bar{U}_o\, a^2}{z} + \sum_j^N \frac{i\,\Gamma_j}{2\pi} \log(z - z_j) + \sum_j^N \frac{i\,\Gamma_j}{2\pi} \log(z - \frac{a^2}{\bar{z}_j}) \tag{4.15}$$

where z_j and Γ_j are the location and the strength of the j th vortex. And we can obtain complex conjugate velocity by deriving equation;

$$\frac{dw(z)}{dz} = \frac{\overline{dz}}{dt} = \left(U - \frac{\bar{U}a^2}{z^2}\right) - \frac{i}{2\pi}\sum_{j}^{N}\Gamma_j\left(\frac{1}{z - z_j} - \frac{1}{z - a^2/\bar{z}_j}\right) \tag{4.16}$$

For details of these expressions, the reader may refer to Sarpkaya & Schoaff (1979), Şuhubi (1968), Milne-Thompson (1973), Sarpkaya (1989).

After determining the upper and lower introduction points, the motion of vortices introduced into the flow from these points with a certain time interval can be calculated by integrating the Eq.(4.16) via using a proper integration scheme. In this study, a first-order Euler integration scheme, i.e.

$$\lambda_j(T + \delta T) = \lambda_j(T) + \frac{\partial \lambda_j}{\partial T}\,\delta T \tag{8}$$

with a time step non-dimensionalized with respect to the free-stream velocity and the radius of the cylinder, ***$\delta T = 0.1$*** is used.

4.1.2 Prediction of introduction points

The potential vortices are introduced into the flow at the locations at radial distances (r_s) out from the separation points (Fig.[4.1]). The simulation used herein allows for the determination of the separation points, and the radial distances are calculated to satisfy the no-slip condition at the separation points at the instant of introduction of new vortices. At Fig.[4.2], Schematic view of the wake formed from a bluff body with variable separation point.

One of the difficulties encountered when applying the inviscid discrete vortex method for a bluff body with variable separation points is prediction of the separation points. A good many studies ignore the movement of the separation points altogether and consider these points fixed at values close to that found in experiments. Herein, two different approaches for calculating the separation points are employed, one of them, the separation points are assumed to be fixed at $\pm 90^\circ$ from the front stagnation point, and the other, they are allowed to move in accordance with the downstream periodicity. For prediction of separation points, Sarpkaya & Schoaff (1979) employed Pohlhausen's quasi-steady state method based on the instantaneous velocity distribution around the cylinder boundary obtained from the potential theory. Herein, we apply a quasi-steady approach similar to the one proposed by Sarpkaya (1968) and Stansby (1981), in which the locations of maximum velocity on the cylinder boundary are taken to be the separation points. For each separation point, velocities are calculated at 40 points on the cylinder with 0.05 degree increment between successive points. At each time step, the points are centred around the separation points determined in the previous time step. Similar procedure is applied for prediction of the stagnation point fluctuations, but of course, this time the minimum velocity location at each time step is taken as the instantaneous stagnation point angle. Therefore, for each instant of calculation, the velocities are calculated at 120 points altogether. However, when doing this , effects of last 10 vortices released from the separation points are not taken into account. Consequently, only the large scale vortices (i.e. clouds formed by point vortices) dictate the motion of the separation and the stagnation points.

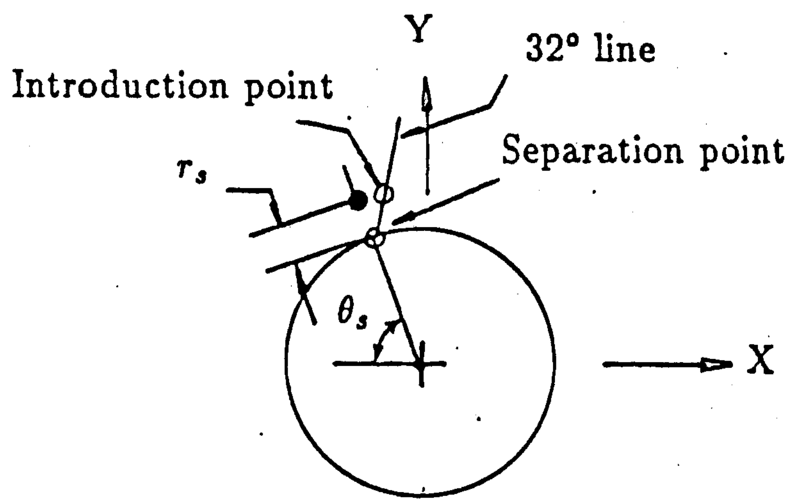

Figure 4.1 Sketch showing the parameters employed for introduction of discrete vortices.

As regard with the radial distance of the point of introduction of the vortices: in some studies, it is defined somewhat arbitrarily and based on experience and trial calculations (Clements, 1973 - Sarpkaya, 1963). However, the velocities at the inner and the outer edges of the shear layers separated from surfaces, the time interval between introduction of vortices and the Kutta condition are interdependent (Sarpkaya, 1989). Therefore, points of introduction and the time step cannot be taken arbitrarily. Herein, the radial distances are determined so as to satisfy the no-slip condition at the separation points at the instant of introduction of new vortices and thus they are allowed to move in harmony with the downstream periodicity (Sarpkaya & Schoaff 1979).

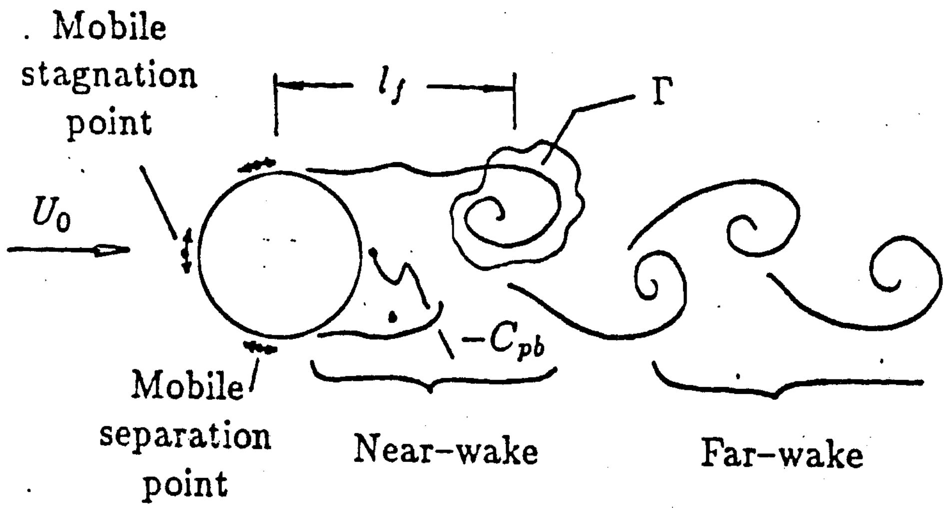

Figure 4.2 Schematic view of the wake formed from a bluff body with variable separation points.

Herein we determine the distance r_s from the cylinder surface along the radial line passing through the separation point Fig.[4.1] with the requirement that the no-slip condition is satisfied at separation point. Therefore the value of r_s is such that;

$$1 + r_s = \frac{1 + |\Gamma_n|/(2\pi U_s)}{1 - |\Gamma_n|/(2\pi U_s)} \tag{4.18}$$

where the velocity U_s is taken as the velocity at the separation point prior to the introduction of the nascent vortex. However, upon determining the radial distances, new vortices are not placed at those distances along the radial lines. Instead, in order to simultaneously satisfy the no-slip and the no-back-flow conditions they are placed on the 32 degree-lines (Fig.[4.1]) as suggested by Sarpkaya (1989).

The circulations of the new vortices released into the flow from the introduction points are calculated from:

$$\Gamma = \frac{1}{2} U_S^2 \, \delta T \tag{4.19}$$

where U_S is the velocity at the point of separation prior to the introduction of a new vortex, and δT is the time increment between successive introductions; U_S and the time increment δT are non-dimensional quantities based on the free-stream velocity in the physical plane and the radius of the cylinder.

4.1.3 Circulation Reduction Scheme

Another difficulty associated with the DVM is that the potential vortices never decay and thus lead to high values in calculated drag and lift coefficients. Although contradicting with an inviscid analysis, to obtain realistic values for these coefficients, a circulation reduction scheme is frequently resorted to. In this study, the heuristic model used for circulation reduction is due to Sarpkaya & Schoaff (1979) in which every vortex in the wake loses its strength in an amount proportional to its current strength and position. The constat of proportionality is such that;

$$\begin{aligned} \beta &= \left(\frac{0.009}{5}\right)T && \textit{for} \quad T<5 \\ \beta &= 0.009 && \textit{for} \quad T>5 \quad \textit{in the region} \quad 0<x<10 \\ \beta &= -0.0009x + 0.018 && \textit{for the region} \quad x\geq 10 \end{aligned} \tag{4.20}$$

All of the Lagrangian DVM applications, point vortices approaching to a solid boundary smaller than a prescribed distance (a cancellation distance) is removed from the flow field just to avoid unrealistically high velocities that would have been induced to them by their images otherwise.

However, in order to quickly provide the evolution of the wake flow, an asymmetry is induced to the developing flow field for a limited time interval. As suggested by Sarpkaya & Schoaff (1979) the vortices on one side of the wake are given small lateral displacements. However, the magnitude of asymmetry is much smaller than that used by them. The form of the asymmetry is;

$$\Delta x = 0.01\left[1 - Cos\left(\frac{\pi\,(T-5)}{4}\right)\right] \qquad \textit{for} \quad 5\leq T\leq 9 \tag{4.21}$$

4.1.4 Calculation of lift, drag coefficients

Lift and drag coefficients are calculated from the Generalized Blasius equation;

$$C_D + i\,C_L = \frac{1}{2}\,i\oint_s \left(\frac{dW}{dz}\right)^2 dz \;-\; i\,\frac{\partial}{\partial T}\,\overline{\oint_s \left(\frac{dW}{dz}\right) dz} \tag{4.22}$$

where the integral are taken round the perimeter (s) of the body first term of right hand side of the equation is solved by using Lagally's theorem and second term is solved by using Residue theorem (For detail, Sarpkaya, 1963). As a result;

$$C_D + i\, C_L = i \frac{\partial}{\partial T} \sum_j^N \Gamma_j \left(z_j - \frac{1}{\bar{z}_j} \right) \tag{4.23}$$

or its other form;

$$C_D + i\, C_L = i \sum_j^N \Gamma_j \left(V_j - V_{ji} \right) - i \sum_j^N \frac{a^2}{\bar{z}_j} \frac{\partial \Gamma_j}{\partial T} \tag{4.24}$$

where $V_j = u_j + iv_j$; j th vortex velocity, $d\Gamma_j/dT$; derivative with respect to non-dimensional time of j th vortex, of course Reduction is caused to be or not. Second form of force equation is more accuracy other than. Image vortex velocity is

$$\begin{aligned} u_{ji} &= \frac{a^2}{|z_j|^4} \left[\left(y_j^2 - x_j^2 \right) u_j - 2\, x_j\, y_j\, v_j \right] \\ v_{ji} &= \frac{a^2}{|z_j|^4} \left[\left(x_j^2 - y_j^2 \right) v_j - 2\, x_j\, y_j\, u_j \right] \end{aligned} \tag{4.25}$$

4.1.5 Calculation of Pressure Coefficient Distributions

Bernoulli's equation for unsteady incompressible flows;

$$p + \frac{1}{2} \rho \left(u^2 + v^2 \right) + \rho \frac{\partial \Phi}{\partial t} = p_\infty + \frac{1}{2} \rho\, U_\infty \tag{4.26}$$

where ϕ is the velocity potential forming the real part of the complex potential W.

Defining the pressure coefficient in the usual way, as

$$C_p = \frac{p - p_\infty}{\frac{1}{2} \rho\, U_\infty} \tag{4.27}$$

Eq.(4.26) is modified into

$$C_p = 1 - (u^2 + v^2) - 2 \frac{\partial \Phi}{\partial T} \tag{4.28}$$

where u and v are the non-dimensional velocity components in x and y directions around the cylinder in the physical plane and ϕ is the velocity potential.

If $d\phi/dT$ is wanted to be calculated numerically, pressure values are unrealistic. So we must calculate them analytically. Let derive equation (4.15) and let write its real component ($\frac{\partial \Phi}{\partial T} = \Re\left(\frac{dW}{dT}\right)$)

$$\frac{\partial \Phi}{\partial T} = \Re\left\{ \frac{i}{2\pi} \sum_j^N \left[\frac{\partial \Gamma_j}{\partial T} \left(\log(z - \frac{a^2}{\bar{z}_j}) - \log(z - z_j) \right) + \left(\frac{1}{z - z_j} V_j - \frac{1}{z - a^2/\bar{z}_j} V_{ji} \right) \right] \right\} \tag{4.29}$$

where V_{ji} is j th image vortex velocity.

Effects of the reduction on the fluctuating quantities such as the separation and stagnation point angles, lift and drag coefficient as well as the wake structure are studied.

4.2 Oscillating Circular Cylinder

Most of the techniques and parameters of this study is the same to the stationary circular cylinder (the previous section), so only different technique and parameters are mentioned in this study.

4.2.1 Free Stream Velocity

The most important difference is not to be constant free stream velocity. x direction of free stream changes by sinusoidal (Fig.[4.23]).

$$U_o = U_m + U_e \, Cos(2\pi f_e T) \tag{4.30}$$

where U_m is mean velocity of free stream, U_e is magnitude of oscillation and f_e is frequency of oscillation. In this study that is supposed cylinder to be stationary and stream oscillates. Non-dimensional magnitude of oscillation is $G_e = \frac{U_e}{2\pi f_e}$.

Non-dimensional oscillation magnitude of the study that the cylinder oscillates is *A/D,* where *A* magnitude of oscillation and *D* is diameter. *A/D* opposes to G_e. In this study, G_e is given 0.3.

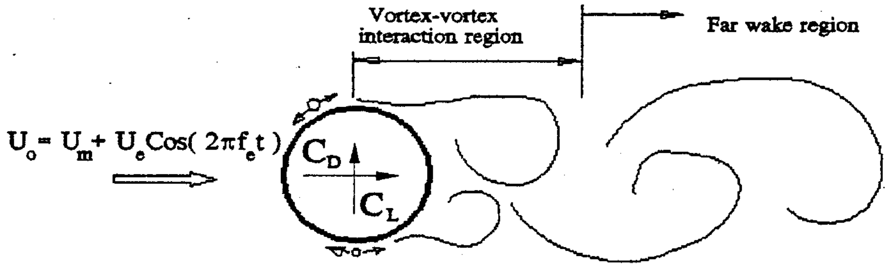

Figure 4.3 Schematic view of the wake formed from a bluff body with variable separation points and with oscillating free stream velocity.

4.2.2 Calculation lift and drag

In this study, we must add a additional term to force equation (Eq.(4.24)). Let's write with new form as;

$$C_D + i\,C_L = i\sum_{j}^{N} \Gamma_j \,(\, V_j - V_{jl}\,) \; - \; i\sum_{j}^{N} \frac{a^2}{\bar{z}_j}\,\frac{\partial \Gamma_j}{\partial T} + 2\pi\, a^2\,\frac{dU_o}{dT} \tag{4.31}$$

4.3 Circular cylinder with splitter plate

Some of techniques and parameters of this study is the same to stationary circular cylinder (Section 4.1) so only different techniques and parameters mentioned in this study.

In this study, motion of the vortices has been calculated in a transformed plane. This plane is obtained by the following set of conformal transformations which maps the points on and outside of the circular cylinder with an attached-plate to points on and outside a circular cylinder with unit radius (Fig.(4.4)):

4.3.1 Conformal mapping from circular cylinder to circular cylinder with splitter plate

This transformation occurs in two steps. First step is transformed from plate to circle (ζ plane to λ plane, See Fig.[4.4]). This transformation is;

$$\zeta = \frac{5}{8}(\lambda + \frac{1}{\lambda}) \tag{4.32}$$

And then from plate to circle with plate *(ξ plane to z)*

$$\zeta = \frac{5}{2}\frac{L_P}{(L_p+1)^2}\left(z + \frac{1}{z}\right) - \frac{5}{4}\frac{(L_P-1)^2}{(L_p+1)^2} \tag{4.33}$$

And let's composed two equation

$$\frac{5}{8}(\lambda + \frac{1}{\lambda}) = \frac{5}{2}\frac{L_P}{(L_p+1)^2}\left(z + \frac{1}{z}\right) - \frac{5}{4}\frac{(L_P-1)^2}{(L_p+1)^2} \tag{4.34}$$

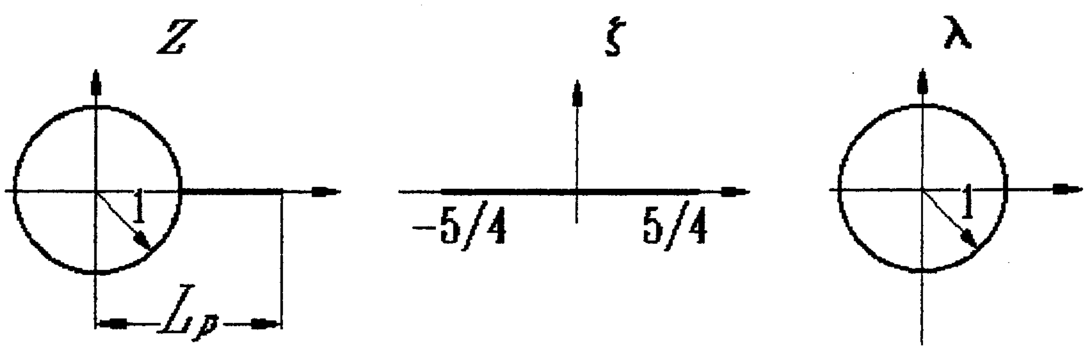

Figure 4.4 Sketch showing the physical plane z and the computational plane λ.

Let's draw z;

$$z = \frac{(L_p+1)^2}{8\,L_p}\left(\lambda + \frac{1}{\lambda}\right) + \frac{(L_P-1)^2}{4\,L_P} \mp \sqrt{\left\{\frac{(L_p+1)^2}{8\,L_p}\left(\lambda + \frac{1}{\lambda}\right) + \frac{(L_P-1)^2}{4\,L_P}\right\}^2 - 1} \tag{4.35}$$

This equation is transformation from circular cylinder to circular cylinder with splitter cylinder. Let's write down inverse transformation;

$$\lambda = \frac{2L_P}{(L_P+1)^2}\left(z+\frac{1}{z}\right)\frac{(L_P-1)^2}{(L_P+1)^2} \mp \sqrt{\left\{\frac{2L_P}{(L_P+1)^2}\left(z+\frac{1}{z}\right)-\frac{(L_P-1)^2}{(L_P+1)^2}\right\}^2-1} \quad (4.36)$$

and Let derive Eq.(4.35) with respect to λ;

$$\frac{dz}{d\lambda} = \frac{(L_P+1)^2}{8\,L_P}\left(1-\frac{1}{\lambda^2}\right) \mp \frac{\left\{\frac{(L_P+1)^2}{8\,L_P}\left(\lambda+\frac{1}{\lambda}\right)+\frac{(L_P-1)^2}{4\,L_P}\right\}\frac{(L_P+1)^2}{8\,L_P}\left(1-\frac{1}{\lambda^2}\right)}{\sqrt{\left\{\frac{(L_P+1)^2}{8\,L_P}\left(\lambda+\frac{1}{\lambda}\right)+\frac{(L_P-1)^2}{4L_P}\right\}^2-1}} \quad (4.37)$$

where $\frac{d\lambda}{dz} = \frac{4L_P}{(1+L_P)^2}$ *as* $z,\lambda \to \infty$ (For more detail the reader refers Çete, 1989 - Çete & Ünal, 1992).

4.3.2 Representation the Flow around the Circular Cylinder with Splitter Plate

Consequently, for the free-stream velocity in the physical plane to be U_0, the complex potential:

$$W_{bf}(\lambda) = \frac{(1+L_P)^2}{4L_P}\,U_0\left(\lambda-\frac{1}{\lambda}\right) \quad (4.38)$$

represents the basic flow around the circular cylinder with unit radius. Then, the total complex potential is obtained by adding this to the complex potential due to N vortices in the flow field, and their images in the cylinder which are required to satisfy the zero normal velocity on the cylinder:

$$W(\lambda) = W_{bf}(\lambda) - \sum_{j=1}^{N}\frac{i\Gamma_j}{2\pi}\left[\ln(\lambda-\lambda_j) - \ln\left(\lambda-\frac{1}{\bar{\lambda}_j}\right)\right] \quad (4.39)$$

where λ^*_j is the complex conjugate of λ_j.

Derivative of this complex potential with respect to the complex co-ordinate λ gives the complex conjugate velocity in the transformed plane. Since the vortices are convected in the transformed plane, Eq.(4.3) is modified to take into account the transformation modulus at vortex locations $|d\lambda/dz|^2$. Therefore, complex conjugate of Eq. (4.3) becomes:

$$\frac{\partial \bar{\lambda}_j}{\partial t} = \left[\frac{\partial W}{\partial \lambda_j} - \frac{i\Gamma_j}{4\pi} \left(\frac{d^2z/d\lambda_j^2}{dz/d\lambda_j} \right) \right] \left| \frac{d\lambda_j}{dz} \right|^2 \tag{4.40}$$

where the second term in the parenthesis represents the Routh correction factor in the transformed plane and complex conjugate velocity is;

$$\overline{\frac{\partial z_a}{\partial t}} = \left[\frac{\partial W}{\partial \lambda_a} - \frac{i\Gamma_a}{4\pi} \left(\frac{d^2z/d\lambda_a^2}{dz/d\lambda_a} \right) \right] \frac{d\lambda_a}{dz}$$

$$\overline{\frac{dz_a}{dt}} = \left[\frac{(1+L_p)^2}{4\,L_p} \left(U - \frac{\bar{U}a^2}{\lambda_a^2} \right) - \frac{i}{2\pi} \sum_{\substack{j \\ \lambda_a \neq \lambda_j}}^{N} \Gamma_j \left(\frac{1}{\lambda_a - \lambda_j} - \frac{1}{\lambda_a - a^2/\bar{\lambda}_j} \right) - \frac{i\Gamma_j}{4\pi} \left(\frac{d^2z/d\lambda_j^2}{dz/d\lambda_j} \right) \right] \frac{d\lambda_a}{dz} \tag{4.41}$$

where z_a is anywhere in the flow and λ_a is its transformed value in the transformed plane. Of course, if there is not a point vortex at z_a location, Routh correction factor will be dropped.

After determining the upper and lower introduction points, the motion of vortices introduced into the flow from these points with a certain time interval can be calculated by integrating the Eq.(4.7) via using a proper integration scheme. In this study, a first-order Euler integration scheme, i.e.

$$\lambda_j(\,T+\delta T\,) = \lambda_j(T) + \frac{\partial \lambda_j}{\partial T}\,\delta T \tag{4.42}$$

with a time step non-dimensionalized with respect to the free-stream velocity and the radius of the cylinder, $\delta T = 0.1$ is used.

4.3.3 Circulation reduction scheme

Another difficulty associated with the inviscid discrete vortex method is that the potential vortices never decay and thus lead to high values in calculated drag and lift coefficients. Although contradicting with an inviscid analysis, in order to obtain realistic values for these coefficients, a circulation reduction scheme is frequently resorted to

(Kawai, 1990 - Sarpkaya & Schoaff, 1979).

In this study ,the model used for circulation reduction is similar to the one employed by Kawai (1990), in which every vortex in the wake loses its strength in an amount depending on its non-dimensional life time (T_v). The form of the proportionality is as follows:

$$\begin{aligned} \beta &= 0.002T_v \quad for \quad T_v<5 \\ \beta &= 0.01T_v \quad for \quad 5 \le T_v \le 20 \\ \beta &= 0 \quad for \quad T_v>20 \end{aligned} \tag{10}$$

Once the introduction points defined by the separation points and the radial distances are determined and the circulation reduction scheme has been employed, a couple of new potential vortices are introduced into the flow field at each time step, and their motion are calculated according to the Eq.(4.40) and (4.42).

However, in order to quickly provide the evolution of the wake flow, an asymmetry is induced to the developing flow field for a limited time interval. As suggested by Sarpkaya & Schoaff (1979), the vortices on one side of the wake are given small lateral displacements. However, the magnitude of asymmetry is much smaller than that used by them. The form of the asymmetry is:

$$\Delta x = 0.01 \left(1 - Cos[\ \pi(T-5)/4\ ] \right) \quad for \quad 5 \le T \le 9 \tag{4.44}$$

It should be noted that, the magnitude of the asymmetric perturbation is decided after many preliminary calculations for different sets of values of the asymmetric perturbation and the constant of proportionality for the reduction. The set of values used for the results presented herein not only provides the stable regime for the circular cylinder without the splitter plate in a very short time but also gives way to values of oscillating quantities such as lift and drag coefficient, which are in agreement with previous numerical and experimental studies (Sarpkaya & Schoaff, 1979).

4.3.4 Calculation of Pressure Distributions and Lift, Drag Coefficients

Lift and drag coefficients are calculated from the instantaneous pressure distributions around the body. In doing this, pressures are calculated at a number of stations on an envelope around the body in the physical plane. The calculation is carried out at every other 10 time increments and at 180 points with equal increments on the circular cylinder, whereas the number of stations on the upper and lower faces of the splitter plate, with equal spacing of 5% of the plate length, vary depending on the plate length.

Distribution of the pressure coefficient (C_p) around the cylinder is calculated from the unsteady Bernoulli's equation:

$$C_p = 1 - (u^2 + v^2) - 2 \frac{\partial \phi}{\partial T} \tag{4.45}$$

where u and v are the non--dimensional velocity components in x and y directions around the cylinder in the physical plane, and ϕ is the velocity potential.

The lift and drag coefficients are obtained by means of integration of the pressure distribution around the cylinder and the splitter plate. In order to eliminate the effect of meaningless pressure values just downstream of separation, a procedure similar to that employed by Stansby (1981) is used: Pressure is assumed to vary linearly between the pressures at stations 5 degrees ahead and 15 degrees after the instantaneous separation angle.

In all of the Lagrangian discrete vortex method applications, point vortices approaching to a solid boundary smaller than a prescribed distance (a cancellation distance) is removed from the flow field just to avoid unrealistically high velocities that would have been induced to them by their images otherwise. As pointed out by Stansby (1981), the pressure coefficient in the base region is sensitive to the cancellation distance. In this study, this distance is chosen to 4% of the radius of the cylinder for both the cylinder and the splitter plate.

The computations were performed using an i860 microprocessor for 11 different plate lengths (L) non-dimensionalized with respect to the diameter of the cylinder (D). These plate lengths are: $L/D = 0$, 0.0625, 0.125, 0.25, 0.50, 0.75, 1.0, 1.25, 1.50, 1.75

and 2.0.

4.4 Calculation procedure

The studies mentioned in this chapter have same calculation procedure. Steps of the calculation are as follows:

- i- Determine the separation points.
- ii- Calculate the induced velocities at the separation points.
- iii- Calculate the strength and radial location of new vortices.
- iv- Calculate the pressure coefficient distribution around the cylinder and on the plate and integrate it to find the drag and lift coefficients.
- v- Determine velocities at introduction points and previously-introduced vortex locations.
- vi- Release new vortices into the flow by convecting them with the velocities found in step v.
- vii- Advance rest of the vortices to their new positions using velocities found in step v.
- viii- Apply reduction to circulation of the vortices.
- ix- Return to step i to introduce new vortices into the flow.

CHAPTER 5

THEORY AND TECHNIQUE OF VORTEX-IN-CELL METHOD AND AN APPLICATION TO FLOW AROUND NACA 0012 AIRFOIL

5.1 Governing Equations

The fundamental equation of a flow for a newtonian fluid is the equation derived from the balance of momentum namely the Navier-Stokes equation. The balance of momentum for a fluid can be written as;

$$\rho \frac{DV}{DT} = \rho g + \nabla \bar{\sigma} \tag{5.1}$$

By taking $\bar{\sigma}$ in consideration according to Stokes's postulates, for an incompressible and constant-viscosity fluid, this equation becomes:

$$\rho \frac{D\vec{U}}{Dt} = \rho \vec{g} - \nabla p + \mu \nabla^2 \vec{U} \tag{5.2}$$

The gravity term is negligible in most cases. Thus the two-dimension form of the Navier-Stokes equations for a constant property fluid are;

$$\begin{aligned} \frac{\partial u}{\partial t} + u\frac{\partial u}{\partial x} + v\frac{\partial u}{\partial y} &= -\frac{1}{\rho}\frac{\partial p}{\partial x} + \nu\left[\frac{\partial^2 u}{\partial x^2} + \frac{\partial^2 u}{\partial y^2}\right] \\ \frac{\partial v}{\partial t} + u\frac{\partial v}{\partial x} + v\frac{\partial v}{\partial y} &= -\frac{1}{\rho}\frac{\partial p}{\partial y} + \nu\left[\frac{\partial^2 v}{\partial x^2} + \frac{\partial^2 v}{\partial y^2}\right] \end{aligned} \tag{5.3}$$

Taking the curl of these two equations and thus eliminating the pressure from them gives "Vorticity Transport Equation" in two-dimension, that is

$$\frac{D\omega}{Dt} = \nu \nabla^2 \omega \tag{5.4}$$

or

$$\frac{\partial \omega}{\partial t} + (\vec{U} \nabla) \omega = \nu \nabla^2 \omega \tag{5.5}$$

where " ω " is defined here as "fluid vorticity".

$$\omega = \frac{\partial v}{\partial x} - \frac{\partial u}{\partial y} \tag{5.6}$$

Consequently the incompressibility assumption $div \vec{U} = 0$, i.e.;

$$\frac{\partial u}{\partial x} + \frac{\partial v}{\partial y} = 0 \tag{5.7}$$

and definition of the stream function ψ as;

$$\frac{\partial \psi}{\partial y} = u \qquad \frac{\partial \psi}{\partial x} = -v \tag{5.8}$$

gives the Poisson's equation;

$$\nabla^2 \psi = -\omega \tag{5.9}$$

5.2 Splitting the Equations

The method proposed by Chorin (1973) in connection with his work on "Slightly Viscous Flow Over a Circular Cylinder" is known as the "Operator Splitting", "Time Splitting" or "Viscous Splitting" algorithm. In this method, at each time step one may solve the convection and diffusion of vorticity sequentially, rather than simultaneously. For 2-D, the Vorticity Transport equation in the non-dimensionalized form, is

$$\frac{D\omega}{Dt} = \frac{1}{Re} \nabla^2 \omega \tag{5.10}$$

where the ***Re*** is based on the cylinder diameter. But the method suggests to separate this equation into two parts as viscous diffusion

$$\frac{\partial \omega}{\partial t} = \frac{1}{Re} \nabla^2 \omega \tag{5.11}$$

and convection

$$\frac{\partial \omega}{\partial t} = -(\vec{U}\ \nabla)\ \omega \tag{5.12}$$

Denoting the solution operations of equation (5.10) and (5.11) as ***D(t)*** and ***C(t)*** respectively, one can mathematically write the description of viscous splitting algorithm which is applied at each of ***m*** time steps of duration ***Δt*** as

$$\omega(m\Delta t) = D(\Delta t)\ C(\Delta t)^m\ \omega(0) \tag{5.13}$$

Here, ***ω(m Δt)*** is the vorticity distribution after "***m***" time step and ***ω(0)*** is the initial distribution (Benson et al., 1989). The accuracy of the method is proved as converging to the Navier-Stokes solutions, under some restrictions by Beale and Majda (As referred to Benson et.al., 1989). Convergence of solution depends on the accuracies of convection and diffusion individually (Benson et al., 1989).

5.3 Diffusion of Vorticity and Boundary Conditions on Circulation

In this study, he diffusion part of vorticity transport equation is solved on the mesh. In two dimensions, non-dimensionalized form of the diffusion equation is;

$$\frac{\partial \omega}{\partial t} = \frac{1}{Re}\left[\frac{\partial^2 \omega}{\partial x^2} + \frac{\partial^2 \omega}{\partial y^2}\right] \tag{5.14}$$

where the Reynolds number is based on the cylinder diameter ***D*** and the free-stream velocity U_∞ i.e. $Re = U_\infty D/v$ Under transformation, this equation takes the form that includes the transformation modulus (Jacobian) between computation and physical planes. Thus, using the mesh circulation values instead of vorticity which assumed to spread uniformly in A, the diffusion equation can be written as follows;

$$\frac{\partial(\Gamma/A)}{\partial t} = \frac{1}{Re}\left[\frac{\partial^2(\Gamma/A)}{\partial x^2} + \frac{\partial^2(\Gamma/A)}{\partial y^2}\right]\left|\frac{d\zeta}{dz}\right|^2 \tag{5.15}$$

The finite difference technique is applied to this equation with proper discretization allowing explicitly calculations in -x direction and implicit in -y direction. The finite difference forms of this equation was given in Appendix A.

The diffusion equation is solved subject to the no-slip boundary condition at the surface. The first order approximation for the surface vorticity, in its circulation form

(Roache, 1972) is employed.

$$\Gamma_w = -\frac{2\,(\psi_{w+1}-\psi_w)}{h}\,\Delta x \tag{5.16}$$

where subscript "ω" stands for the value at the wall, "$w+1$", for the neighbouring grid to the wall "h" is the distance neighbouring grid to the wall and Δx is the constant mesh spacing in $-x$ direction. Since the flow is impulsively started, the wall circulation values at the start of the motion are determined by the stream function values of the basic flow. As indicated by Roache higher degree of circulation boundary condition requires more computational time and for some cases improper results.

For the solution of the Poisson's Equation for the stream function periodicity is imposed at the right and left boundaries of the computation plane, and at the upper boundary the stream function values induced by the discrete vortices and their images in the body are taken as the boundary condition. At the lower boundary describing the wall, the stream function value is taken as zero. After calculating the diffused vorticity across the mesh and therefore determining the new vorticity field, the Poisson's Equation is solved again and the stream function values at grid points are used to calculate the convection velocities of vortices. Consequently, the vortices are convected to their new positions at the end of each time step.

5.4 Convection of Vorticity

The method described above produces high number of discrete vortices in the flow field. The Vortex-in-Cell method employed in this study provides an effective way to calculate the convection velocities for these vortices.

In its simplest form, VIC technique requires allotments of circulation of each vortex occupying a cell to the four surrounding mesh points according to the bilinear area weighting scheme; in another words, the total circulation of a mesh point is defined by summing the contribution from all of the vortices resident in the four surrounding cells. If the circulation of a vortex is Γ then the contribution this vortex assigned to the four surrounding points on a cartesian mesh (Fig.[5.1.(a)]) is calculated by;

$$\Gamma(i) = \frac{\Gamma A_i}{\sum_{k=1}^{4} A_k} \tag{5.17}$$

This assignment gives the mesh circulations (i.e. the right hand side) used in the

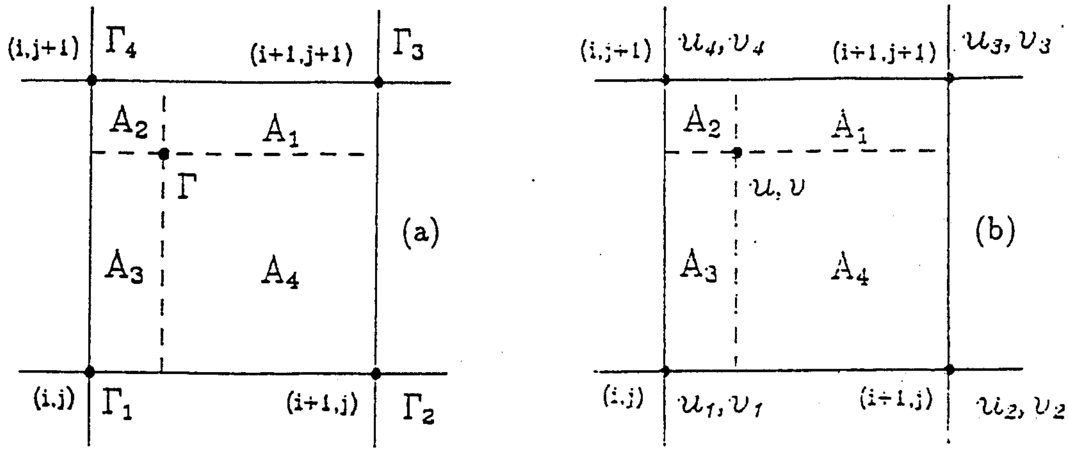

$$\Gamma_i = \Gamma . A_i / \sum_{k=1}^{4} A_k \qquad (u,v) = (u,v)_i . A_i / \sum_{k=1}^{4} A_k$$

Figure 5.1 Interpolation procedures for circulation and velocity.

solution of Poisson's equation. With the stream function values determined from the solution of Poisson's equation (see section 5.5) the mesh velocities are calculated also taking into consideration the transformation moduli.

$$\begin{aligned} u &= \frac{\partial \psi}{\partial y} \left| \frac{d\xi}{dz} \right|^2 \\ v &= -\frac{\partial \psi}{\partial x} \left| \frac{d\xi}{dz} \right|^2 \end{aligned} \tag{5.18}$$

Known the mesh velocities, an area weighting scheme, in reversed direction (Fig.[5.1.(b)]) then gives the convection velocities of the discrete vortices as follows;

$$\begin{aligned} u_p &= \sum_{k=1}^{4} \frac{u(k)\, A_k}{A} \\ v_p &= \sum_{k=1}^{4} \frac{v(k)\, A_k}{A} \end{aligned} \tag{5.19}$$

where A is the total cell area. Consequently the vortices are advanced to their new locations, by a first order approximation:

$$x_p(t+\Delta t) = x_p(t) + u_p(t)\Delta t$$
$$y_p(t+\Delta t) = y_p(t) + v_p(t)\Delta t \tag{5.20}$$

where x_p and y_p are the orthogonal coordinates of vortex P, u_p and v_p are the velocities in -x and -y directions obtained at the previous calculation step.

5.5 Solution of Poisson's Equation

The stream function values required to be determine the convection velocities of the discrete vortices are obtained using Poisson's equation in its circulation form:

$$\nabla^2 \psi = -\frac{\Gamma}{A} \tag{5.21}$$

Many of the algorithms developed for the simple Poisson's equation fall into two apparently distinct categories: those based on Fourier decomposition in one dimension, using Fast Fourier Transform (FFT) techniques, and those based on block cyclic reduction. In present study, the former is used. This brings a restriction on the type of solution domain, although some other direct methods do not: If the solution domain is a rectangular ***NxM*** grid, ***N,*** being the number of mesh points in x direction in which the Fourier transformation is taken, is restricted to be power of 2,i,e. $N = 2^k$ $(k = 1, 2, \ldots)$.

Taking the fourier transform along x direction reduces Poisson's equation into a tridiagonal system of equations. As described before, the boundary conditions at top and bottom in transformation plane are given as Dirchlet type. For surface, the stream function value is zero. On the other hand, the FFT technique is used in this study assumes periodicity of stream function at the left and right boundaries. Since the Poisson's equations is a linear equation the super position principle is applied and the stream function corresponding to a non-zero circulations distribution is added onto the stream function of the basic flow. (see section 5.7)

A detailed comparative study can be found in the review article of Temperton (1979). The discretized form of Poisson's equation is given in Appendix B.

5.6 Amalgamation of Vortices

For a number of reasons, in numerical studies with the discrete vortices, amalgamation or merging of two or more vortices into a single one is generally resorted technique: Amalgamation

- can eliminate the unrealistically large velocities induced by the point vortices
- Shorten the computing time by reducing the number of vortices, and
- can simulate some naturally occurring merging

By smearing the vortex onto a mesh it occupies, the VIC technique automatically eliminates the large velocities induced by the discrete vortices. However, due to production of large number vortices, the VIC technique without an amalgamation procedure becomes computational impractical.

Since the amalgamation is an approximation, there is no correct or guaranteed way to perform it. It should be used with care and, if possible, verified that it does not introduce unacceptably large errors. But unfortunately, it is difficult to assess the more elusive effects of merging on the numerical predictions since the problem is highly non-linear and its results depend on many different parameters which can easily be intermingled.

There are two merging schemes examined in this study. One of them is to associate the point vortex existing in a cell with the diffused vorticity at the four surrounding mesh points diffused vorticity without taking account their being like or unlike signed. Other one goes to a discrimination between like and unlike signed vortices. The oppositely signed vortices are combined when the distance between them is less than prescribed value to mimic the cancellation of oppositely signed vorticity which is the major mechanism of enhanced energy dissipation in turbulent flow. This length is defined to be shorter than the one for amalgamation of like signed vortices. When merging the like signed vortices the total circulation and linear momentum are conserved. But the second moment of vorticity distribution decreases and velocity fields before and after merging are not identical. This generally causes the discontinuities in the calculated force if either the generalized Blausius theorem or the time rate of change of first moment of circulation is used. Discrimination between like and unlike signed vortices gives large number of vortices thus increases the computing time although it is more accurate to simulate the viscous effects.

5.7 Solution Domain and Conformal Transformation

As a necessity of using hybrid scheme for flow computations, a proper grid should be produced around the body in order to simulate accurately the diffusion and convection processes. For a successful simulation the grid should be fine enough to cover at least three or more mesh in the boundary layer (Roache, 1972). To extend this fine grid structure into a region far from the body an impractically large number of grid points are required. However since the large scale structures are the dominant feature of the flow far downstream a coarser mesh is sufficient there. For the y locations of grid points the following expression is used:

$$y = A + \frac{\sqrt{A^2 + 4\ BC(J-1)}}{2B} \tag{5.22}$$

where ***A=J-1-D.*** By assigning different values to the parameters ***B,C,D,*** various grid structures can be produced in transformation plane which provides different definitions in the boundary layer and different locations for the outer boundary of the computational domain.

The transformation between the computation (rectangular) and the physical domains is achieved in two stages:

- transformation from semi-infinite plane to plain cylinder,
- transformation from plain cylinder to the airfoil (NACA 0012).

<u>Stage 1- Transformation from semi-infinite plane to plain cylinder</u>

Calling semi-infinite plane as ξ plane, plain cylinder plane as ζ plane, the expression for this transformation is;

$$\zeta = R \exp(-i\alpha\xi) \tag{5.23}$$

where ζ and ξ represent complex coordinates

$$\zeta = \zeta_R + i\ \zeta_I \qquad\qquad \xi = \xi_R + i\ \xi_I$$

in semi infinite plane and the plain cylinder plane respectively and R is the radius of cylinder and α is step size in angular direction. For this stage the differential quotient of the mapping function is;

$$\frac{d\zeta}{d\xi} = -i\ \alpha\ R \exp(-i\alpha\xi) \tag{5.25}$$

Stage 2- Transformation from plain cylinder to airfoil (NACA 0012)

Using Jukowski transformation formulae, transformation between these two plane was proved as follows:

$$z = A\left(\zeta + \delta + \frac{c^2}{\zeta + \delta} \right) \tag{5.26}$$

where ***c***, ***δ*** and ***A*** are constant related to the thickness, camber specifications and scale factor of the airfoil. Eq.(5.26) with $c^2 = 0.8061$ and $\delta = -0.06474$ closely defines NACA 0012 airfoil profile and A is selected 1/1.8 so, the airfoil chord (*c*) is equal 2. *z* represents the complex coordinate in the physical plane (i.e. NACA 0012 profile), and the corresponding differential quotient of the mapping function is

$$\frac{dz}{d\zeta} = A\left(1 - \frac{c^2}{(\zeta + \delta)} \right) \tag{5.27}$$

From foregoing expressions, the global differential quotients of the composite mapping is product of these two quotients. That is;

$$\frac{dz}{d\xi} = \frac{dz}{d\zeta}\frac{d\zeta}{d\xi} \tag{5.28}$$

The stream function of the basic flow around a circular cylinder placed in a uniform flow can be easily expressed in the intermediate plane of circular cylinder. However, in order to determine the corresponding basic flow in the physical plane this stream function expression should be multiplied by the limit value of the differential quotient of the transformation passing from physical plane to the intermediate one (i.e. plain cylinder plane). The limit, as ζ goes to infinity, is;

$$\lim_{\zeta \to \infty} \frac{dz}{d\zeta} = A \tag{5.29}$$

5.8 The Calculation of Force and Pressure Coefficient Distribution

Force due to vortex shedding is determined by the total rate of change of first moment of circulation. Approach is applicable to viscous flows as well as inviscid flows (Wu, 1981). Therefore the expression for the vortex force is

$$F_v = -i\rho\frac{d\beta}{dt} \tag{5.30}$$

where ß is the first moment of vorticity field:

$$\alpha = \int_{R_L} \vec{r} \times \vec{\Omega} \; dR \tag{5.31}$$

where $\vec{r}$ is the position of the vortex; R_L includes all the region outside of the body. Consequently the discrete version of the force expression in terms of mesh circulation Γ_k can be written as follows;

$$F_v = - i \rho \frac{\partial}{\partial t} \sum_{k=1}^{N} \Gamma_k z_k \tag{5.32}$$

where z_k is the physical plane complex coordinates. Actually, the mesh points do not change with time but circulations do. Thus the equation takes the following form;

$$F_v = - i \rho \sum_{k=1}^{N} z_k \frac{\partial}{\partial t} \Gamma_k \tag{5.33}$$

Dimensionless force coefficient follows as;

$$C_{fv} = \frac{F_v}{\frac{1}{2} \rho U^2 d} \tag{5.34}$$

where U is the free stream velocity and d is the cylinder diameter. The real and imaginary parts of this expression are dimensionless drag (C_D) and lift (CL) coefficients respectively.

If the Navier-Stokes equation in primitive variables are considered at the wall together with the definition of vorticity and the no-slip boundary condition, it is possible to derive the following expression.

$$\left. \frac{\partial p}{\partial s} \right|_{wall} = - \nu \left. \frac{\partial \omega}{\partial n} \right|_{wall} \tag{5.35}$$

where p is the pressure, n and s are coordinates in the normal and tangential directions. The vorticity of the surface and its neighbouring using the first order approximation can be written as follows;

$$\omega_{i,wall+1} = \frac{\Gamma_{i,wall+1}}{\Delta n\ \Delta s}$$
$$\omega_{i,wall} = -\frac{3}{\Delta n^2}\left(\psi_{i,wall+1} - \psi_{i,wall}\right) - 0.5\,\omega_{i,wall+1} \quad (5.36)$$

The pressure distribution around the surface of the profile is obtained by integrating as follows;

$$\Delta p_{i,wall} = -\nu\left(\omega_{i,wall+1} - \omega_{i,wall}\right)\frac{\Delta s}{\Delta n} \quad (5.37)$$

where Δn and Δs are the increments the normal and tangential directions.

The calculation procedure of the time-splitting solution of the Navier-Stokes equations is given as follows;

- Interpolate circulation onto mesh
- Solve Poisson's equations for ψ Adjacent to solid boundaries
- Create circulation at solid boundary and diffuse circulation for entire mesh
- Solve Poisson's equation for entire mesh
- Create modified circulation at solid boundary
- Diffuse circulation adjacent to solid boundary
- Amalgamate or release diffused circulation
- Evaluate force and pressure distributions
- Difference stream function to obtain velocity field
- Interpolate velocity onto point vortices and convect them

CHAPTER 6

RESULTS AND DISCUSSIONS

6.1 Results and Discussion of Stationary Circular Cylinder

In this study, the main concern has been to clearly demonstrate the effects of employing a circulating-reduction scheme and assuming fixed and variable separation point to the fluctuating quantities as well as to the wake structure, and the discrete vortex method has been shown to predict the mean and fluctuations velocity fields behind a cylinder in agreement with experimental findings.

Similar to the previous studies Sarpkaya & Schoaff (1979) making use of the inviscid DVM, the global structure of the circular cylinder wake is successfully simulated (Fig.[6.1]). Of course, with this method there is no intention of predicting the fine scale structure of vortices. The predicted wakes should be observed only globally: The discrete vortices originally released from introduction points form clouds of vortices global structure of whose resembles the actual vortex street wake.

The effect of circulation reduction to the wake structure is demonstrated in (Fig.[6.1]). For comparison, the structures are sampled at the same phase of the wake oscillation: For each case the fluctuating lift passes through minimum. Obviously, narrower wakes are associated with vortices of lower strength, and thus the reduction causes the wake-width to decrease with respect to the case in which no reduction is applied. Also evident in Fig.[6.1] is that when the reduction is applied, irregularity of the far wake due to high induced velocities are eliminated and thus the vortex street wakes become more organized for longer downstream distances.

As regard with corresponding variations in related quantities: In the case of fixed separation points, the rates of circulation fed into the flow from the upper and the lower introduction points have almost the same time-mean value regardless of whether the reduction is applied or not (Fig.[6.2.(b)] and Fig.[6.3.(b)]). Also, a low frequency variation in the mean value of the rate of circulation is evident for the case of no-reduction. However, when the reduction is applied, the variation (Fig.[6.3.(b)]) has almost a steady mean value. Additionally, the fluctuating part of rate of circulation exhibits a more organized variation in the case of reduction. In fact, these characteristic of variation with respect to are also evident in the mean and fluctuating parts of the other fluctuating quantities such as the radial distances of introduction from the separation points r_s (Fig.[6.2.(d)] and [6.3.(d)]). In accord with the feed back of the downstream unsteadiness, the radial distances show nearly sinusoidal small variations. Similar to the variations with respect to time of the rates of circulation fed into the flow from the upper and the lower separation points, the radial distances of the introduction points at the upper and the lower surfaces of the cylinders are almost π out of phase with each other. Additionally, variations of r_s and $D\Gamma/DT$ on the same side of the cylinder are in phase.With the circulations-reduction in progress, the fluctuating drag and lift forces are taken down to values which are in agreement with those found experimentally (Dwyer & McCroskey, 1973) (Fig.[6.2.(a)] and [6.3.(a)]). The time value of the drag coefficient is about ***1.28*** and the lift coefficient fluctuates $\pm$***0.8,*** whereas when there is no reduction the corresponding values for the drag and the lift coefficient are ***1.85*** and $\pm$ ***1.85*** respectively. Similarly, the reduction leads to a more realistic value ***(-1.45)*** for the time-value of the base pressure coefficient (Fig.[6.3.(c)]).

When the separation points as well as stagnation point are allowed to move in harmony with the periodic vortex wake, variations of the fluctuating quantities become more organized with respect to the case of fixed separation points: The low frequency variations of the mean value of r_s and $D\Gamma/DT$ with respect to time are absent in the case of variable separations points (Fig.[6.2.(b)], [6.4.(d)], [6.2.(d)], [6.5.(f)]. Due to an increase, in comparison with the case of fixed separation points,of effectiveness of the feedback of downstream unsteadiness, the variable separations points leads to somewhat larger values of the time mean value of the drag coefficient and the lift coefficient fluctuations (Fig.[6.2.(a), [6.5.(c)].

Despite the fact that prediction of the separation -and the stagnation point- angles are based on a very simple approach, the variations of these angles are, relative to those achieved by the quasi-steady Polhlhausen's Approach Sarpkaya & Schoaff (1979), in better agreement with those found experimentally. The separation angles exhibit $\pm$***2.75*** fluctuations around the mean value of ***80°,*** whereas the amplitude of fluctuation of the stagnation point angles is nearly ***2°*** (Fig.[6.6.(a)], [6.6.(b)]). For the case in which the reduction is applied and the separation points are allowed to move, the Strouhal number based on the diameter of the cylinder ***(f2a\\U_0)*** is ***0.22.***

The variations within a period of wake fluctuations of the pressure coefficient distributions around the cylinder are demonstrated in Fig.[6.6] and this figure insensible (see Fig.[1.5] and Blevins, 1974). The time difference between the distributions at successive non dimensional times are equal *($\Delta T=2$)*, and the arrows at the centre of the cylinder indicate the instantaneous lift and drag coefficients. Except a very small region in front of the cylinder, all the pressure values indicate suction. Naturally, the variation of the pressure distribution is accord with that of the wake structure. Fig.[6.4] is produced using DVM with the variable separation points and reduction, the variation within a period of wake fluctuations of the pressure coefficient distributions around the cylinder produced in this study is in a good agreement with experimental result (see section 1.2, Fig.[1.5]).

Using this case giving a better agreement with experiments, the velocities in the free stream (x) and the vertical (y) directions at 240 selected points are calculated. These 240 measurement station are shown in Fig.[6.8]. The variations of the velocity components with respect to time is obtained at these measurement stations (Figs. 6.10, 11, 12, 13). The average velocity profiles at various x/a location are given Fig.[6.9], where a is the radius of the cylinder and U_o is free stream velocity. In addition, the contours of the average and rms value of the x and y components of the velocity fluctuations are plotted in Figs.[6.14,15,16,17]. The measurement plne is between $y/a = 2.$ and $.0$ but because body geometry is symmetric, the contours are symmetric with respect to the centerline of the wake. Similar to the experimental studies (e.g. Durgin & Karlsson, 1971), a velocity profile with high shear in the near wake change into a typical far wake profile. That is the rate of shear reduces with increasing x/a . Additionally, the acceleration at the shoulder of the cylinder is evident. The contours of velociyt fluctuations in x and y directions are also similar to those obtained experimentally: At the centerline of the wake, $y/a=0$, the frequency of U velocity fluctuation is twice that of vortex shedding. However at the location where y/a is not equal zero, it seen that the frequency of u and v velocity fluctuations is the same. The magnitude of V velocity fluctuations decrease while y/a is increasing, whereas the magnitude of u velocity fluctuations first increases and then decreases. The y/a location where the magnitude of u velocity fluctuations is maximum correspond to the y/a location where the average velocity is equal to half of the free stream velocity like expected. These properties are clearly seen in Fig.[6.14,15,16,17].

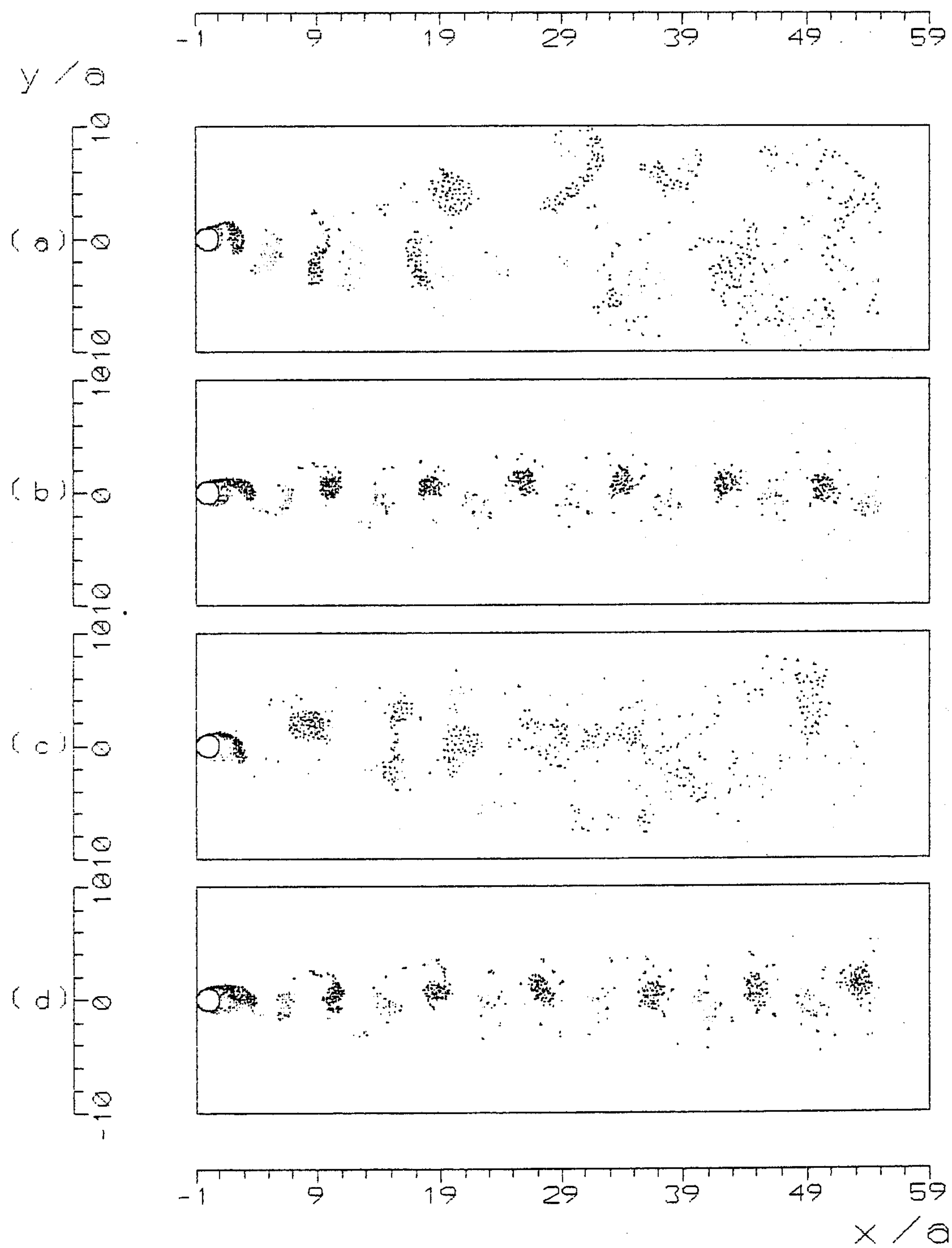

Fig.6.1. Discrete vortex distributions corresponding to the cases of fixed separation points, without reduction (a); with reduction (b), and variable separation points, without reduction (c); with reduction.

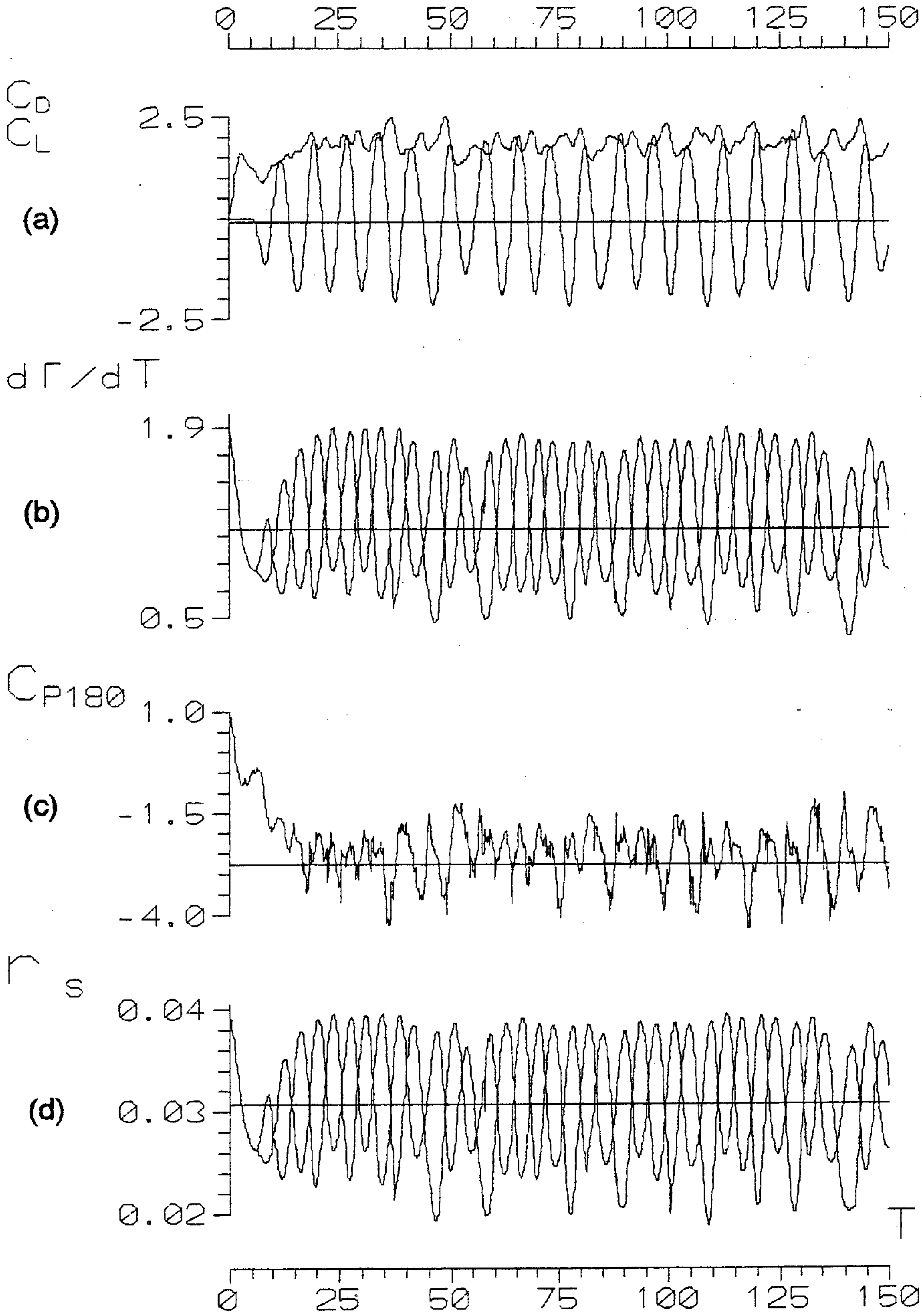

Fig.6.2. Variation with respect to nondimensional time T of, Drag and lift coefficient (a); Rate of creation of circulation (b); Base pressure coefficient (c); and radial distance of introduction points at both sides of cylinder (d) for the case of No-reduction/Fixed separation points.

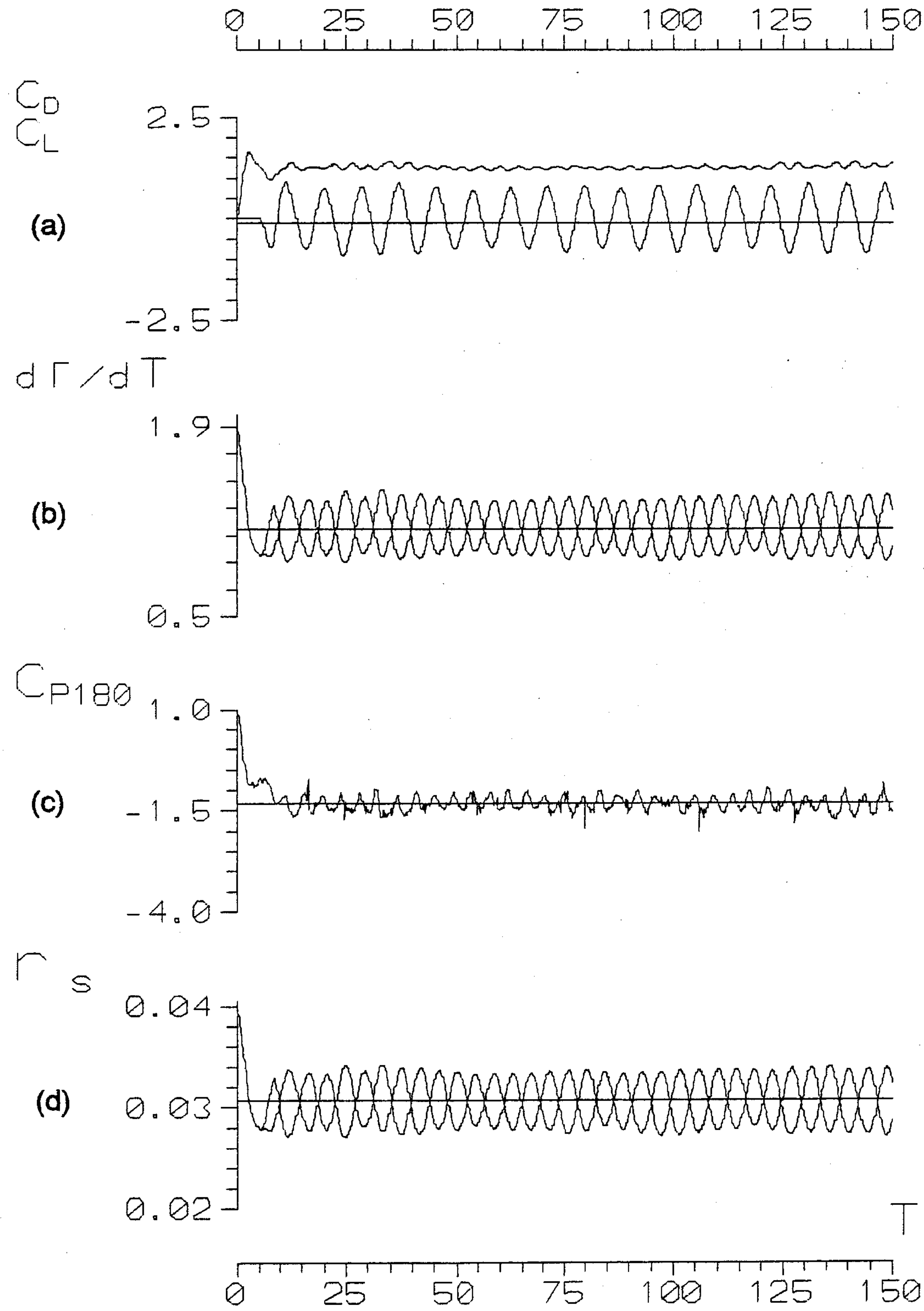

Fig.6.3. Variation with respect to nondimensional time *T* of, Drag and lift coefficient (a); Rate of creation of circulation (b); Base pressure coefficient (c); and radial distance of introduction points at both sides of cylinder (d) for the case of Reduction/Fixed separation points.

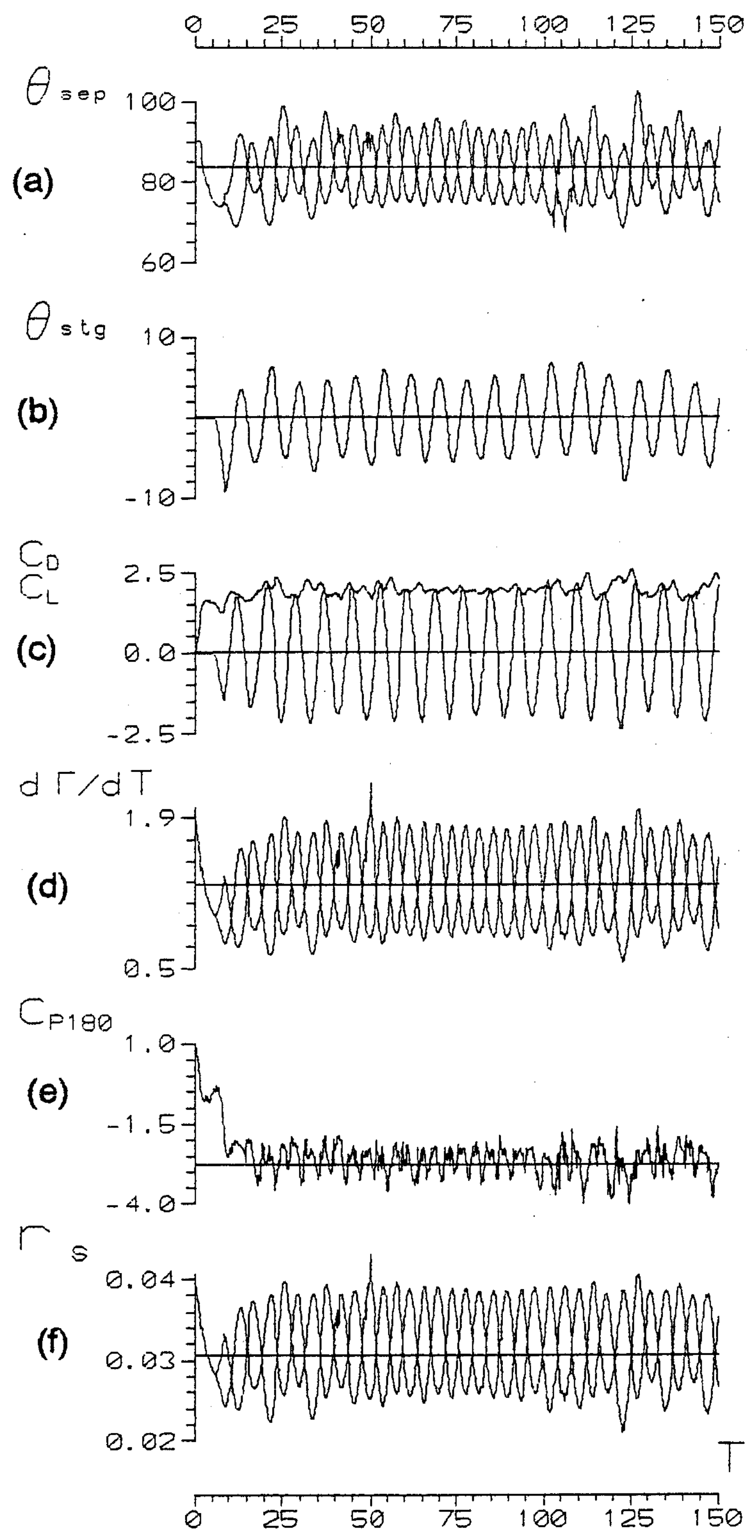

Fig.6.4. Variation with respect to nondimensional time T of, separation angles at upper and lower surfaces of cylinder (a); Stagnation angle (b); Drag and lift coefficient (c); Rate of creation of circulation (d); Base pressure coefficient (e); and radial distance of introduction points at both sides of cylinder (f) for the case of No-reduction / Variable separation points.

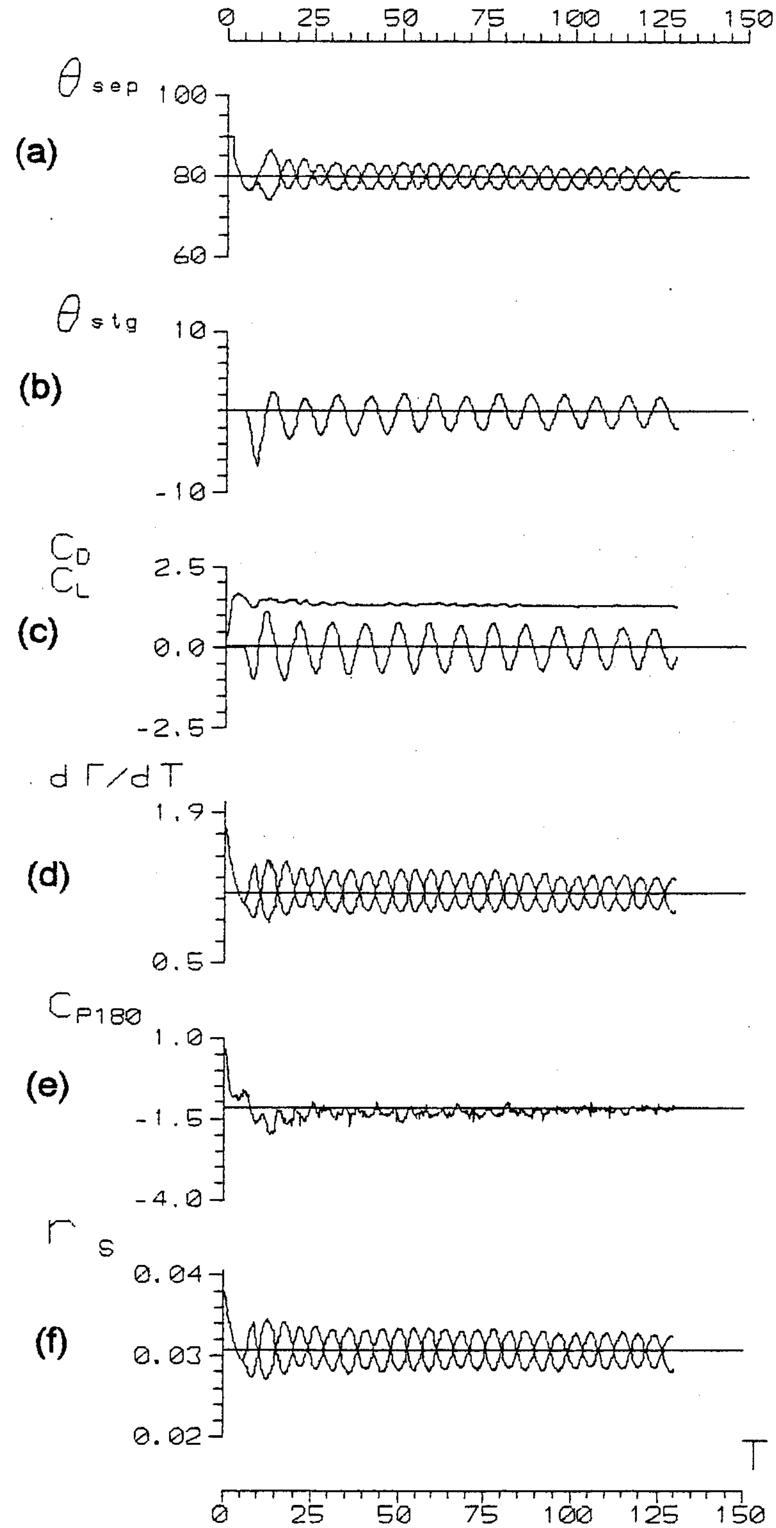

Fig.6.5. Variation with respect to nondimensional time *T* of, separation angles at upper and lower surfaces of cylinder (a); Stagnation angle (b); Drag and lift coefficient (c); Rate of creation of circulation (d); Base pressure coefficient (e); and radial distance of introduction points at both sides of cylinder (f) for the case of Reduction / Variable separation points.

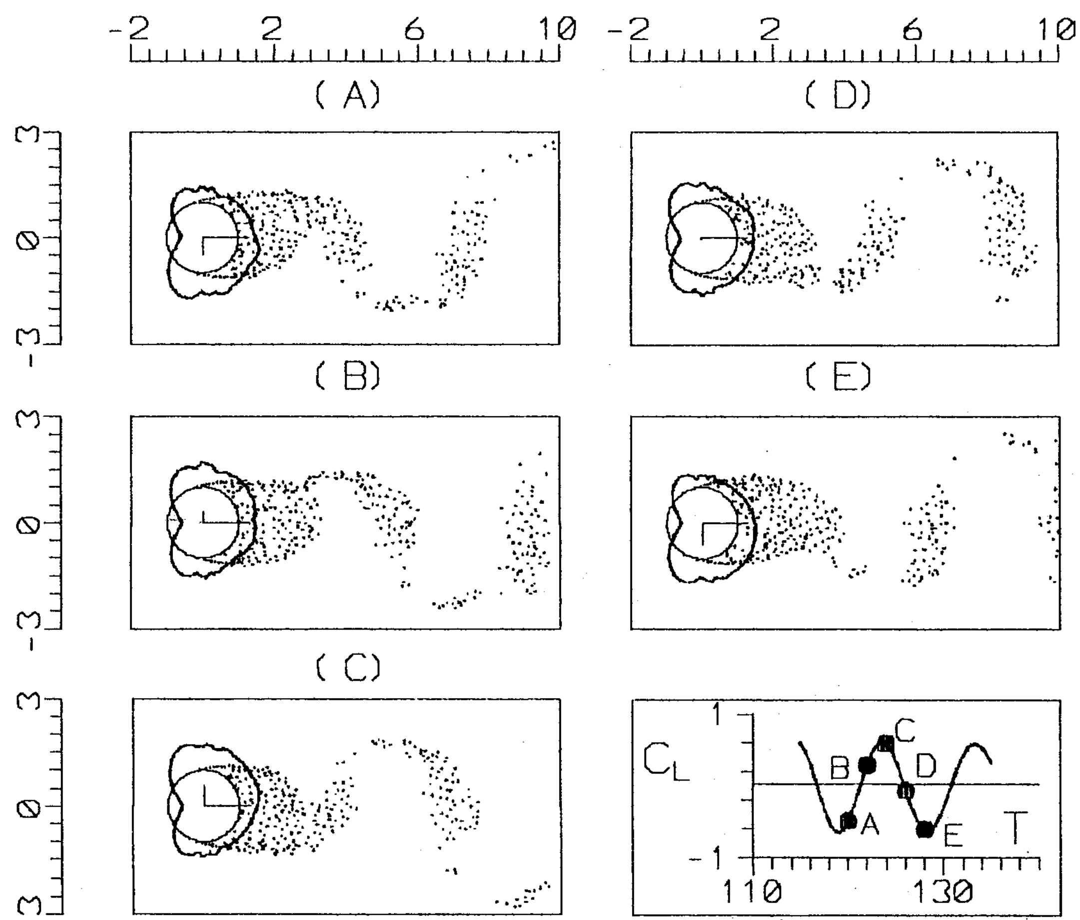

Fig.6.6. Pressure coefficient distributions in relation with the wake structure. Nondimensional time corresponding to each case is indicated on the C_L vs T variation.

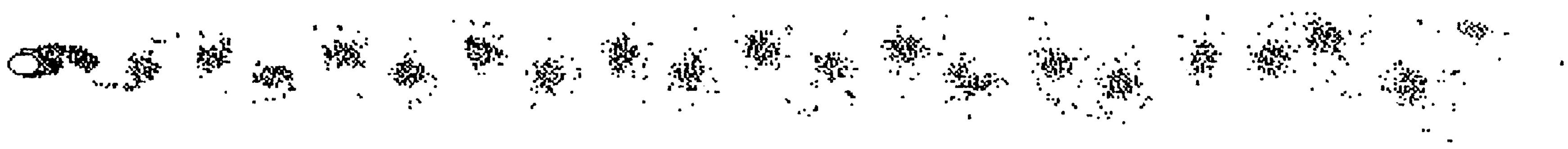

Fig.6.7. The wake structure of circular cylinder (Karman vortex street).

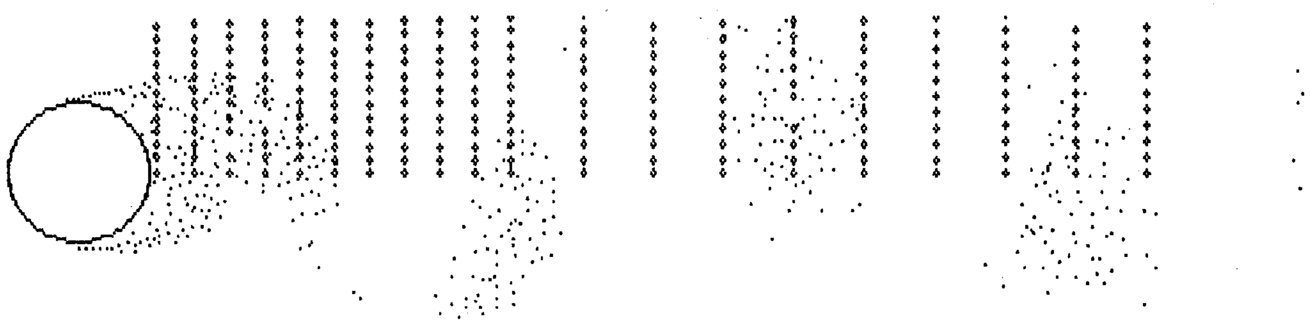

Fig.6.8. The velocity measurement stations.

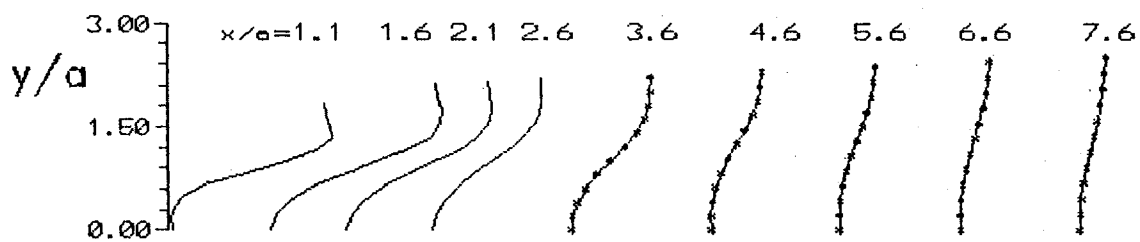

Fig.6.9. The average velocity profiles for various x/a locations.

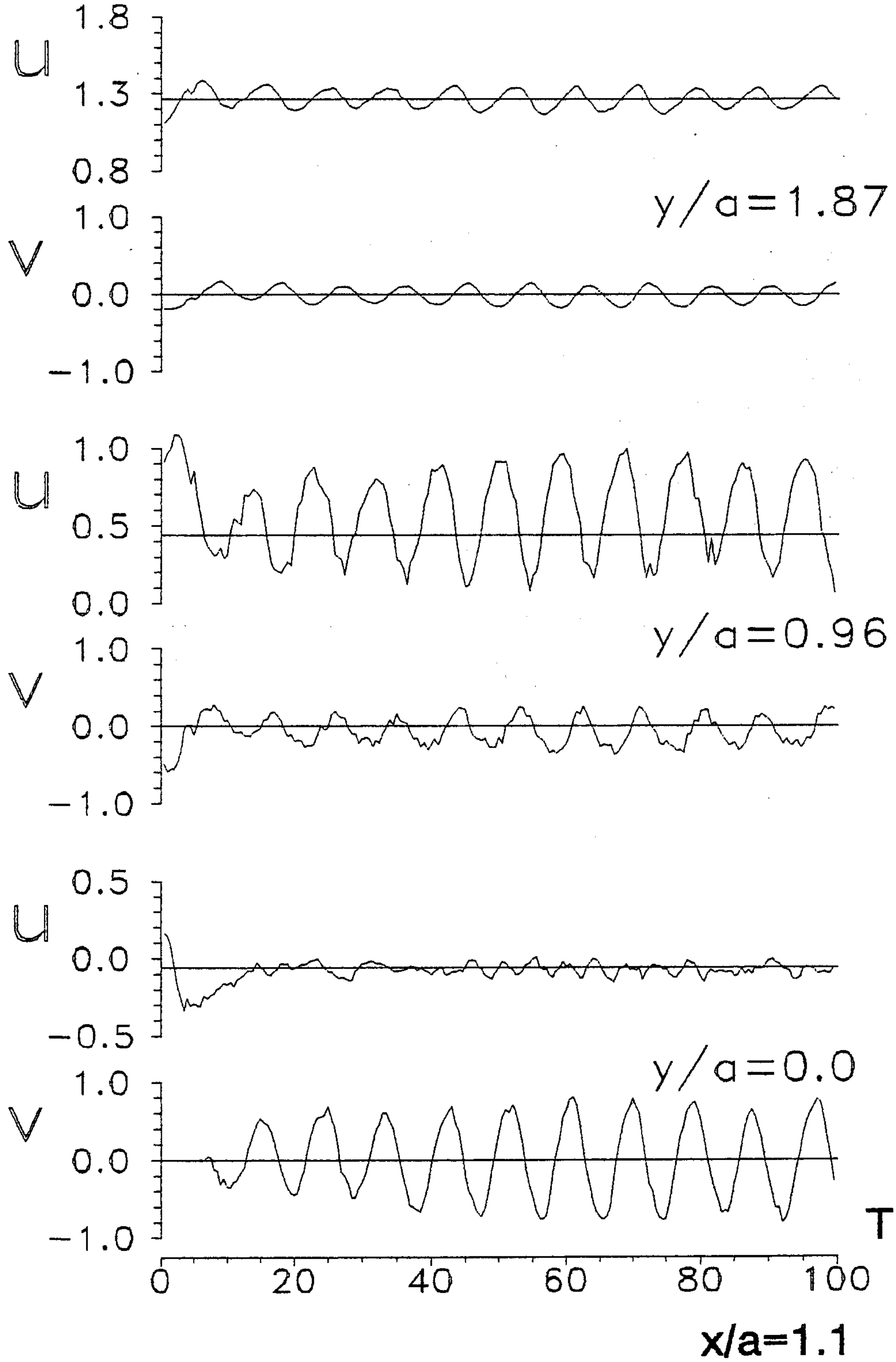

Fig.6.10. The velocity fluctuations with respect to time at ***x/a=1.1***, for various ***y/a*** locations.

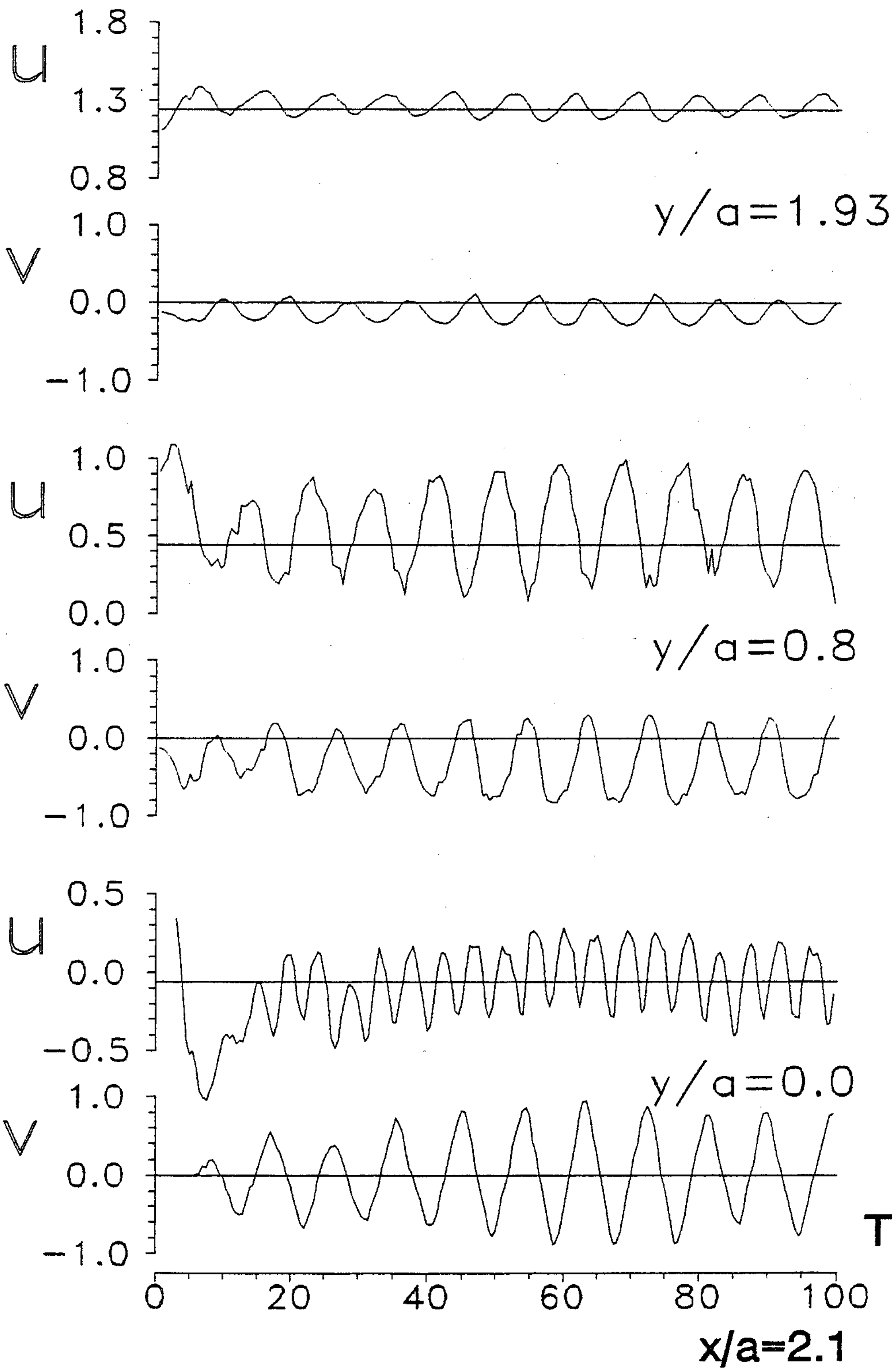

Fig.6.11. The velocity fluctuations with respect to time at $x/a=2.1$, for various y/a locations.

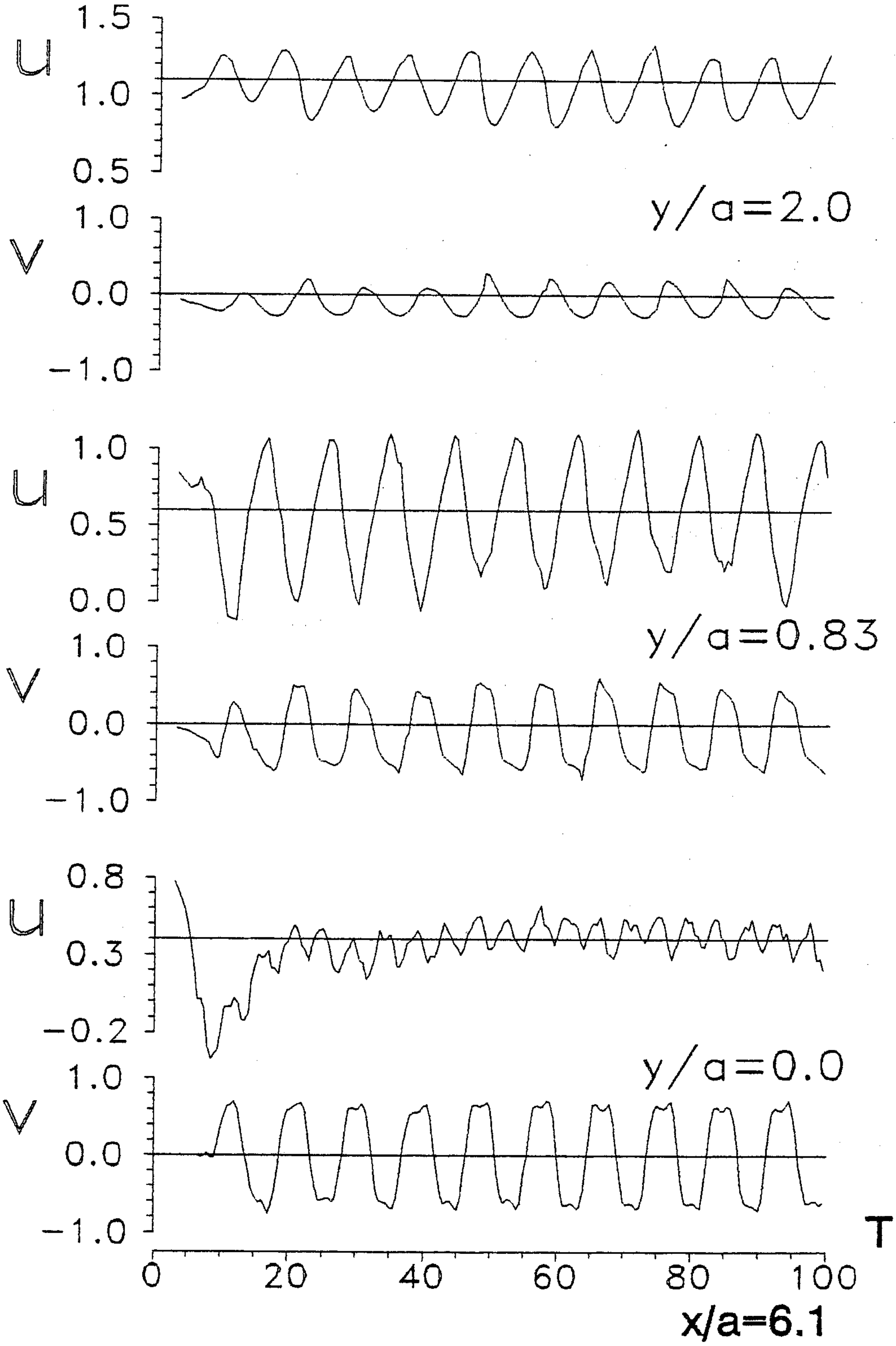

Fig.6.12. The velocity fluctuations with respect to time at ***x/a=6.1***, for various ***y/a*** locations.

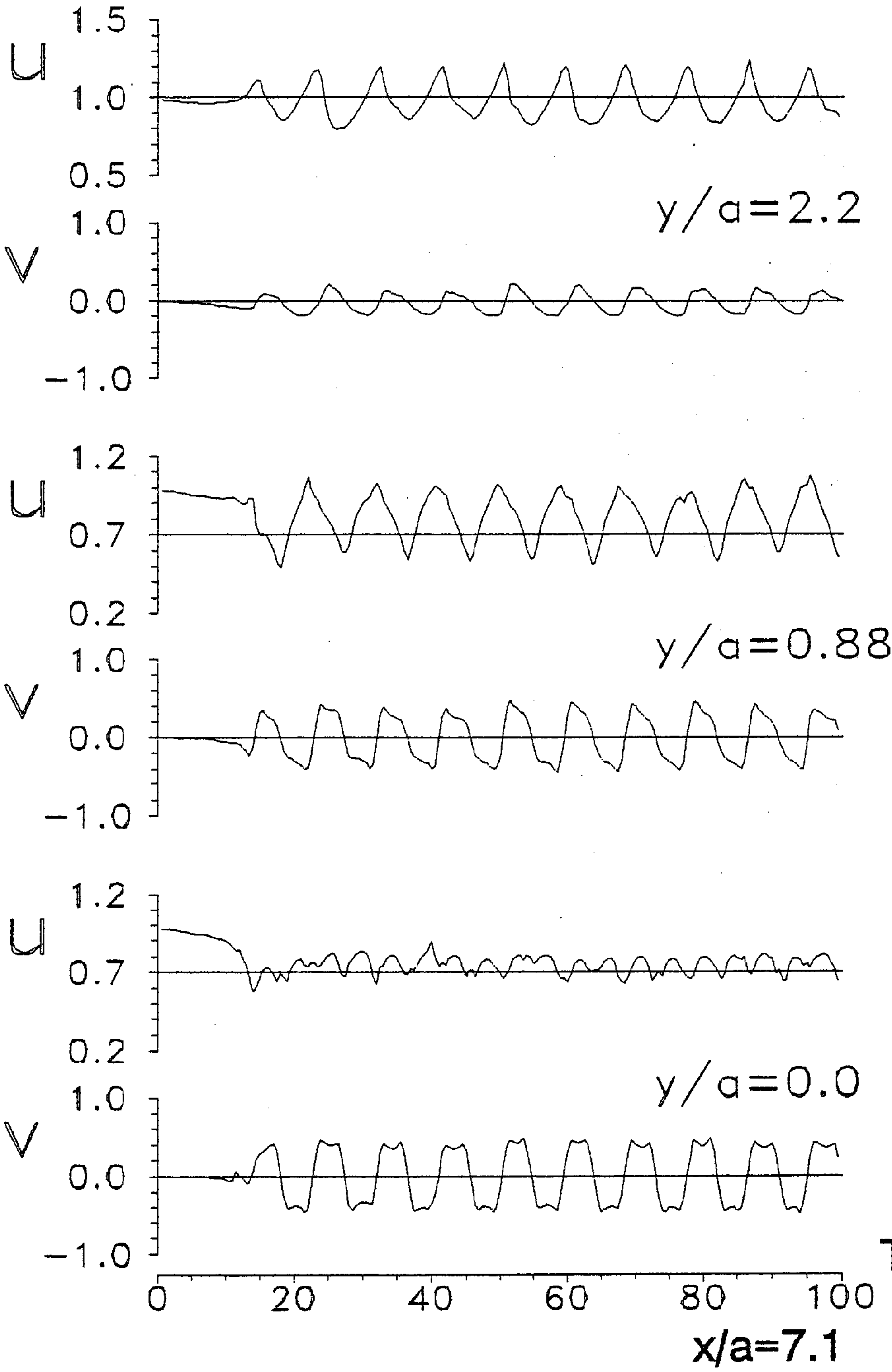

Fig.6.13. The velocity fluctuations with respect to time at $x/a=7.1$, for various y/a locations.

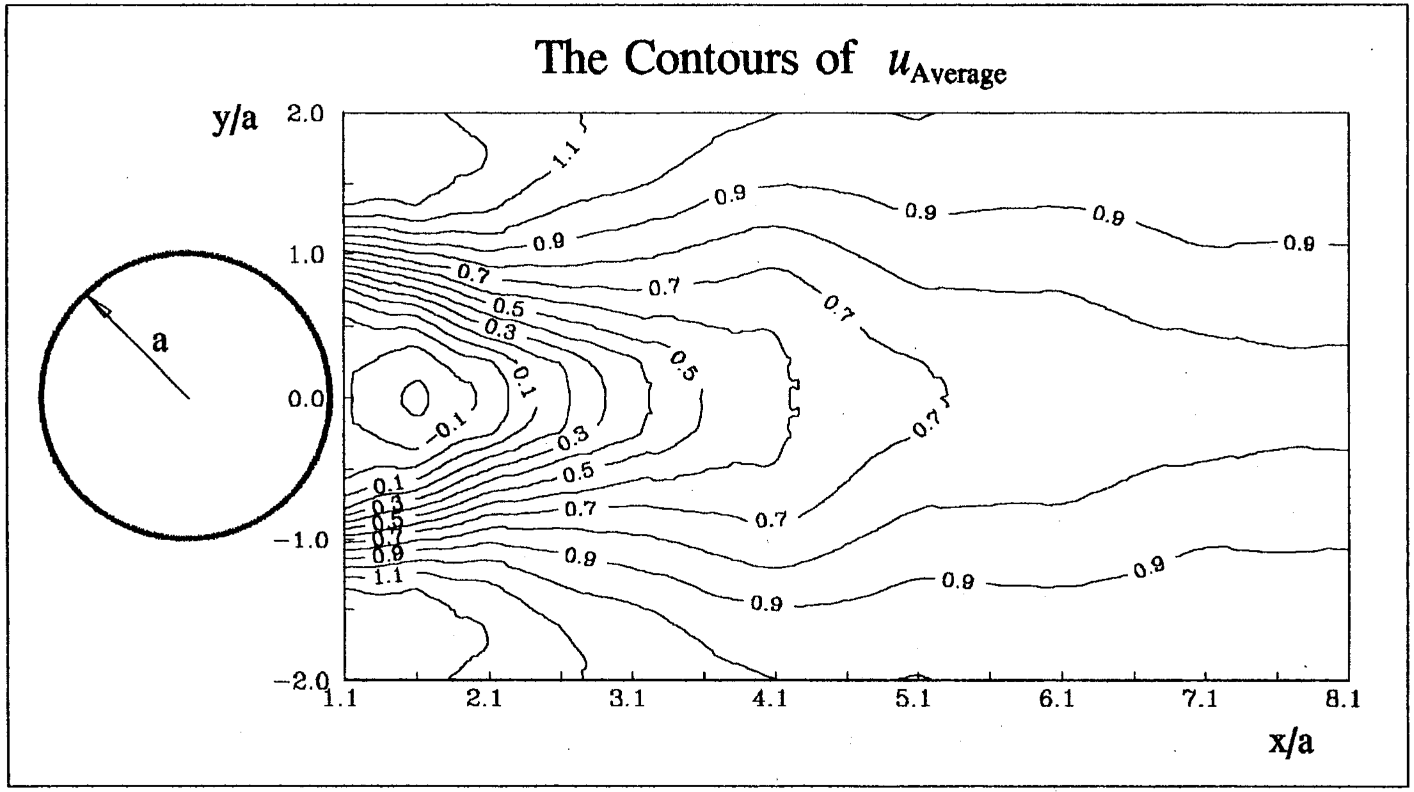

*Fig.*6.14. The average *U* velocity contours behind the circular cylinder.

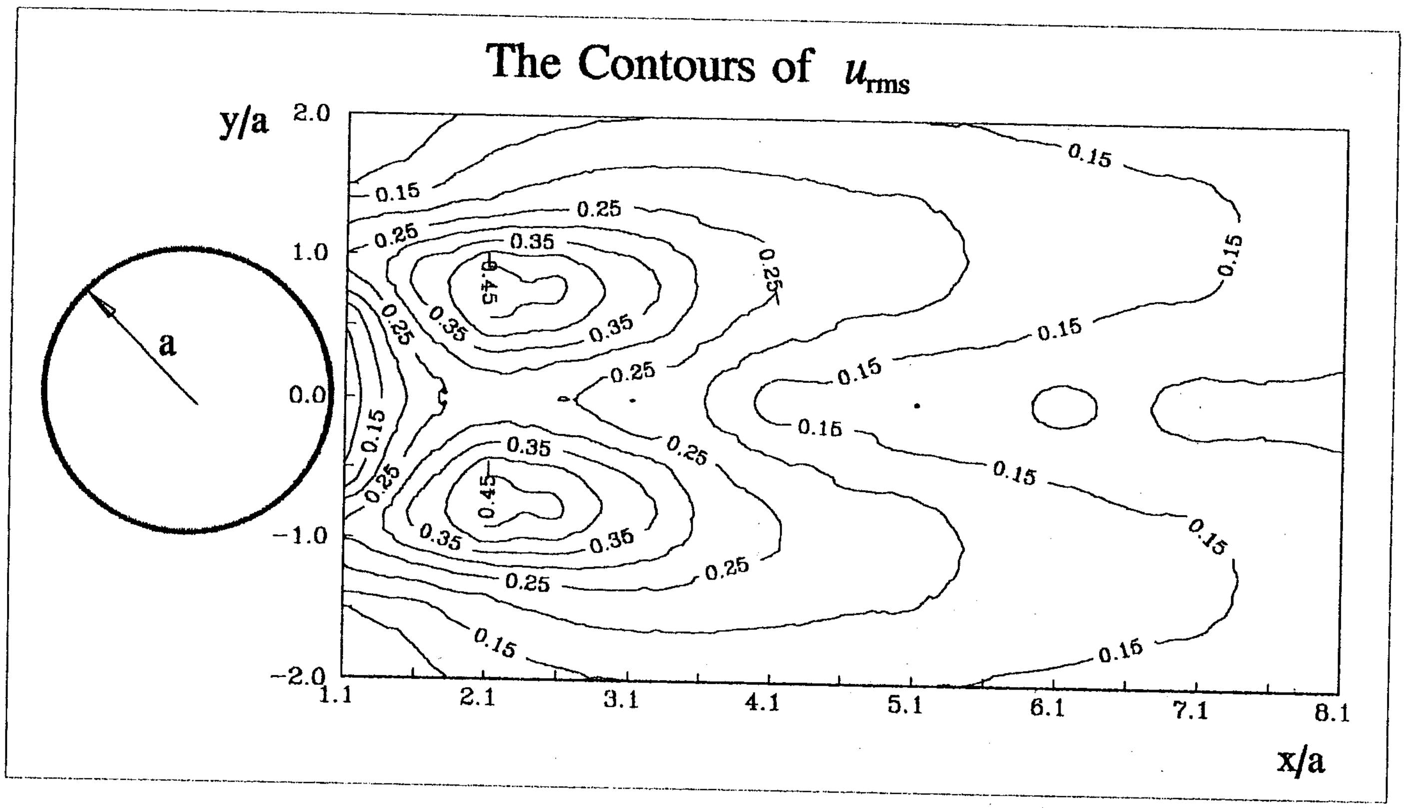

Fig.6.15. The rms value contour of *U* velocity fluctuations behind the circular cylinder.

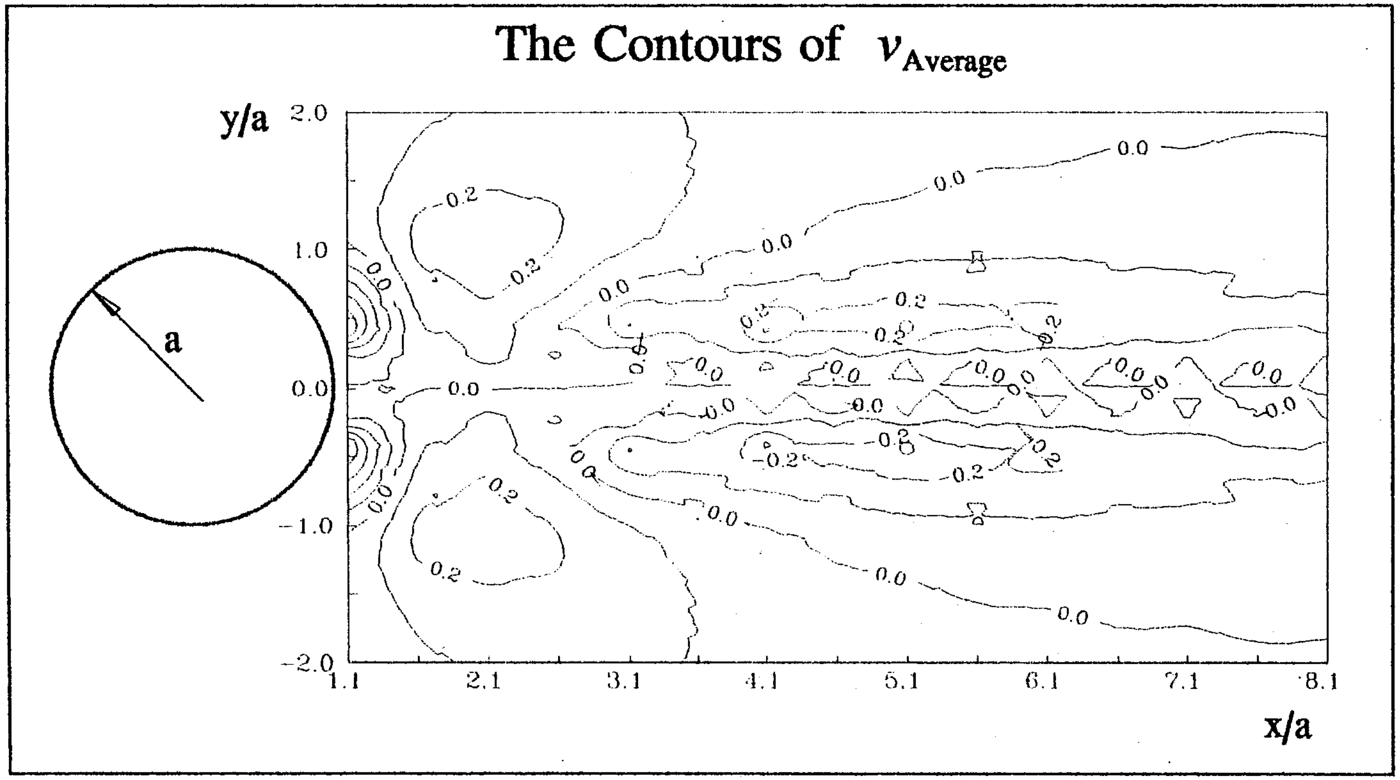

*Fig.*6.16. The average *V* velocity contours behind the circular cylinder

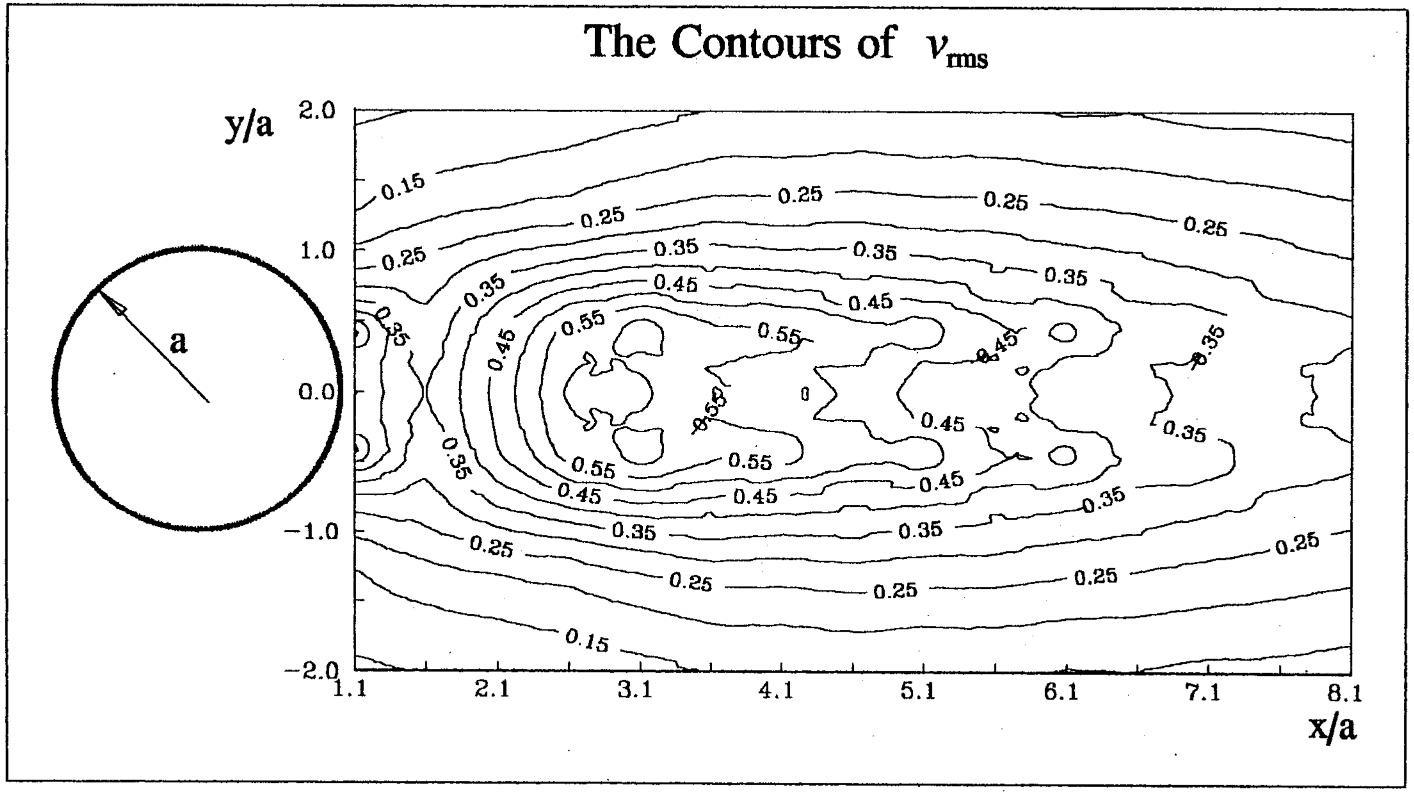

Fig.6.17. The average *V* velocity contours behind circular cylinder.

6.1 Results and Discussion of Oscillating Circular Cylinder

In this study, effects of longitudinal sinusoidal oscillations of free stream on wake structure and loading of a circular cylinder has been investigated by means of the lagrangian discrete vortex method. In this study the amplitude of oscillation is ***0.3*** and the other parameter f_e/f_o^* varies. f_o^* is the natural vortex shedding frequency and $f_e=0$ corresponds to the freely developing wake with the natural vortex shedding frequency of $f_o^*=0.1$. The computations were performed for f_e/f_o^* $=$***0.5, 1., 2., 3.*** and ***4.***.

In an experimental study, interesting results about near wake of oscillating cylinders have been found by Öngören & Rockwell (1988). A symmetric vortex formation at oscillation frequency at the upper and lower surface is observed (case S); if $f_e/f_o^*=2$, because of groups of vortices forming in opposite directions with respect to the centerline of the wake, a asymmetric vortex street with half the oscillation frequency is obtained (case A-II, Fig.[6.18]). The vortex formation changes to a symmetric structure at the case of $f_e/f_o^*=4$ (case A-IV), while it is asymmetric in the case of $f_e/f_o^*=3.0$ As for the case of A-I, an asymmetric vortex formation with natural vortex shedding frequency resembles the classical Karman vortex street. Fig.[6.19] shows the fluctuation of the rate of change of strength of the point vortices released into the flow field from the upper and lower separation points of the cylinder ($d\Gamma/dT$; here, T stands for the non dimensional time obtained by using the cylinder diameter (a) and mean free stream velocity U_m, i.e., $T=U_m t/a$). When there is no external effect ($f_e/f_o^*=0$), the fluctuations at the upper and lower sides of the cylinder are π out of phase and the fluctuation frequency is equal to the natural vortex formation frequency (f_o^*). f_s is determined as ***0.1*** and corresponding Strouhal number $St=f2a/U_o$ is in accordance with the experiments. The change of lift coefficient with respect to time is at the same frequency. Periodical vortex formation results in the fluctuation of the lift coefficient with the same rhythm (Fig.[6.20]). As seen in Fig.[6.21], large scale vortices with π out of phase formed from cylinder and travelled to the downstream gives way to the asymmetric wake structure. When the frequency of free stream oscillation is half of the natural vortex formation frequency (f_e/f_o^*), vortex formation frequency (f_s) does not differ very much from its free value as clearly seen in the fluctuation of the lift coefficient in Fig.[6.20]. However, $d\Gamma/dT$ variation has not a mean, steady value as in the case of $f_e/f_o^*=0$, but fluctuation at oscillation frequency Fig.[6.19].

When $f_e/f_o^*=1.0$, C_L versus T variation (Fig.[6.20]) puts forth an evident reduction at the large scale vortex formation frequency. When the the vortex formation frequency (f_s) approaches the oscillation frequency (f_e) or its subharmonics, the decrease of the vortex formation frequency is also observed in the experimental studies (Barbi, et.al., 1986). $d\Gamma/dT$ variation at the upper and lower separation points corresponding to this case, as a result of symmetric forcing of free stream, shows phase difference of less then π. However, the downstream wake is in an asymmetric structure similar to the case $f_e/f_o^* = 0.$ (Fig.[6.21,22]). There is also similar phase relation between $d\Gamma/dT$ - T variations at the upper and lower separation points for $f_e/f_o^* = 2.$ and $3.$ When $f_e/f_o^* = 2.$, $d\Gamma/dT$ - T variation indicates that there exist two pairs of small scale vortex formation from upper and lower separation points. Moreover, it is seen that, there exists a difference in strength of vortices formed almost in synchronization from the upper and lower sides. A vortex forms from the upper side together with a vortex with lesser strength from the lower side, and at the succeeding oscillation period $T_e = 1/f_e$ opposite is observed and this repeats almost perfectly. It appears that each of the large scale vortices formed from the upper and lower sides comes out as a result of grouping of a large scale vortex formed with a small scale vortex formed from the opposite side. And, as a result of this vortex-vortex interaction, a regular overall wake formation is obtained at the half out the oscillation frequency (Fig.[6.21,23]). Locking of vortex formation frequency to the half at the oscillation frequency is a feature clearly seen also in experimental works (Griffin & Ramberg, 1976 - Detemple-Laake & Eckelmann, 1989). Equalization of vortex formation frequency (f_s) to the natural vortex formation frequency of no-oscillation case is clearly observed in the lift coefficient variation (Fig.[6.20]). However, the vortex-vortex interaction mechanism suggested here is different from that observed by work of Öngören & Rockwell (1988). In this experimental work, A-III regime explained in previous pages is observed, but the suggested regime here is A-IV in A-III contrary to A-IV, grouping of large-small vortex is observed only in one side of the wake region. For the cases $f_e/f_o^* = 3.$ and $4.$, as similar to the case $f_e/f_o^* = 2$, as a result of large-small vortex interaction, wake structure is formed by vortices at $f_s = f_o^*$ frequency (Fig.[6.21]). Interactions, which are effective in reaching to this overall structure, can be proposed by starting with the variation of $d\Gamma/dT$-dT as follows: when $f_e/f_o^* = 3$, in natural vortex formation period (T_o^*) triple small scale vortices form from the upper and lower separation points in mutual phase agreement. Each vortex formed from one side is met by a larger vortex and a smaller vortex formed from the other side. And, as a result of this interaction between the vortices, far wake structure is actually formed by vortices with the natural formation period (T_o^*). The lift coefficient fluctuates at the frequency of the formation of this large scale vortices which is not different from natural frequency (f_o^*) (for $f_e/f_o^* = 3$ and 4, the difference at T axis in Fig.[6.19,20] must be taken into account.). When $f_e/f_o^* = 4$, the resulting vortex formation frequency (f_s) is again almost the same with natural formation frequency (f_o^*). For $f_e/f_o^* = 3$ and 4, although the small scale symmetric vortex formations at f_e frequency are observed in the experimental work of Öngören & Rockwell (1988), there is no observation for the for the far wake structure. Another character observed in the experimental works is that the lift coefficient increases higher and higher as it is reached to the synchronization regime. The work presented here confirms this observations (Fig.[6.20]). As conclusion, in spite of near wake structure displaying different configurations depending on the oscillation frequency, overall far wake structure is interestingly universal independent from the oscillation frequency. Interaction among vortices is the cause of reaching to this universal structure

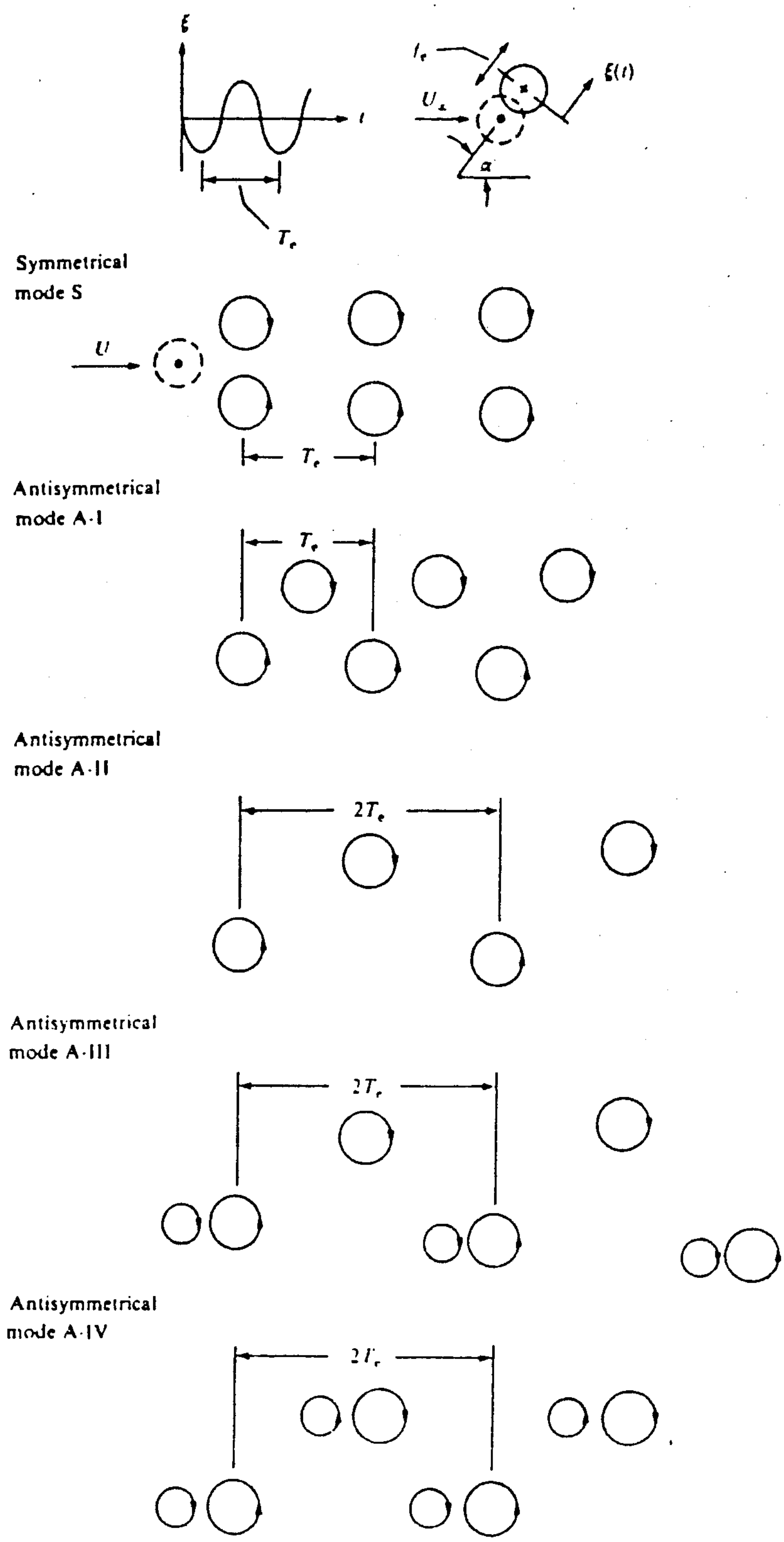

Fig.6.18. Representation of basic modes of vortex formation from an oscillating cylinder (Öngören & Rockwell, 1988).

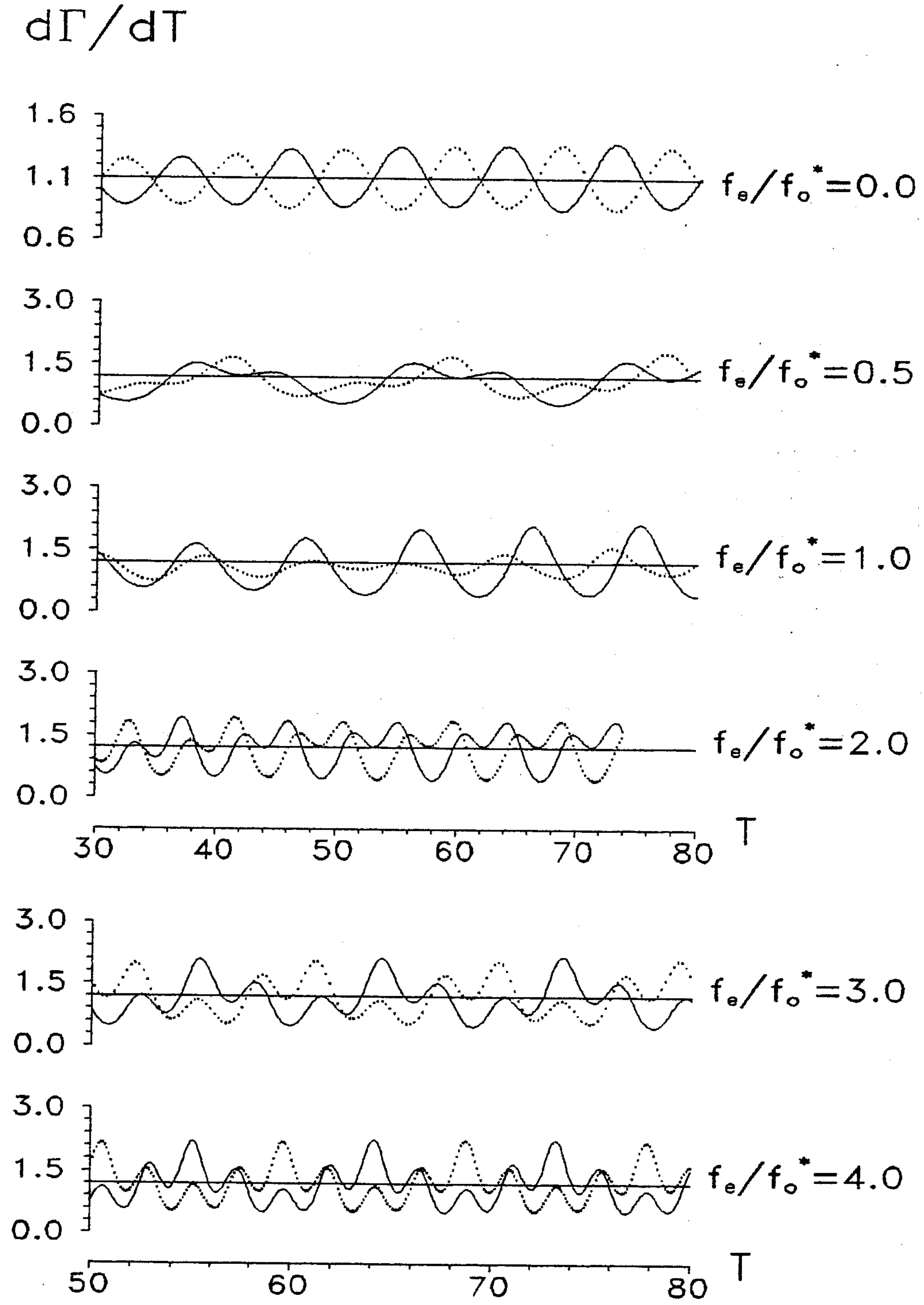

Fig.6.19. The variation of change of circulation with respect to time ($d\Gamma/dT$) depending on the rate f_e/f_o^*

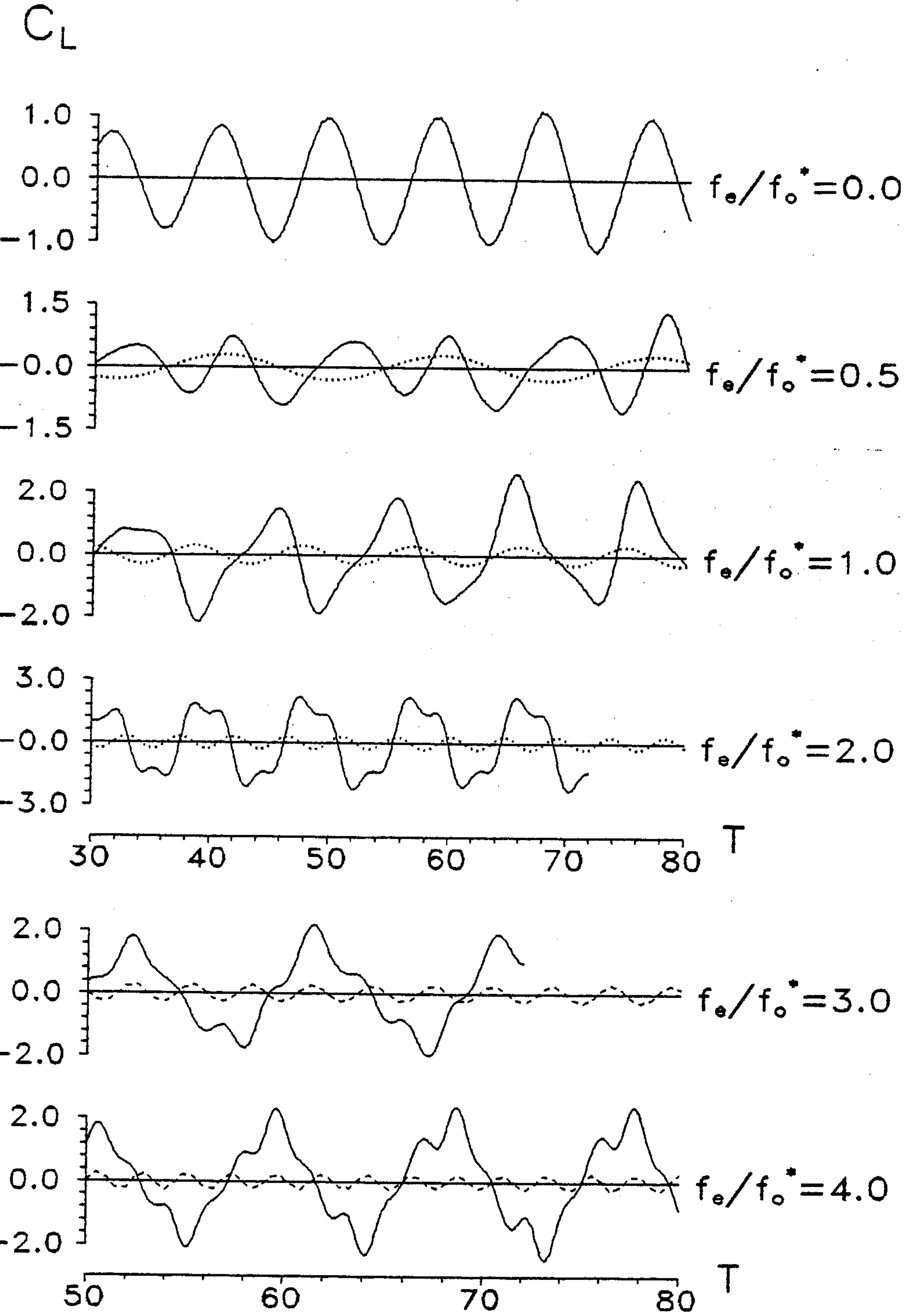

Fig.6.20. The variation of lift coefficient (C_L) with respect to time depending on f_e/f_o^*, (------) is for the free-stream oscillation.

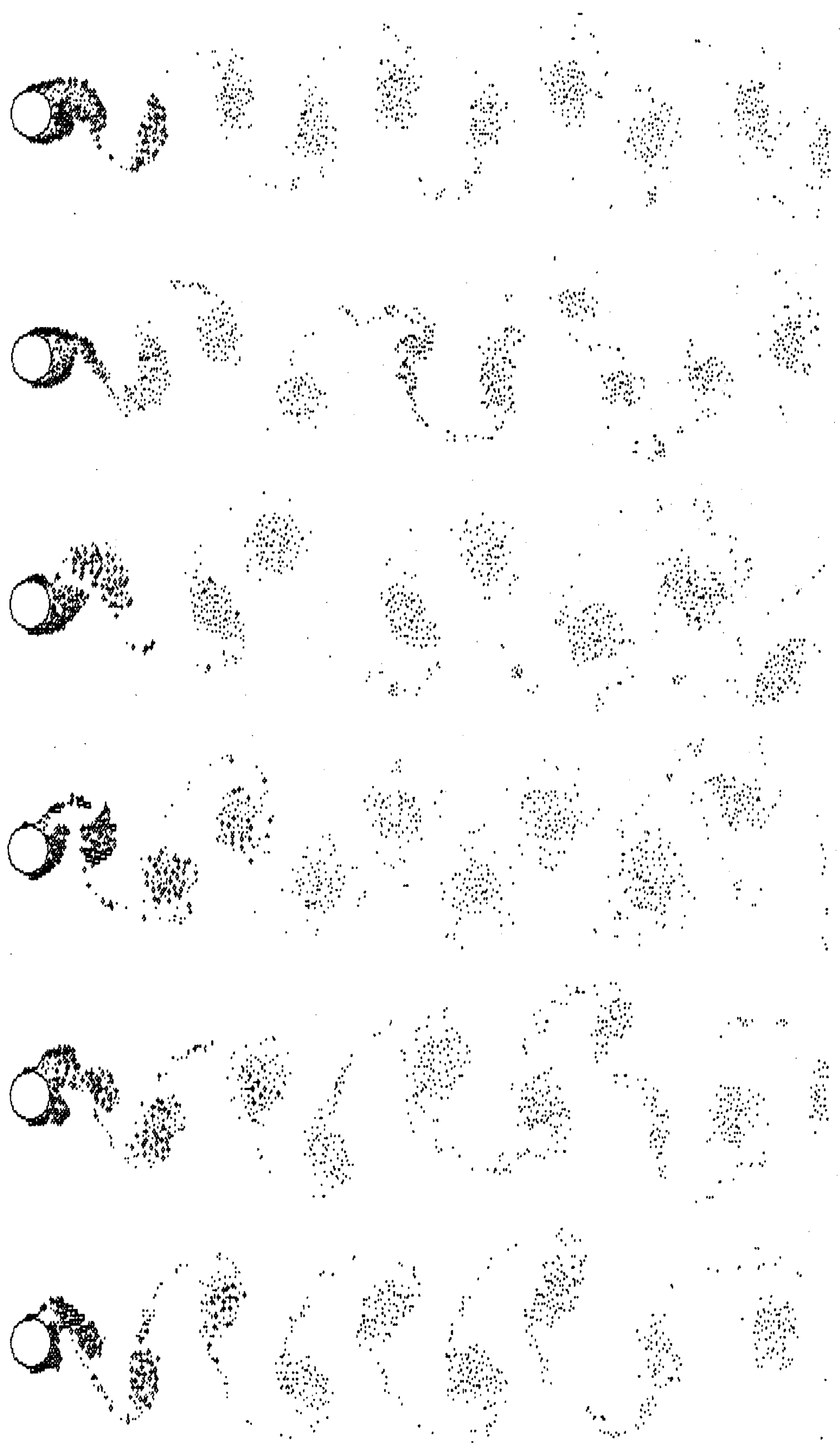

Fig.6.21. Wake structures for the cases $f_e/f_o^*=0, 0.5, 1, 2, 3$ and 4 from top to bottom respectively.

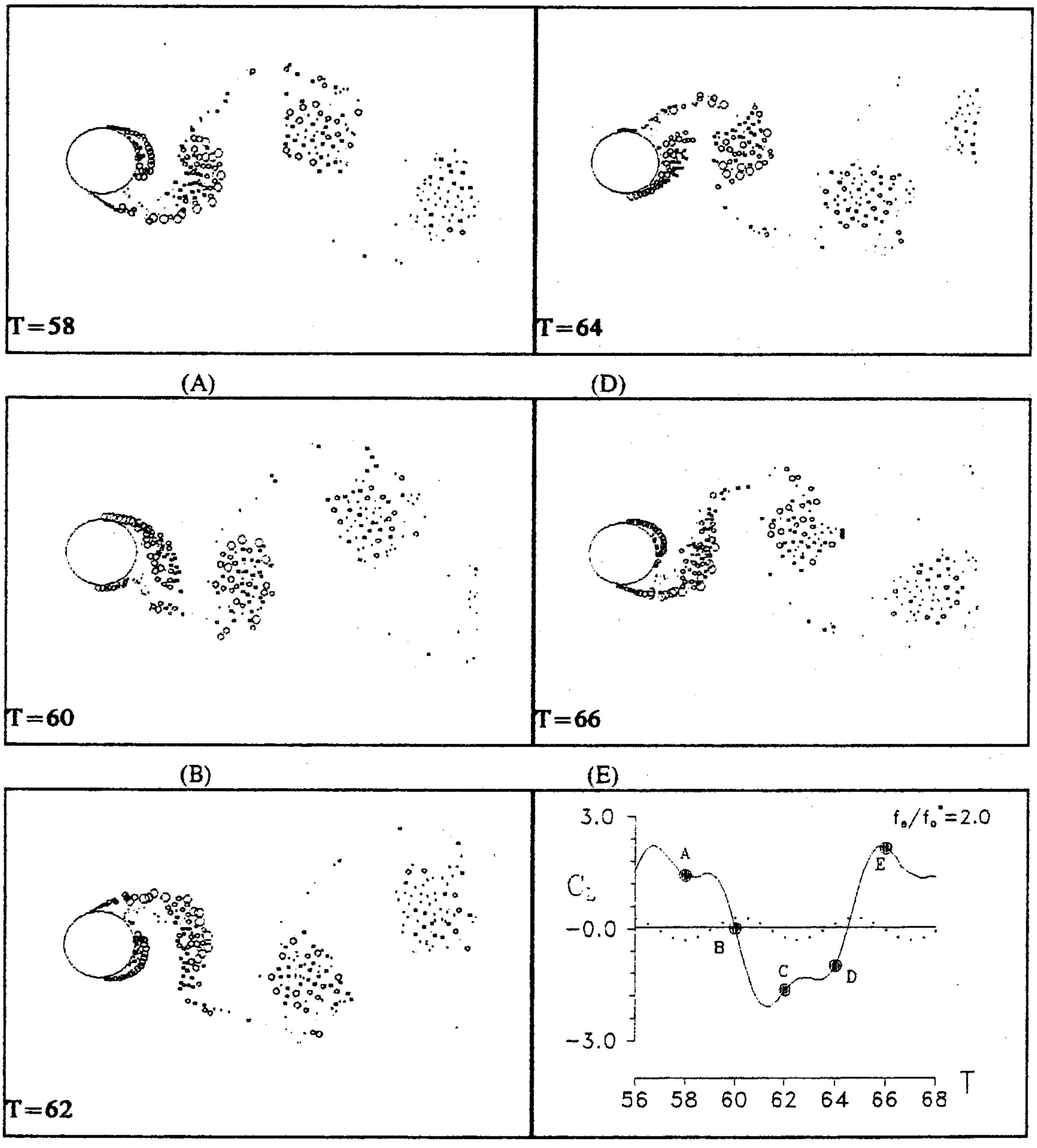

Fig.6.22. The point vortex distribution for the case $f_e/f_o^*=2.0$ in a period. Nondimensional time corresponding to each case is indicated on the C_L vs T variation.

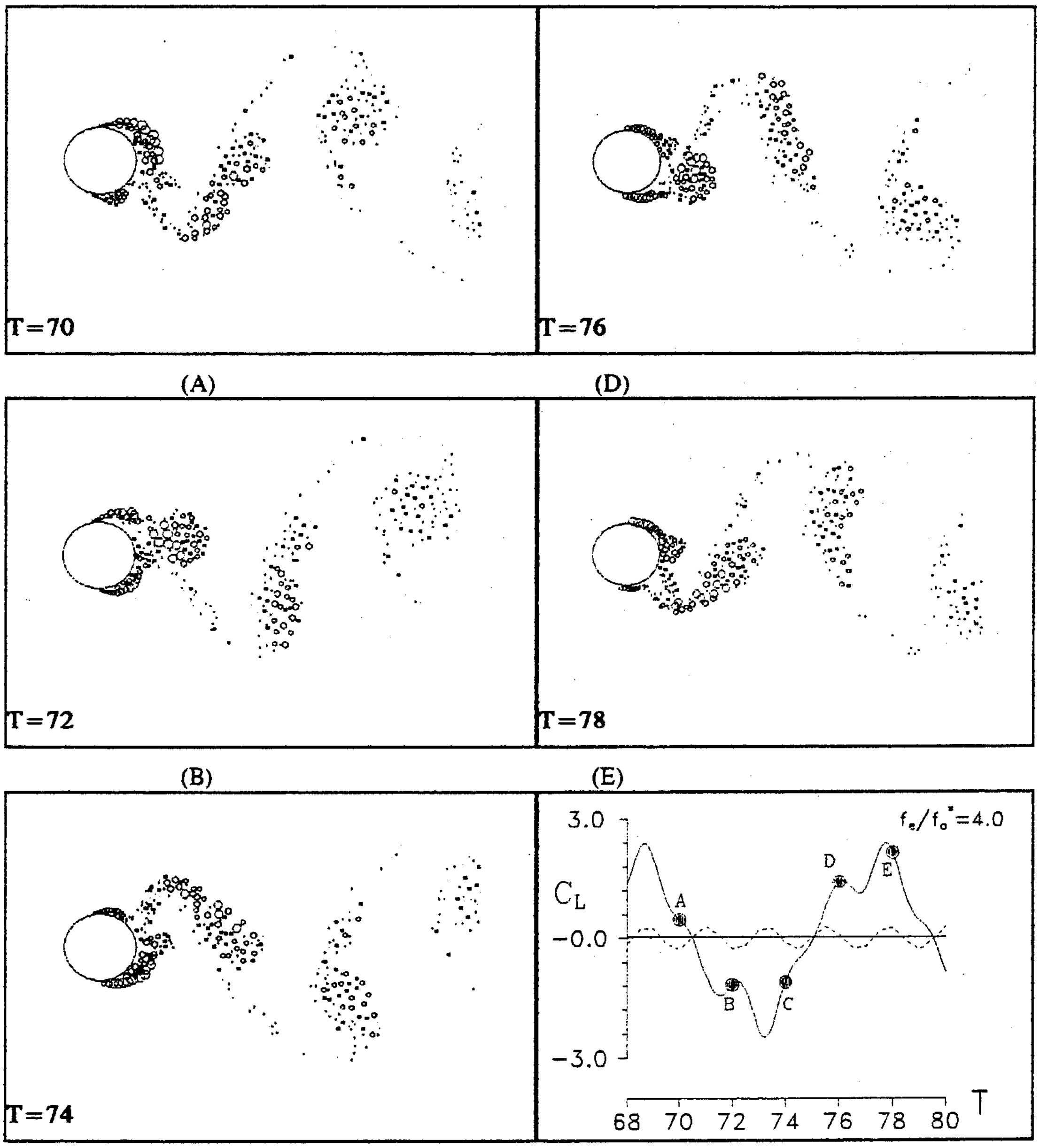

(C)

Fig.6.23. The point vortex distribution for the case $f_e/f_o^*=4.0$ in a period. Nondimensional time corresponding to each case is indicated on the C_L vs T variation.

6.2 Results and Discussion Circular Cylinder with splitter plate

The calculation results for the cylinder without the plate are in good agreement with both numerical and experimental studies (Sarpkaya & Schoaff, 1979): Time mean value of the drag coefficient (**C_D**) is 1.1; the lift coefficient (**C_L**) has a mean amplitude of about 0.68 and a Strouhal frequency of ***$St = 0.22$;*** and the separation points (Θ_{sep}) fluctuate nearly sinusoidally with an amplitude of ***2.6*** degrees about a mean value of ***77*** degrees, while the stagnation angle has a fluctuation amplitude of ***2*** degrees.

Discrete vortex distributions in Fig.[6.24] show the effect of the splitter plate on the flow structure. These distributions correspond to non-dimensional times at around ***95*** at which the fluctuating lift passes through a minimum in each case. Several experimentally-observed features (Apelt, et.al., 1973) of the flow are evident in this figure: With the action of the splitter plate, interaction between the separated layers decreases, the vortices form further downstream of the body, and the width of the wake decreases accordingly. Irregularity of the vortex street for the cases with a long splitter plate is also observable.

To quantify the variation of the length of formation of the vortices (***l_f***), a method proposed by Bearman (1965) was used. According to this method, streamwise velocity fluctuations at vortex shedding frequency were calculated at a number of stations along a line parallel to the wake-centreline and at ***$y = D/4$***. Then, the distance (***x/D***) between the location at which the velocity fluctuation peak occurred and the centre of the cylinder is called the vortex formation distance. The variation of the rms value (***u_{rms}/U_o***) of the velocity fluctuation with respect to the non-dimensional downstream distance for various plate lengths is shown in Fig.[6.25]. For the cylinder without the plate both the ***u_{rms}*** level and ***l_f/D*** agree well with those obtained experimentally, which are calculated to be ***0.4*** and ***1.2*** correspondingly.

The formation length information deduced from Fig.[6.25] is shown in Fig.[6.26], where variation of the rms value of the lift coefficient is also demonstrated. The formation length variation is in accordance with the experiment of Apelt, et.al. (1973) based on flow visualization: A short splitter plate causes the vortices to form much further downstream with respect to the case without the plate, and for longer plates, the formation distance remains essentially the same.

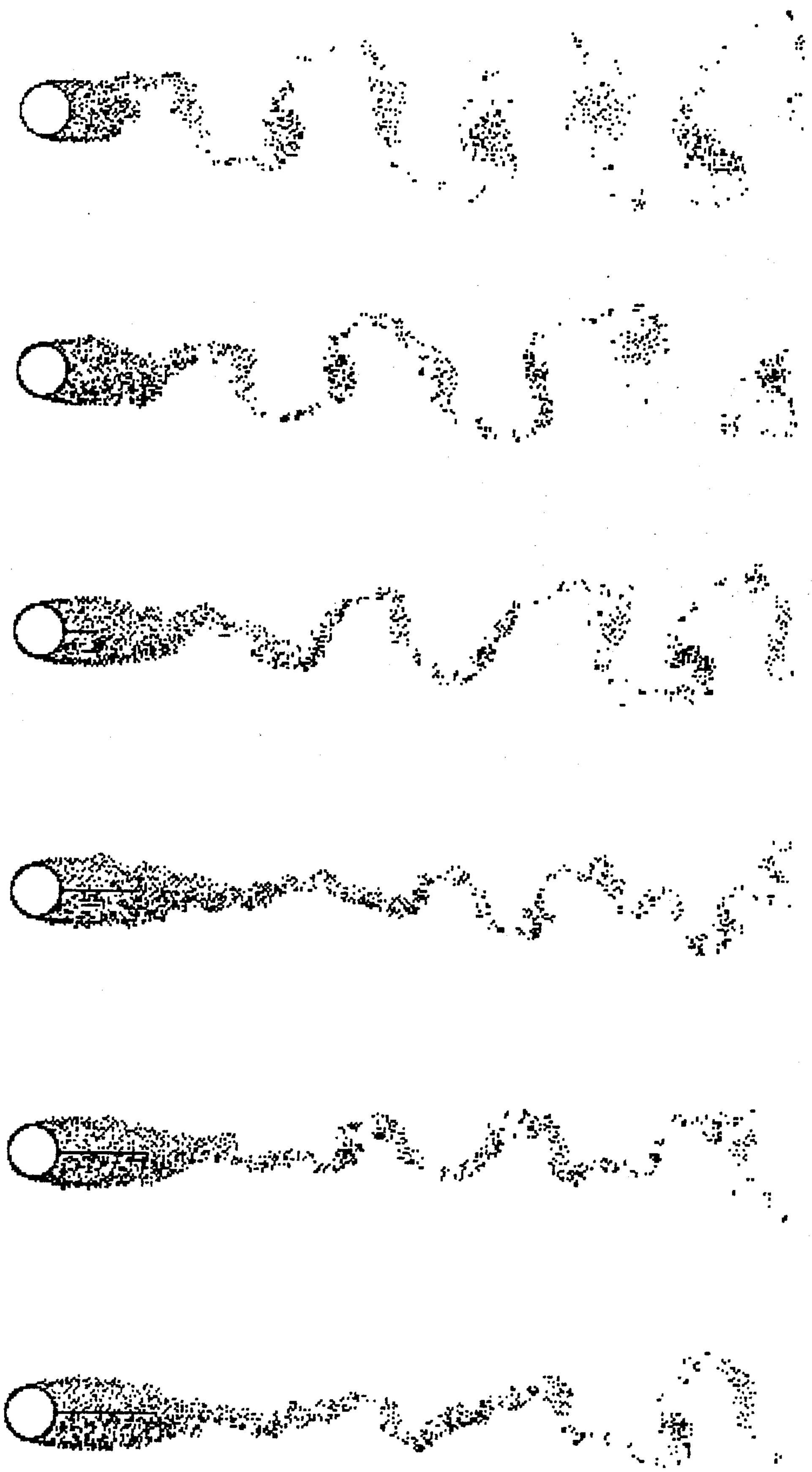

Fig. 6.24 Effect of splitter plate on flow structure. *L/D=0, 0.125, 0.5, 1.5, 1.75* and *2*, from top to bottom.

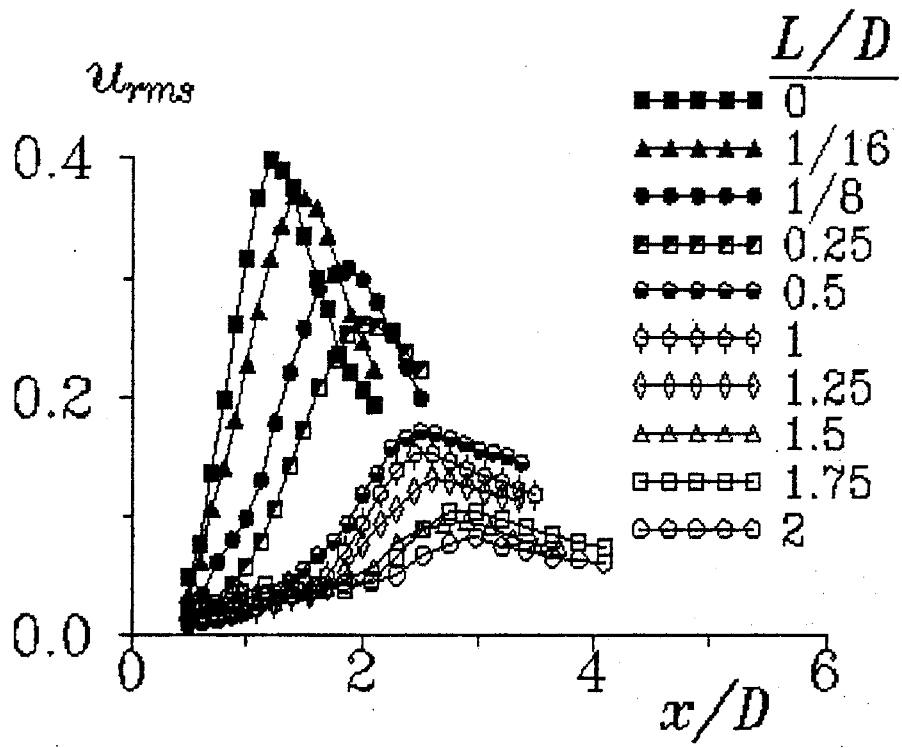

Fig. 6.25 Variation with downstream distance of the rms value of streamwise velocity fluctuations for various splitter plate lengths.

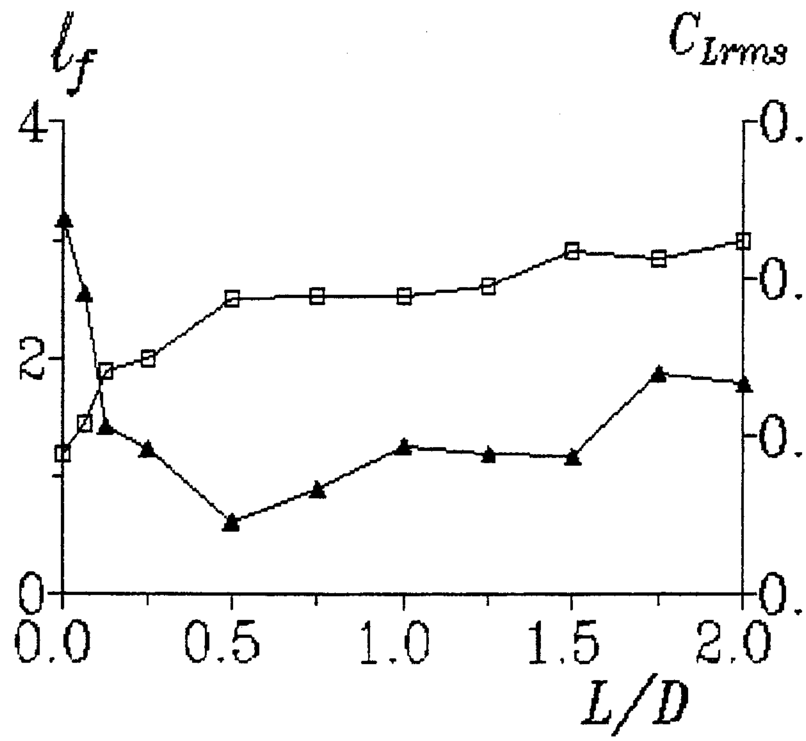

Fig. 6.26 Variation with downstream distance of formation length (l_f: □) and lift coefficient fluctuation (C_{Lrms}: ▲).

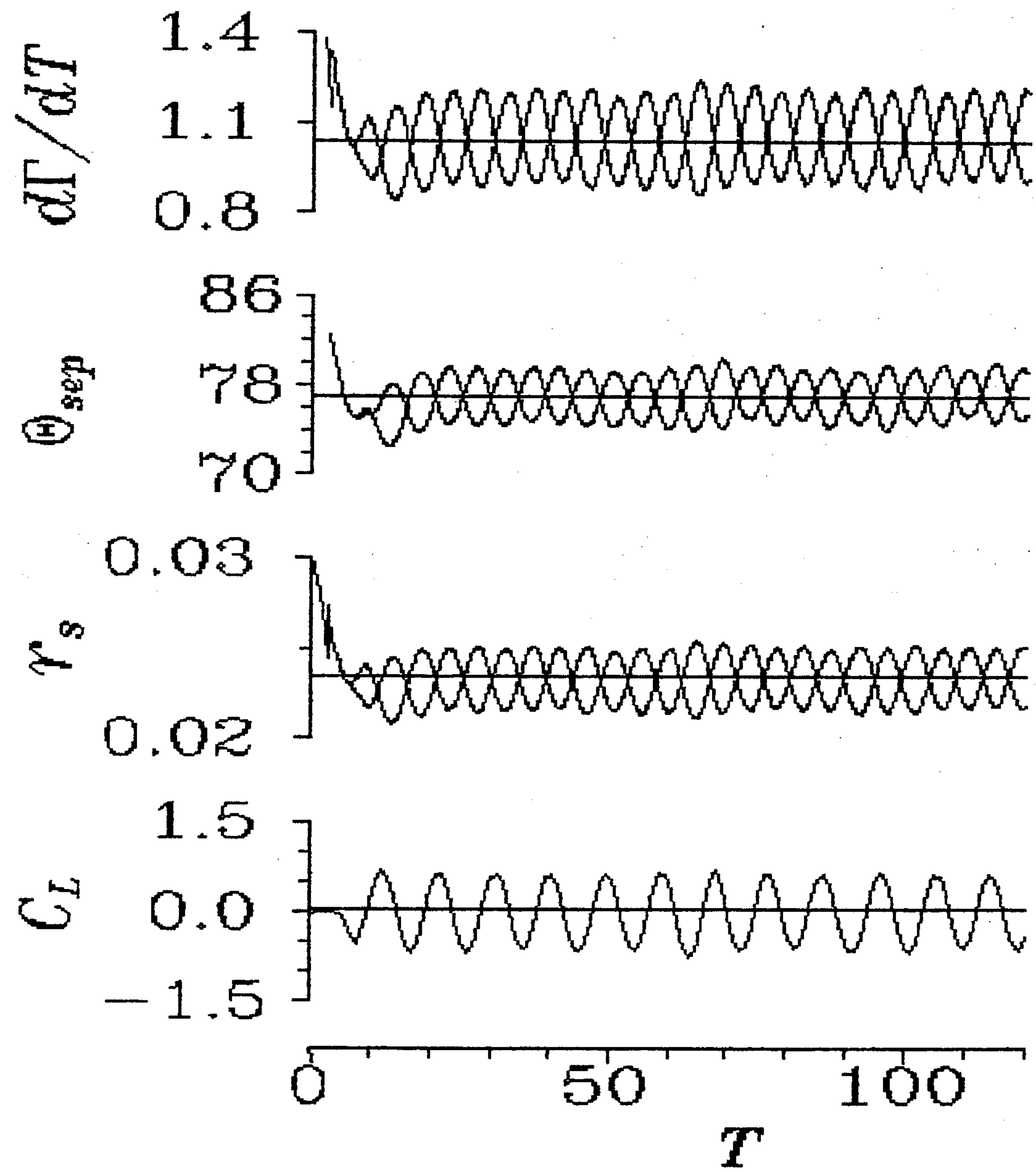

Fig. 6.27. Variation with time of various fluctuating quantities for $L/D=0$.

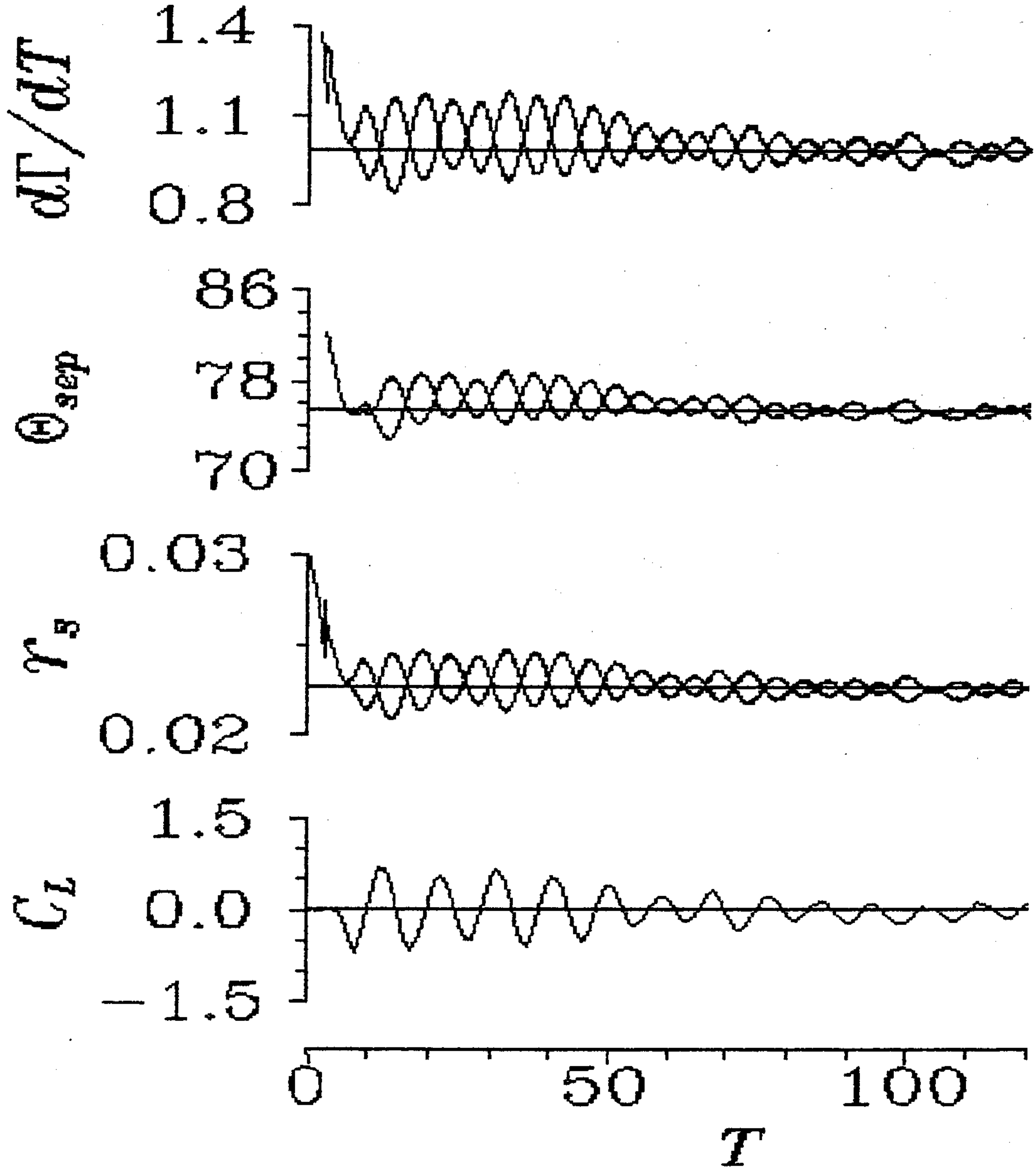

Fig. 6.28 Variation with time of various fluctuating quantities for $L/D=0.125$.

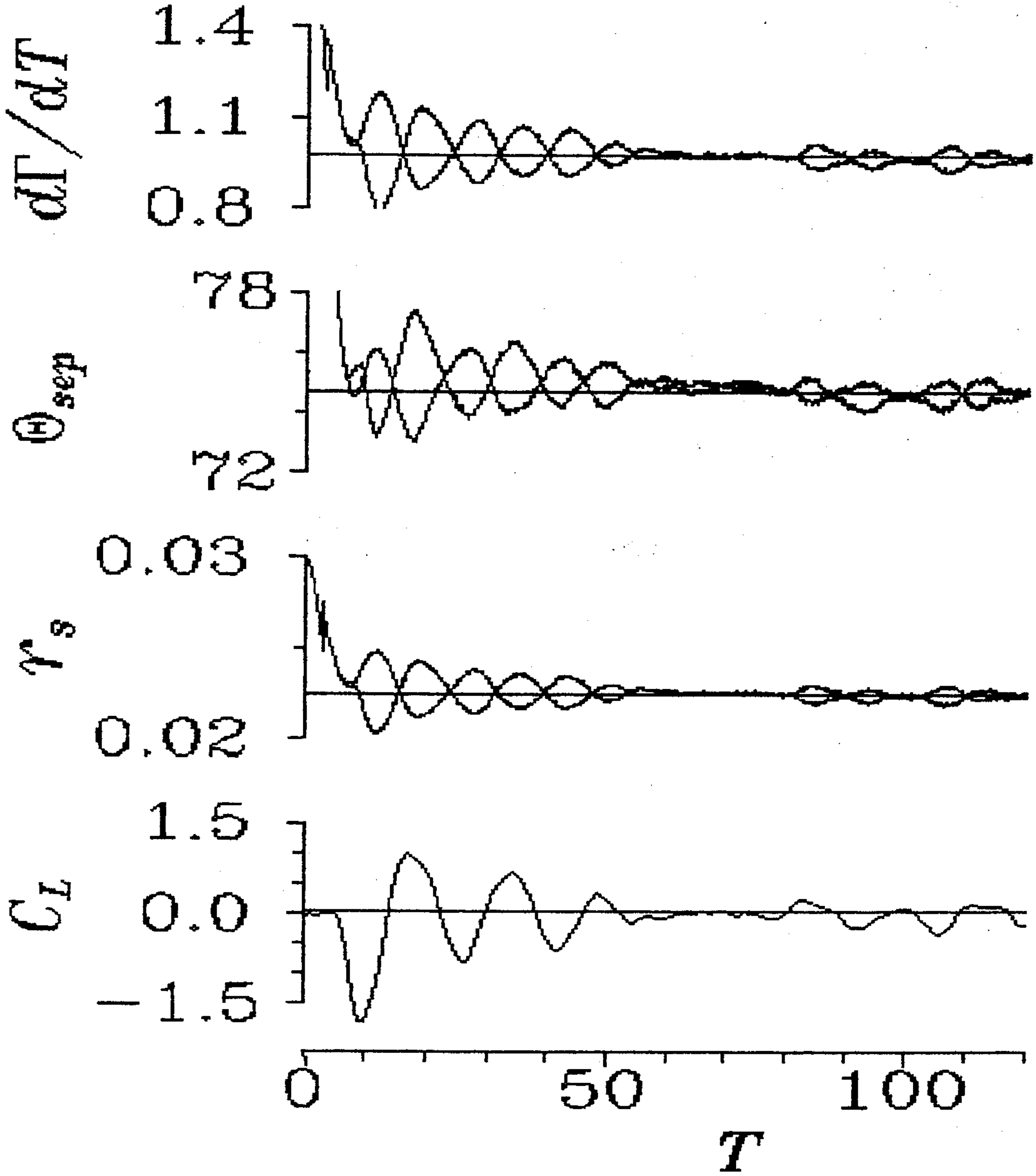

Fig. 6.29 Variation with time of various fluctuating quantities for $L/D=1$.

Parallel to this variation in the formation length, a weakening in the strength of fully formed vortex is expected. A clear indication of this weakening is seen in Fig.[6.25] where the maximum fluctuation level is decreasing with increasing plate length. Corresponding to the abrupt increase in the formation length for short plate lengths, there is a sudden decrease in the fluctuation level with increasing plate length. These changes in the strength and the formation length of the fully-formed vortex reflect into the variation of the lift coefficient (Fig.[6.26]).

Variation with respect to the non-dimensional time of the fluctuations of: the rate of circulation fed into the separated layers from upper and lower separation points ($d\Gamma/dT$); the upper and lower separation angles (Θ_{su}, Θ_{sl}); the radial distances of introduction (r_s); and the lift coefficient (C_L) are shown in Fig.[6.27-30). For the case of circular cylinder without the splitter plate ($L/D=0$), a stable regime is reached at about $T=20$. Whereas, for the cases with splitter plates, fluctuations become intermittent and therefore it becomes difficult to mention about a stable regime (Fig.[6.28-30]).

In accord with the observation of Apelt, et.al.(1973) a very short splitter plate ($L/D=0.125$) reduces the oscillation of the separation points greatly (Fig.[6.27,28]). With a longer plate, oscillations of the separation points are further stabilized (Fig.[6.29]). This is accompanied by reductions in $D\Gamma/DT$ and the lift coefficient (C_L) fluctuations.

It should be noted that, in attaining the time traces of the fluctuating quantities presented herein, the magnitude of the initial asymmetry is not chosen arbitrarily. It is found out that the behaviour of the simulated wake, and the time required to elapse before attaining a nearly stable regime for the short plate lengths including the case without the plate, changes appreciably depending on the set of values for the reduction parameter and the magnitude of the initial asymmetry. On the other hand, for long splitter plates (i.e.$L/D \geq 1.75$), the simulated wake is not so sensitive to the magnitude of the initial asymmetry. Therefore, after many preliminary runs for different sets of values, the final set ($\beta=0.95$ and 0.01 for the magnitude of the artificial asymmetry) is determined by requiring that it lead to small elapsed-times for reaching the nearly stable regime of flow for all of the plate lengths, and for the case without the plate, give way to values in various characteristics such as drag and lift coefficients which are in agreement with experiments.

Fig.[6.32] shows the variation with respect to splitter plate length of the Strouhal number deduced from the lift fluctuations (Fig.[6.31]). Just as the same with that done for determining the other mean quantities such as the force coefficients (C_D, C_L), the

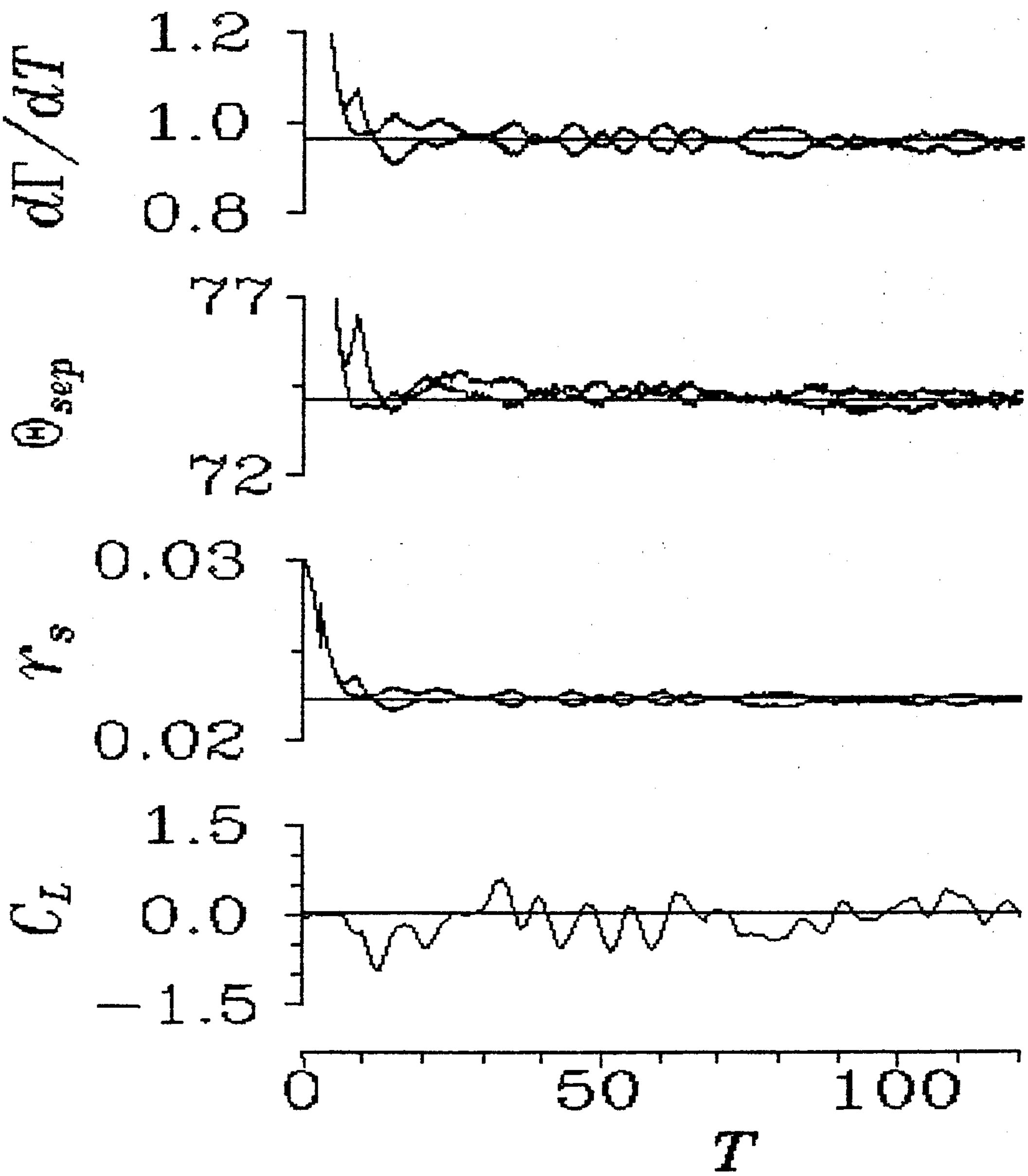

Fig. 6.30. Variation with time of various fluctuating quantities for $L/D=2$.

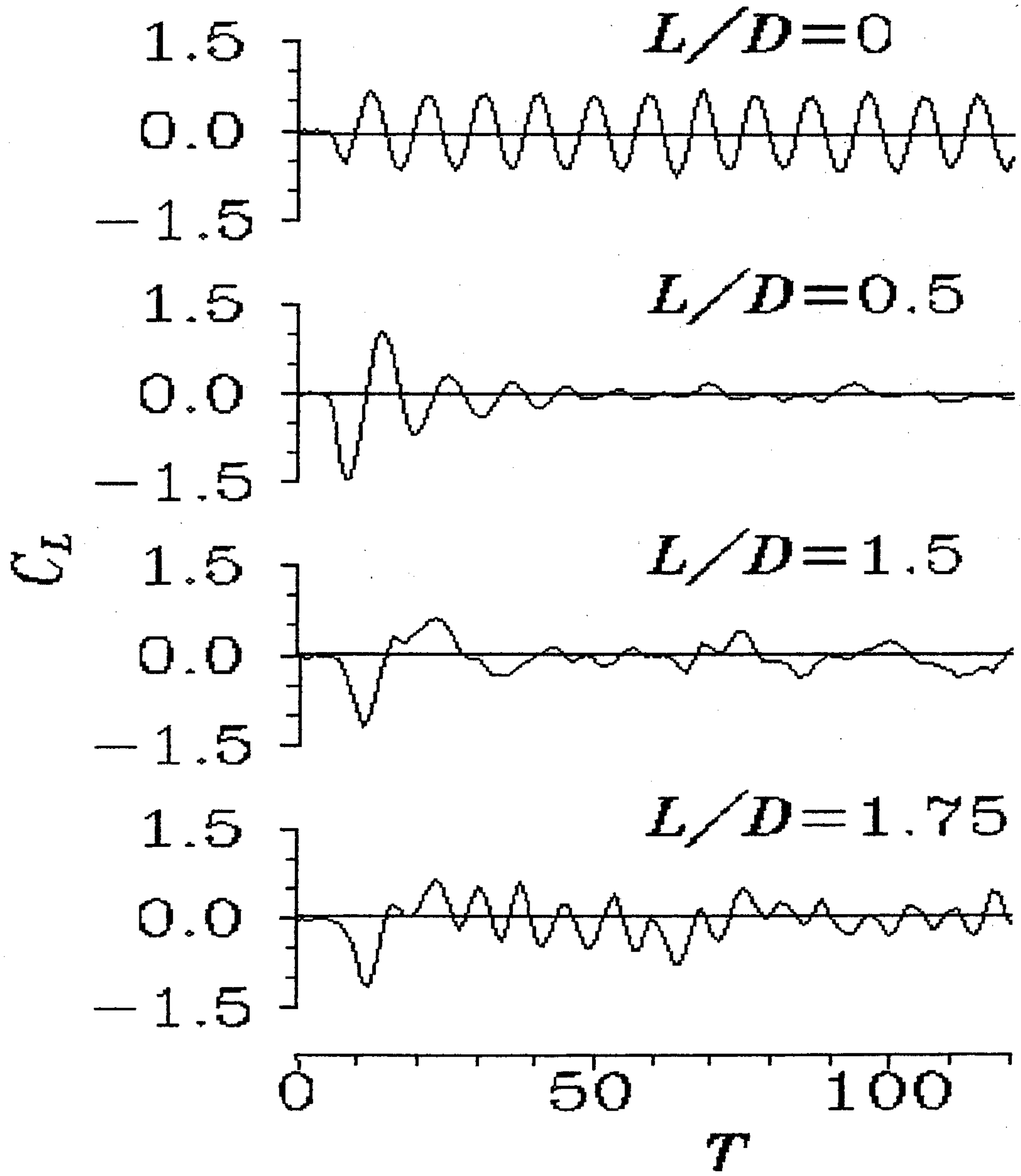

Fig. 6.31. Variation with time of lift coefficient (C_L) for various splitter plate lengths (L/D).

Strouhal number is calculated by means of a Fast Fourier Transform routine by considering the parts of the data that are thought not to carry signs of the initial asymmetry (i.e. non-dimensional times after about 60).

When compared with its experimental counterparts, except the range of very short plate lengths, the present simulation paves way to Strouhal numbers which differ greatly from the experiments for a wide range of splitter plate lengths. Up to ***L/D = 0.25,*** there is a good agreement and the predicted value for ***L/D = 2*** coincides with that measured by Apelt, et.al. (1973). It should be added that the Strouhal number variation calculated by Kawai (1990) shows similar characteristics.

Along with the intermittency mentioned above, the fluctuating quantities do not have a well-defined frequency for the cases with splitter plate. For example, as also evident in the time traces shown in Fig.[6.27-30], the rms spectra of the lift coefficient fluctuations do not indicate a single frequency (Fig.[6.33]). This is in contrast to the case without the plate.

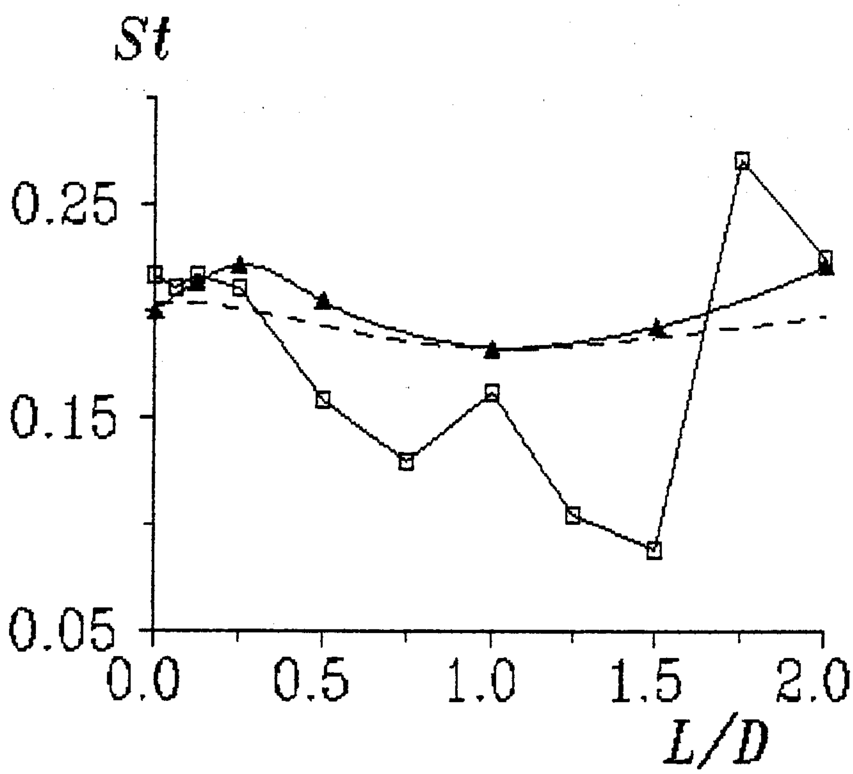

Fig. 6.32. Variation of Strouhal number (***St***) with respect to splitter plate length (***L/D***). Apelt et. al. (1973): ▲; Gerrard (1966): —; present simulation: □.

Another point in relation with the predicted-frequency variation as function of the splitter plate length is that, it is an outcome of employing a reduction scheme such as the one used for the results presented here. Calculations without employing any reduction scheme shows that, although the variations of the formation length of fully formed vortex

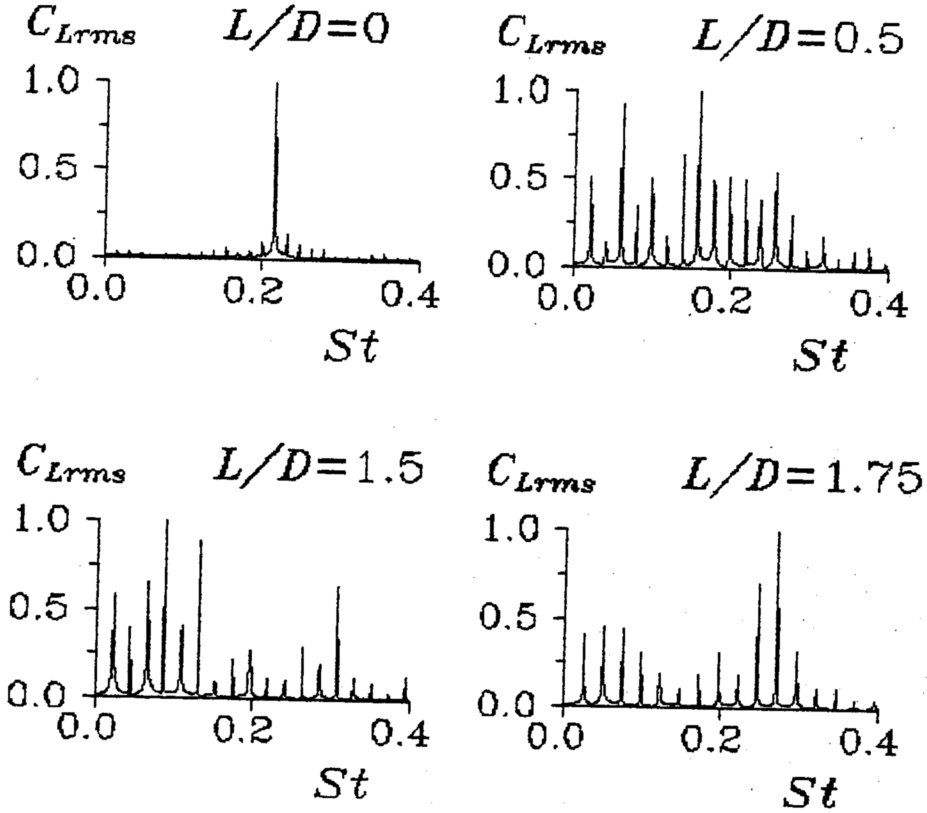

Fig. 6.33. Spectrum of lift coefficient fluctuations (C_{Lrms}) for various plate lengths (L/D).

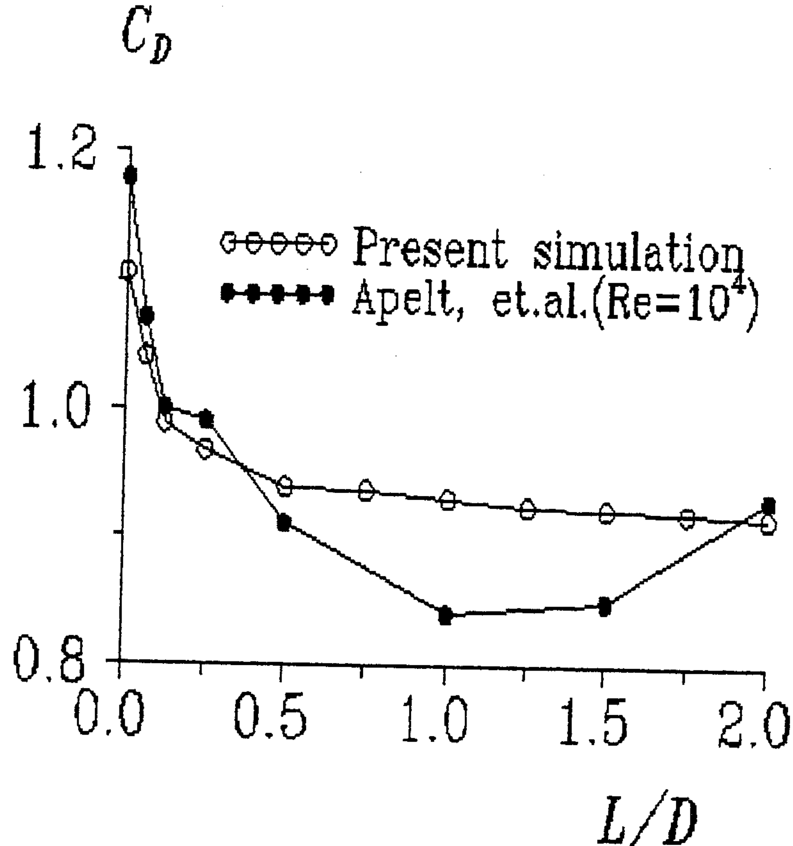

Fig. 6.34 Variation of mean drag coefficient (C_D) with respect to splitter plate length (L/D).

and the drag coefficient follow similar trends to those presented in this study, the Strouhal number continuously decreases with increasing plate length. For plate lengths (***L/D***) larger than ***1.5,*** the simulated wake does not even respond to an artificial asymmetry.

As to the mean drag coefficient (C_D), the predicted values sharply reduces at first and than continually decreases with increasing plate length. The sharp reduction is in agreement with the experiment (Apelt, et.al., 1973), but the recovery of the drag coefficient to a higher value for long plate lengths is not predicted. Additionally, for a large range of plate lengths, the simulation gives higher values in comparison with the experiment.

To conclude, the present Lagrangian discrete vortex simulation with a heuristic model for vorticity reduction paves way to determination of many experimentally-observed characteristics of the unsteady wake.

6.3 Results and Discussion of Airfoil

In setting up the computational model of a real system, the determination of computational parameters such as the Reynolds number, the size of the integration time step and size of mesh cells constitutes the first problem. Of course, the grid should be fine enough and the time step sufficiently small so that increased temporal or spatial resolution will not affect results.

The grid dependent hybrid method employed in this study requires a proper grid to calculate the velocity field through the use of Poisson's equation, and to solve the diffusion port of the vorticity transport equation. In close neighbourhood of the body, the grid must be fine enough for representation of the boundary layer accurately. On the other hand, the grid should extend far enough in streamwise direction so that the rotational fluid cannot reach to the outer boundary of the solution domain during the calculations. All of the computations are carried out in a rectangular domain obtained conformally transforming the physical flow domain (i.e., the region outside of the airfoil) (Fig.[6.35,36]). The above mentioned constraints lead to grid expanding in direction perpendicular to the lower boundary of the rectangular domain (in -y direction) corresponding to the body boundary. Whereas, in direction parallel to the lower boundary (in -x direction), a constant spacing is employed in order to obtain a numerical solution of Poisson's equation by making use of Fast Fourier Transformation technique. The rate of expansion of the cell size in -y direction is chosen to be less than *1.2.* The grid structure satisfying these restrictions is shown in Fig.[6.35], whereas Fig.[6.36] shows the corresponding grid structure in the physical plane. In the computational plane, ratio of the successive mesh spacings is not greater than *1.15* and the number of mesh point is *128* in -x direction and *170* in -y direction. This grid structure was considered sufficient for calculations at $Re = 1000$. The time step choosen is *0.0025* .

Result of the time step splitting algorithm at $Re = 1000$ are obtained for 15 different incidences. These are $0^\circ, 3^\circ, 4^\circ, 8^\circ, 12^\circ, 13^\circ, 14^\circ, 15^\circ, 16^\circ, 17^\circ, 18^\circ, 20^\circ,$ 22° and 24°. The numerical study by Sampath (1977) and Wu & Sankar (1977) forms a basis of comparison.

All the result can be classified into four types with respect to incidence. The first type is the unseparated boundary layer. The second type is state of trailing edge separation and a resulting narrow wake, the third type is state of strong trailing edge separation, weak leading edge separation and medium width wake and the fourth type is state of leading edge and trailing edge separation and a wide wake. In Fig.[6.37,38,39], the point vortex distributions corresponding these four types of flow are plotted. The point vortex distributions for the cases of $\alpha=13^{\circ}, 16^{\circ}, 18^{\circ}$ are also shown in Fig.[6.40,41,42]. Although, there is no separation at $\alpha=0^{\circ}, 3^{\circ}, 4^{\circ}$, the resulting narrow wake develops an instability and thus a wavy far wake. For larger incidences a bluff body wake type flow exist behind the profile.

The colour coded vorticity distributions for the types of flow mentioned above are shown in Fig.[6.43]. The contours of vorticity distributions and streamline pattern for various incidence are shown in Fig.[6.44,45,46].

The colour coded vorticity distributions, pressure distributions on the airfoil surface, streamline patterns and velocity profiles on the airfoil surface at certain nondimensional times for various small incidences are shown in Fig.[6.47,48,49]. Since these figures include only case of small incidence, the instantaneous quantities is assumed to nearly represent quantities of the steady state or time average. This assumption will not be valid for larger incidences with large scale flow separation in Fig.[6.50,51,52,53]. These figures include the colour coded vorticity distributions, pressure on the airfoil surface, streamline patterns and velocity profiles on the airfoil surface at certain nondimensional times which are indicated by bold circles in (C_L) versus nondimensional time graphics. The time average of quantities shown in Fig.[6.50,51,52,53] are demonstrated in Fig.[6.54]. Fig.[6.50,51,52,53] demonstrates the wake evolution at a high incidence. At the beginning of a period (Fig.[6.50]), fully developed vortex from the trailing edge corresponds to minimum lift. At a later time (Fig.[6.51]), the leading edge large scale vortex becomes more dominant in comparison with that forming from the trailing end and the instantaneous lift increases. When the leading edge large scale vortex fully develops (Fig.[6.52]), the lift reaches to its maximum value.

In the time average sense, the leading and the trailing edge vortices produce a high suction on the upper face and thus a high time mean lift coefficient Fig.[6.54]. The velocity profiles in Fig.[5.50.(b),51.(b),52.(b),53.(b)] clearly shown separated region corresponding to the large scale vortices.

Variations for various incidences of lift and drag coefficients (C_L, C_D) with respect to nondimensional time Fig.[6.55,56,57,58,59,60]. With increasing incidence, both of these coefficients experience increases in their mean values and the fluctuation amplitudes. The lost of lift (stall) has been obtained later then $\alpha=22^{\circ}$. This is quite high for the flow with high Reynolds number (see Chapter 2 for the flow around airfoil). Results obtained in this study $\alpha=0^{\circ}$ and 3° are in agreement with computations of Sampath (1977). The rate of lift coefficient with respect to incidence measured experimentally for high Reynolds numbers is in good agreement with the analytical value according to inviscid theory by until the stall. Owing to its low Reynolds number, results of this study does not show the same agreement. Another disagreement with high Reynolds number flows is that the the stall occurs at about 22°. The rms value of lift and drag coefficient fluctuations (C_{Lrms}, C_{Drms}) are shown in Fig.[6.61.(b)]. The rapid increase of C_{Lrms} corresponds to the first existence of the leading edge separation. Spectrum of lift coefficient fluctuations (C_{Lrms}) for various incidence are demonstrated in Fig.[6.62]. The nondimensional frequency of shedding (or lift coefficient fluctuations), the Strouhal number, can be determined from

$$St = \frac{f\,h}{U_o}$$

where f is frequency of flow, h is the height of the airfoil with its incidence and U_o is the free stream velocity and therefore the Strouhal numbers (St) for $\alpha = 12^\circ$ and 24° are **0.42** and **0.35** correspondingly. Fig.[6.63] shows the lift and drag coefficient (C_L, C_D) variations with respect to nondimensional time given from Sampath (1977). Additionally, the pressure distributions calculated by Sampath (1977) on the airfoil surface for $\alpha = 0^\circ$ and 3° are shown in Fig.[6.65,66]. The corresponding variations of the study herein is shown in Fig.[6.64] and Fig.[6.67,68].

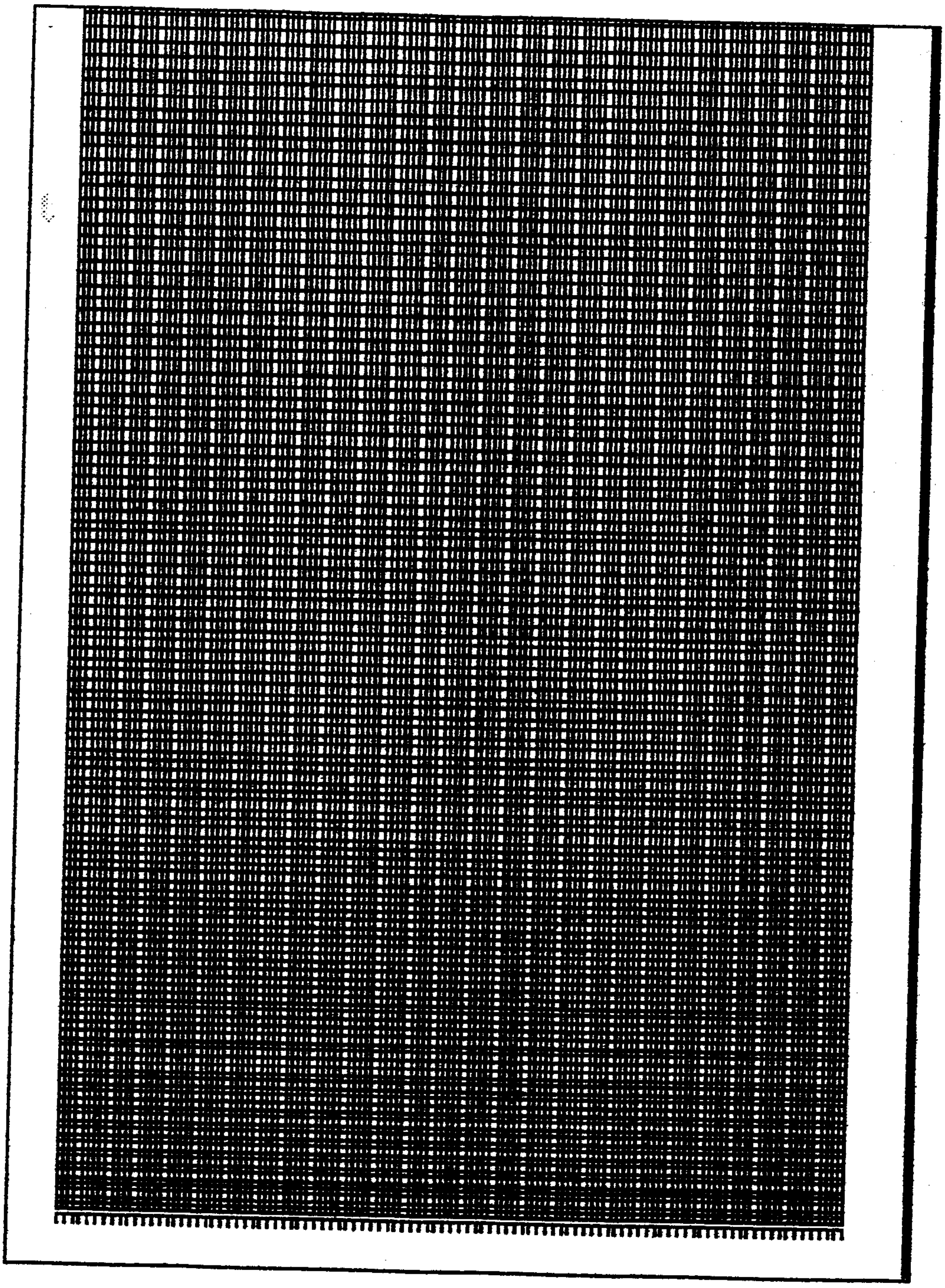

Fig.6.35. Grid structure in transformation (computation) plane.

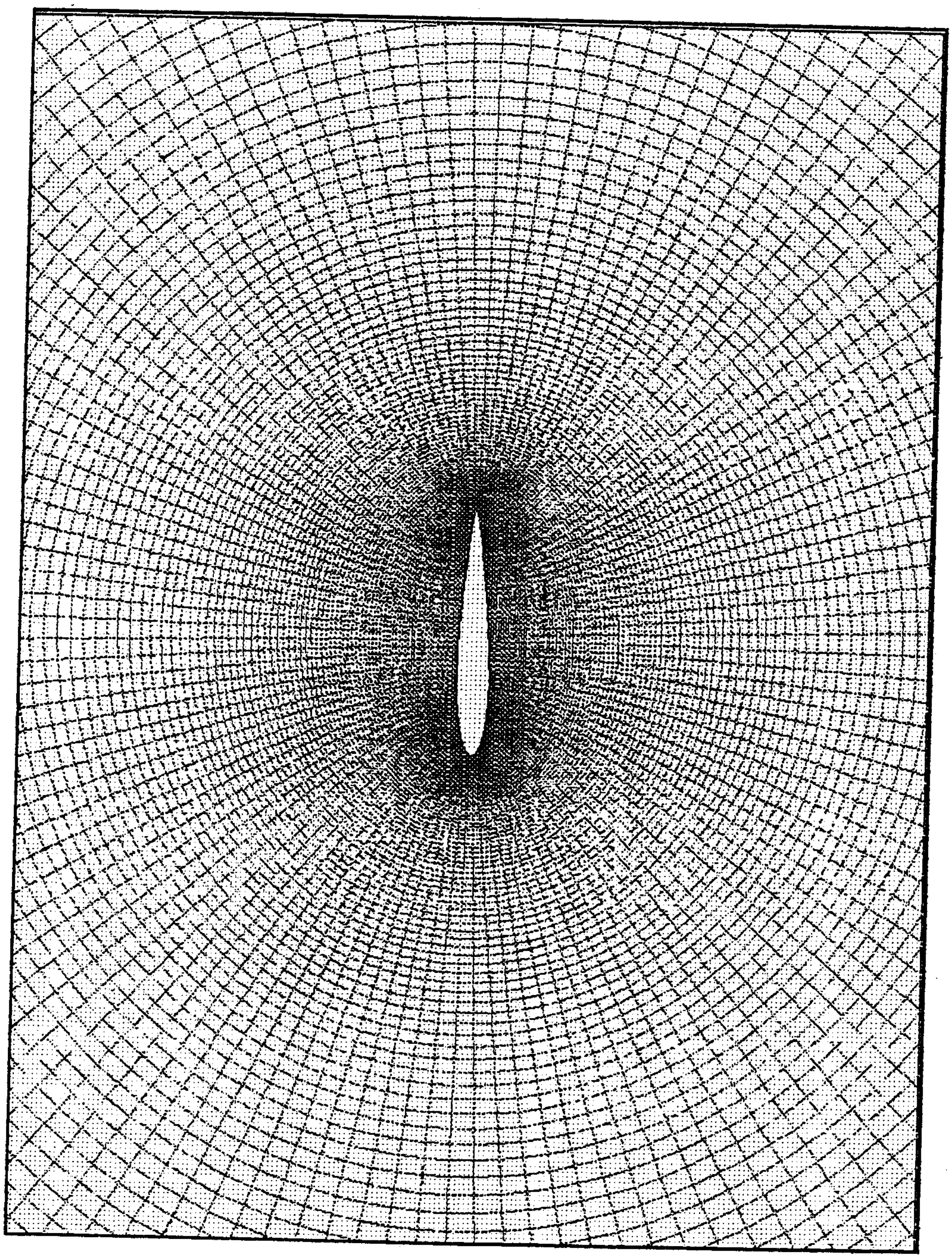

Fig.6.36. Grid structure in physical plane.

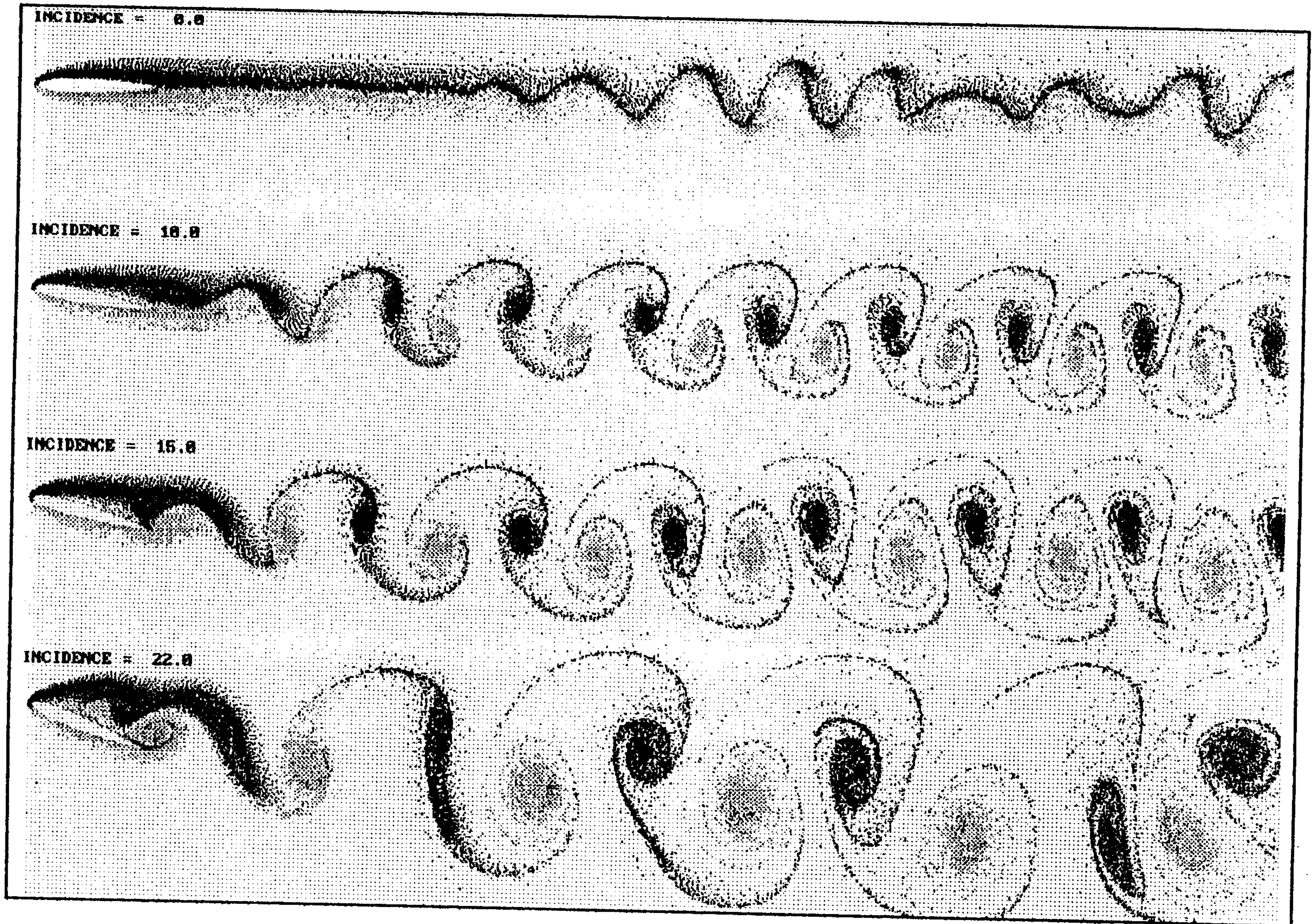

Fig.6.37. Discrete vortex distributions for α=*0., 10., 15., 22.*

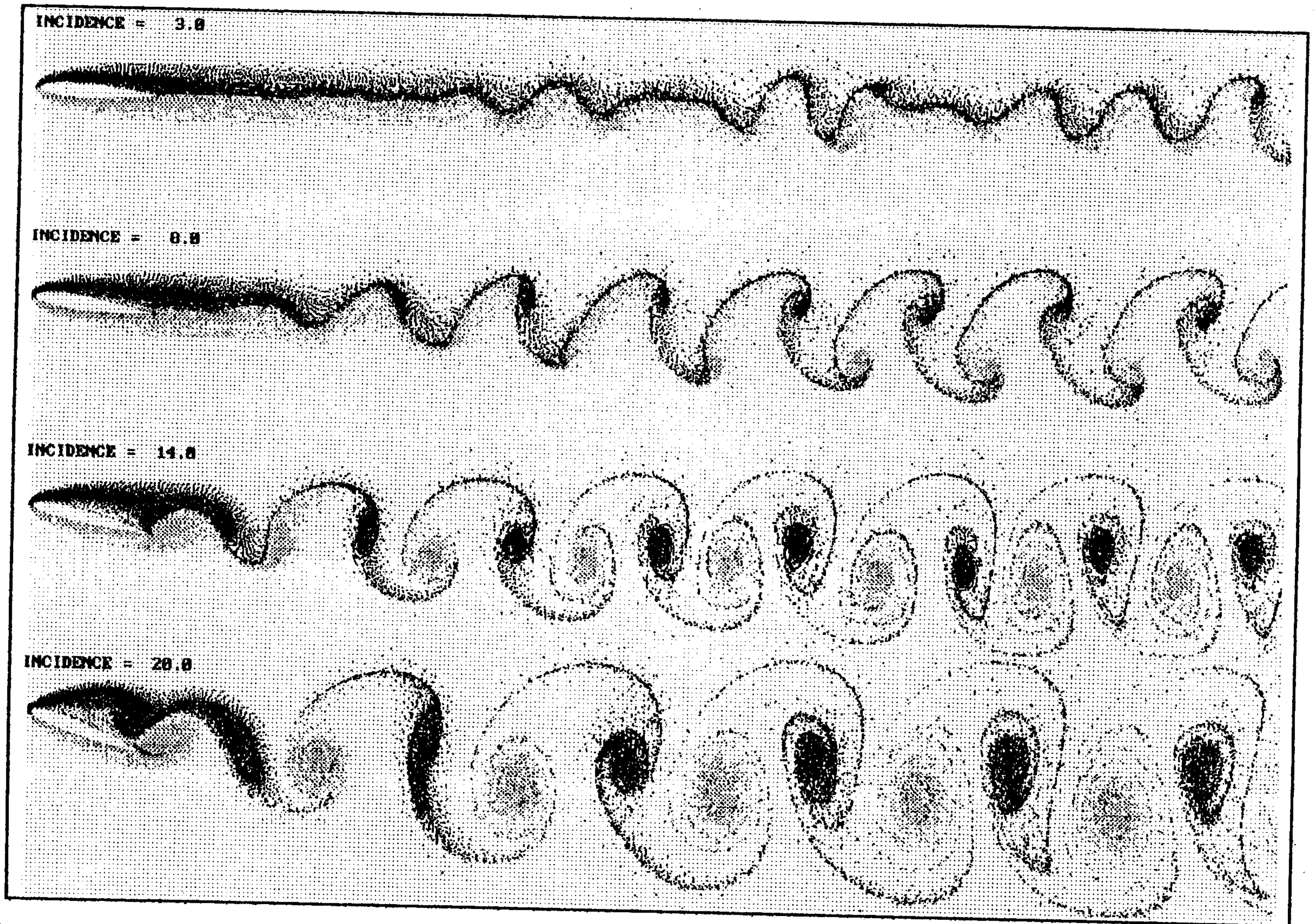

Fig.6.38. Discrete vortex distributions for α=*3., 8., 14., 20.*

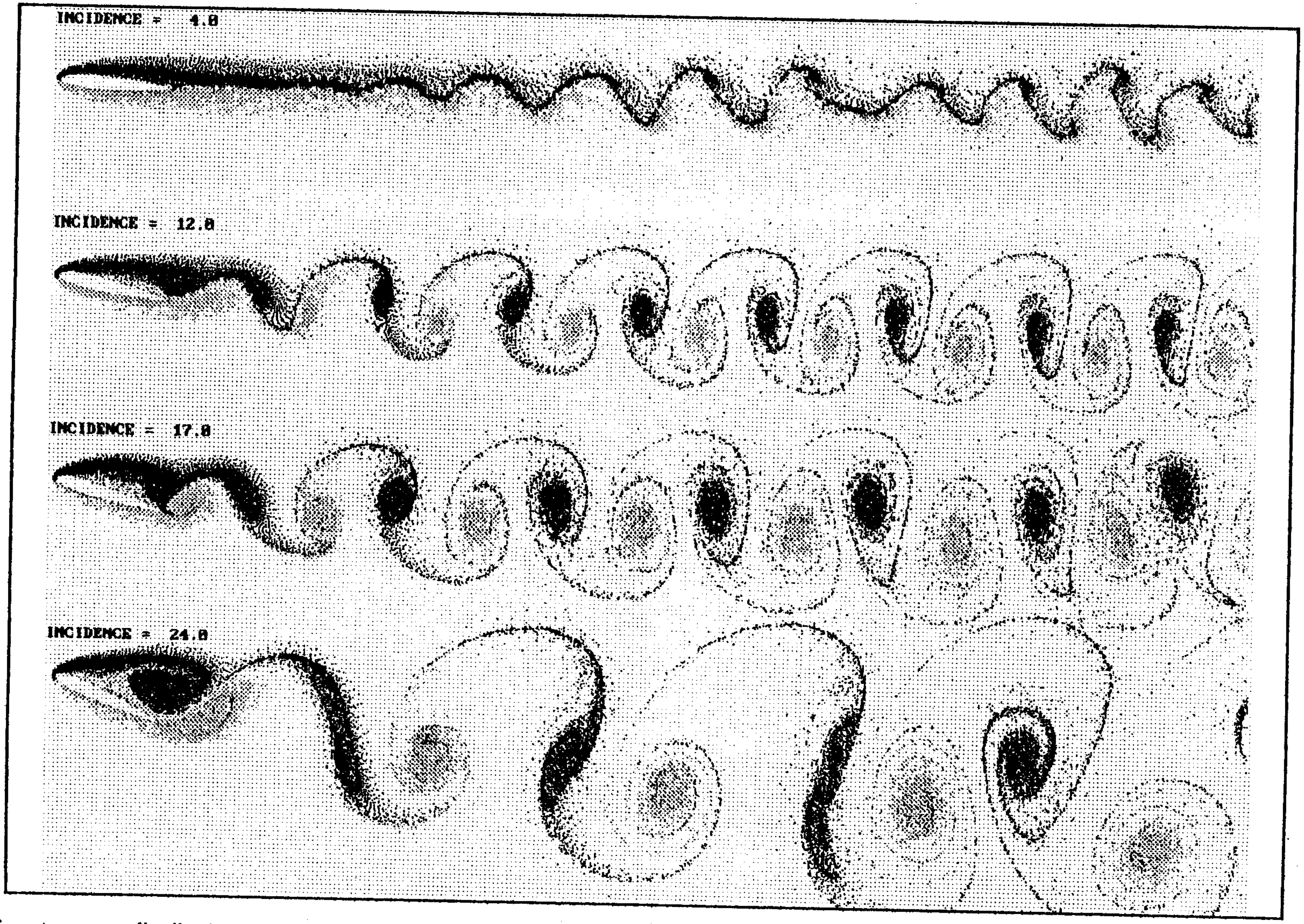

Fig.6.39. Discrete vortex distributions for α=*4., 12., 17., 24.*

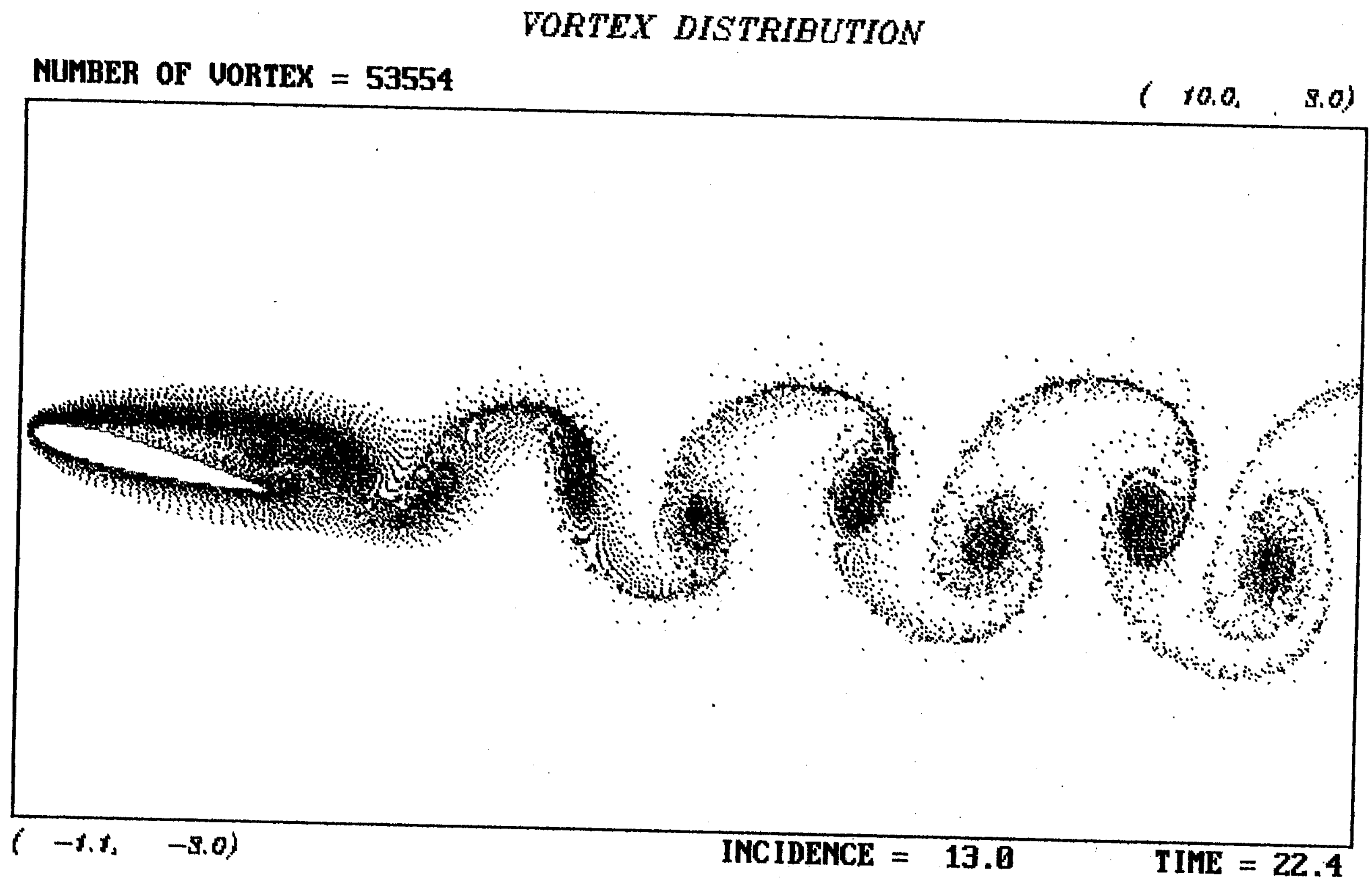

Fig.6.40. Discrete vortex distributions for α=*13.*

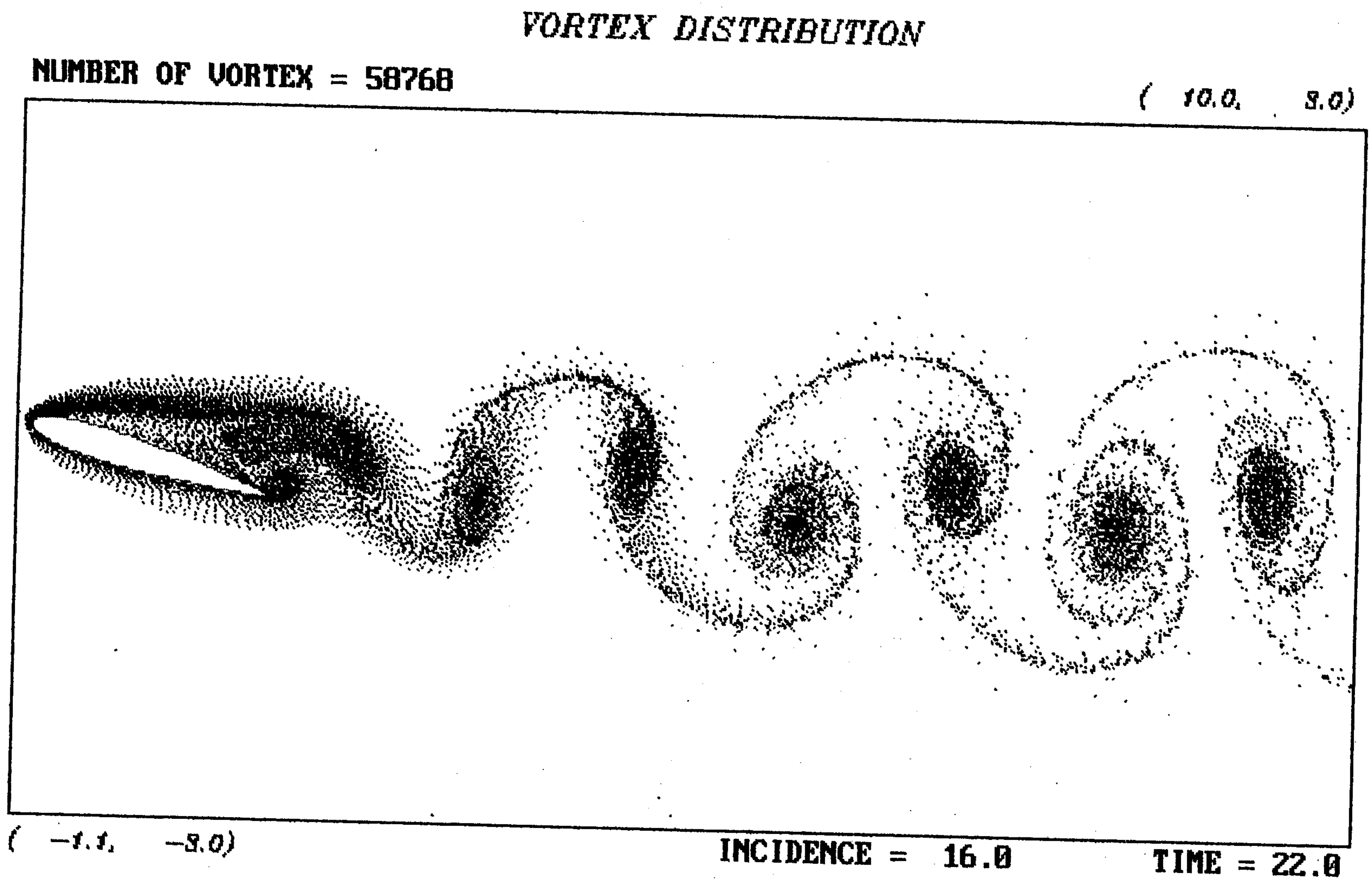

Fig.6.41. Discrete vortex distributions for α=*16.*

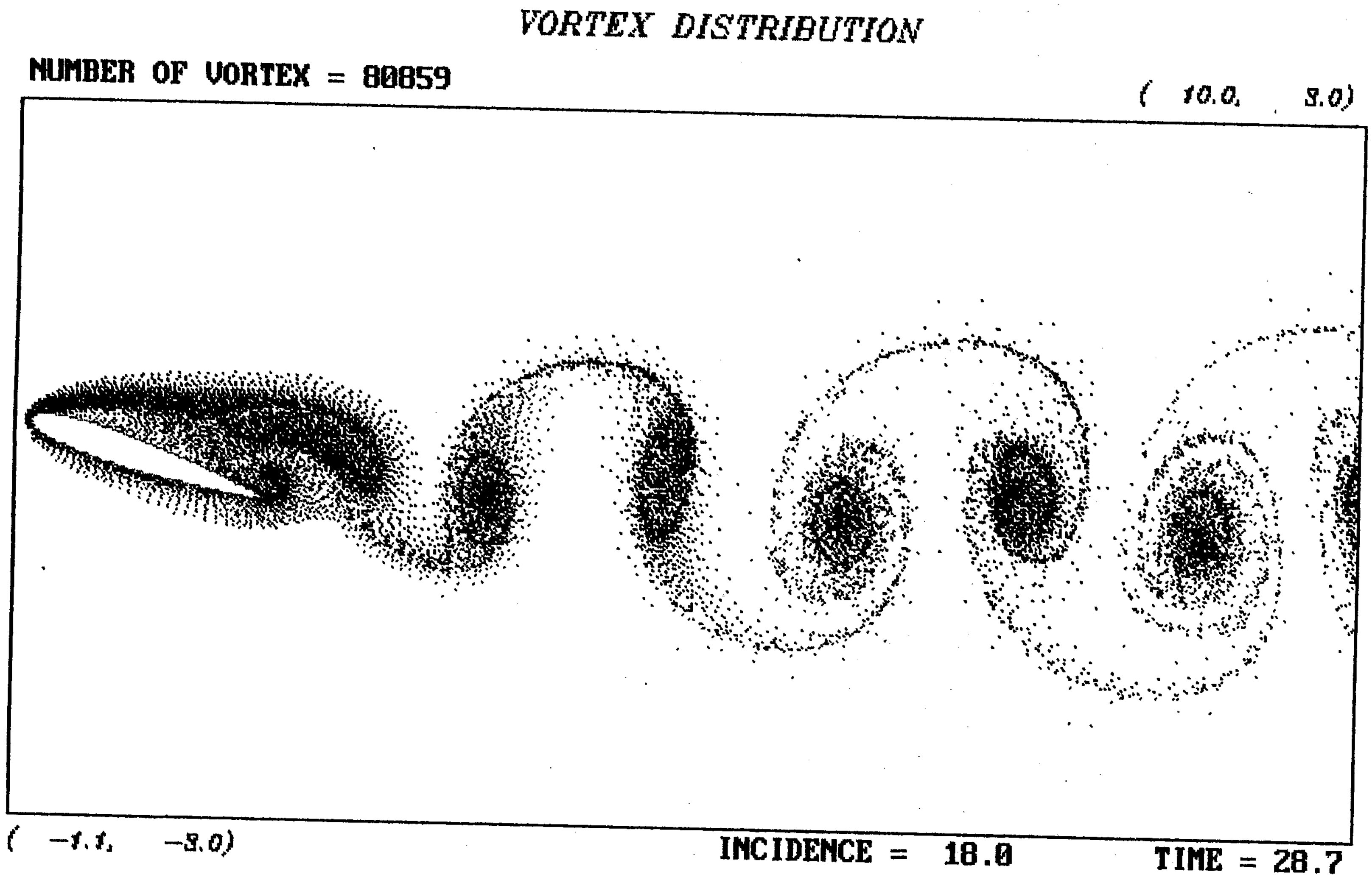

Fig.6.42. Discrete vortex distributions for α=*18.*

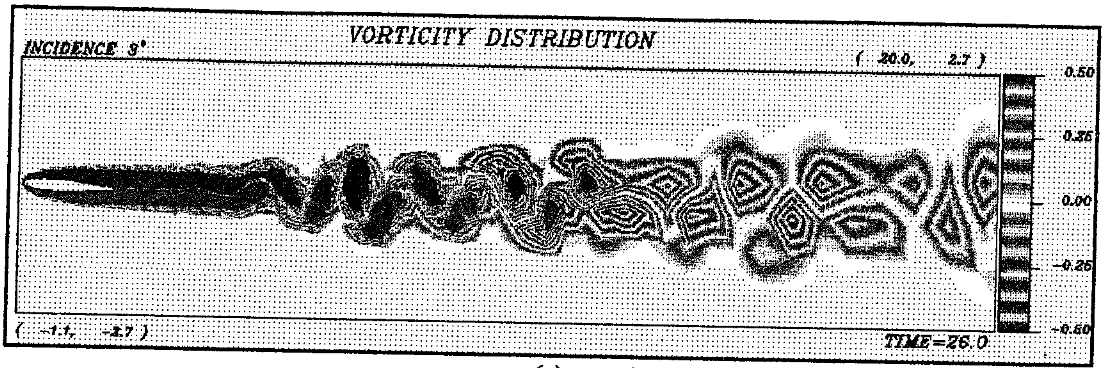

(a)

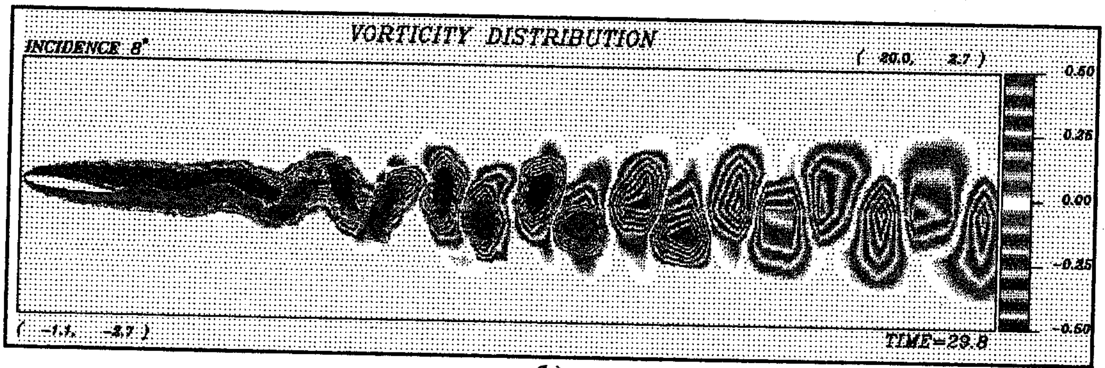

(b)

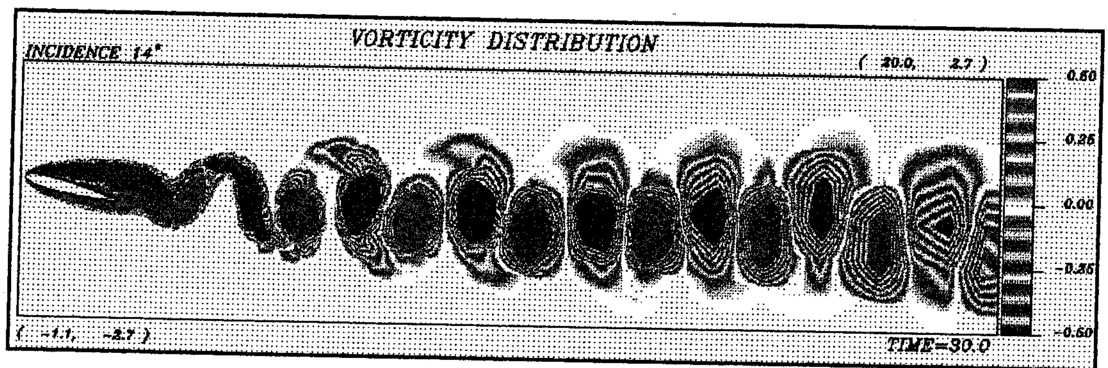

(c)

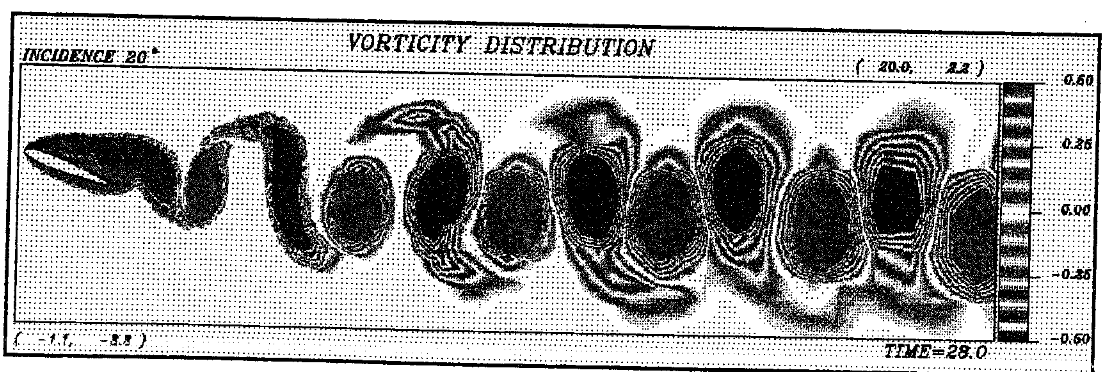

(d)

Fig. 6.43. Colour coded vorticity distributions for α=3°, 8°, 14°, 20°

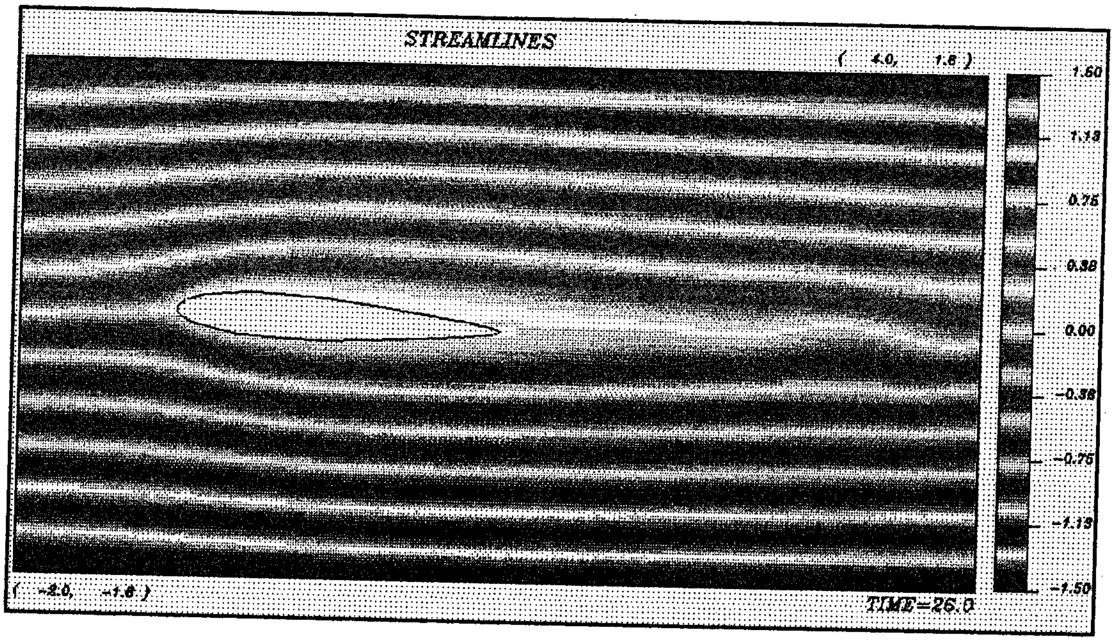

(a)

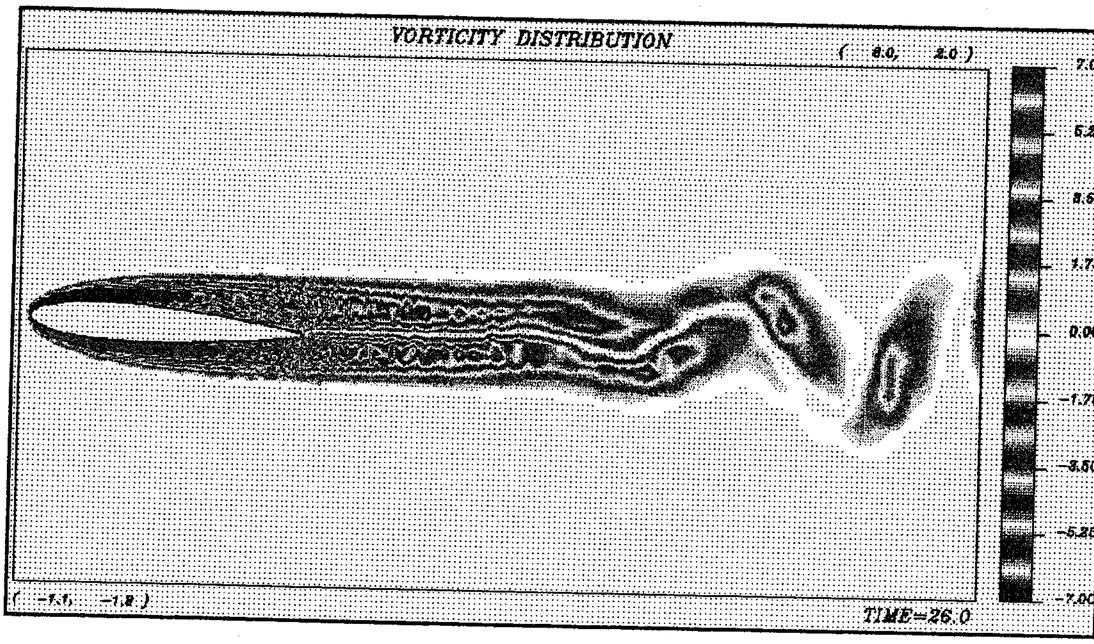

(b)

Fig. 6.44. For $\alpha=3°$, colour coded streamlines (a); and vorticity distributions (b).

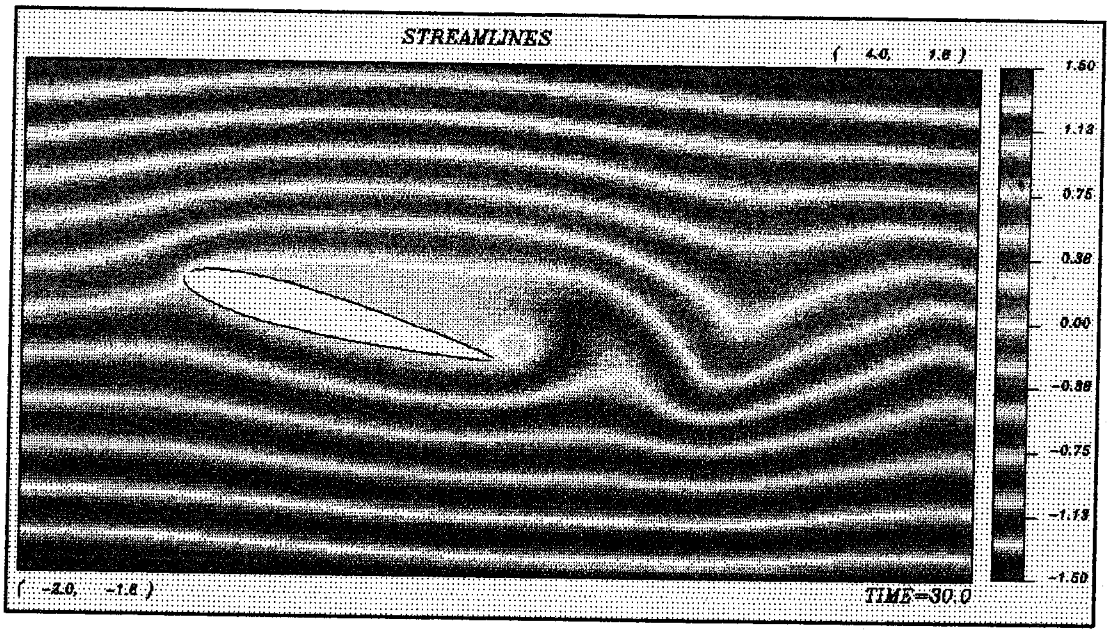

(a)

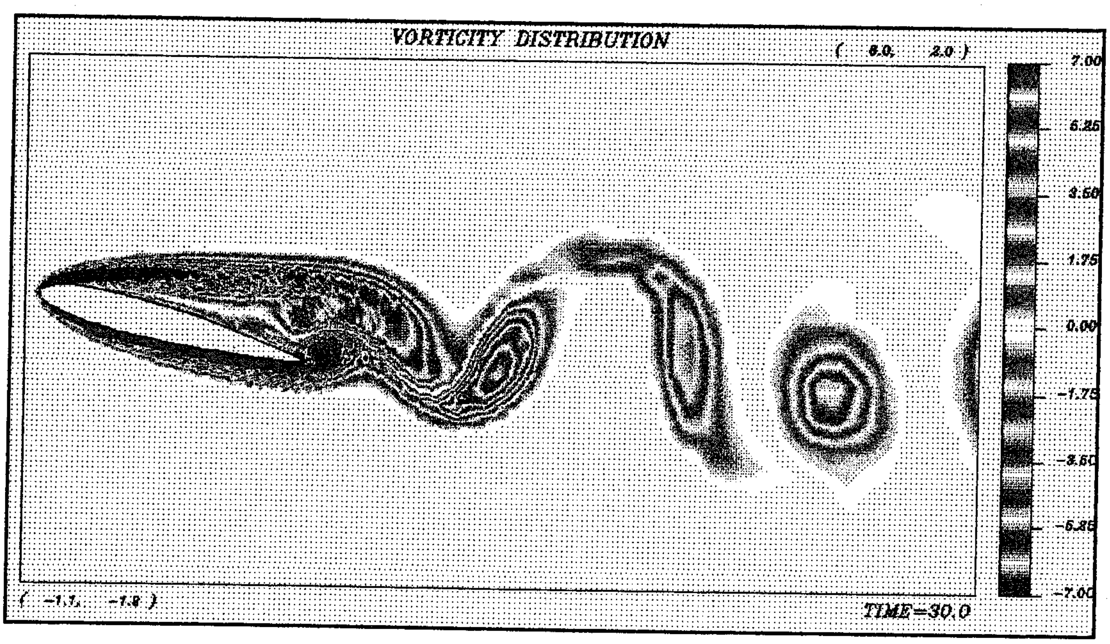

(b)

Fig. 6.45. For α=*14°*, colour coded streamlines (a); and vorticity distributions (b).

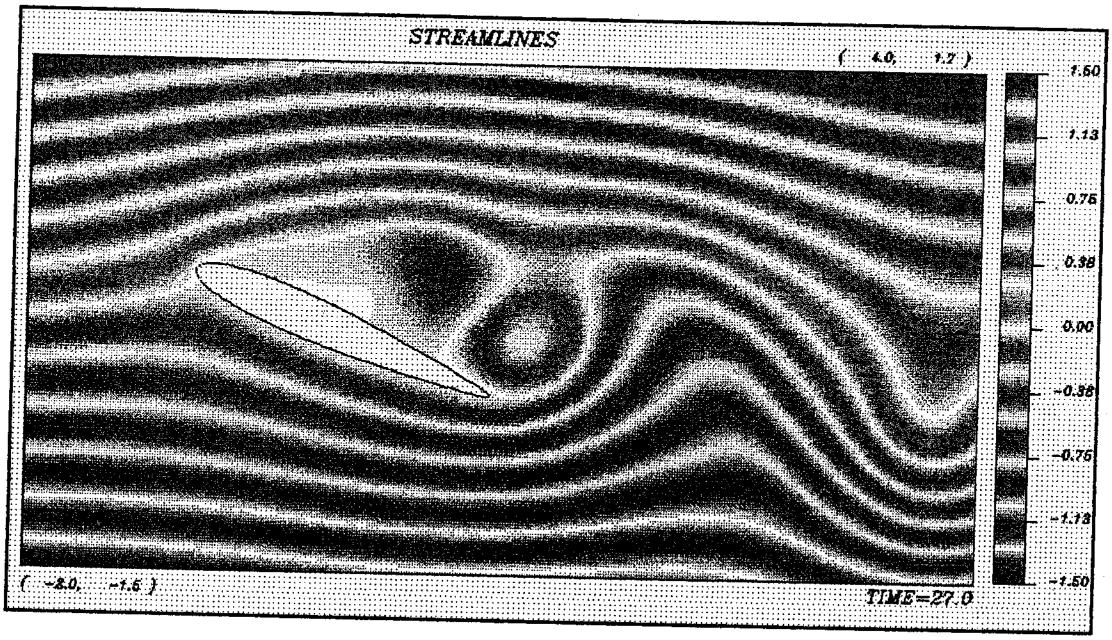

(a)

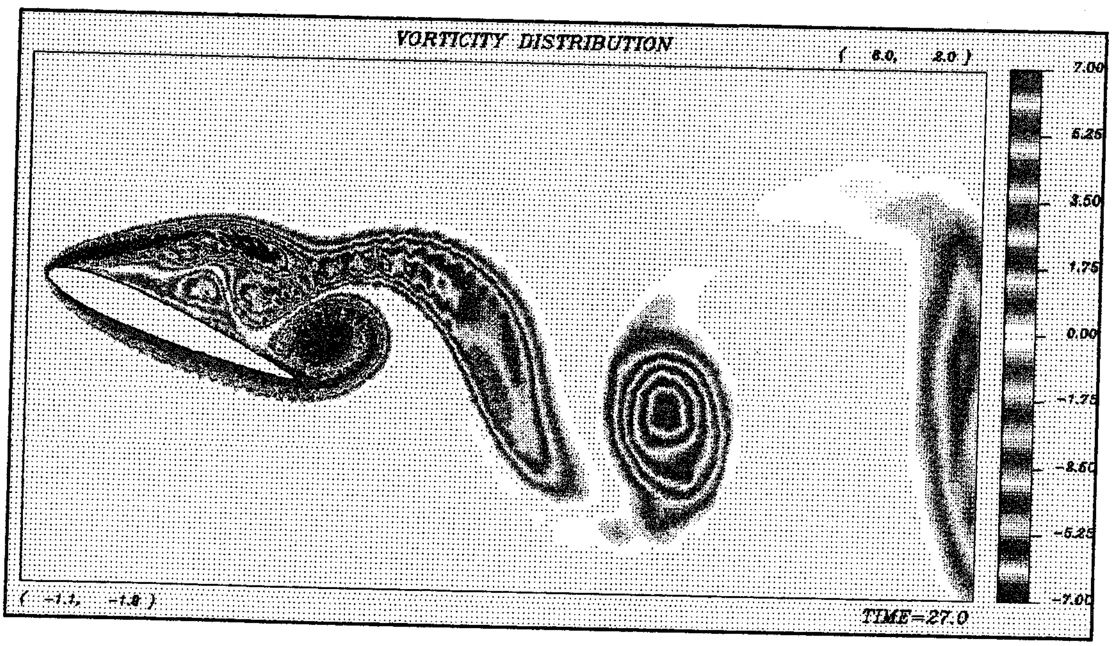

(b)

Fig. 6.46. For α=*22°*, colour coded streamlines (a); and vorticity distributions (b).

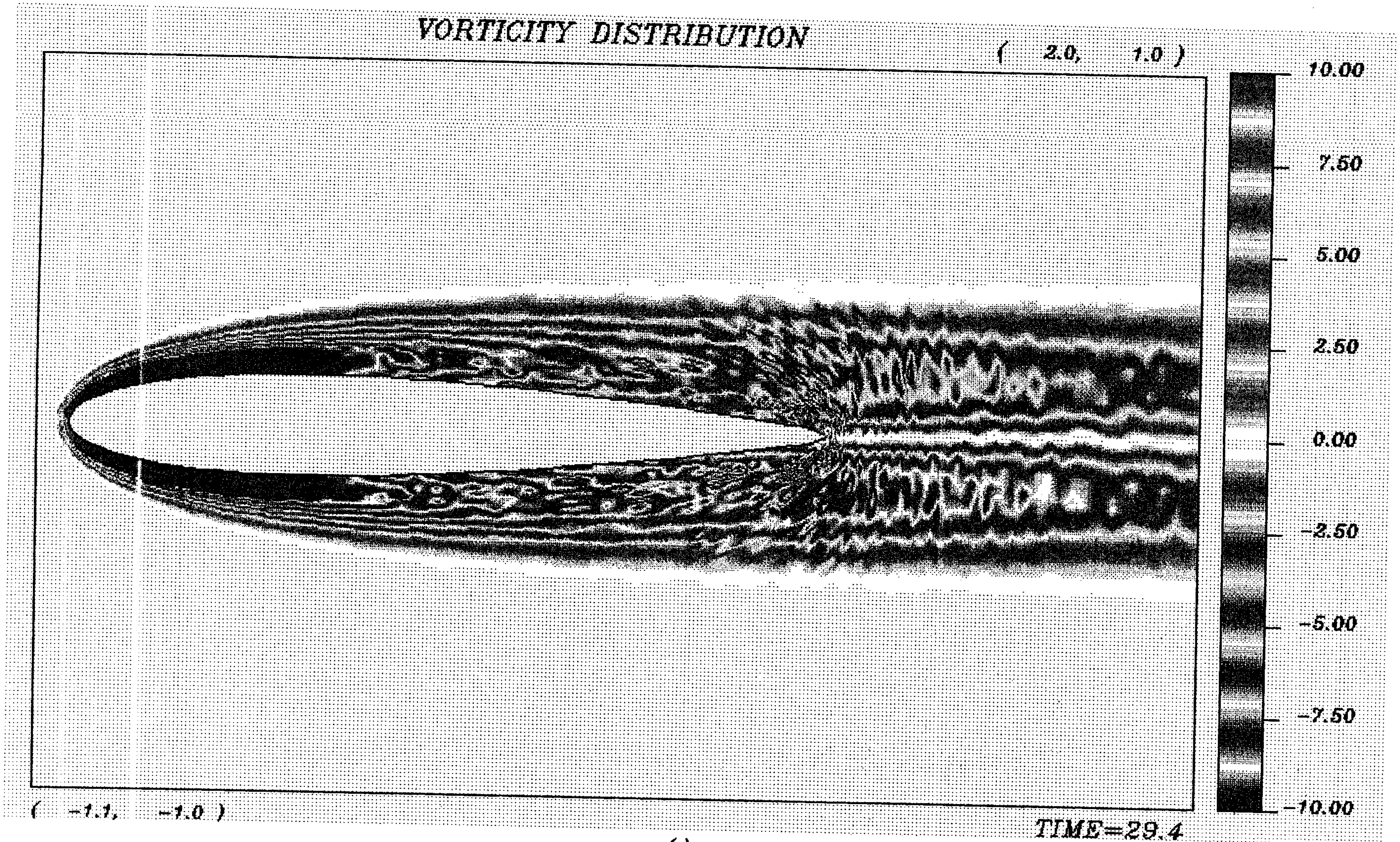

(a)

(For legend see next page)

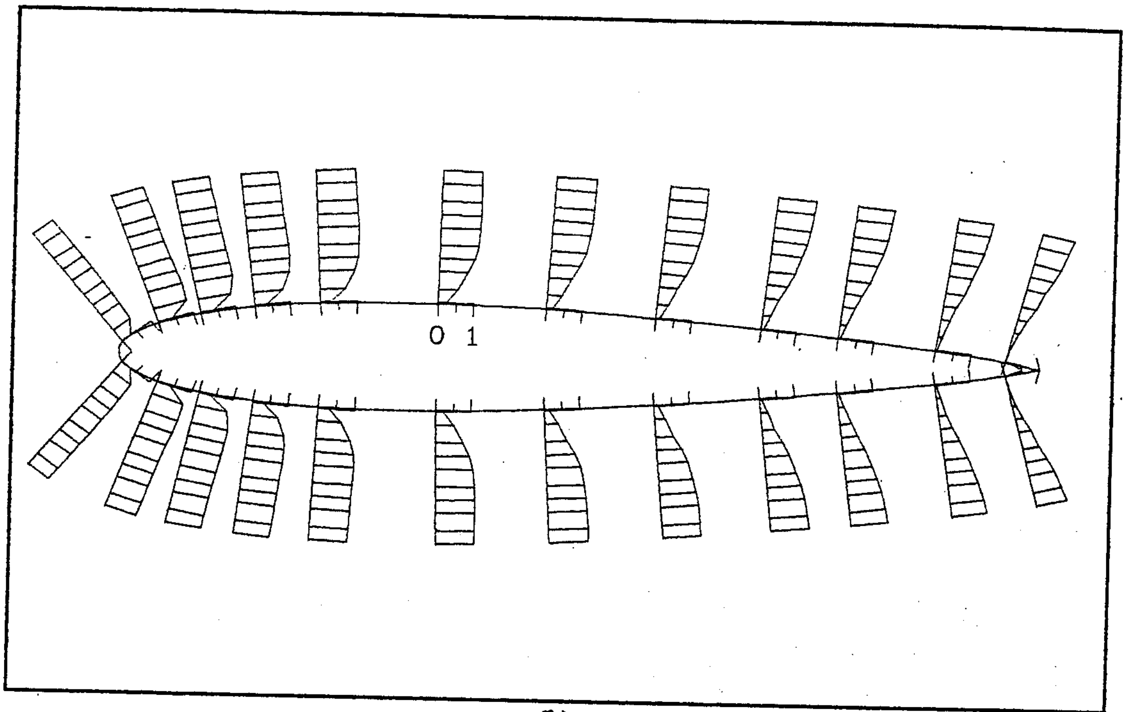

(b)

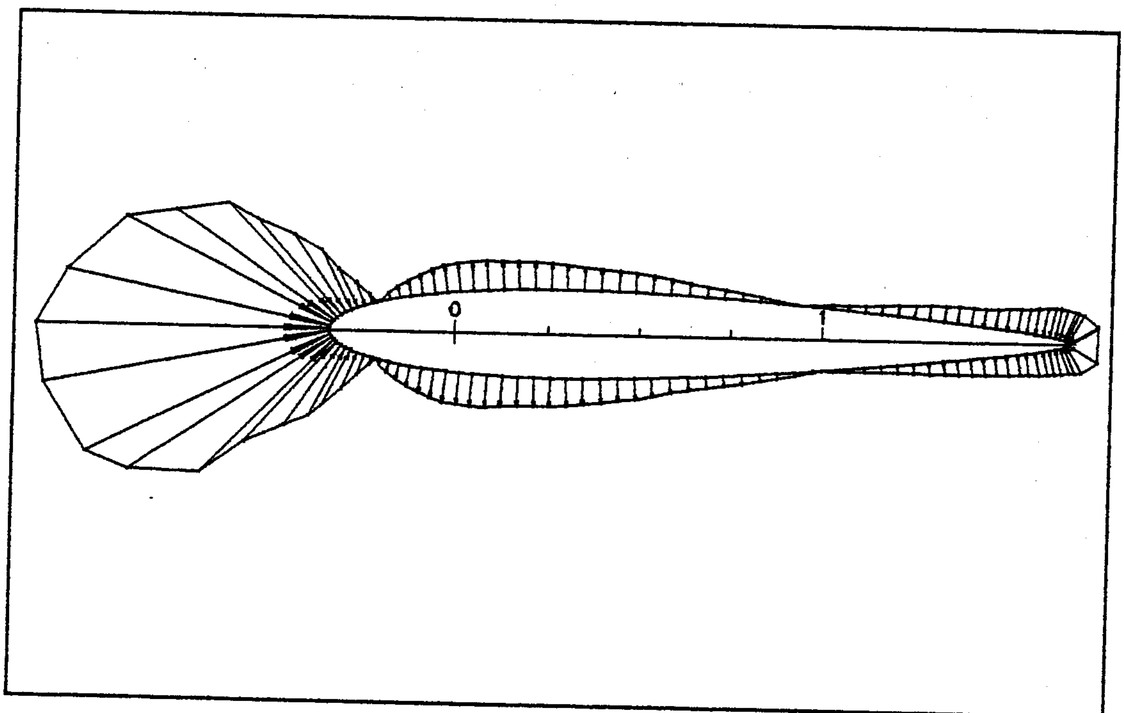

(c)

Fig.6.47. For $\alpha=0^{\circ}$, colour coded vorticity distributions (a); velocity profiles on the body surface (b); and pressure distribution on the body surface (c).

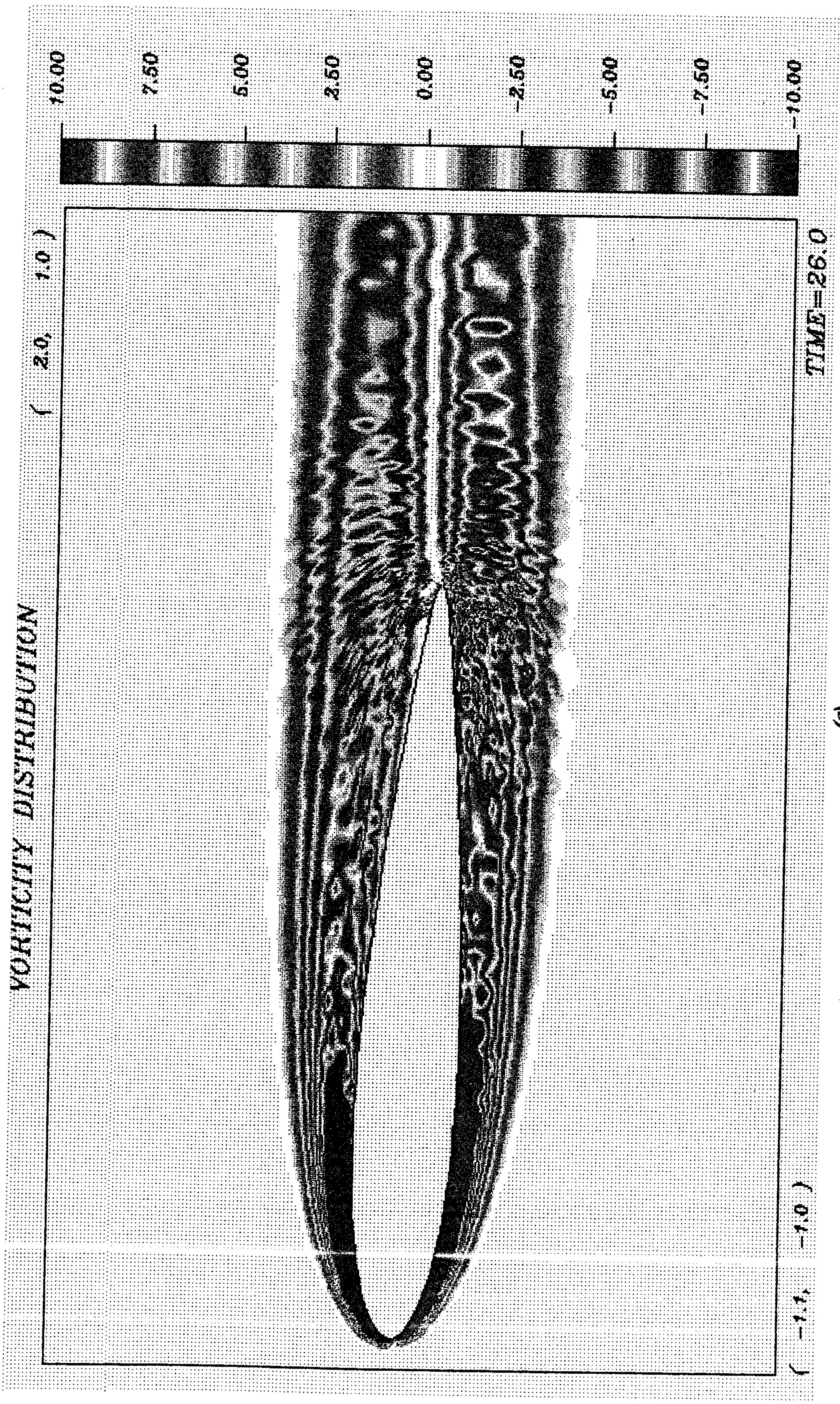

(a)

(For legend see next page)

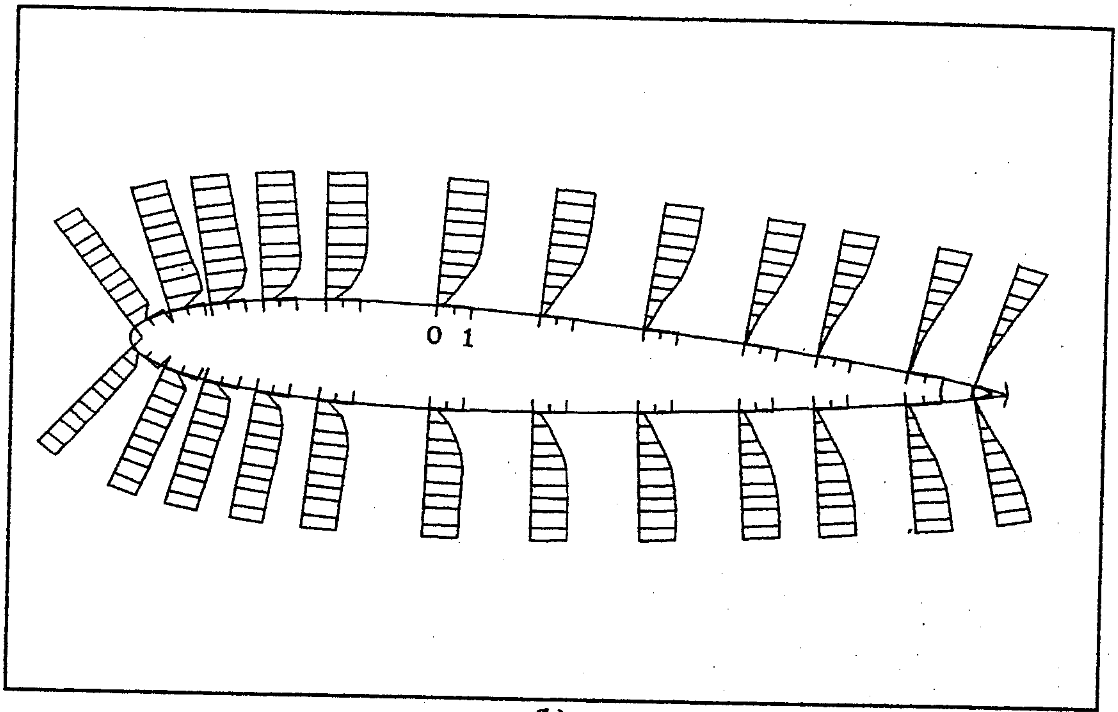

(b)

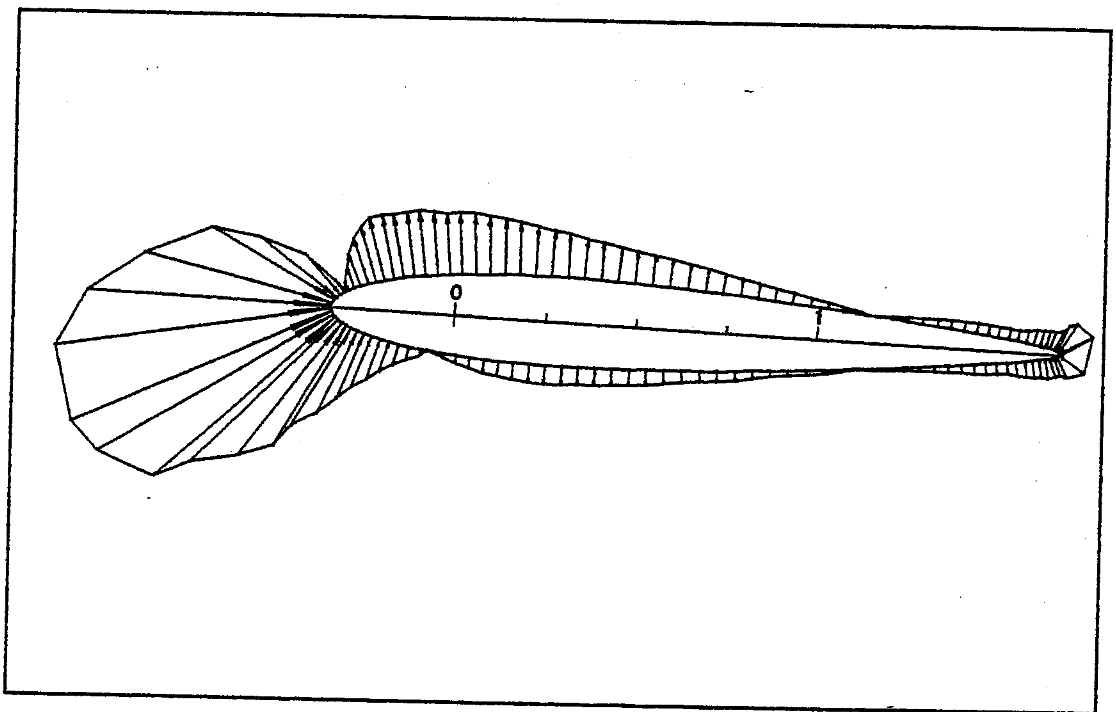

(c)

Fig.6.48. For $\alpha=3^{\circ}$, colour coded vorticity distributions (a); velocity profiles on the body surface (b); and pressure distribution on the body surface (c).

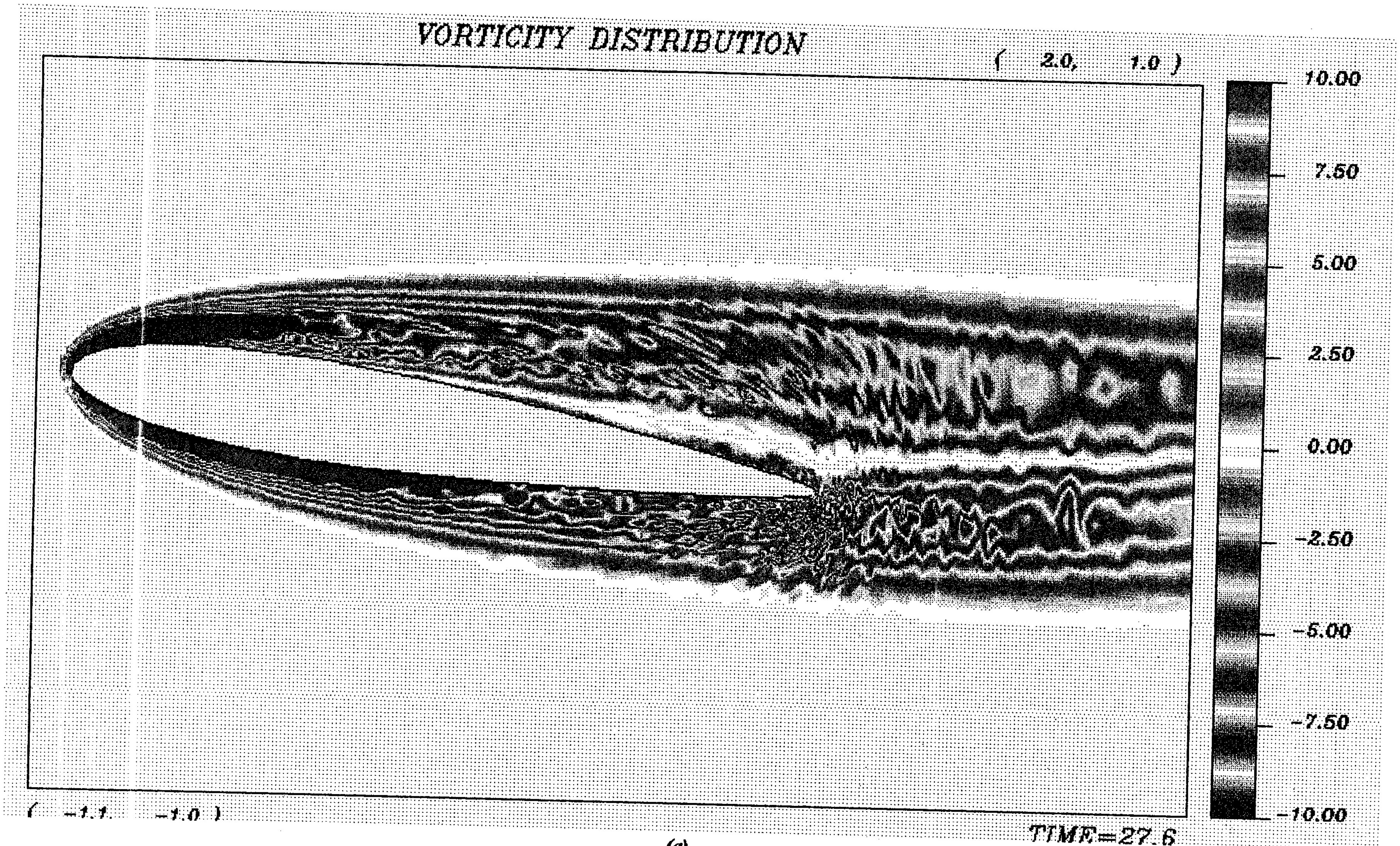

(a)

(For legend see next page)

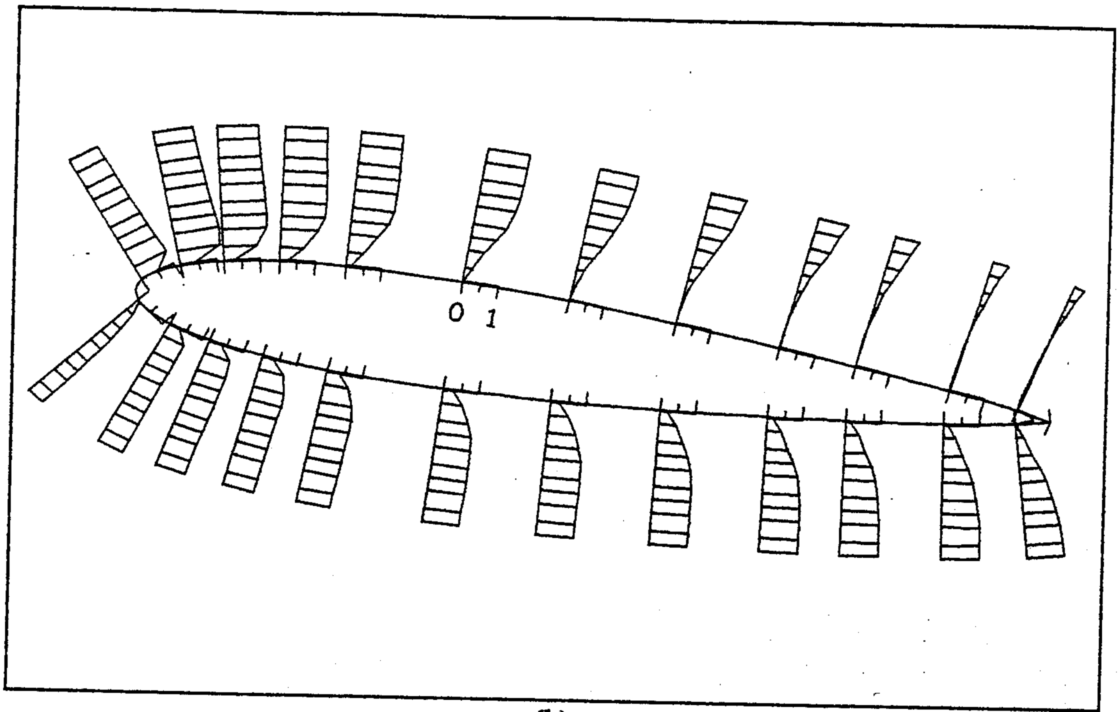

(b)

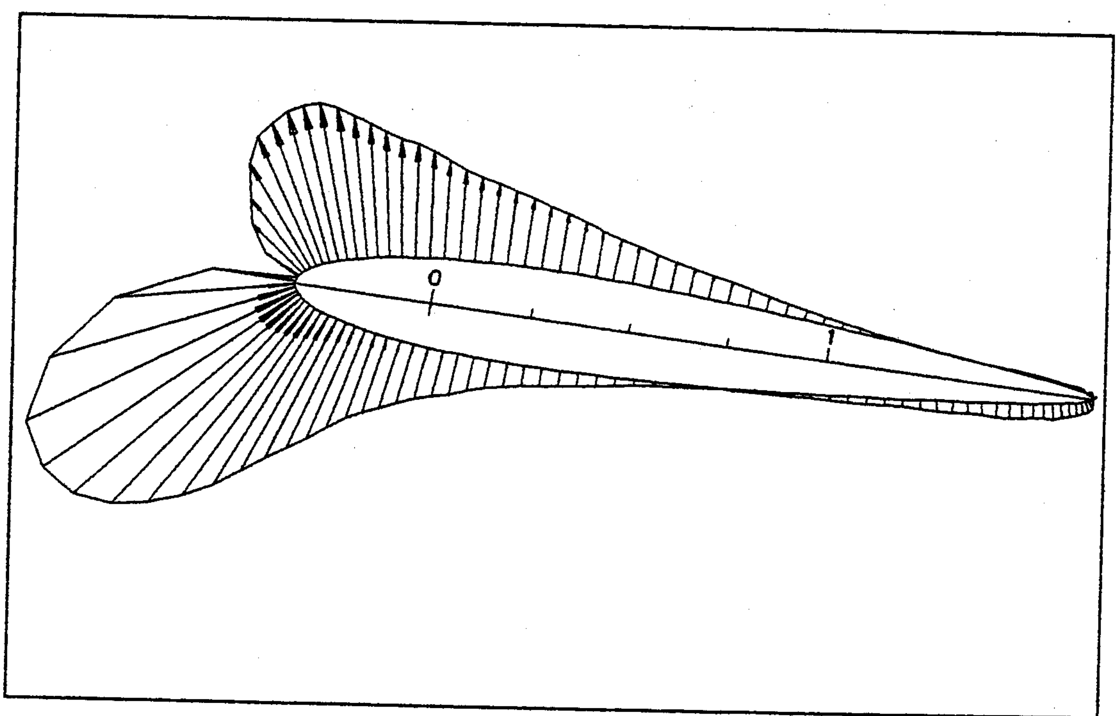

(c)

Fig.6.49. For $\alpha = 8^\circ$, colour coded vorticity distributions (a); velocity profiles on the body surface (b); and pressure distribution on the body surface (c).

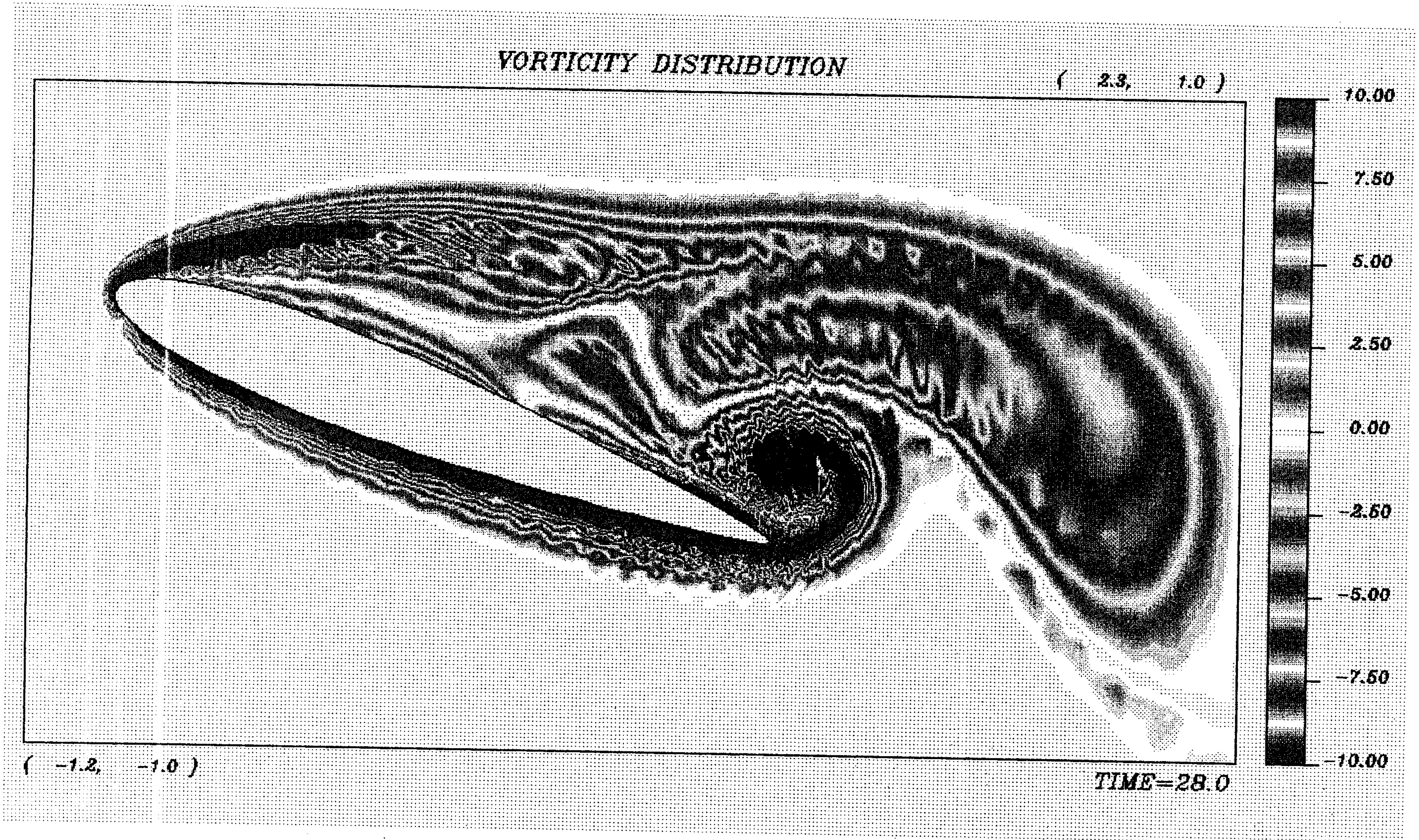

(a)

(For legend see next page)

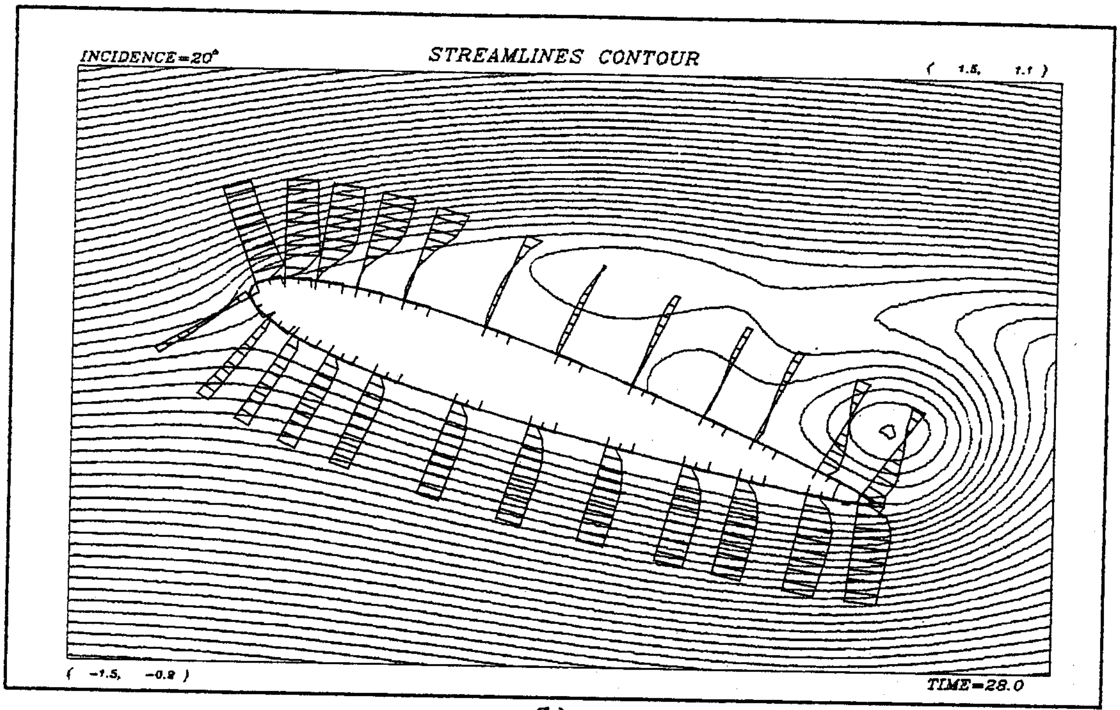

(b)

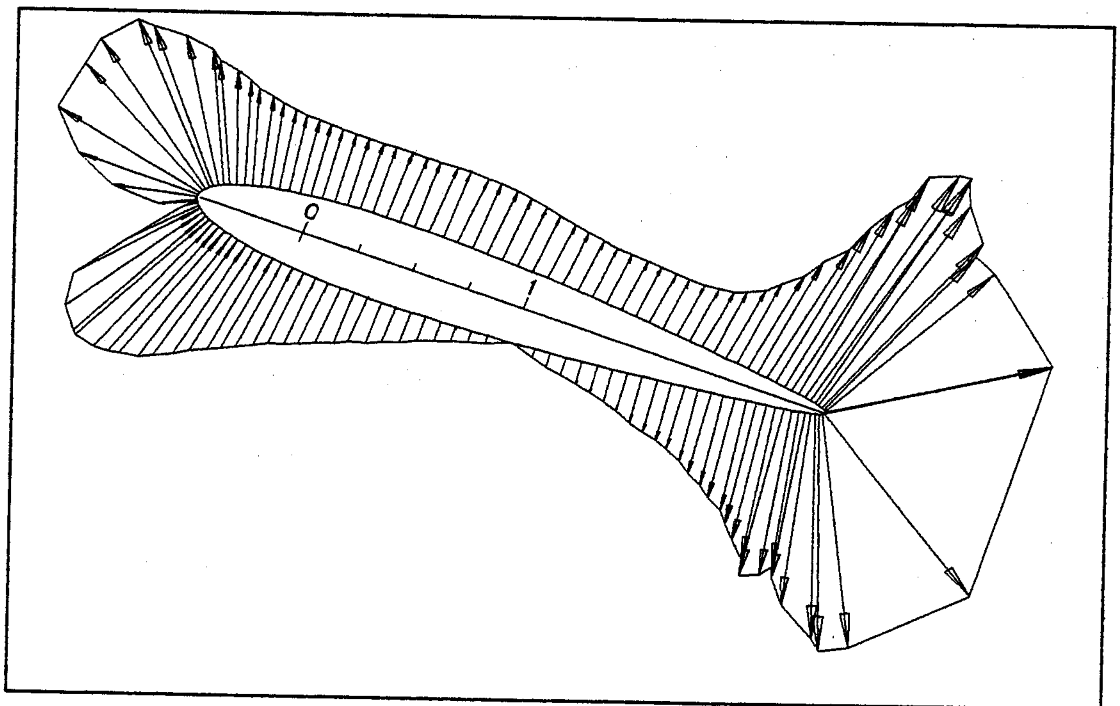

(c)

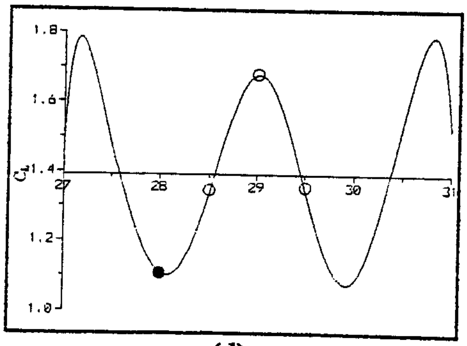

(d)

Fig.6.50. For $\alpha=20^{\circ}$ and $T=28.0$, colour coded vorticity distributions (a); velocity profiles on the body surface and streamlines pattern (b); pressure distribution on the body surface (c); and C_L with respect to nondimensional time (d). Bold circle on the C_L-T diagram indicates $T=28.0$.

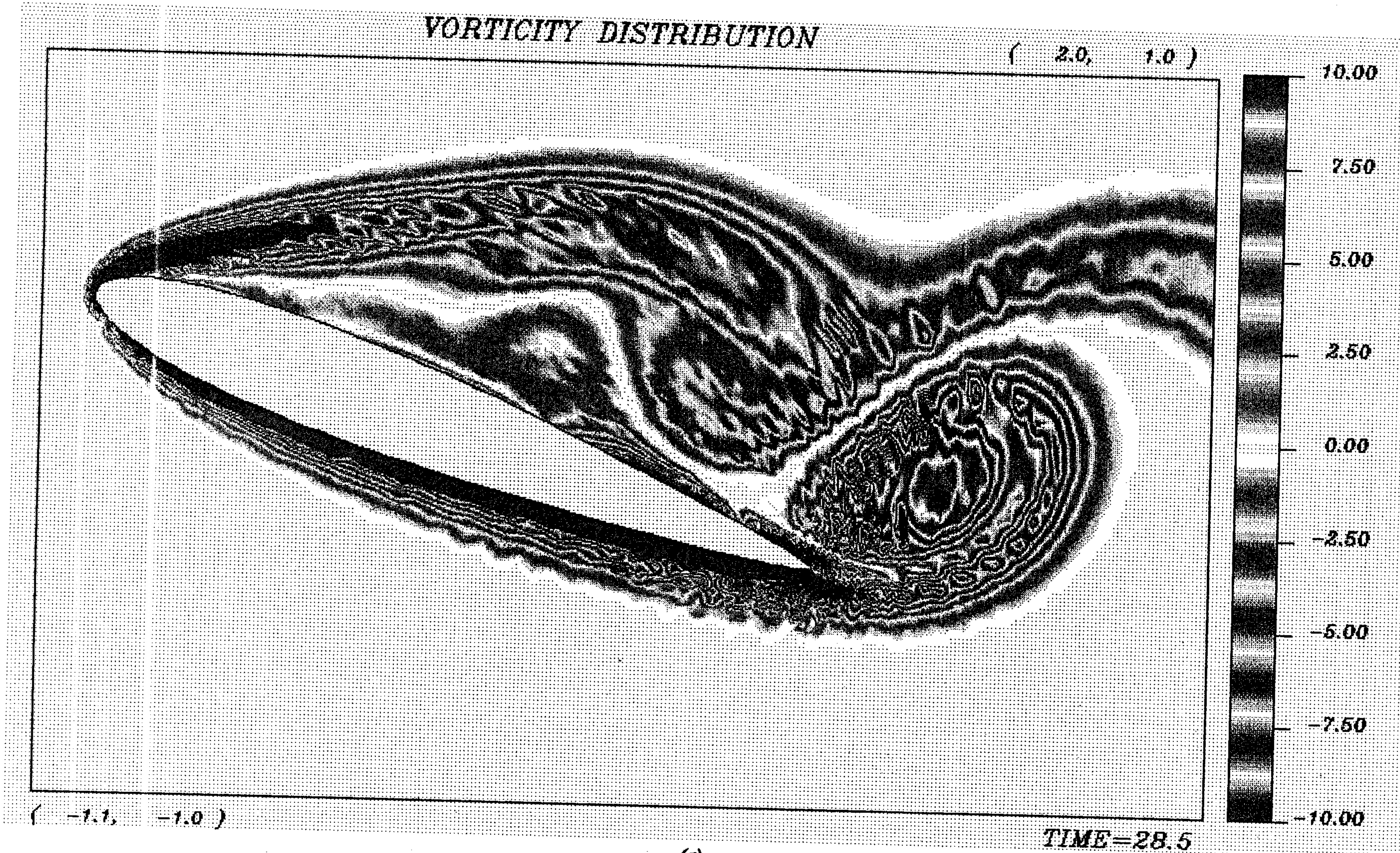

(a)

(For legend see next page)

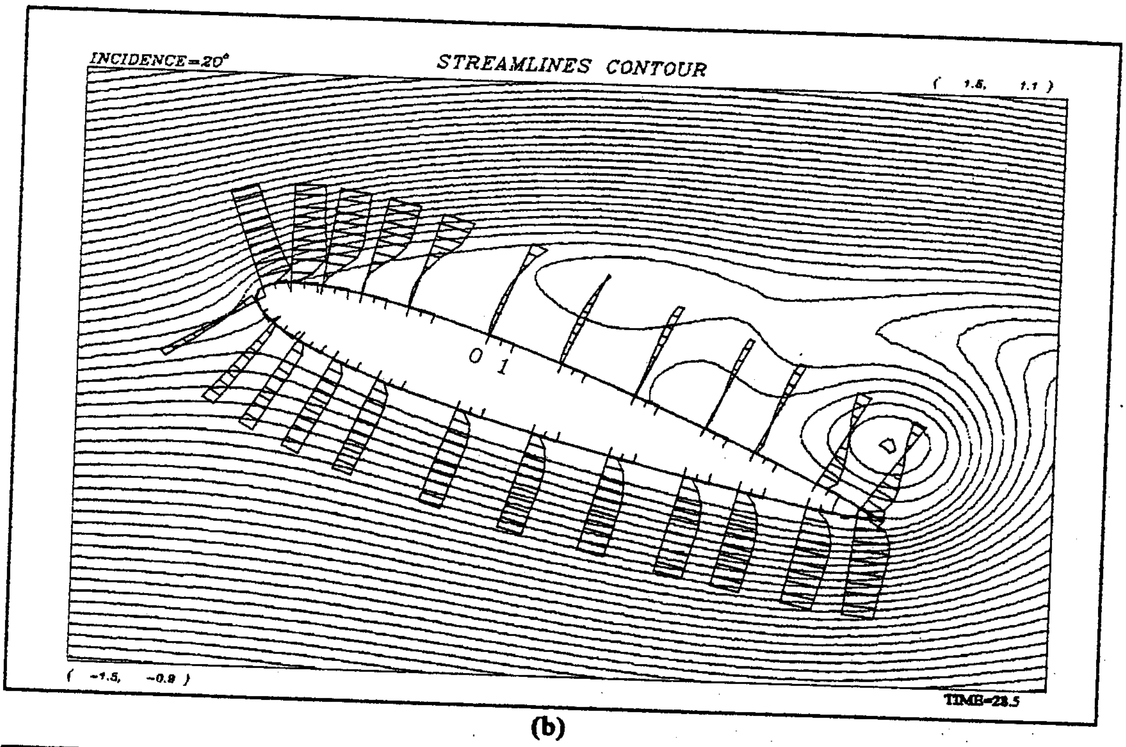

(b)

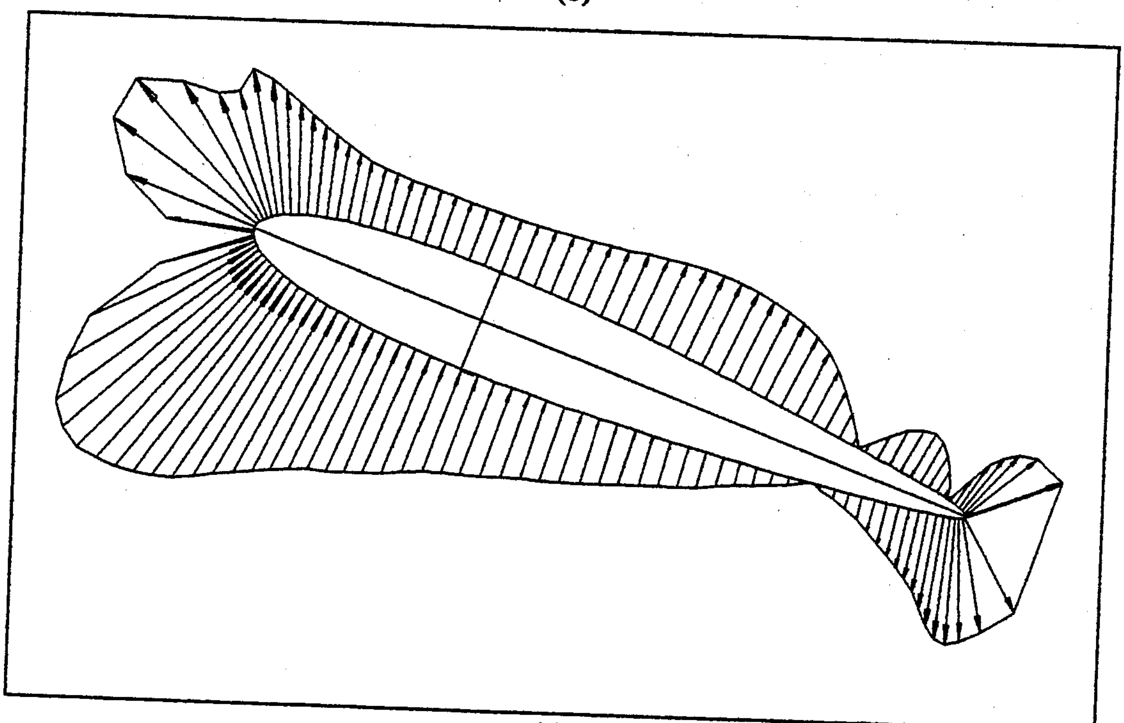

(c)

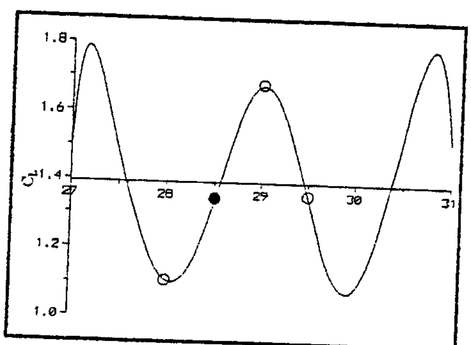

(d)

Fig.6.51. For $\alpha=20^{\circ}$ and $T=28.5$, colour coded vorticity distributions (a); velocity profiles on the body surface and streamlines pattern (b); pressure distribution on the body surface (c); and C_L with respect to nondimensional time (d). Full circle on the C_L-T diagram indicates $T=28.5$.

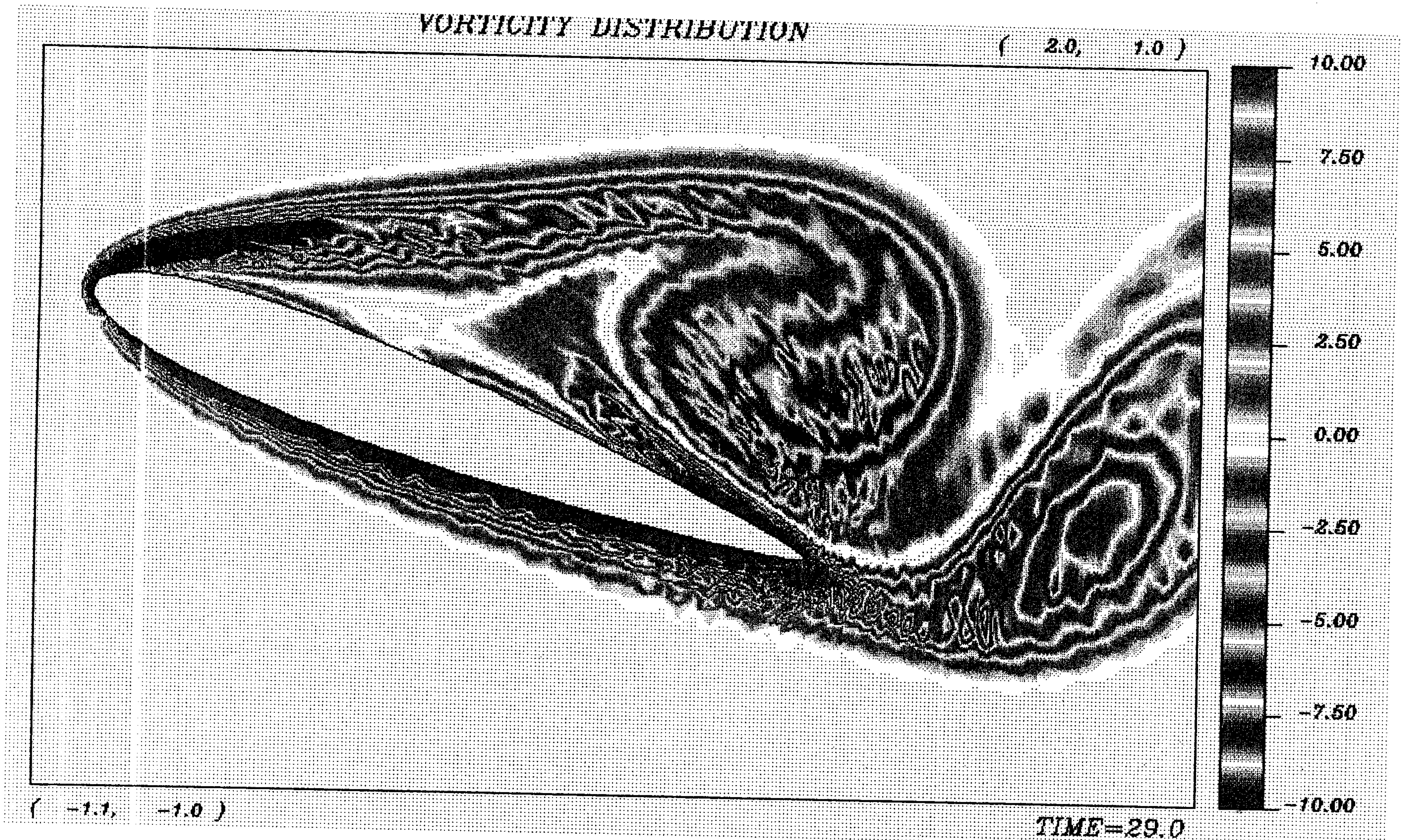

(a)

(For legend see next page)

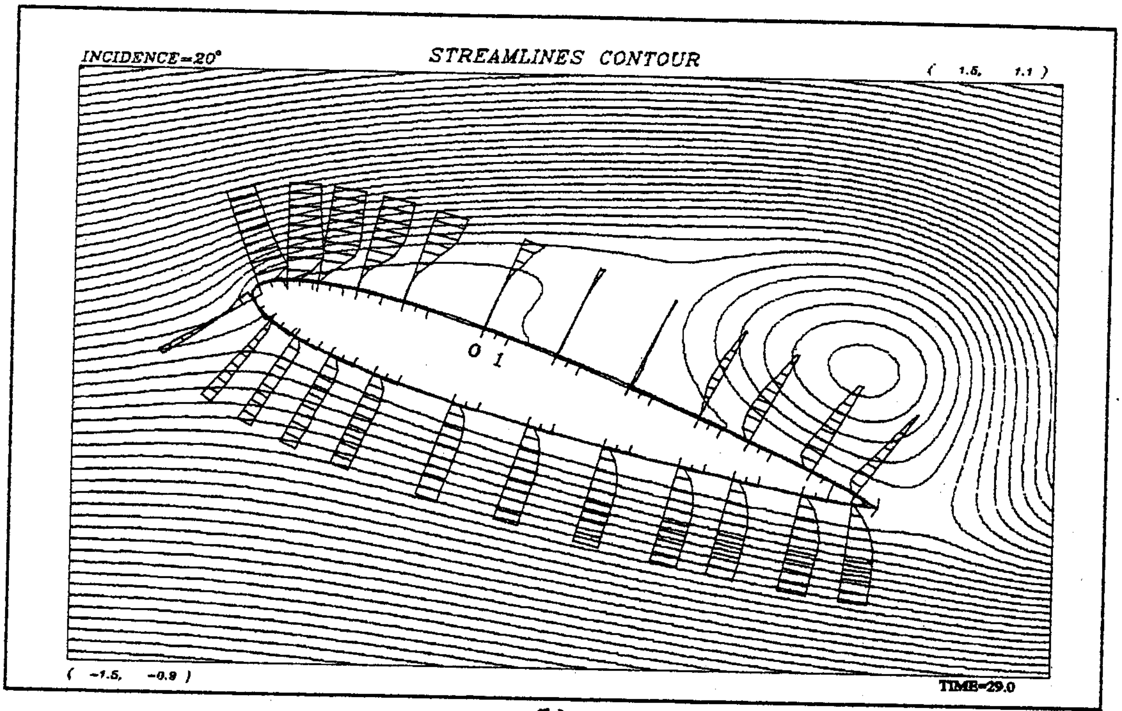

(b)

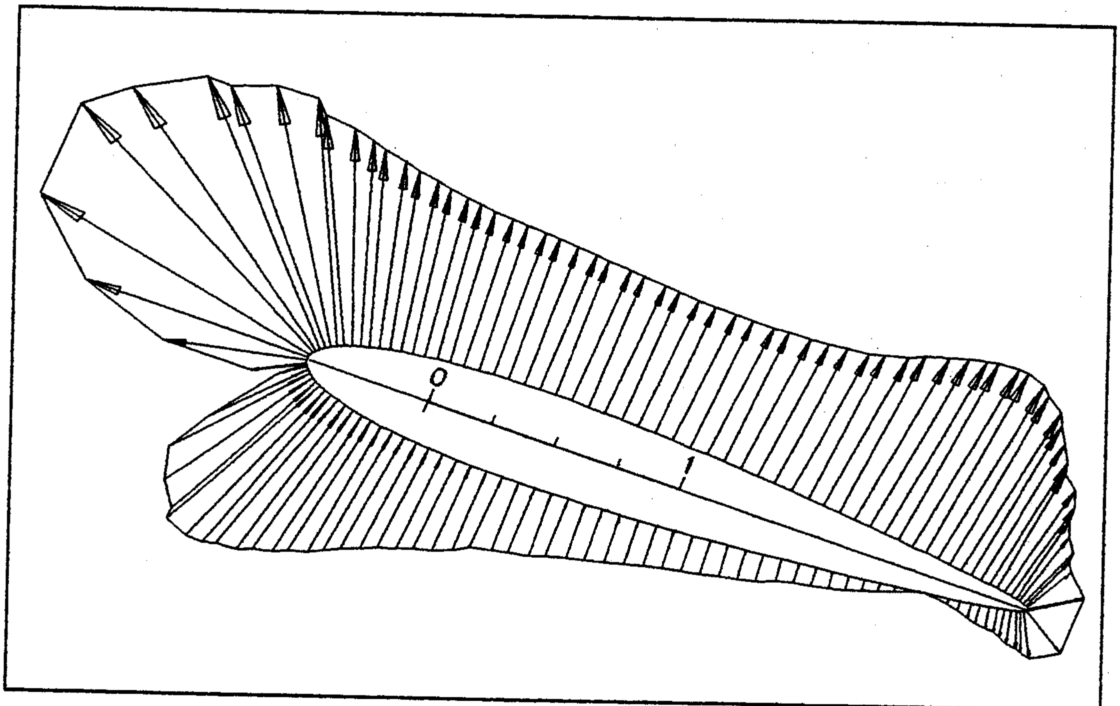

(c)

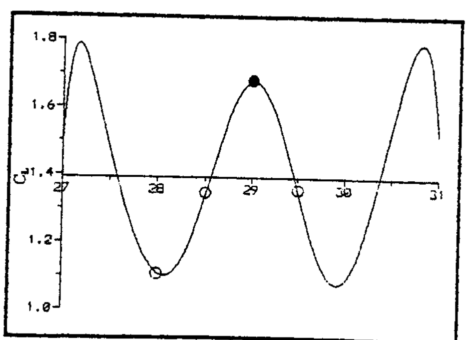

(d)

Fig.6.52. For $\alpha=20^{\circ}$ and $T=29.0$, colour coded vorticity distributions (a); velocity profiles on the body surface and streamlines pattern (b); pressure distribution on the body surface (c); and C_L with respect to nondimensional time (d). Bold circle on the C_L-T diagram indicates $T=29.0$.

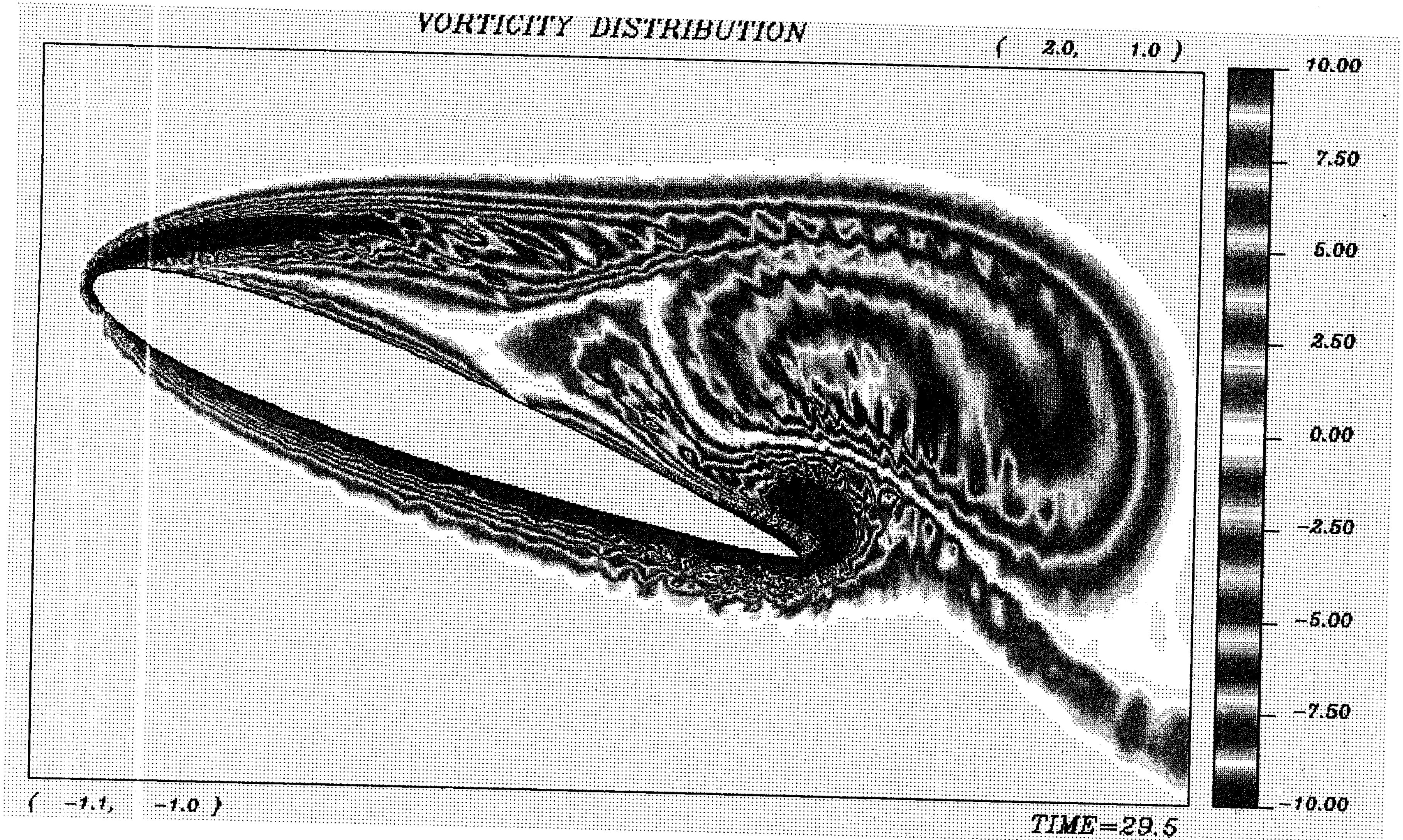

(a)

(For legend see next page)

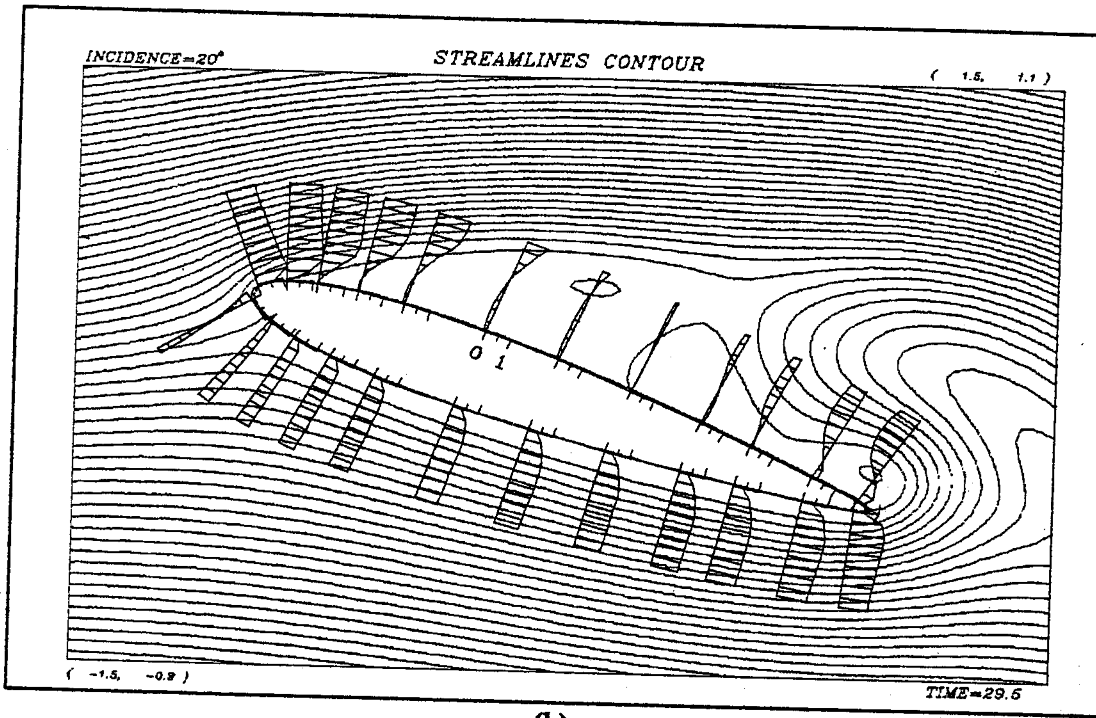

(b)

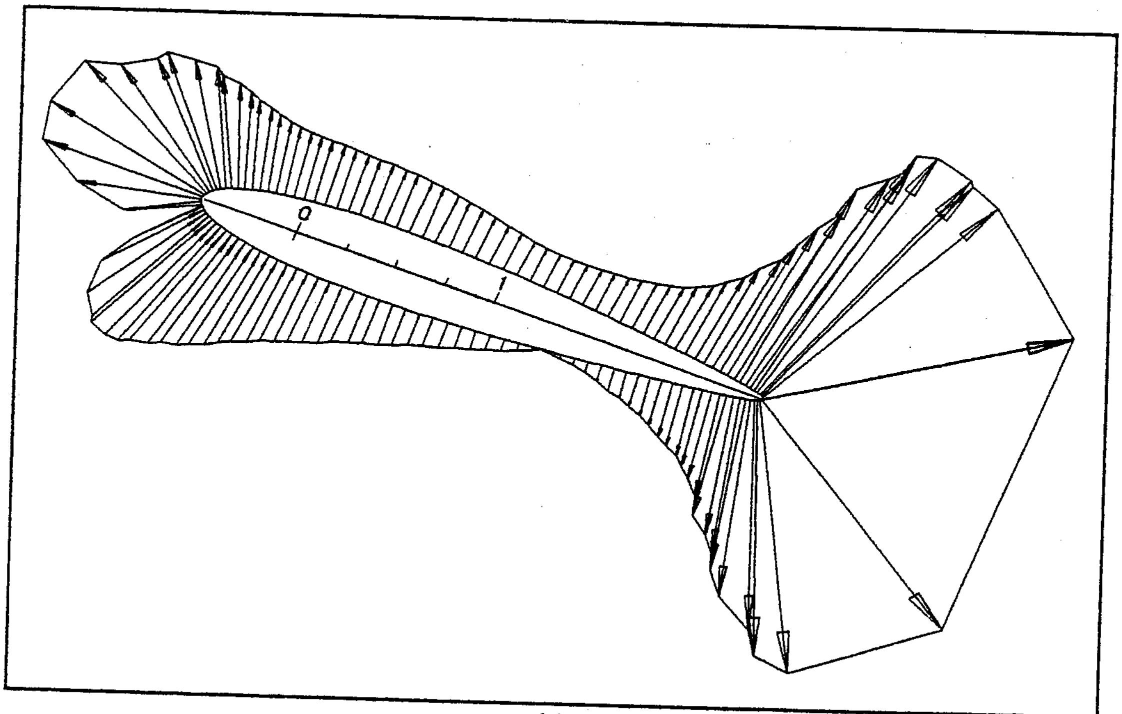

(c)

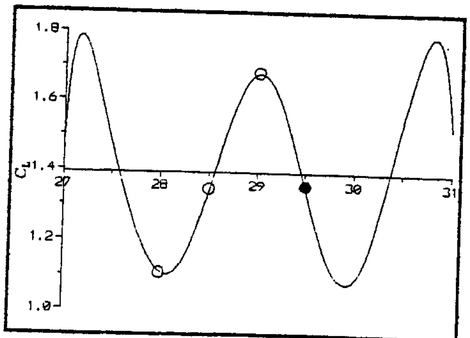

(d)

Fig.6.53. For $\alpha=20^{\circ}$ and $T=29.5$, colour coded vorticity distributions (a); velocity profiles on the body surface and streamlines pattern (b); pressure distribution on the body surface (c); and C_L with respect to nondimensional time (d). Full circle on the C_L-T diagram indicates $T=29.5$.

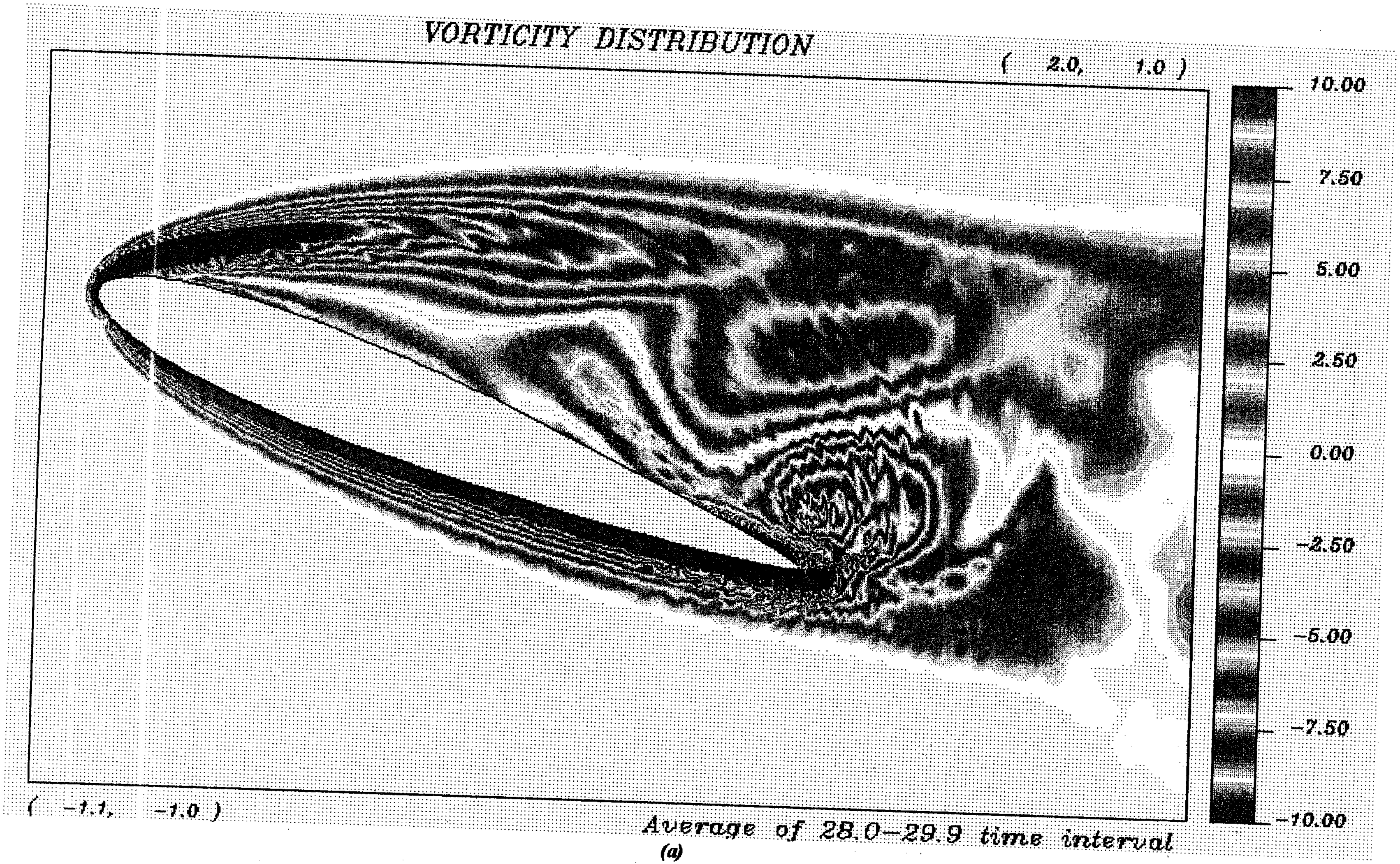

(a)

(For legend see next page)

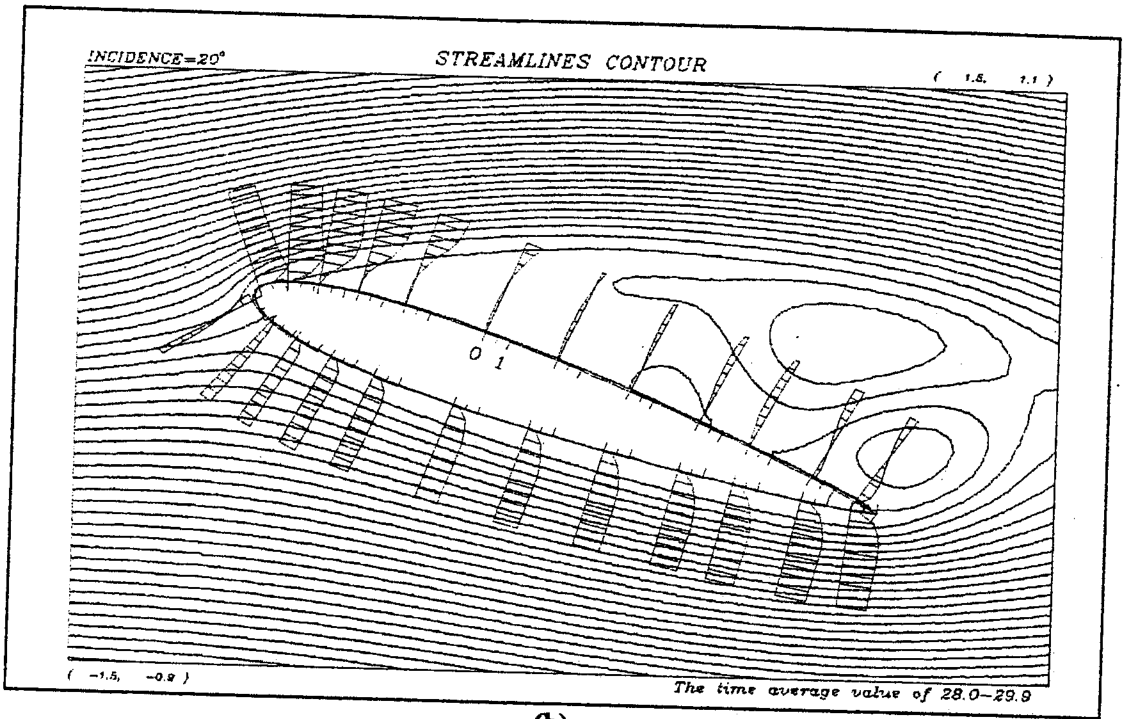

(b)

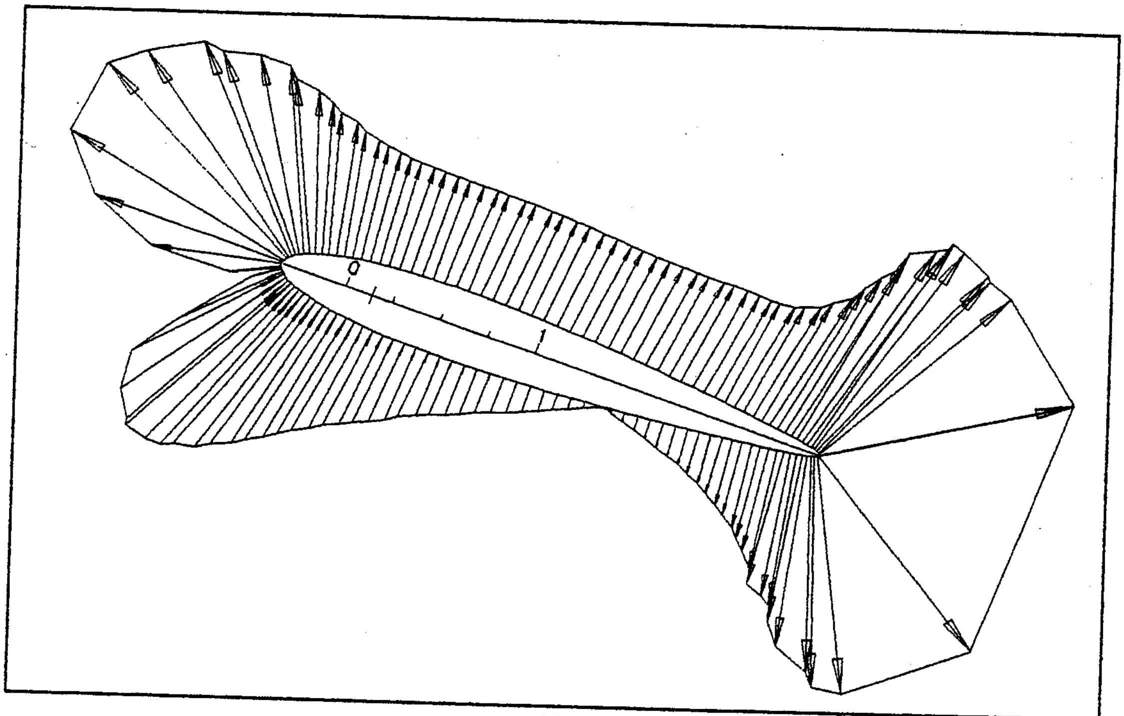

(c)

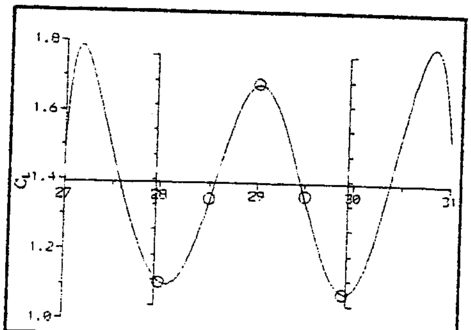

(d)

Fig.6.54. For $\alpha=20^\circ$ and average values in ***28.0-29.9*** nondimensional time interval of colour coded vorticity distributions (a); velocity profiles on the body surface and streamlines pattern (b); pressure distribution on the body surface (c); and C_L with respect to nondimensional time (d).

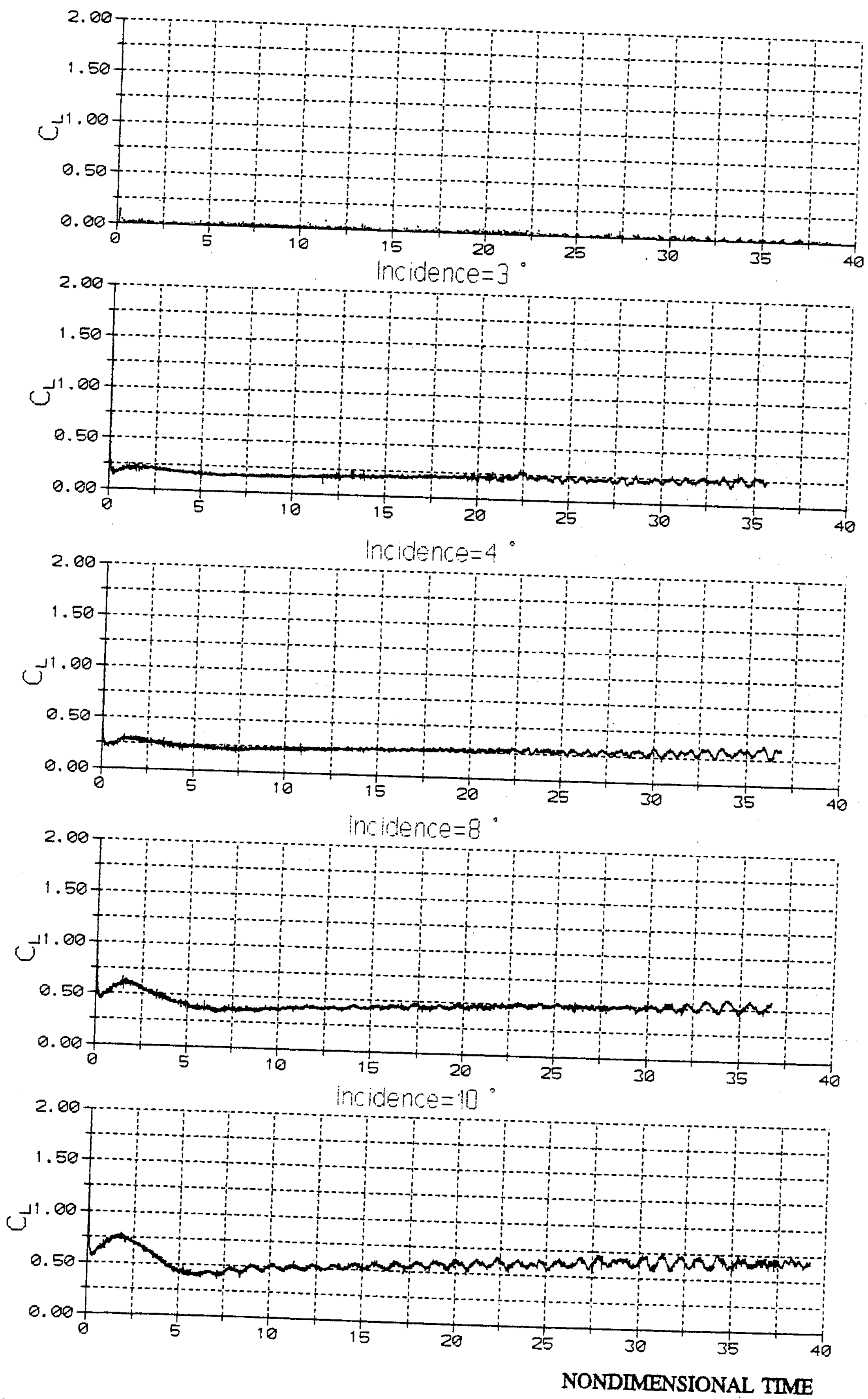

Fig.6.55. The variation of lift coefficient C_L vs. nondimensional time with respect to incidence.

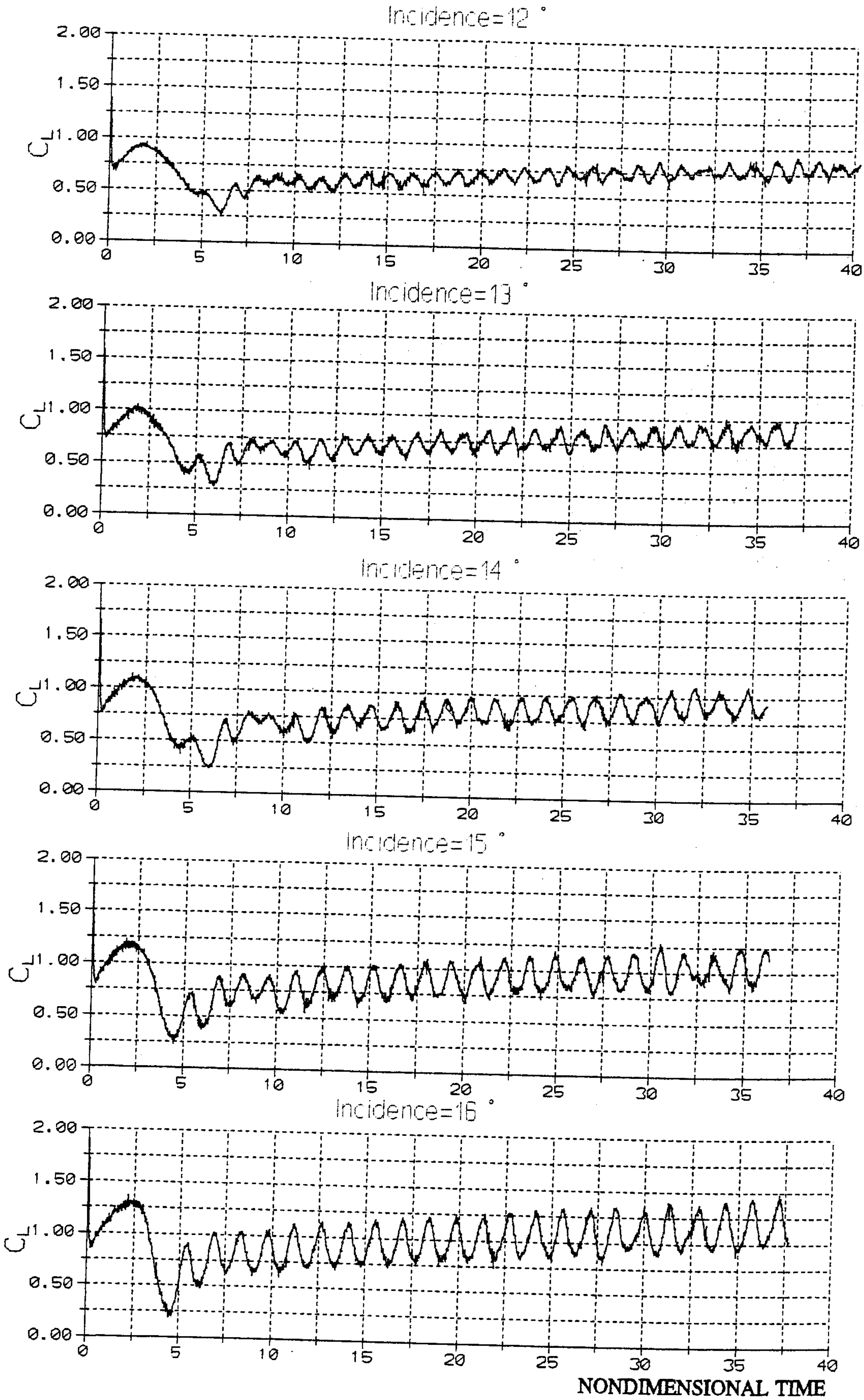

Fig.6.56. The variation of lift coefficient C_L vs. nondimensional time with respect to incidence.

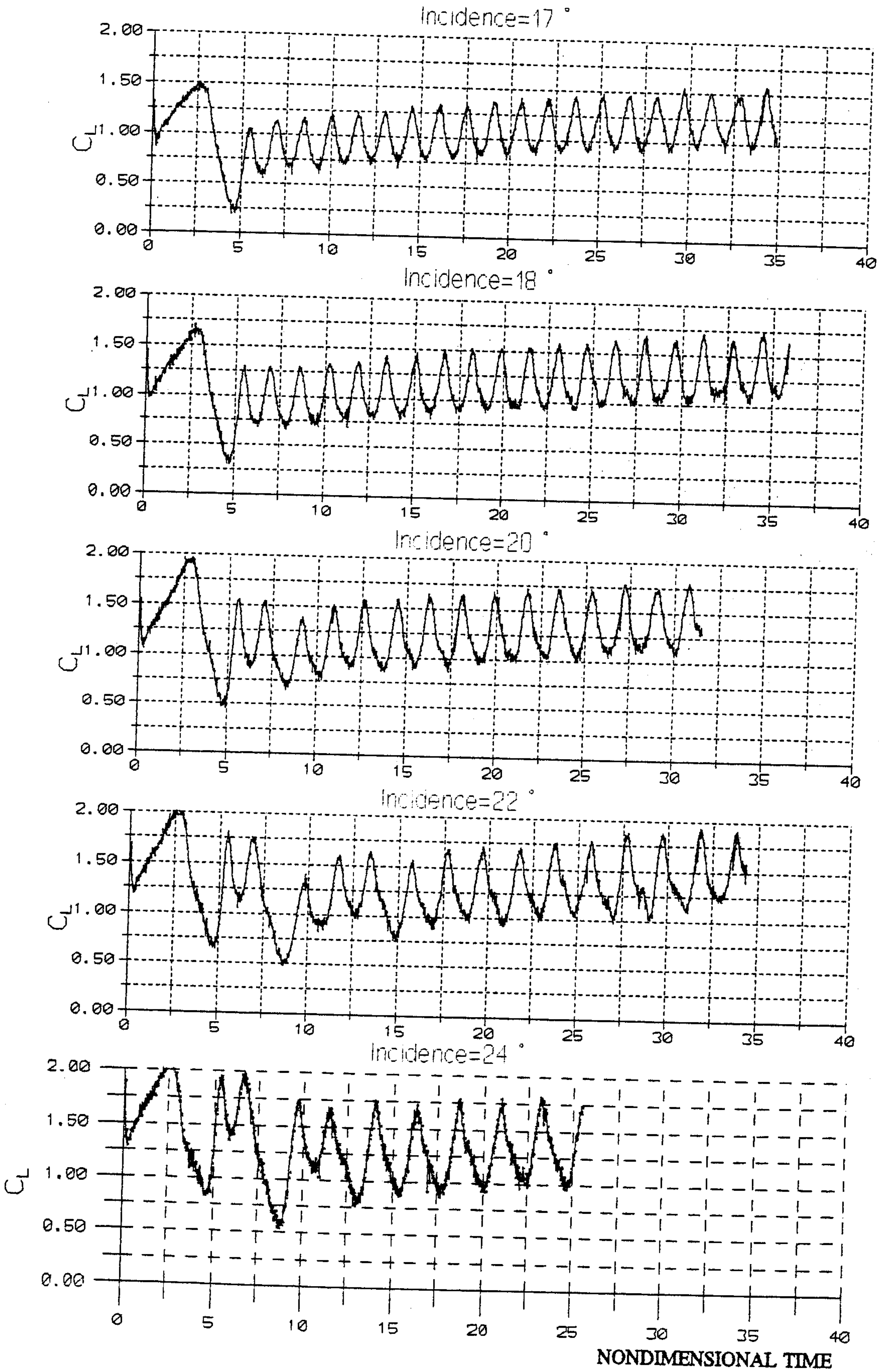

Fig.6.57. The variation of lift coefficient C_L vs. nondimensional time with respect to incidence.

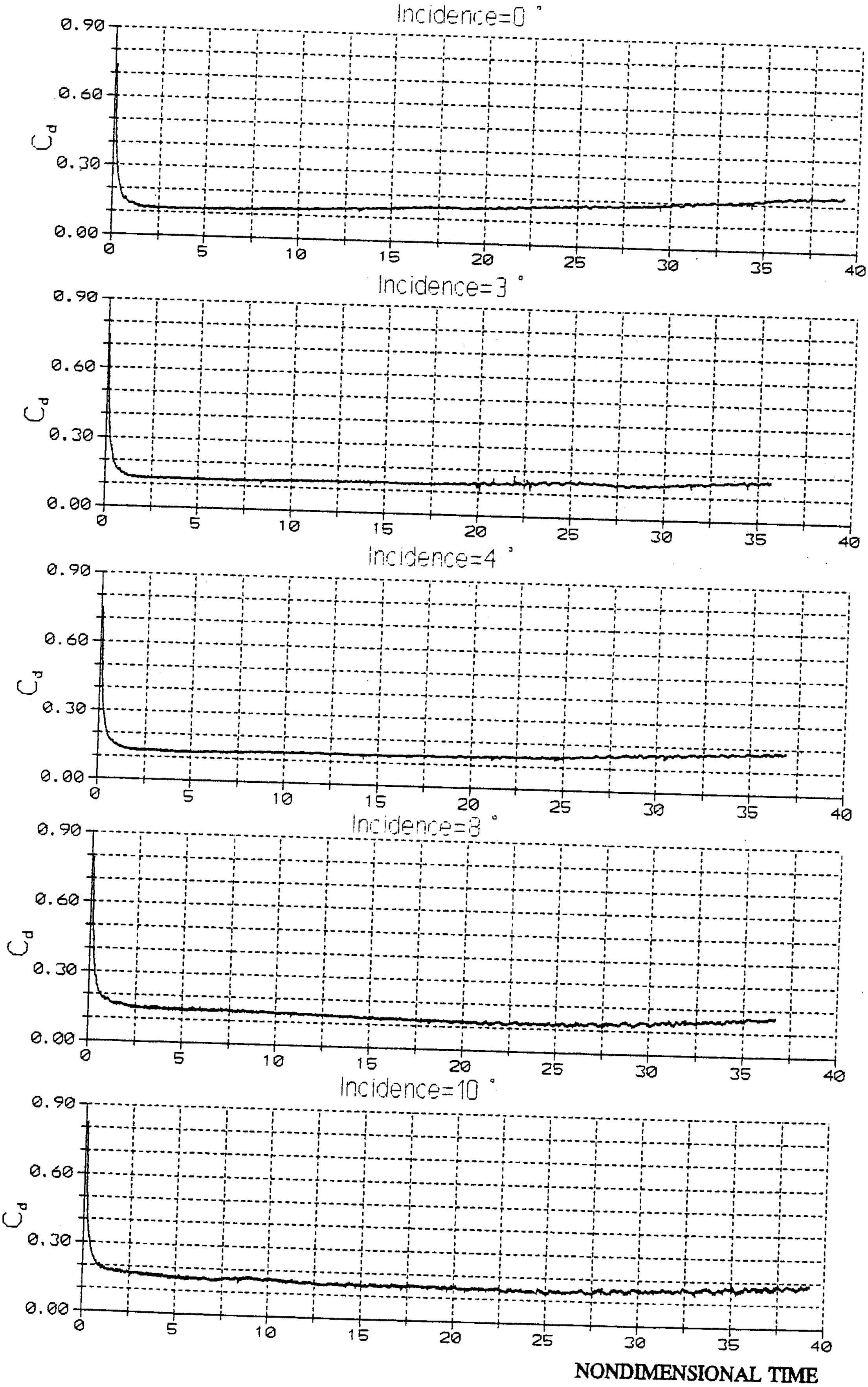

Fig.6.58. The variation of drag coefficient C_D vs. nondimensional time with respect to incidence.

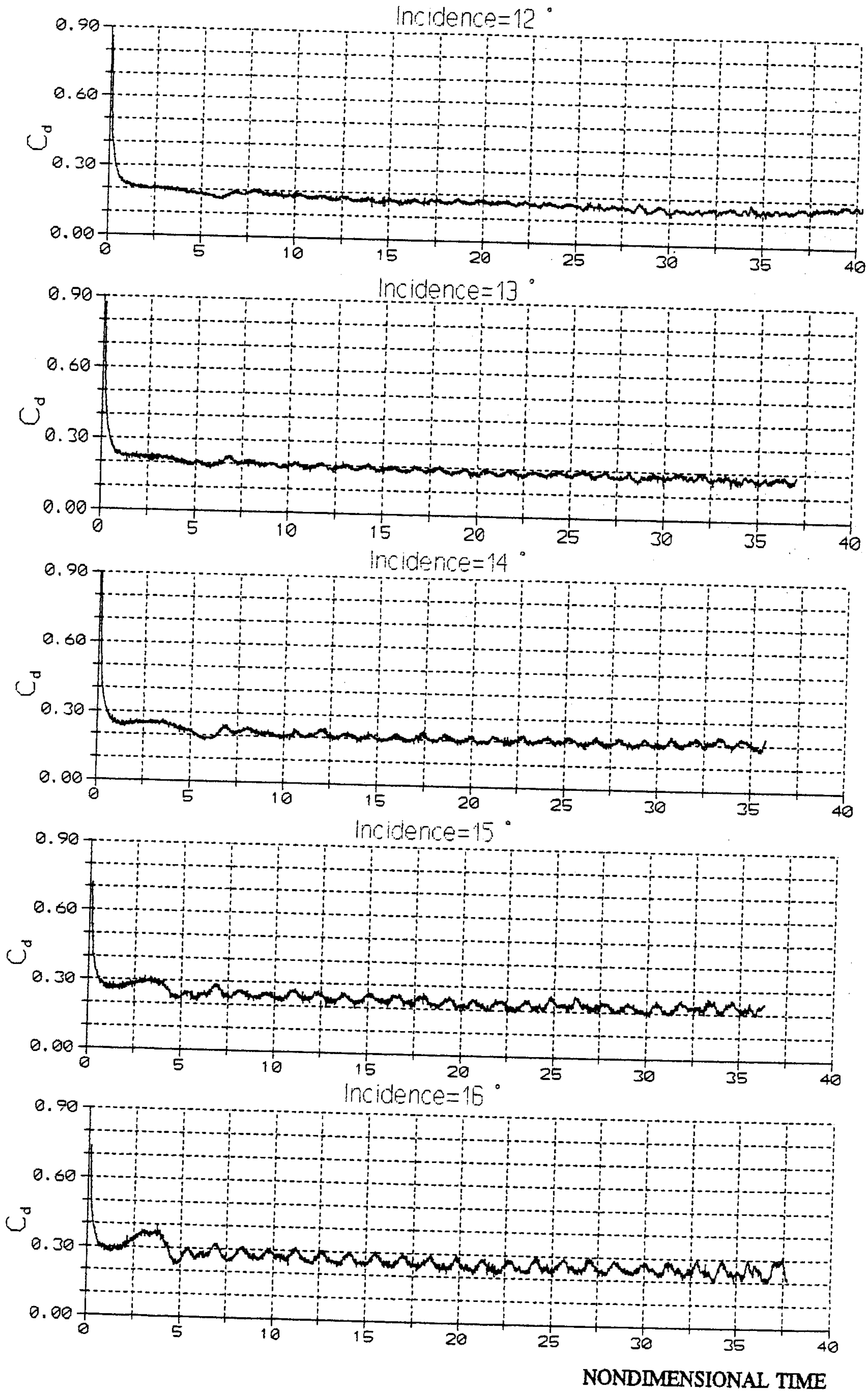

Fig.6.59. The variation of drag coefficient C_D vs. nondimensional time with respect to incidence.

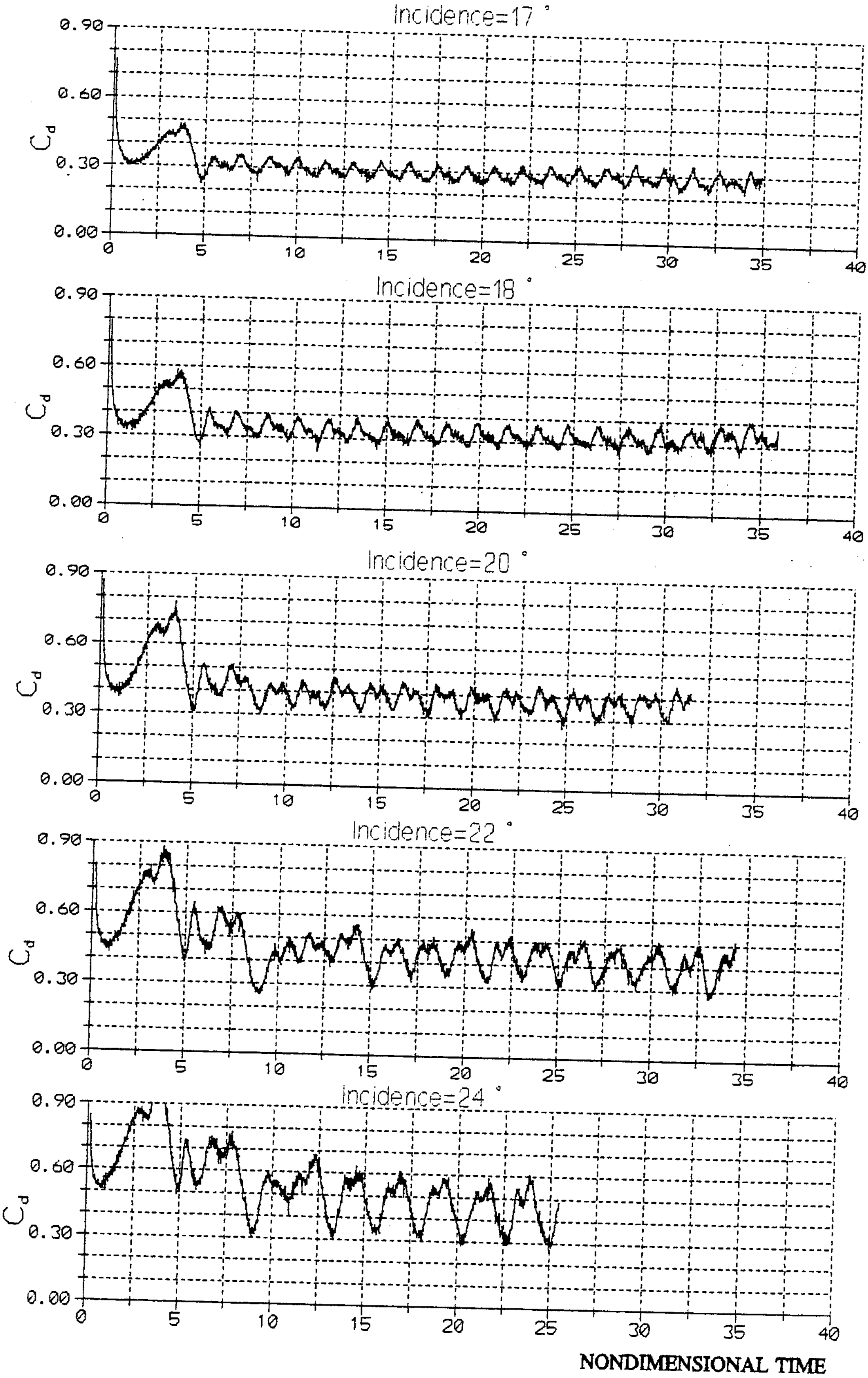

Fig.6.60. The variation of drag coefficient C_D vs. nondimensional time with respect to incidence.

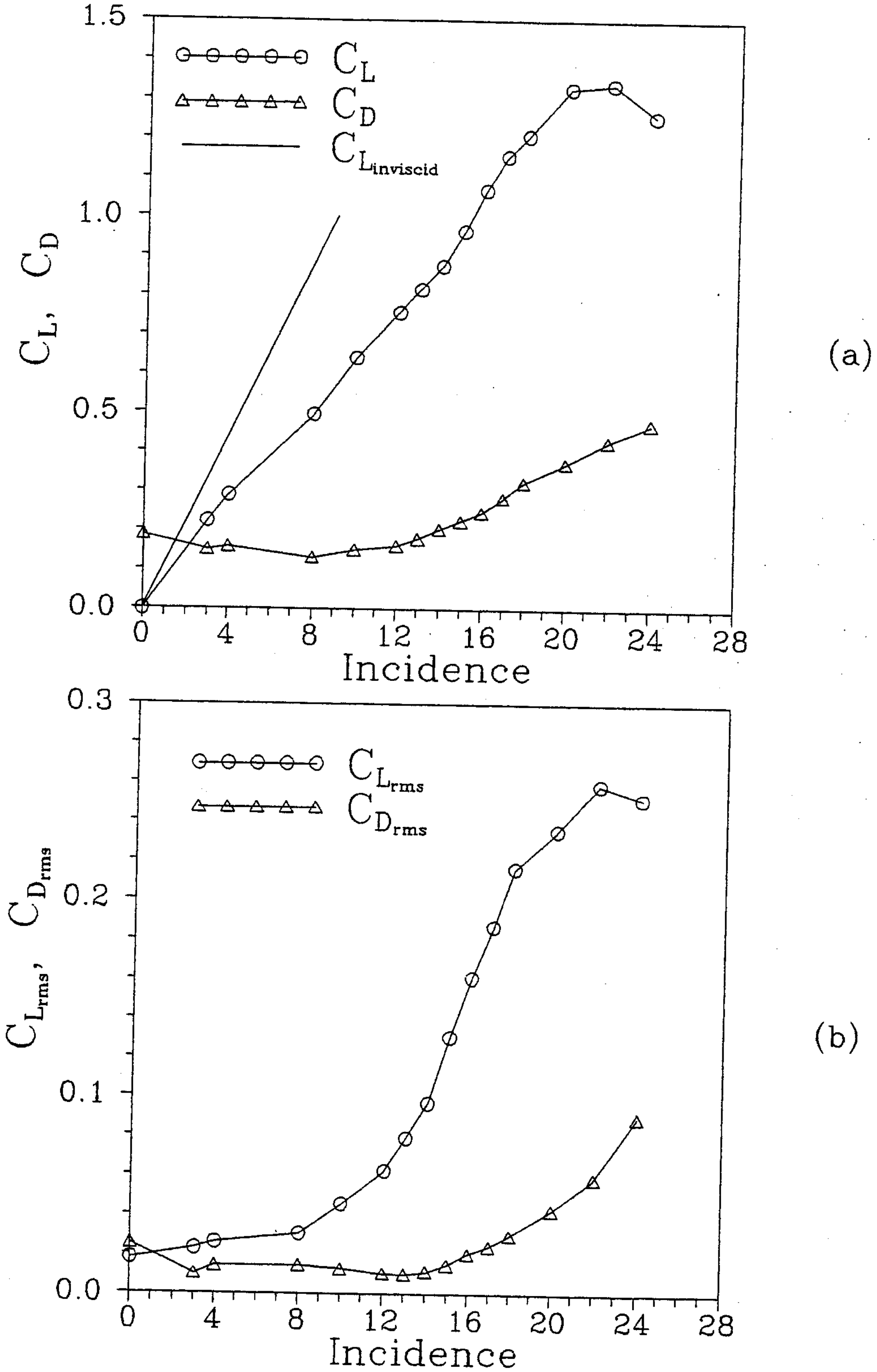

Fig.6.61. Variations of lift coefficient C_L and drag coefficient C_D vs. incidence (Straight line is lift coefficient with respect to inviscid theory) (a); rms value of C_L and C_D fluctuations with respect to time vs. incidence (b).

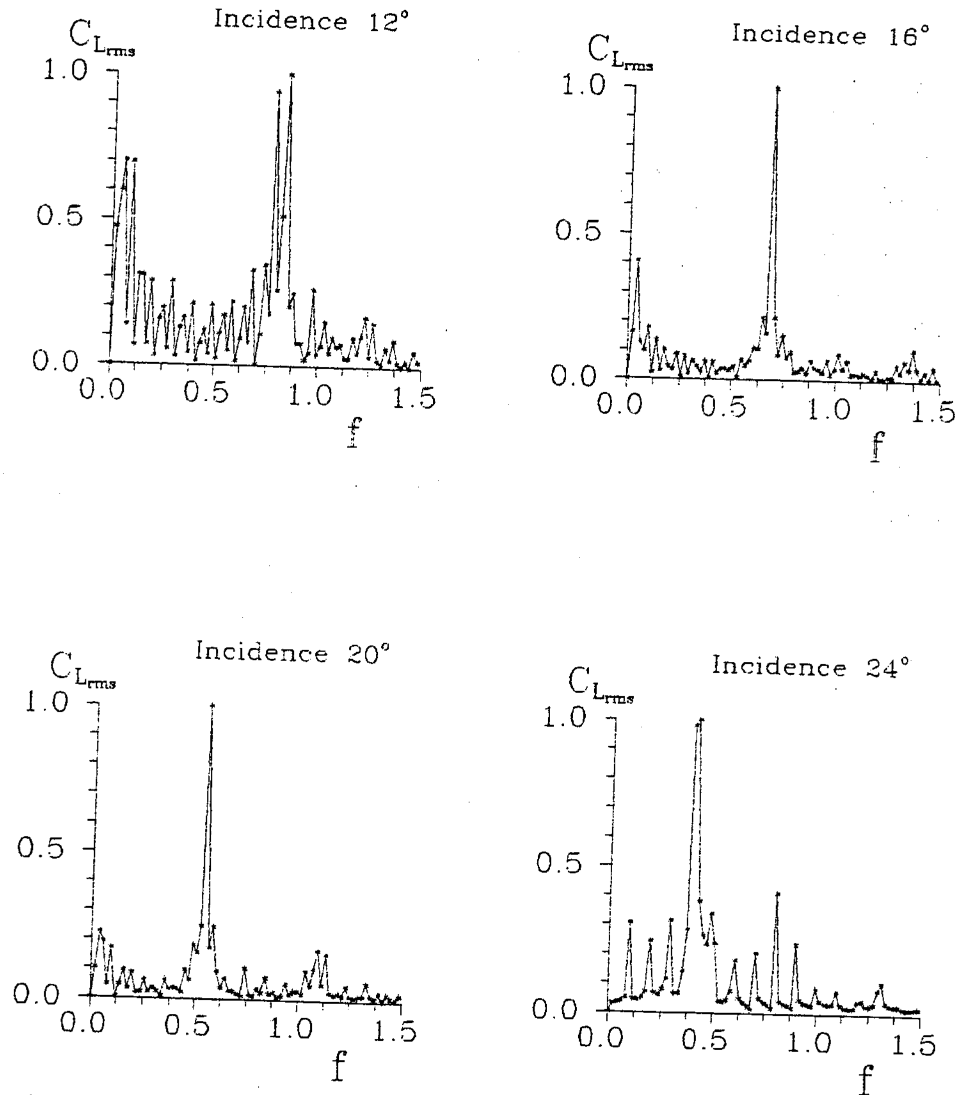

Fig.6.62. Spectrum of lift coefficient fluctuations (C_{Lrms}) for various incidence.

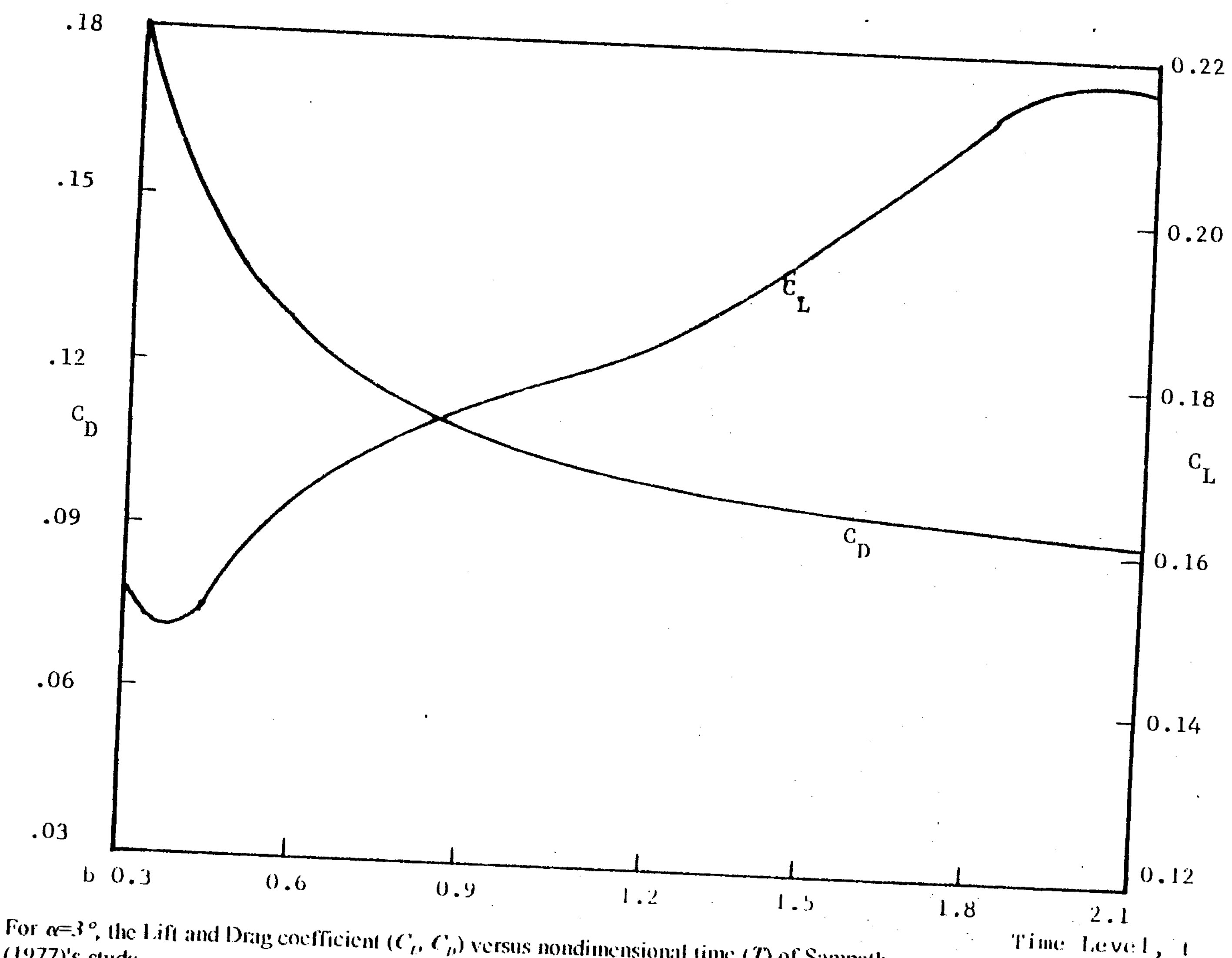

Fig.6.63. For $\alpha=3°$, the Lift and Drag coefficient (C_L, C_D) versus nondimensional time (T) of Sampath (1977)'s study.

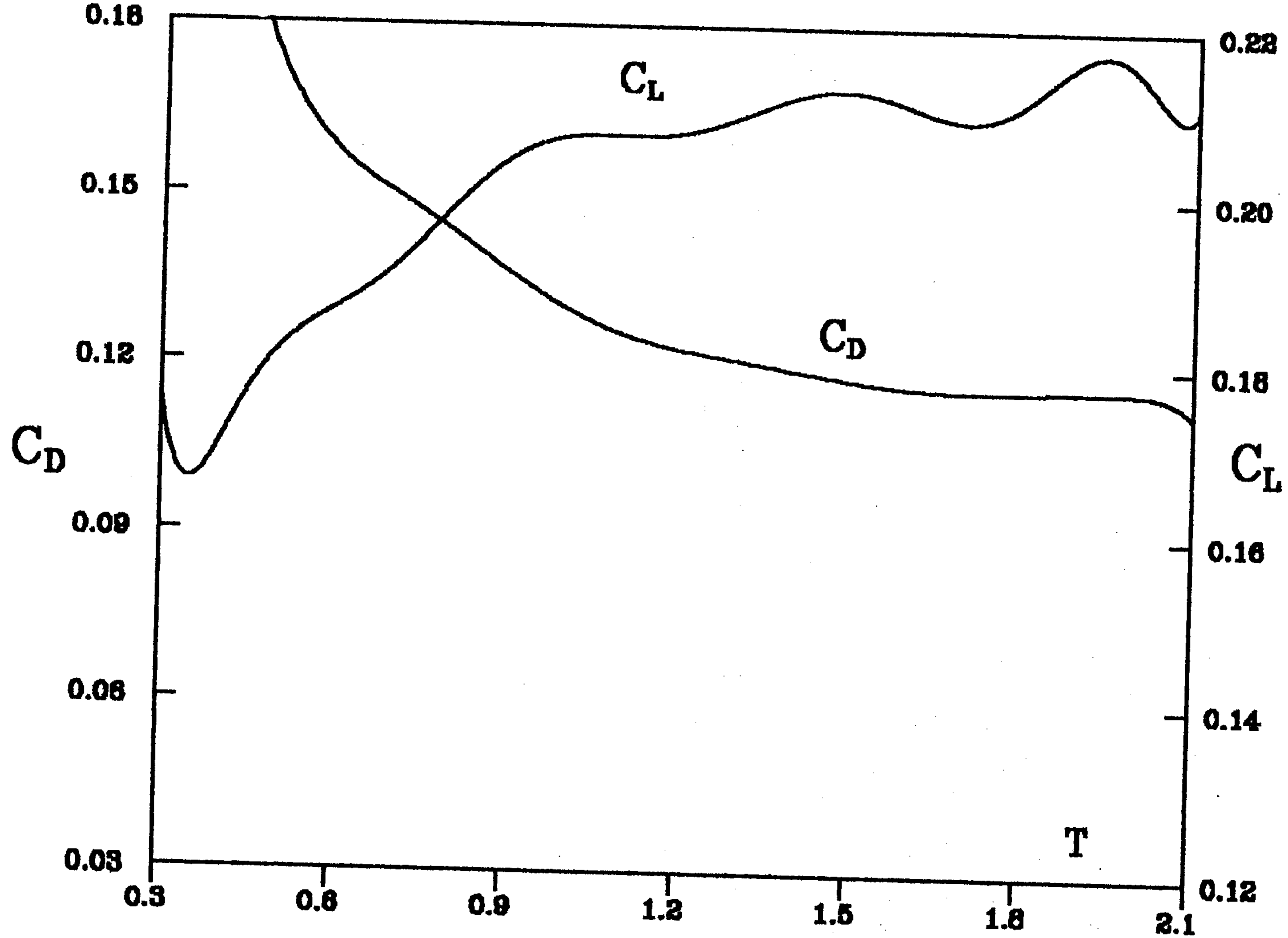

Fig.6.64. For $\alpha=3°$, the Lift and Drag coefficient (C_L, C_D) versus nondimensional time (T).

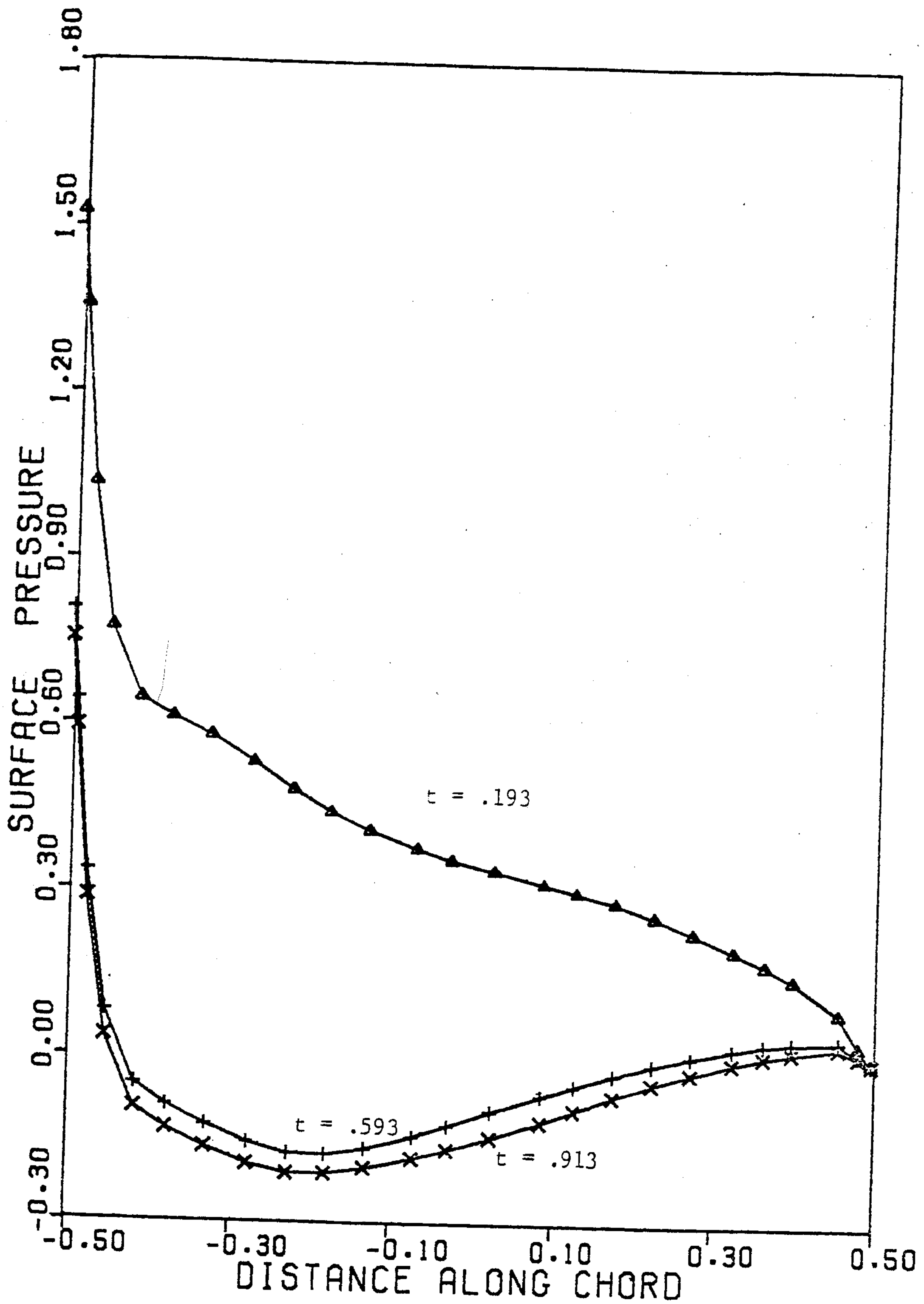

Fig.6.65. At $\alpha=0^{\circ}$, Pressure distribution on the airfoil surface of Sampath (1977)'s study. Reference pressure is trailing edge pressure which is assumed to be zero.

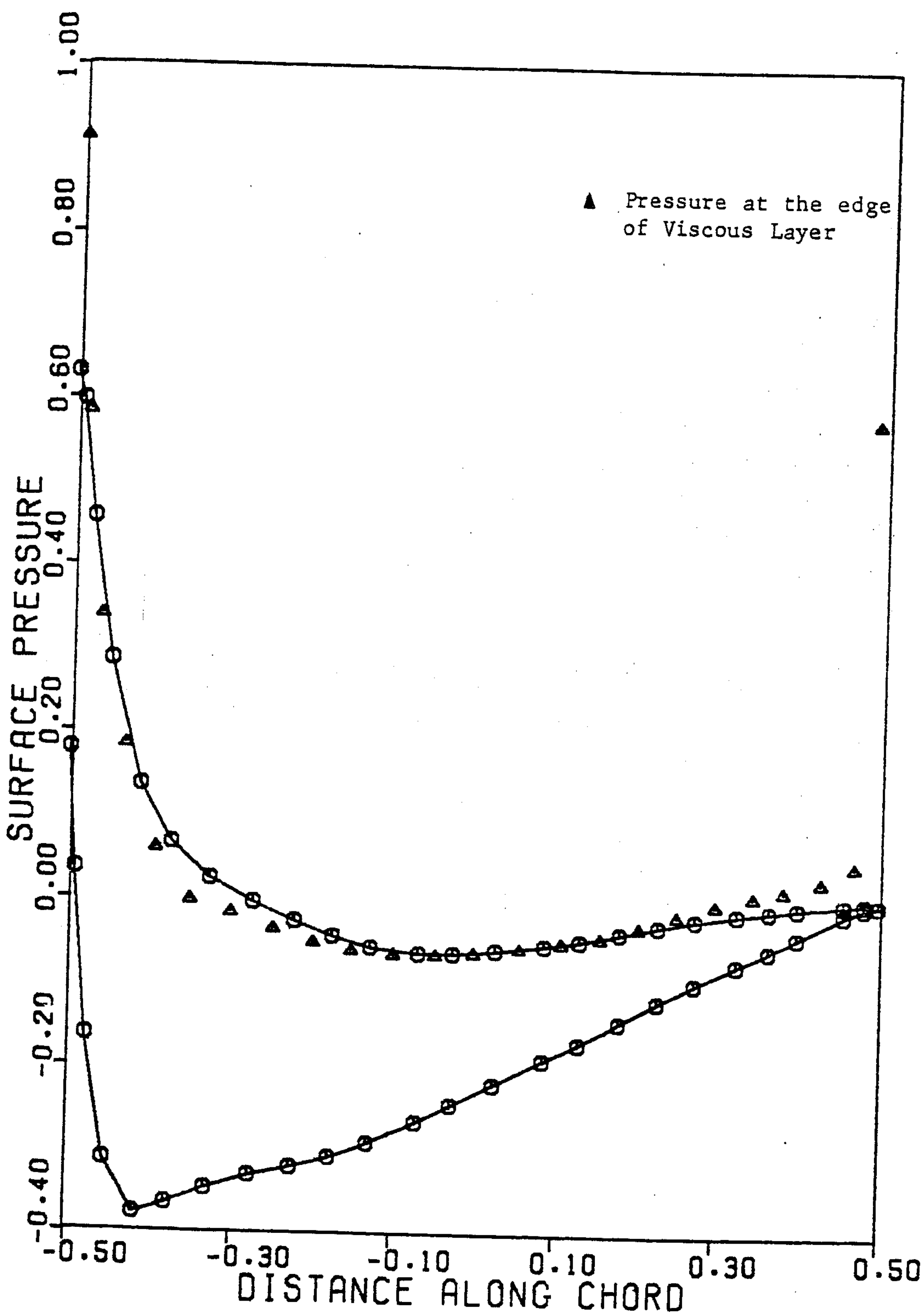

Fig.6.66. At $\alpha=3^{\circ}$, Pressure distribution on the airfoil surface of Sampath (1977)'s study. Reference pressure is trailing edge pressure which is assumed to be zero.

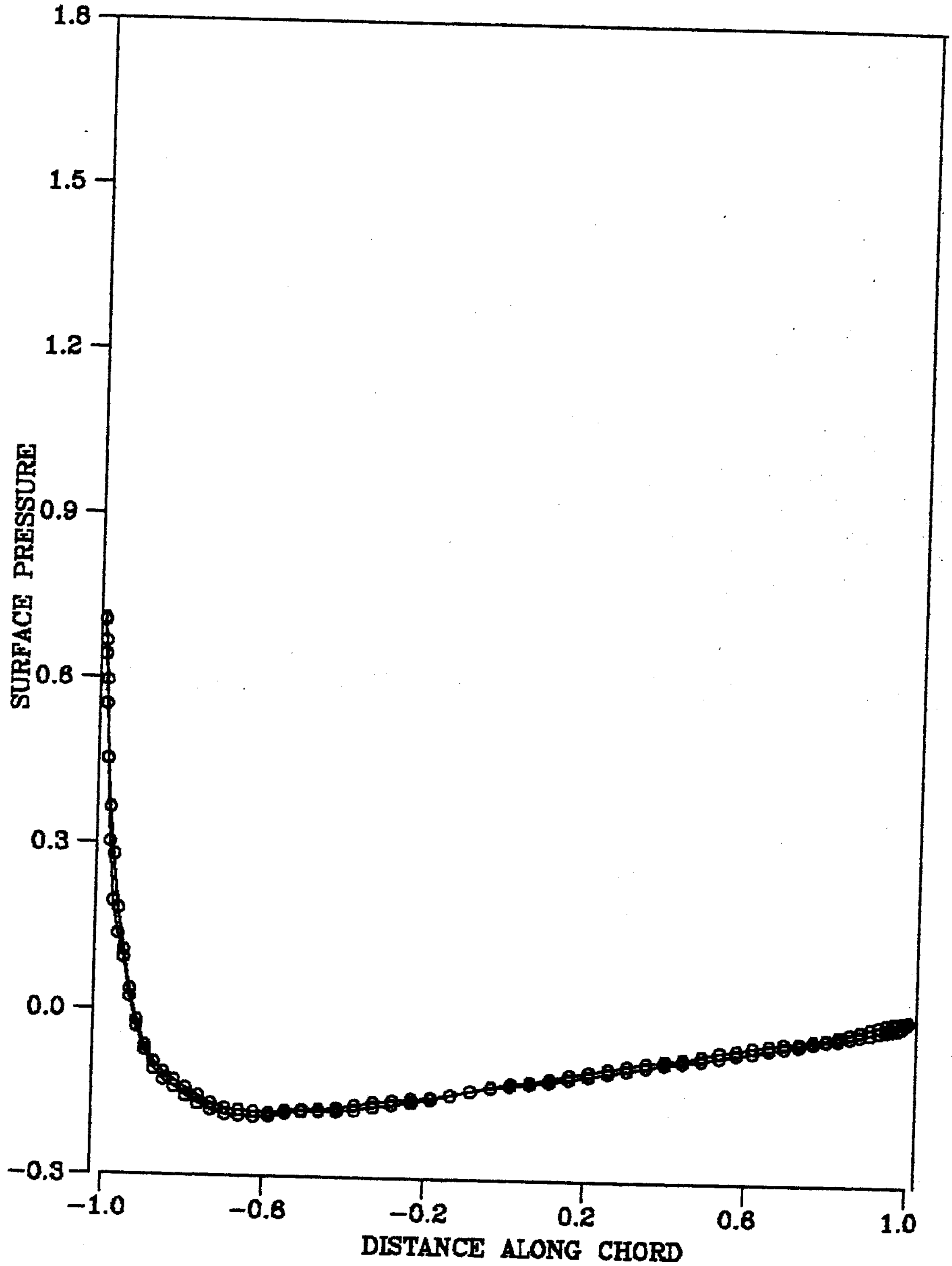

Fig.6.67. At $\alpha=0^{\circ}$ and $T=29.4$, Pressure distribution on the airfoil surface. Reference pressure is trailing edge pressure which is assumed to be zero.

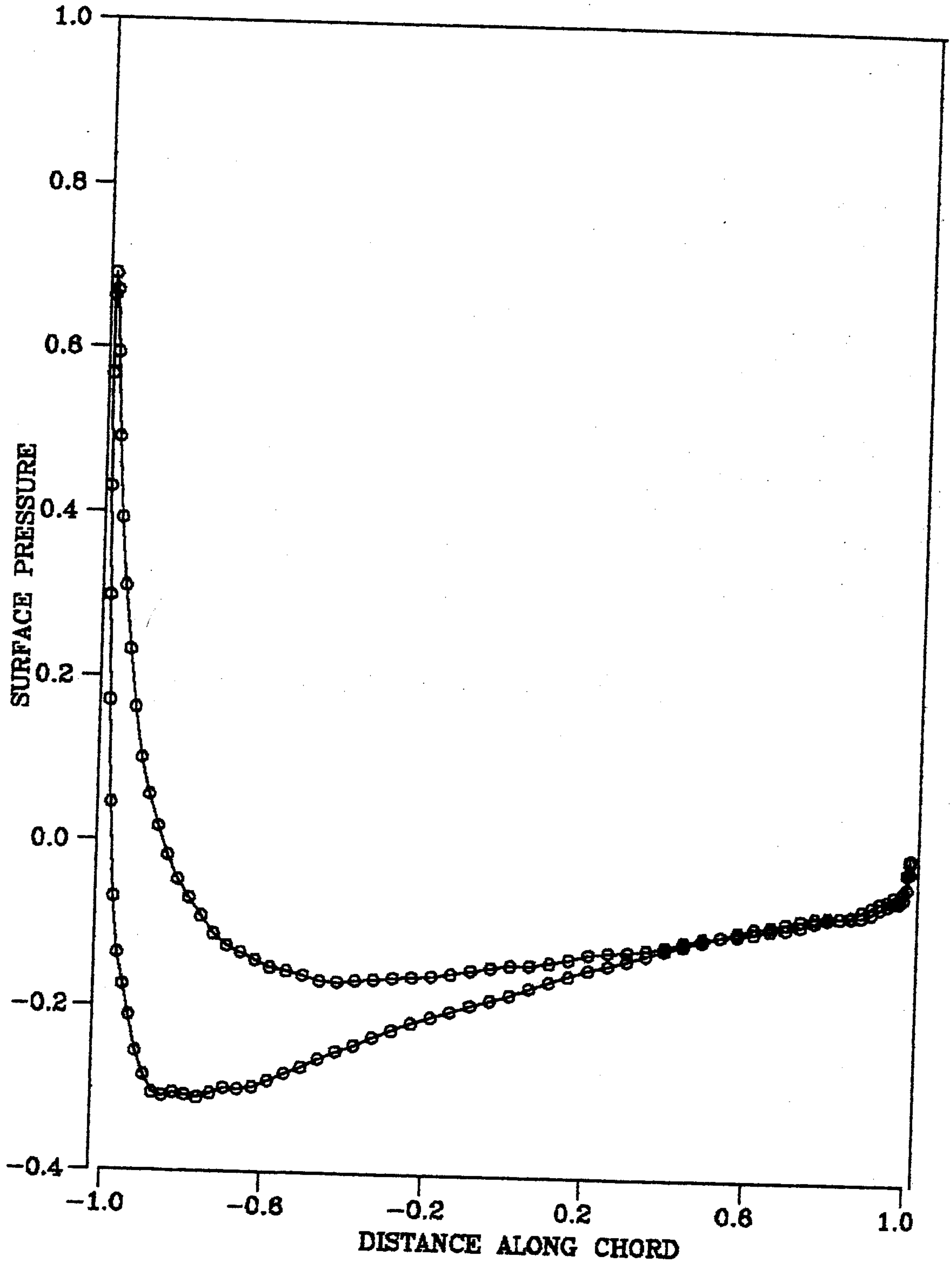

Fig.6.68. At $\alpha=3^{\circ}$ and $T=26.0$, Pressure distribution on the airfoil surface. Reference pressure is trailing edge pressure which is assumed to be zero.

REFERENCES

Apelt, C.J., West, G.S. & Szewczyk, A.A., (1973), The Effects of Wake Splitter Plates on The Flow Past a Circular Cylinder in the Range $10^4 < Re < 5x10^4$, JFM, Vol. 61, part 1, pp 187-198.

Barbi, C., Favier, D.P., Maresca, C.A. and Telions, D.P., (1986), Vortex Shedding and Lock-On of a Circular Cylinder in Oscillatory Flow, JFM, Vol. 170, pp 527-544, 1986.

Bearman, P.W., (1965), Investigation of the Flow Behind a Two Dimensional Model with a Blunt Trailing Edge and Fitted with Splitter Plates, JFM, Vol. 21, Part 2, pp 241-255.

Benson, M.G., Bellamy-Knights, P.G. & Gerard, J. H., (1989), A Viscous Splitting Algorithm Applied to Low Reynolds Numbers Flows Around a Circular Cylinder, Journal of Fluids and Structures 3, pp 439-479.

Blevins, R.D., (1974), Flow-Induced Vibration, Von Nostrand Reinhold Co.

Cete, A.R. & Unal, M.F., (1992), Effects of Splitter Plate on Wake Formation from a Circular Cylinder, Proceedings of the First European Computational Fluid Dynamics Conference, 7-11, September, Brussels, Belgium, Vol. 1, pp 349-356.

Cete, A.R., (1989), The Effect of Splitter Plate on the Wake of a Circular Cylinder, Discrete Vortex Method, Graduation Thesis, Istanbul Technical University.

Chang, P.K., (1970), Separation of Flow, Pergamon Press.

Chorin, A.J., (1973), Numerical Study of Slightly Viscous Flow, JFM, Vol. 57., Part 4, pp. 785-796.

Clements, R.R., (1973), An Inviscid Model of Two Dimensional Vortex Shedding, JFM, Vol. 57, part 2, pp 321-336.

Cozens, P.D., (1988), Numerical Modelling of Roll Damping on Bores, Ph.D. Thesis, Faculty of Engineering, University of London.

Detemple-Laake, E. and Eckelmann, H., (1989), Phenomenology of Karman Vortex Streets in Oscillatory Flow, Experiments in Fluids, Vol. 7, pp 217-227.

Dwyer, H.A., and McCroskey, W.J., (1973), Oscillating Flow Over a Cylinder At Large Reynolds Number, JFM., Vol. 61, pp 753-767.

Gerard, J.H., (1966), The Mechanics of the Formation Region of Vortices Behind Bluff Bodies, JFM, Vol. 25, part 2, pp 401-413.

Goldstein, M.A., et. al., (1965), Modern Developments in Fluid Dynamics, Vol. II, Dover Public ations, Inc.

Graham, J.M.R. & Cozens, P.D., (1988), Vortex Shedding from Edges Including Viscous Effects, Fluid Dynamics Research, Vol. 3, pp 111-114.

Graham, J.M.R., (1980), The Forces on Sharp-Edges Cylinders in Oscillatory Flow at Low Keulegan-Carpenter Number, JFM, Vol. 97, part 1, pp 331-346.

Griffin, O.M. & Ramberg, S.E., (1970), Vortex Shedding From a Cylinder Vibration in Line with an Incident Uniform Flow, JFM., Vol. 79, pp 237-271.

Houghton, E.L., Carpenter, P.W., (1993), Aerodynamics for Engineering Students, Fourth Edition, Edward Arnold Co.

Kawai, H., (1990), Discrete Vortex Simulation for Flow around a Circular Cylinder with a Splitter Plate, Journal of Wind Engineering and Industrial Aerodynamics, 33, pp 153-160.

Meneghini, J.R. & Bearman, P.W., (1993), Numerical Simulation of High Amplitude Oscillatory-Flow About a Circular Cylinder Using a Discrete Vortex Method", AIAA Shear Flow Conference, July 6-9, Orlando.

Milne-Thompson, L.M., (1973), Theoretical Aerodynamics, 4th Edition, MacMillan Co.

Misirlioglu, A., (1992), Passive Control of Wake From a Circular Cylinder with a Splitter Plate; Viscous VIC Simulation, M.Sc. Thesis, Istanbul Technical University.

Ongoren, A. and Rockwell, D., (1988), "Flow Structure from on Oscillating Cylinder Part 2. Mode Competition in the Near Wake", JFM, Vol. 191, pp 225-245.

Roache, P.J., (1972), Computational Fluid Dynamics, Hermosa Publishers.

Roshko, A., (1955), On the Wake and Drag of Bluff Bodies, Journal of Aeronautical Sciences, pp 124-132.

Sampath, S., (1977), A Numerical Study of Incompressible Viscous Flow Around Airfoils, Ph.D. Thesis, Georgia Institute of Technology.

Sarpkaya, T. & Schoaff, R.L., (1979), Inviscid Model of Two Dimensional Vortex Shedding by a Circular Cylinder, AIAA J., Vol. 17, No 11, pp 1193-1200.

Sarpkaya, T., (1963), Lift, Drag and Added Mass Coefficients for a Circular Cylinder Immersed In a Time Dependent Flow, Journal of Applied Mechanics, pp 13-15.

Sarpkaya, T., (1968), An Analytical Study of Separated Flow About Circular cylinder, Trans. Am. Soc. Mech. Engrs. J. Basic Engin., 90, pp 511-520.

Sarpkaya, T., (1989), "Computational Method with Vortices-The 1988 Freeman Scholar Lecture", Journal of Fluids and Engineering, Vol. 111/5.

Schlichting, H., (1979), Boundary Layer Theory, 7th Edition, McGraw & Hill Co.

Smith, C.A., Karamcheti, K., (1975), Aerodynamic Sound Generation due to the Interaction of an Unsteady Wake with a Rigid Surface, Second Aeroacoustics Conference, AIAA, paper, No 75-454

Stansby, P.K. & Dixon, A.G.,(1982), The Importance of Secondary Shedding in Two Dimensional Wake Formation at Very High Reynolds Numbers, Aeronautical Quarterly, pp 105-123.

Stansby, P.K., (1981), A numerical Study of Vortex Shedding form One and Two Circular Cylinders, Aeronautical Quarterly.

Strykowski, P.S. & Sreenivosan, K.R., (1990), On the Formation and Suppression of Vortex Shedding at Low Reynolds Number, JFM, vol. 218, pp 71-107

Suhubi, E., (1968), Akışkanlar Mekaniği, Istanbul Teknik Universitesi, Insaat Fakultesi Matbaasi.

Temperton, C., (1979), Direct Methods for the Solution of the Discrete Poisson Equation; Some Comparison, Journal of Computational Physics 31, pp 1-20.

Unal, M.F. & Rockwell, D., (1988), "On Vortex Formation From a Cylinder. Part 2: Control by Splitter Plate Interference", JFM, Vol. 190, pp 513-529.

Unal, M.F., Yilmaz, A. and Cete, A.R., (1992), Discrete Vortex Simulation of Wake rom a Circular Cylinder", The Proceedings of Tenth Anniversary Symposium Department of Aeronautical Engineering, pp 45-54.

Wu, J.C., (1981), "Theory of Aerodynamics Force and Moment in Viscous Flow", AIAA J., 19, No 4.

Wu, J.C., Sankar, N.L., (1977), A Numerical Study of Unsteady Viscous Flows Around Airfoils, Agard Conference Proceedings, No 227, Paper No. 24.

Yilmaz, A., (1990), Modifications of Wakes From Bluff Bodies; Inviscid and Viscous Discrete Vortex Method, M.Sc. Thesis, Istanbul Technical University.

APPENDIX A

Finite Difference Forms on Rectangular Mesh

The basis of the approximation of flow equations used in this study is the Eulerian concept of discretising the flow field onto a mesh to calculate quantities such as velocity and circulation. According to this concept, equations are derived for a rectangular mesh and each term in flow equations, used for the diffusion and convection processes are obtained in discretized form. First and second order difference formulae are used for constant mesh spacing in -x direction and expanding unequal, mesh spacing in -y direction. Also the Fourier transformation of Poisson's equation as taken in -x direction. The discretized forms can be derived by using Taylor series expansion. In general, let f(x) be a function whose differences are required to be established at a point "p", provided that f_{p-1}, f_p, f_{p+1} are given.

For the unequal mesh spacing, definition of mesh intervals is;

$$\Delta y_p = y_{p+1} - y_p \tag{A.1}$$

$$\Delta y_{p-1} = y_p - y_{p-1} \tag{A.2}$$

and the ratio of these is

$$s = \frac{\Delta y_p}{\Delta y_{p-1}} \tag{A.3}$$

Taylor series with the definitions above are:

$$f_{p+1} = f_p + f_p^{\prime} \Delta y_p + \frac{1}{2} f_p^{\prime\prime} \Delta y_p^2 + \frac{1}{6} f_p^{\prime\prime\prime} \Delta y_p^2 + \ldots \tag{A.4}$$

$$f_{p-1} = f_p - f_p^{\prime} \Delta y_{p-1} + \frac{1}{2} f_p^{\prime\prime} \Delta y_{p-1}^2 + \frac{1}{6} f_p^{\prime\prime\prime} \Delta y_{p-1}^2 + \ldots \tag{A.5}$$

Subtracting equation (A.4) from equation (A.5) gives

$$f_p^{/}=\frac{f_{p+1}-f_p-1}{\Delta y_p+\Delta y_{p-1}}+\frac{1}{2}f_p^{///}\frac{\Delta y_p}{s}(1-s)+O(\Delta y_p)^2 \tag{A.6}$$

Taking only the first term in the right hand side gives a first order accuracy; for s = 1 accuracy is second order. A second order accurate expression for $f_p^{//}$ obtained from A.4 and A.5 is as follows

$$f_p^{///}=\frac{2s}{s+1}\frac{sf_{p-1}-(1+s)f_{p+1}}{\Delta y_p^2} \tag{A.7}$$

From these foregoing expression it is now easy to discretise the equations in the finite difference form proper for the solution on a rectangular mesh in cartesian coordinates. Thus the diffusion equation in two-dimension becomes;

$$\omega_{i,j}^{k}=\omega_{i,j}^{n}+\Delta t\nu\left[\frac{\omega_{i-1,j}-2\omega_{i,j}^{n}+\omega_{i+1,j}^{n}}{\Delta x_i^2}\right.$$
$$\left.+\frac{2s}{(s+1)}\frac{s\omega_{i,j-1}-(1+s)\omega_{i,j}^{n}+\omega_{i,j+1}}{\Delta y_j^2}\right]\left|\frac{\partial\zeta}{\partial z}\right|_{i,j}^2 \tag{A.8}$$

where $\left|\frac{d\zeta}{dz}\right|_{i,j}^2$ term is the transformation modulus, "n" refers the condition at time "t" and "k" refers to the intermediate condition between "t" and "t + Δt". In fact, the method uses mostly the circulation values as mentioned before. Mesh circulation is defined here as;

$$\Gamma_{i,j}=\omega_{i,j}\Delta x_i\frac{(\Delta y_j+\Delta y_{j-1})}{2} \tag{A.9}$$

then in terms of circulation the diffusion equation can be rewritten as;

$$\Gamma_{i,j}^{k} = \Gamma_{i,j}^{n} + \Delta t\nu\left[\frac{\Gamma_{i-1,j}^{n}-2\Gamma_{i,j}^{n}+\Gamma_{i+1,j}^{n}}{\Delta x^2}+\frac{2s}{s+1}\frac{(\Delta y_j+\Delta y_{j+1})}{\Delta y_j^2}\right.$$
$$\left.\left(\frac{s\Gamma_{i,j-1}}{(\Delta y_{j-1}+\Delta y_{j-2})}-\frac{(1+s)\Gamma_{i,j}^{n}}{(\Delta y_j+\Delta y_{j-1})}+\frac{\Gamma_{i,j+1}^{n}}{(\Delta y_{j+1}+\Delta y_j)}\right)\right]\left|\frac{\partial\zeta}{\partial z}\right|_{i,j}^2 \tag{A.10}$$

Mesh velocities appear in discretized form as follows;

$$u_{i,j}=\frac{\Psi_{i,j+1}-\Psi_{i,j-1}}{\Delta y_j+\Delta y_{j-1}}\left|\frac{d\zeta}{dz}\right|_{i,j}^2 \tag{A.11}$$

$$v_{i,j}=\frac{\psi_{i+1,j}-\psi_{i-1,j}}{2\Delta x}\left|\frac{d\zeta}{dz}\right|^2_{i,j} \tag{A.12}$$

and Poisson's equation is;

$$\frac{\psi_{i-1,j}+\psi_{i+1,j}}{\Delta x_i^2}+\frac{2s}{s+1}\,\frac{s\psi_{i,j-1}-(1+s)\psi_{i,j}+\psi_{i,j+1}}{\Delta y_i^2}$$

$$=-\frac{2\Gamma_{i,j}}{\Delta x_i(\Delta y_j+\Delta y_{j-1})} \tag{A.13}$$

APPENDIX B

Fast Solver for Poisson's Equation

In Appendix A is has been found that the discretized form of Poisson's equation is

$$\frac{\psi_{i-1,j}-2\psi_{i,j}+\psi_{i+1,j}}{\Delta x_i^2}-\frac{2s}{s+1}\frac{s\psi_{i,j-1}-(1+s)\psi_{i,j}+\psi_{i,j+1}}{\Delta y_j^2}$$

$$=-\frac{2\Gamma_{i,j}}{\Delta x_i(\Delta y_j+\Delta y_{j-1}}\qquad\text{(B.1)}$$

This equation is solved by a direct method. In doing this, it is rearranged to form a tridiagonal system suitable for the use of Gaussian elimination technique:

Taking the Fourier transformation of the above equation along -x direction; one obtains;

$$-k^2\Psi_{i,j}+\frac{2s}{s+1}\frac{s\Psi_{i,j-1}-(1+s)\Psi_{i,j}+\Psi_{i,j+1}}{\Delta y_j^2}=-\frac{2G_{i,j}}{\Delta x_i(\Delta y_j+\Delta y_{j-1})}\qquad\text{(B.2)}$$

where "k" is the wave number of transformation, "G" is the transformation of circulation and "Ψ" is transformation of "ψ" along x direction that is;

$$\Psi=\int\psi\,\exp(-ikx)dx\qquad\text{(B.3)}$$

or in discretized form

$$\Psi_{i,k}=\sum_{j=0}^{N-1}\exp(2\pi ijk/N)\psi_{i,j}\qquad(k=0,1,2,\dots N-1)\qquad\text{(B.4)}$$

Using this transformation, Poisson's equation becomes

$$\alpha_j \Psi_{k,j+1} + \beta_j \Psi_{k,j} + \epsilon_j \Psi_{k,j+1} \tag{B.5}$$

with the coefficients α, ß, ϵ;

$$\alpha_j = \frac{2s}{(s+1)}, \quad \beta_j = (-k^2 \Delta y_j^2 - 2s), \quad \epsilon_j = \frac{2_s^2}{(s+1)} \tag{B.6}$$

This tridiagonal system may now be solved by Gaussian elimination technique to obtain Ψ values for the entire mesh. Then taking the reverse transformation of Ψ by using the expression below gives the stream function ψ values on the mesh.

$$\psi_{i,k} = \sum_{k=0}^{N-1} \exp(-2\pi ijk \,/\, N)\Psi_{i,j} \qquad (j=0,1,2,\ldots N-1) \tag{B.7}$$

CURRICULUM VITAE

Ali Ruhşen ÇETE was born in Gaziantep on April 29, 1966. He graduated from Gaziantep High School in 1983. He obtained his B.Sc. degree from Istanbul Technical University, Department of Aeronautical Engineering, in 1989. Same year he started M.Sc. studies in Aeronautical Engineering at Institute of Science and Technology of ITU. Throughout He has been employed as a research assistant by the Faculty of Aeronautics and Astronautics during that period. He is married.